Electroosmosis in Nanoporous Membranes: Connecting Material Properties to Flow Behaviour

Leese, Hannah

Award date:
2013

Awarding institution:
University of Bath

Electroosmosis in Nanoporous Membranes: Connecting Material Properties to Flow Behaviour

Hannah Leese

A thesis submitted for the degree of Doctor of Philosophy

University of Bath

Department of Chemical Engineering

May 2013

Declaration

This thesis comprises original work except for any collaboration acknowledged and highlighted within the text. Chapter 6 Section 6.1 presents results from the collaboration with Mr Kah Peng Lee and the modelling in Section 6.2 of AFM force measurements was conducted by Mr Chu Wu. In Chapter 8, the modelled data was conducted by Dr Francesco Calabrò and Dr Davide Mattia.

Abstract

The development of nanoporous materials has received considerable attention in nanofluidic studies in recent years. Furthering earlier research, the present thesis offers a systematic study of two nanoporous materials—nanoporous alumina membranes and carbon nanotube membranes—with a view to establishing their electroosmotic and fluid-flow behaviour at the nanoscale. The nanoporous alumina membranes were studied for their own electroosmotic and fluid-flow properties, and utilised as templates for the production of the carbon nanotube membranes also investigated in this study. The advanced control provided by the fabrication processes of both materials allowed for systematic investigations into the effects of pore diameter and surface chemistry on both electroosmotic and pressure-driven flows.

Nanoporous alumina membranes were developed with pore diameters of < 10 nm. The effect of nanostructure and surface chemistry on macro wetting properties was analysed in detail. Flow enhancements were observed in hydrophilic alumina nanochannels with inner diameters of 40 to 25 nm. Atomic force microscopy force measurements provided further insight into fluid-solid interactions at the nanoscale. A systematic investigation of nanoporous alumina DC electroosmotic pumps with pore diameters down to 8 nm was also undertaken with sodium tetraborate buffer operated at $\Delta V = 10$ V. Concentration polarization was identified as the principal challenge to sustained electroosmotic flow. By optimising the electroosmotic process, particularly the rig design and buffer concentration, an EO pump was developed with a lifetime of up to 4 hours.

Carbon nanotube membranes with a range of pore diameters were also investigated for their electroosmotic and pressure-driven flow properties. The synthesis of carbon nanotubes was optimised to obtain unblocked and functioning membranes. Flow enhancements were observed in engineered carbon nanotube membranes with pore diameters down to 16 nm. Electroosmotic flow rates in carbon nanotube membranes were similar to those of nanoporous alumina. Two electrolytes—sodium tetraborate and sodium chloride—were investigated in electroosmotic flow experiments with carbon nanotube membranes. This allowed for further investigation of electroosmosis and electric double layer overlap.

Acknowledgements

I am indebted to my supervisor, Dr Davide Mattia, for his constant support and guidance throughout my time at Bath. Thank you for your patience, dedication and commitment.

I have been extremely lucky to work with talented people who have inspired and supported my work. First and foremost, with my deepest gratitude, I thank my good friends Kah Peng Lee, Paulina Morawska, Sofia Bekou, Dr Justin O'Byrne Ania Sobolewska, Ben France, Corinne Jeffs, Will Lewis, Eleni Shiko, Sarah Jones, Daniel Minett, Dr Victoria Rocha-Garcia, Anyela Ramirez-Canon, Dave Miles, Rhodri Owen, Dr Massi Vezzoli and Alejandro Hengstenberg.

Academics of the department have been very supportive and have continually encouraged me. Thank you Dr Tom Arnot, Professor Julian Chaudhuri, Dr Tim Mays, and Dr John Chew.

Thanks to my collaborators at the University of Melbourne: Mr Chu Wu, Dr Rico Tabor, Dr Ray Dagastine and Professor Derek Chan. Thanks also to my collaborators at the University of Bristol: Miss Georgia Pilkington, Mr Benoit Quignon and Dr Wuge Briscoe.

I would not have been able to carry out much of the work presented here without the support and expertise of John Bishop, Mervyn Newnes, Paul Frith, Philip Jones and Fernando Acosta. Thank you to Dr John Mitchells and Ursula Potter at the Microscopy and Analysis Suite for your teaching and support. And thank you to the people who always brightened up my day, Sue, Paul, Elaine and Amy.

Thank you to my family, Mumms and Mark. W, Dad, Sherelle, Nanna and Grandpa, Nanny and Grandad, for your constant support, love and encouragement.

Mark, thank you always.

And ultimately this work would not have been possible without the support of the EPSRC, who provided the funding for my project as well as funding opportunities such as the Nanoaccess and EPSRC Delivery Fund.

For Mark

Table of Contents

List of Figures

List of Tables

Nomenclature

a	Radius of a channel (m)
A_{eff}	Effective membrane area (m^2)
A	Total surface area (m^2)
A_0	Droplet area on flat surface (m^2)
A_S	Drop-solid contact area (m^2)
At	Area of triangle (m^2)
b_0	Slip length (m)
B	Barrier oxide layer (m)
C	Drag constant (-)
c_0	Bulk electrolyte concentration (mol m^{-3})
D	Particle diameter (m)
D_s	Surface diffusion (m^2 s^{-1})
D_C	Interpore spacing (m)
D_P	Pore diameter (m)
D_P*	Critical pore diameter (m)
Du	Dukhin number (-)
e_0	Charge of an electron (C)
E	External electric field (V m^{-1})
ΔE	Streaming Potential
f	Solid surface fraction (-)
F	Faraday's constant (C mol^{-1})
F_{app}	Apparent force (kg m s^{-2})
F_{DLVO}	DLVO forces (kg m s^{-2})
F_H	Hydrodynamic force (kg m s^{-2})
F_K	Force from spring (kg m s^{-2})
F_T	Total flow rate (sccm)
h_0	Initial separation (m)
I	Current (A)
I_D	Intensity D-band (a.u)
I_G	Intensity G-band (a.u)
J_{exp}	Experimental volumetric flux (m^3 m^{-2} s^{-1})
J_{HP}	Hagen-Poiseuille volumetric flux (m^3 m^{-2} s^{-1})
K	Force constant (N m^{-1})
k_b	Boltzmann constant (kg m^2 s^{-1} K^{-1})
L	Membrane thickness (m)
l	Length (m)
n	Number of pores (-)
ΔP	Pressure difference (Pa)
p_1, p_2	Pressure (Pa)
Pt	Platinum (-)
Q	Volumetric flow rate (m^3 s^{-1})
Q_{avg}	Average volumetric flow rate (m^3 s^{-1})
Q_{eo}	Electroosmotic volumetric flow rate (m^3 s^{-1})
Q_{exp}	Experimental volumetric flow rate (m^3 s^{-1})
$Q_{\Delta P}$	Pressure-driven volumetric flow rate (m^3 s^{-1})
$Q_{\Delta P}$*	Normalised pressure-driven volumetric flow rate (m^3 s^{-1})
Q_{HP}	Hagen-Poiseuille volumetric flow rate (m^3 s^{-1})

Q_T	Total volumetric flow rate ($m^3\ s^{-1}$)
r	Radius (m)
r_f	Roughness ratio (-)
R	Capillary Radius (m)
R_d	Pore Radius (m)
R_d	Resistance between electrode and membrane surface (Ω)
R_T	Total resistance (Ω)
ΔS	Cantilever deflection (m)
t	Time (s)
T	Temperature (°C)
v	Ionic mobility ($m^2\ s^{-1}\ V^{-1}$)
V	Voltage (V)
V_{app}	Effective voltage (V)
V_{dec}	Decomposition potential (V)
V_{eff}	Applied voltage (V)
V_F	Final voltage (V)
V_I	Initial voltage (V)
V_t	LVDT velocity ($m\ s^{-1}$)
V_1, V_2	Volume (m^3)
u	Electroosmotic velocity ($m\ s^{-1}$)
u_r	Fluid velocity at the centre of two surfaces ($m\ s^{-1}$)
u_z	Fluid velocity z-direction ($m\ s^{-1}$)
W_A	Work of adhesion ($J\ m^{-2}$)
W_{EDL}	Interaction energy of EDL (J)
W_{vdW}	Interaction *vdW* (J)
X_0	LVDT position (m)
z	Ionic charge (-)

α	Experimental constant (-)
α_{exp}	Thermal expansion coefficient (K^{-1})
β	Experimental constant (-)
δ	Penetration depth (m)
δ_{CP}	Concentration polarisation thickness (m)
δ_{max}	Maximum concentration polarisation thickness (m)
ε	Flow enhancement factor (-)
ε_0	Vacuum Permittivity ($F\ m^{-1}$)
ε_r	Dielectric constant (-)
γ_{LV}	Surface tension of liquid and vapour ($N\ m^{-1}$)
γ_{SV}	Surface tension of solid and vapour ($N\ m^{-1}$)
γ_{SL}	Surface tension of solid and liquid ($N\ m^{-1}$)
κ	Conductivity ($S\ m^{-1}$)
λ	Correction factor (-)
λ_D	Debye length (m)
μ	Viscosity (Pa s)
η	Thermodynamic efficiency
π_e	Film pressure of adsorbed vapour ($J\ m^{-2}$)
ϕ	Porosity (-)
ρ	Density ($kg\ m^{-3}$)
ρ_E	Charge density ($C\ m^{-1}$)

σ	Conductance (S)
τ	Tortuosity (-)
θ_{CB}	Cassie-Baxter contact angle (deg)
θ_{exp}	Experimental contact angle (deg)
θ_W	Wenzel contact angle (deg)
θ_Y	Young contact angle (deg)
ζ	Zeta potential (V)

Abbreviations

AFM	Atomic Force Microscopy
Al_2O_3	Aluminium Oxide or Alumina
APCA	Apparent Contact Angle
BNNT	Boron Nitride Nanotube
CA	Contact Angle
$C_2H_2O_4$	Oxalic acid
CNT	Carbon Nanotube
CP	Concentration Polarisation
CVD	Chemical Vapour Deposition
cCVD	Catalytic Chemical Vapour Deposition
DC	Direct Current
DI	Dionised
DLVO	Derjaguin and Landau, Verwey and Overbeek Theory
DWNT	Double Wall Nanotube
EDL	Electric Double Layer
EKP	Electrokinetic Phenomena
EO	Electroosmosis
EOF	Electroosmotic Flow
FESEM	Field Emission Scanning Electron Microscopy
FIB	Focus Ion Beam
FOTS	Fluoro-octyltrichlorosilane
FWHM	Full Width Half Maximum
HA	Hard Anodization
HCl	Hydrochloric acid
HF	Hydrofluoric acid
HNO_3	Nitric acid
HPLC	High Performance Liquid Chromatography
HTS	Hydrothermal Sealing
H_3PO_4	Phosphoric acid
H_2SO_4	Sulfuric acid
LVDT	Linear Variable Differential Transformer
KCl	Potassium Chloride
MA	Mild Anodization
MD	Molecular Dynamics
MCP	Microchannel Glass Plates
MWNT	Multi Wall Nanotube
$Na_2B_4O_7$	Sodium Tetraborate
NaOH	Sodium Hydroxide
NPAM	Nanoporous Alumina Membrane
NT	Nanotube

OTS	Octadecyltrichlorosilane
PAA	Porous Anodic Alumina
PSD	Position Sensitive Detector
PVFc	Poly(vinylferrocene)
sccm	Standard cubic centimetre per minute
SEM	Scanning Electron Microscopy
SiC	Silicon Carbide
SWCNT	Single Wall Carbon Nanotube
TEM	Transmission Electron Microscopy
vdW	van der Waals

Chapter 1

Introduction

Fluid behaviour has been the subject of extensive research for many years, studied in disciplines as diverse as membrane science, electrokinetics, and cell physiology. But these fields placed their emphasis on macroscopic behaviour and outcomes, overlooking the effects of intermolecular forces and fluid-solid physiochemical interactions. With the development of engineered nanomaterials, however, it has become both possible and necessary to develop a greater understanding of fundamental nanofluidics. Understanding fluid behaviour at the nanoscale, including under conditions of electroosmosis (EO), is a crucial step towards realising new membrane technologies such as those applied to water filtration.

1.1 Nanoporous Materials

Of the nanoporous materials so far engineered, nanofluidic studies have paid particular attention to carbon nanotubes (CNTs). Exhibiting fluid flow rates significantly higher than those projected by continuum fluid mechanics, CNTs opened the possibility of enhancing the efficiency of current membrane technologies. Investigations in this area were encouraged by numerical simulations of nanoscale steady state flow in CNTs with diameters of 1 - 2 nm (Hummer et al. 2001; Supple and Quirke 2003; Qiao and Aluru 2003). These further supported the prospect of an increase in flow velocity and a breakdown of classical fluid mechanics models. This behaviour was attributed to the almost frictionless interaction between the graphite wall and the liquid molecules (Supple and Quirke 2003; Kalra et al. 2003; Supple and Quirke 2004). These studies challenged previous predictions that pressure-driven velocity profiles would remain parabolic at this scale (Travis et al. 1997).

Carbon nanotubes are not, however, the only engineered nanomaterials to have attracted significant attention. Nanoporous alumina membranes (NPAMs) have been valued as ideal template materials, since their size and structure at the

nanoscale can be fully controlled. Indeed, they have primarily been used as templates for the production of other nanotube materials, including CNTs themselves. The present study has taken two approaches to NPAMs. On the one hand, they have been used to engineer CNTs for a systematic study of fluid flow at the nanoscale, a study which has paid particular attention to surface chemistry, pore diameter, and material wetting properties. On the other hand, fluid behaviour in NPAMs themselves has also been afforded significant attention, again examining fluid flow as a function of surface chemistry, pore diameter, and material wetting properties. This has allowed the determination of the relationships between these variables and, ultimately, to establish the optimum conditions for fluid flow. This will prove a useful contribution to fundamental aspects of nanofluidics and an important step towards realising nanofluidic applications.

1.2 Electroosmosis

The systematic study of fluid flow in CNTs and NPAMs undertaken in this thesis was extended further with the investigation of electroosmosis at the nanoscale. Electroosmotic pumping of liquids has previously been used in microfluidics as a replacement for mechanical pumping. The advantage of EO pumping over mechanical pumping is the ease with which it can be integrated into microfabricated processes and devices. With stable electroosmotic flow (EOF), a no-moving-parts, pulse-free pump can be produced (Brask et al. 2005). To date, however, EO pumps have not been practically applied because of their inefficiency and short lifetimes.

The present study seeks to address fundamental questions which remain regarding electroosmotic flow at the nanoscale. In particular, it considers the effect of electric double layer (EDL) overlap on EOF. This was achieved by observing EOF through the CNT membranes and NPAMs discussed above. At the same time, it also examines the possible viability of EO in practical systems such as water filtration or lab-on-a-chip applications, by assessing such challenges as efficiency, continuity, pump longevity, and concentration polarisation (CP).

1.3 Aims and Objectives

Engineered nanoporous materials, nanofluidic flow, and electroosmotic flow offer exciting possibilities for future applications. However, substantial fundamental work is still required before such projects can come to fruition. Despite the promising results of water flow in CNTs, no systematic study has yet been undertaken into the effect of variables such as surface chemistry, wettability, pore diameter, and material structure on nanofluidic flow. Nor has the possibility of further enhancing flow through the application of electroosmotic pumping been studied in sufficient depth. The overall aim of this thesis is therefore to provide a systematic investigation of these variables, utilising NPAMs and CNTs to do so. This will require that the following objectives are met:

- Produce high quality NPAMs and CNT membranes for nanofluidic and electroosmotic flow investigations.
- Engineer membranes with narrow pore distributions and controlled pore diameters of between 5 - 100 nm.
- Fully characterise NPAMs and CNT membranes using SEM, TEM, AFM, and Raman spectroscopy.
- Use these materials to establish whether classical continuum models (including the no-slip boundary condition) hold for fluid flow at the nanoscale.
- Determine fluid behaviour at NPAM surfaces utilising AFM.
- Assess the effect of surface chemistry on the wetting properties of CNTs and NPAMs and thus on fluid flow.
- Determine the effect of EDL overlap on electroosmotic flow through CNTs and NPAMs.
- Compare the efficiencies of mechanical and electroosmotic pumping, and provide full analysis of the limitations of electroosmosis.

Meeting these objectives will allow this thesis to accomplish its overall aim of establishing the effect of variables such as surface chemistry, wettability, pore diameter, and material structure on nanofluidic and electroosmotic flow.

1.4 Thesis Overview

The following chapter (Chapter 2) presents an overview of relevant literature in nanofluidics and electroosmosis. This chapter has been divided into three main sections. The first section discusses material development, the second wetting properties and transport at the nanoscale, and the third introduces electroosmosis, including electroosmosis at the nanoscale. Detailed experimental procedures have been provided in Chapter 3.

The first of the results chapters (Chapter 4) presents detailed characterisation and analysis of NPAMs by FESEM and AFM. It presents consistent and reproducible nanostructured materials whose structural parameters have been highly controlled. It also discusses results regarding the manipulation of NPAMs with hydrothermal treatment. Chapter 5 presents a systematic investigation of the wetting properties of nanostructured alumina. This study connects the effect of surface chemistry and the size of nanostructures with their wetting properties, highlighting the effects of nanostructure form and surface roughness. Chapter 6 observes the effect of pore diameter on liquid flows at the nanoscale. This chapter is divided into two parts. A short first section introduces collaborative work on water flow enhancement in hydrophilic nanochannels. The second section utilises AFM for the detection of flow on and through NPAMs, establishing that the no-slip boundary condition cannot apply.

Chapter 7 presents findings regarding EO in NPAMs. It also utilises the controlled structure of porous alumina for a systematic analysis of the effects of pore diameter, buffer concentration, applied voltage, and concentration polarisation on EOFs. The final results chapter (Chapter 8) takes advantage of the structure of alumina to present results regarding fluid flow and electroosmosis through CNT membranes. In this chapter CNTs are fully characterised with FESEM, TEM, and Raman spectroscopy. These techniques were also employed to analyse wetting properties, pressure-driven flows, and EOFs in CNT membranes, whose pore diameters, surface chemistry, and surface charge differ from NPAMs. Chapter 9 concludes the present study and discusses possible future work which could be undertaken using this thesis as a platform. A summary of the way in which the thesis is structured has been shown in a flow diagram in Figure 1.1.

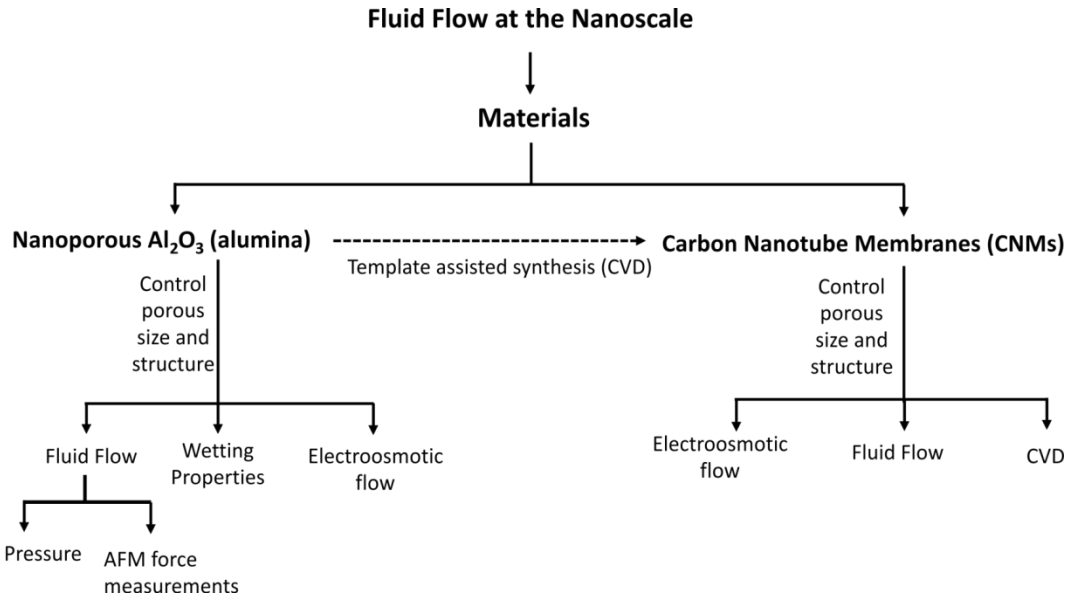

Figure 1.1 Summary flow chart of the research conducted throughout this thesis.

Chapter 2

Fluid Flow and Electroosmosis at the Nanoscale: From Material Development to Application

Electroosmosis (EO) was first observed by F. F. Reuss in 1809. Applying a potential across an electrolyte inside a U-tube with a clay plug, Reuss observed the liquid level rise on one side (Reuss 1809). What he observed was the bulk motion of the electrolyte (within the channel of a charged surface), produced when the external electric field was applied to the diffuse layer of ions known as the electric double layer (EDL). By the late nineteenth-century, this phenomenon had become known as electroosmosis (Quincke 1861; Helmholtz 1879).

Subsequent research in this area has taken further steps to understand the interactions and properties of electroosmosis. There has also been progress in the development of EO pumps, which has not only expanded our understanding of fundamental nanofluidics but has also made possible applications such as lab-on-a-chip. More recently, electroosmosis has found application as a pulse-free, no-moving-parts pumping method for lab-on-a-chip and microfluidic applications (Chuan-Hua and Santiago 2002; Takamura et al. 2003; Prakash et al. 2006).

This chapter will address the fundamental aspects of electroosmosis and how it has been exploited in the applications noted above. It will review the development of materials which have been used throughout the present research and explain why they are some of the most suitable materials in the study of fluid flow and electroosmosis at the nanoscale. The chapter will first report, however, on the development of two materials which have been utilised for nanofluidic studies, including the study of electroosmosis at the nanoscale. These materials, which have been utilised throughout the present study, are nanoporous alumina membranes (NPAMs) and carbon nanotube (CNT) membranes. These materials have been selected due to their versatility and, in the case of porous alumina, ease of fabrication. The CNTs offer a change in surface chemistry but retain the same control of porous structure and pore diameter. Table 2-1 compares and summarises the materials with their counter-parts. This chapter will also discuss

the need to understand the surface properties and wetting behaviour of these materials as part of nanofluidic and electroosmotic research.

Table 2-1 Selection of nanoporous materials

Material	Pore Size Distribution	Fabrication Method	Advantages	Disadvantages
NPAMs	Narrow	Anodization	Inexpensive, control	Fragile
CNTs	Narrow	CVD in NPAM	Control	Fragile
Silica	Narrow	CVD in NPAM	Control	Similar surface chemistry to alumina
Silicon Nitride	Narrow	Laser Interferometric Lithography	Control	Expensive
Polymers	Large	Imprint Lithography, block copolymers, spinning	Flexible	Low control, high tortuosity

2.1 Material Development and Characteristics

The primary material developed throughout this research has been nanoporous alumina. This is an attractive material for the studies undertaken here due to the high degree of dimensional control offered by the anodization process. Nanoporous alumina membranes have a self-ordering cylindrical nanoporous structure and their pore size can be controlled to a high degree by adjusting the anodization parameters. The ordered structure has extremely straight channels (tortuosity, τ approaching unity), with negligible branching and therefore narrow pore distribution. These cylindrical pores also have a high aspect ratio, as the pores are in the nanometre range and their thickness (or length of the cylindrical channel) is in the micrometre range. The thickness of the materials can also be controlled by adjusting the anodization parameters. The degree of control over the structure of these porous materials makes them ideal for studying the fundamentals of fluid flow at the nanoscale and, by utilising the properties of the NPAMs, they also become perfect templates for other materials (in this study, carbon nanotubes).

2.1.1 Anodization of Aluminium

The study and production of NPAMs through the electrochemical oxidation (anodization) of aluminium has attracted continued interest for over seventy years.

The first major development in the anodization of aluminium and the connection between structure and anodization parameters was reported in the 1940s and 1950s (Edwards and Keller 1941; Keller et al. 1953). As noted by Keller et al. anodic oxide coatings can be classified according to whether the electrolyte used for the anodization results in a porous or nonporous structure. The former structure forms when there is a balance between growth and dissolution of the oxide layer (where a steady current is possible) but the latter scenario is found when the oxide formed in the anodization is resistant to dissolution by the electrolyte (Keller et al. 1953). There is now a wealth of literature in this area, inspiring a range of ideas for applications and a variety of methods for optimizing the anodization process. The aim of this section is to explain first the importance of aluminium pre-treatment in obtaining ordered hexagonal porous structures. It will then move on to suggest possible growth mechanisms for the porous structure and the anodization conditions that make this possible.

It is generally accepted that anodizing potential is proportional to both the pore diameter (~ 1.25 nm V^{-1}), the interpore spacing (~ 2.5 nm V^{-1}), and the growth rate of porous alumina (this will be discussed later in greater detail). As a brief introduction to the formation and structure of alumina, however, Equations 2.1 - 2.3 and Figure 2.1 show the dissolution/growth of the oxide during anodization in acid and the hexagonal cell porous structure of the alumina. The self-organised anodic porous alumina is represented schematically as a close-packed array of hexagonally arranged cells containing pores in each cell centre with the barrier layer still intact (Figure 2.2). The porous structure is formed as the alumina is locally dissolved by hydrogen ions produced when an electric field is applied (Sadasivan et al. 2005). By tuning the conditions, such as the anodizing potential, anodizing time, and the temperature, concentration and pH of the electrolyte, it is possible to obtain pore diameters ranging from a few to hundreds of nanometres.

At the anode (alumina): $2Al + 3H_2O \rightarrow Al_2O_3 + 6H^+ + 6e^-$ (2.1)

Dissolution of alumina: $Al_2O_3 + 6H^+ \rightarrow Al^{3+} + 3H_2O$ (2.2)

At the cathode: $6H^+ + 6e^- \rightarrow 3H_2$ (2.3)

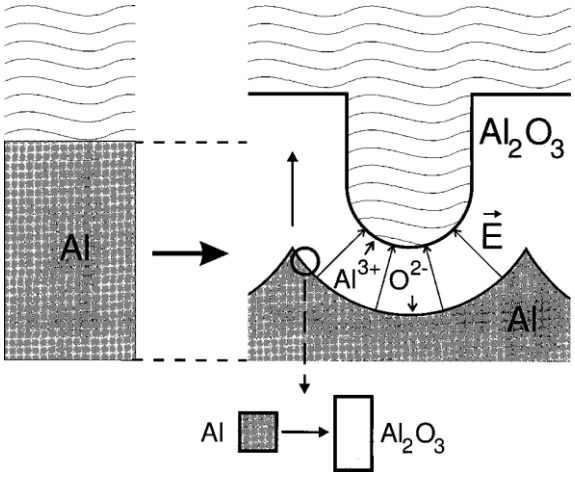

Figure 2.1 Expansion of aluminium during anodization (Jessensky et al. 1998).

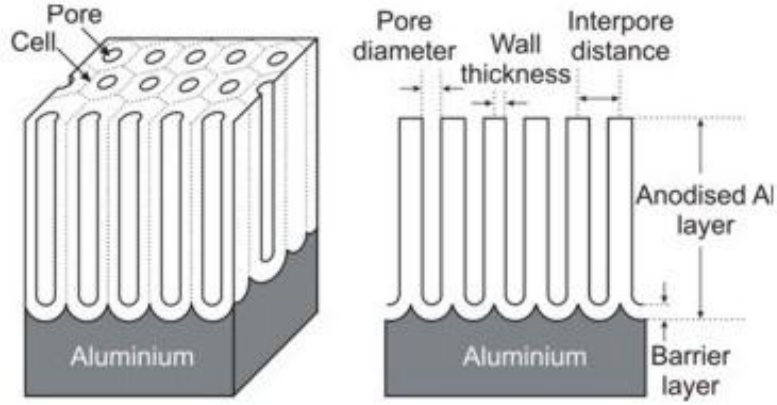

Figure 2.2 Schematic representations of the structure of anodic porous alumina and cross-sectional view (Sulka 2008a).

2.1.1.1 Pre-treatment Conditions

Various preparation steps need to be completed before the actual anodization of aluminium. Rolling aluminium to produce thin foils alters the metal crystal structure, with grains being deformed and rearranged, producing substantial mechanical stress. Annealing can relieve these stresses and so leads to a reorganization of the crystalline structure. Some studies have taken several steps before carrying out anodization (Montero-Moreno et al. 2007), whereas the majority of reports anneal the aluminium at temperatures ranging from 400 °C for 5 h (Sulka 2006) to 600 °C for 5 h (Yu et al. 2006). After annealing aluminium, samples are degreased. This step is necessary to remove any residual organic substances on the surface of the aluminium. Electropolishing (the subsequent

step) can then act efficiently to polish the surface of the aluminium. There are a variety of methods for degreasing using ultra-sonication; a common one places the aluminium sample in acetone (with varying times of 5 to 15 minutes) (Xu et al. 2003) but more complex solutions have also been used such as $HF:HNO_3:HCl:H_2O$ = 1:10:20:69 (Li et al. 1998).

As noted above, electropolishing is the final step before the anodization procedure. A common solution used to electropolish aluminium is a ratio of 1:5 perchloric acid:ethanol, 20% by volume. This method is used to reduce the roughness of the samples and leads to enhanced pore organisation (Bwana 2008), with perchloric acid often regarded as resulting in the smoothest surfaces (Rauf et al. 2009). Reports have shown that when aluminium samples are not electropolished the regularity and ordering of the pores is greatly reduced (Wu et al. 2002; Miney et al. 2003). The electropolishing step has therefore been associated with pore size dependence and the ordering of pores. The influence of perchloric acid and ethanol solution on the surface roughness of aluminium has been investigated by using different volume percentages of the solution and by increasing temperatures (Yu et al. 2007). It was found that surface roughness and pore size strongly depend on temperature, applied potential, and polishing time. High temperatures during electropolishing can increase the depths of the natural grain boundaries of aluminium, boundaries which are observable in some SEM imaging of anodized alumina. The grain boundary patterns are in the micrometre size range and it is therefore considered that they do not have substantial influence on the size or ordering of the nanopores of alumina (Jessensky et al. 1998).

Over the past decade research has sought to explain why electropolishing in ethanol-perchloric acid solutions is successful in promoting ordered arrays of alumina from aluminium (Zhao et al. 2006; Bandyopadhyay et al. 1996). During electropolishing, a double layer forms on the liquid electrolyte side near the constant-potential metal surface due to the fact that ions are attracted to it when the electropolishing potential is applied. It was concluded that the selective adsorption of ethanol due to variations in the potential gradient on the aluminium surface was an important factor in explaining the surface patterns (Bandyopadhyay et al. 1996). Another group also considered the effect which the composition of the perchloric/ethanol solution used for electropolishing has on the

surface pattern of aluminium. It was observed that specific perchloric:ethanol ratios have a current limit which can hinder the effectiveness of the electropolishing process (Ma et al. 2009). The results also suggested that perchloric acid is necessary to achieve the low pH value which ensures the aluminium ionises in Al^{3+} and that the ethanol molecules are acting as shielding molecules that can stabilise surface aluminium atoms.

2.1.1.2 Anodization Parameters

There are several parameters that must be balanced during the anodization process in order to obtain high quality NPAMs. These include acid concentration, pH, temperature, stirring, applied voltage and, as explained in detail above, pre-treatment methods of the aluminium substrate. The one-step anodization of aluminium was the first method to be fully developed which produced both barrier and porous alumina membranes (O'Sullivan and Wood 1970). There are standard conditions for different electrolytes that produce the most uniform structures. The conditions vary with electrolyte: for 0.5 - 1.0 M sulfuric acid the optimum potential is 20 V at 1 °C, for 0.3 M oxalic acid 40 V at 14 °C, and for 0.4 M phosphoric acid, 125 V at 20 °C (Masuda et al. 1993; Sulka 2008b; O'Sullivan and Wood 1970). Using different electrolytes in the process expands the array of pore diameters that can be achieved. Sulfuric acid gives the smallest pore diameters (~ 8 to 32 nm), followed by oxalic acid (~ 36 to 100 nm) and phosphoric acid (~ 150 to 300 nm).

It should be noted here that the use of a constant voltage in the anodization process is known as potentiostatic anodizing and has been widely used to prove the relation between anodizing voltage and pore diameter and oxide growth, both of which can be inferred by plotting anodizing current against anodization time under potentiostatic conditions. The voltage-time profile normally shows a rapid surge of current density at the beginning of the process and a gradual drop with increasing anodization time as the growth rate steadies (see Figure 2.5). Constant current density (for porous structures) has also been widely used and this is known as galvanostatic anodizing. Constant voltage is sometimes inappropriate because of the initial surge in current which can result in rapid film thickening. Galvanostatic anodizing can be used to keep current density constant and voltage-

time plots can be obtained instead (Jessensky et al. 1998). All membranes fabricated throughout this thesis used potentiostatic anodization.

In 1995 the first two-step anodization process to obtain highly ordered alumina nanoporous structures was proposed (Masuda and Fukuda 1995), and it is now more commonly used than the one-step method due to its ability to produce highly ordered pores of varying diameters on both sides of the material (not just the barrier layer side). The two-step anodization process is similar to one-step anodization in that the pre-treatments, system set up, and conditions are identical. The key difference is that the aluminium undergoes anodization twice and the first anodization oxide film is removed. For the first step, anodization is reduced considerably in time (from 10 minutes for sulfuric (Sulka 2006) to an hour for oxalic (Sigurdson et al. 2009)) in order to form a first alumina layer which is then removed, leaving an ordered template (often called 'scallop' indents) for subsequent pore growth with the second anodization step. Some fabrication methods completed a longer first anodization step than the second, but the membranes produced with a shorter first step were of the same quality as those produced with a longer first step.

2.1.1.3 Mild- and Hard-Anodization

Mild anodization (MA) is defined as the anodization of aluminium under low potential or current density, for long periods of time and low temperatures, in both one- and two-step anodization processes. The electrolytes commonly used for this type of anodization are 0.3 M oxalic acid and 0.5 - 1.0 M sulfuric acid. More recently a hard anodization (HA) process has been considered. In this case, the process is completed under high potentials (up to 250 V) in oxalic acid, phosphoric acid, and other electrolytes such as malonic acid (Ono et al. 2005) for short periods of time. HA dramatically increases the rate of the oxide growth. It is still being experimentally tested to determine pore ordering and structure under such high potentials. Applying potentiostatic high potentials risks destroying the aluminium due to localized increases in temperature caused by the large immediate increase of current. Effective cooling for the systems is therefore of utmost importance. Figure 2.3 shows SEM micrographs of typical cross sections of porous anodic alumina films formed under high-current density (195 V,

1500 A m^{-2}). The pore channels are parallel throughout the film and display good pore arrangement.

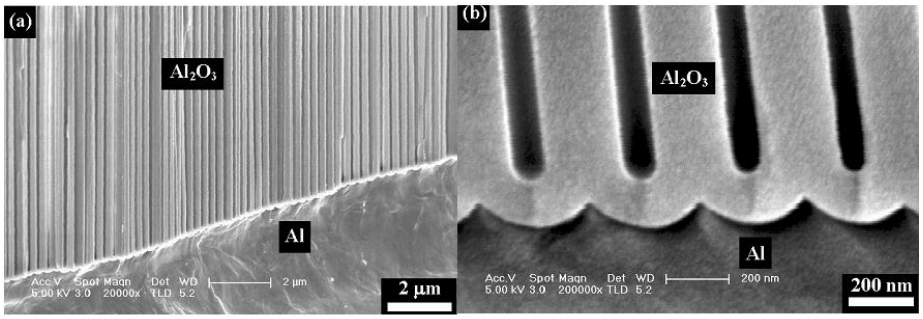

Figure 2.3 FESEM of the cross section of nanoporous alumina films under high current density (Li et al. 2006).

Recently there have been attempts to achieve uniform pore growth under HA conditions using sulfuric acid (Schwirn et al. 2008). This is a desirable process, as it would enable sub-100 nm pore diameters to be obtained over a much reduced time span. Two different methods were used, the first was taken from previous work, in which the aluminium was anodized under galvanostatic conditions and then switched to potentiostatic conditions after reaching a designated target (40 - 70 V) (Chu et al. 2005). When this method was repeated in other work it was found to produce low quality ordering and poor mechanical properties, exhibiting cracks and structural defects (Figure 2.4) (Schwirn et al. 2008).

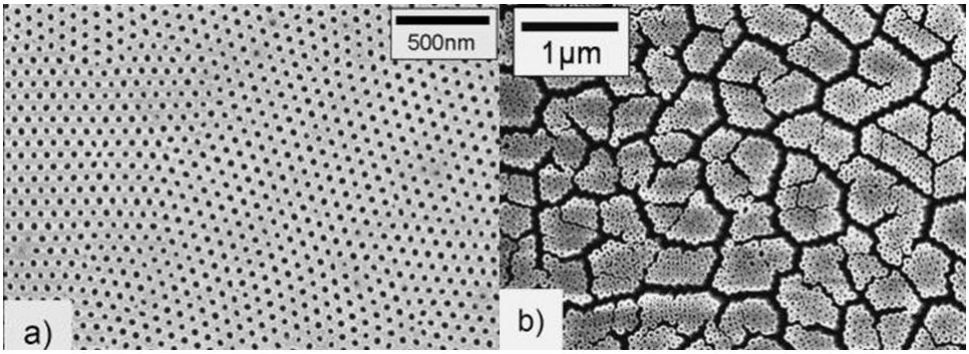

Figure 2.4 SEM images of a) potential target (U_T) = 40 V using sulfuric acid using only the potentiostatic method b) U_T = 65 V changing from galvanostatic conditions to potentiostatic conditions (Schwirn et al. 2008).

2.1.1.4 Porous Oxide Growth Mechanism

The self-ordering mechanism which produces the hexagonal porous structure in alumina is still not fully understood. Several of the original studies optimised the parameters of the anodization process. They exploited the fact that pore diameter, interpore spacing, barrier oxide layer thickness, and the thickness of membrane are all functions of applied voltage. However, a complete understanding of how pores form is still lacking. Several other recent studies have attempted to fill in the gaps (Pashchanka and Schneider 2011; Wang et al. 2012; Reis et al. 2012) and this section will outline their finding and suggested mechanisms.

Between 1950 and 1980 several publications provided the first insights into pore growth and pore formation in the anodization of aluminium. Keller et al. evaluated the simultaneous dissolution and formation of the oxide, finding that a barrier oxide layer initially formed on top of the aluminium metal. It was proposed that at points across the barrier oxide layer there is dissolution of the oxide, and that the current flow 'repairs' this damage. This results in a rise in local temperature leading to a higher dissolution rate. As this mechanism perpetuates, it leads to pore formation (Keller et al. 1953). It was argued that because voltage and current fields about a point tend to be spherical the advancing front of the oxide would be spherical if the pore was a point source. O'Sullivan et al. advanced this work further with an in-depth study into the formation of porous alumina and the effect of electrolyte, temperature, anodization voltage, and current. Even though Keller et al. observed a relationship between 'forming voltage' and 'cell size', O'Sullivan et al. was the first full study to tie together the linear dependence of the anodization voltage on all the dimensions of porous alumina apart from porosity (O'Sullivan and Wood 1970).

In 1998 Jessensky et al. provided further explanation of the self-ordering aspect of porous alumina, supporting previous work which suggested that an initial barrier oxide layer forms under potentiostatic conditions. Though the nucleation of the porous structure is still not fully defined by this work, it does suggest that the barrier oxide layer causes the oxide to become insulating to ionic conduction (which is why an initial drop in current is observed shown in Figure 2.5) causing the pores to nucleate. The steady-state growth of ordered pores is also

characterised by a balance between the field-enhanced oxide dissolution at the oxide/electrolyte interface at the pore bottoms and the formation of oxide at the metal/oxide interface due to the migration of O^{2-}/H^{+} ions through the bottom oxide layer (Jessensky et al. 1998). Anions from the electrolyte are incorporated into the barrier layer and walls of alumina and therefore larger concentrations of anions from the electrolyte are to be found in the barrier layer compared with the inner walls of the alumina structure (Table 2-2). It is therefore important to have an excess of electrolyte for the duration of the anodization process.

Table 2-2 Percentage of incorporated anions in porous oxide layer (Sulka 2008a).

Electrolyte	$C_2H_2O_4$	H_3PO_4	H_2SO_4
Anion content (%)	0.1 – 0.3	2 – 3	10 – 13

It is evident that the rate of current decrease, the time at which the minimum current is observed, and the steady-state forming current density, depends directly on the anodization conditions (applied potential, temperature, and electrolyte type and concentration).

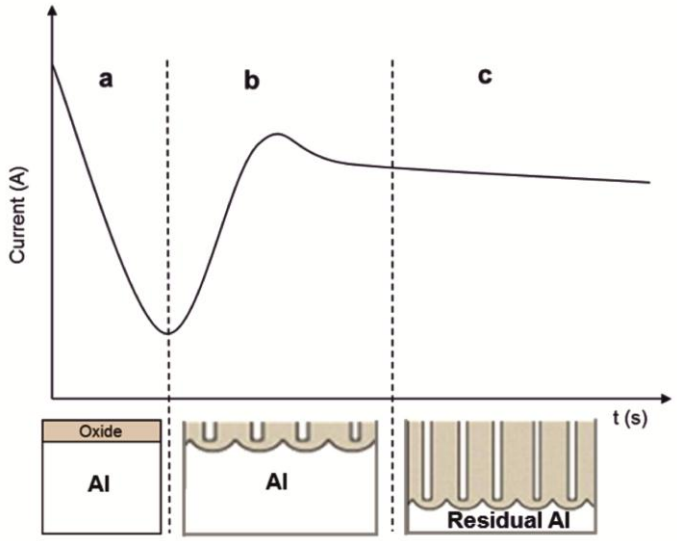

Figure 2.5 Schematic illustration of the kinetics of porous oxide growth under potentiostatic conditions.

The most recent studies have turned to theoretical modelling to further explain the nucleation and self-organisation of pores produced in the anodization of aluminium. One study used the analogy of the Raynard-Bénard convection cells to explain the self-ordering nature of porous alumina. This particular paper

challenges most publications in the area, suggesting that, whilst there is a dissipative self-organization process, this is not the field-assisted dissolution accepted previously. It is suggested instead that electrolyte current near the aluminium anode is organized in the same way as Rayleigh-Bénard convection currents (Pashchanka and Schneider 2011). A simple model was provided which, it was argued, could predict the anodization parameters necessary to create a porous film. An electrolyte which had never been used for anodization before was chosen and, although the structure was not as pristine as others, an organised porous oxide was produced. The only unconvincing aspect of this model is that it relies on the barrier layer forming at the end of the anodization process by colloidal particles sedimenting at the pore bottoms. It is unlikely that the barrier oxide layer forms at the end of the process in this way because it contains a larger percentage of anions than the rest of the structure (from analysis on the composition of the barrier oxide layer). This indicates that the barrier layer is being continually dissolved and oxidised throughout anodization, incorporating more anions from the electrolyte during the whole process.

A very recent study uses two approaches to analyse the nucleation of porous growth in alumina. The first approach was a scaling method applied to explain pattern nucleation when metal corrosion is coupled with erosion of the thin oxide layer subject to a high field, which drives ion migration. The second approach used a non-equilibrium statistical growth model (Reis et al. 2012). This work supports the conclusions of original studies which suggested that corrosion at the metal/oxide interface is coupled with dissolution at the oxide/solution interface due to ion migration across the oxide layer.

2.1.2 Template-Assisted Synthesis of CNT Membranes

The idea of template-assisted synthesis was first developed by a group at the University of Florida (Martin 1994; Parthasarathy et al. 1995) where several templating methods had been invented and tested. This new template-assisted method opened new directions in many subject areas and the possibility of using templates for various materials remains very attractive (Yin et al. 2001; Yang et al. 2003; Travis et al. 2007; Herderick et al. 2007).

Due to the high degree of control and range in fabrication, NPAMs present themselves as the perfect candidates for template-assisted syntheses. As mentioned earlier, NPAMs have been used for several purposes, from the fabrication of metal nanowires (gold, silver and copper) to the synthesis of polymer nanotubes. But the most attractive aspect of nanoporous alumina membranes from the point of view of this research is the possibility of depositing carbon inside NPAMs for the production of CNT membranes. It is appropriate to note here that the carbon deposited within the template NPAM is known as turbostratic graphite. It is generally considered that the carbon structure formed through the CVD process is made up of nanocrystalline graphite with an average grain size of 2 nm to 10 nm turbostratic carbon and that amorphous carbon is obtained if the deposition time is long enough (Li et al. 2007; Mattia 2007). Thus, when the notation CNT is used in this thesis it refers to turbostratic carbon nanotubes produced by non-catalytic chemical vapour deposition (CVD).

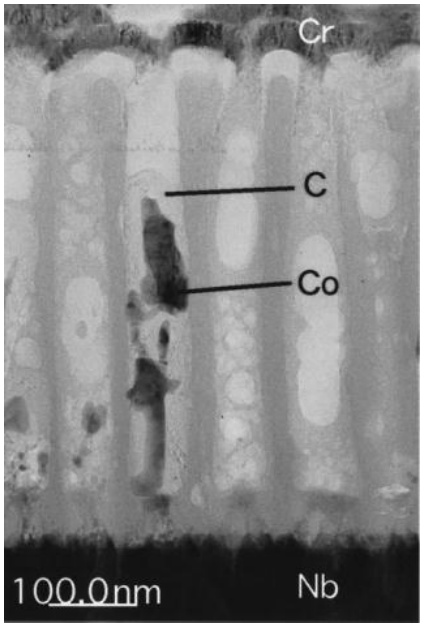

Figure 2.6 Cross-sectional TEM image after the CNTs growth process. The surface was covered with carbon and Cr films to protect the fine structures (Iwasaki et al. 1999).

CNT membranes have been produced in several ways in recent years, and studies have used both catalytic and non-catalytic CVD. After Martin published template-assisted synthesis methods in 1994, several publications considered the possible deposition of carbon inside porous alumina. The first study to produce CNTs using the template method developed by Martin was by Kyotani et al. (Kyotani et

al. 1995; Kyotani et al. 1996). This encouraged a flurry of research which used catalyst based syntheses rather than the non-catalytic CVD of Kyotani et al. (Che et al. 1998; Suh and Lee 1999; Li et al. 1999; Iwasaki et al. 1999). These studies inserted catalysts (cobalt or nickel) inside channels of alumina and, by pyrolyzing ethylene or acetylene at 700 - 900 °C, formed CNT arrays (Figure 2.6).

More recently, CNT arrays/CNT membranes have been produced via non-catalytic CVD, as it is far more favourable for the desired applications that these materials are produced without the catalyst embedded within the channels (Mattia and Gogotsi 2008). The same goes for the production of graphene for graphene electrodes (Sun et al. 2012). The structure of the carbon deposited inside the template via non-catalytic CVD is turbostratic and amorphous, differing from the structure of catalytically produced CNTs which exhibit a much more ordered graphitic structure (Che et al. 1998). The overall reaction during the deposition of carbon inside the template is:

$$C_2H_4 \rightarrow 2C(s) + 2H_2(g) \tag{2.4}$$

As well as this reaction, there are several other reactions producing numerous intermediate products: acetylene, methane, and benzene are the main compounds produced, but 1,3-butadiene can also be produced (Norinaga et al. 2006).

2.1.2.1 Carbon Nanotubes

A detailed review of the anodization process has been presented thus far, looking closely at how the porous structure is formed and the uses of this material. As discussed in Section 2.1.2, one of the main applications of nanoporous alumina, apart from as a membrane in its own right, is as a template. This section will therefore focus on carbon nanotubes, the material fabricated through the use of NPAM as a template in this thesis.

The original class of materials we now know as CNTs were first observed in 1991 by Iijima following the discovery of the C_{60} molecule by a group at Rice University, Texas, in 1985. The CNTs were fabricated from arc-discharge synthesis and characterised using transmission electron microscopy, which

revealed co-axial tubes of graphitic sheets like those shown in Figure 2.7a (Iijima 1991). Two years later Iijima et al. produced the first single wall (SW) CNTs (seamless cylinders of rolled graphene sheets) (Iijima and Ichihashi 1993). Since then much research both experimental and theoretical has been undertaken to exploit the properties that CNTs possess. This has resulted in a large range of 'CNT' materials. One part of this family of carbon materials are CNTs produced via non-catalytic CVD. Consequently, the properties of CNTs are extremely sensitive to their degree of graphitization and diameter (Vaisman et al. 2006). Some of the most favourable properties of CNTs are their superior electronic and mechanical properties, leading to possible applications as reinforcement materials (Gojny et al. 2004; Tai et al. 2004), field emission sources (Sugie et al. 2001), super-capacitors (Frackowiak and Béguin 2002), molecular sensors (Kong et al. 2000) and, for the interests of this study, for fast water flow (Holt et al. 2006; Shannon et al. 2008) (this is discussed in greater detail in Section 2.2.1).

The template-assisted synthesis of CNTs expanded the family of this class of materials. The majority of CNTs fabricated in this way have used NPAMs, but multiple fabrication methods have been reported as discussed in Section 2.1.2. The structure of these materials varies depending on whether a catalyst was used or not. CNTs fabricated using catalysts such as Ni, Co and Fe have more graphitic structures compared to those fabricated without a catalyst, which are turbostratic in nature and must be annealed to obtain a structure equivalent to that of MWCNTs (Mattia et al. 2006). However, these turbostratic materials have still shown favourable properties, especially with regard to water flow (Whitby et al. 2008). They have straight, long walls, with open ends and small wall thicknesses relative to the internal diameter of the bore (Mattia and Gogotsi 2008). Their disordered carbon structure leads to more moderate mechanical and physical properties, such as a lower electrical conductivity compared to catalytic CVD (cCVD) nanotubes (Saito et al. 1998).

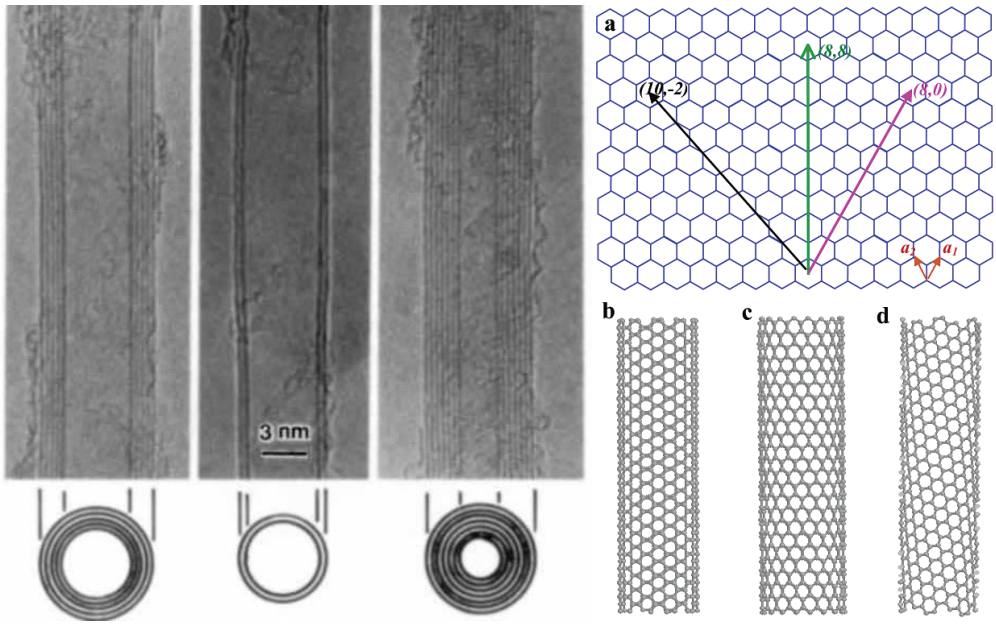

Figure 2.7 Left: Electron micrographs of the first CNTs produced by Iijima (Iijima 1991) and Right: a) Schematic honeycomb structure of a graphene sheet SWCNT can be formed by folding the sheet along lattice vectors. The two basis vectors $\mathbf{a_1}$ and $\mathbf{a_2}$ are shown. Folding of the (8,8), (8,0), and (10,-2) vectors lead to b) armchair, c) zigzag, and d) chiral tubes, respectively (Dai 2002).

2.2 Wetting Properties and Transport at the Nanoscale

How liquids wet surfaces still interests scientists two hundred years after Thomas Young laid down the foundation of this branch of science with his seminal equation (Young 1805):

$$cos\theta_Y = \frac{\gamma_{SV}-\gamma_{SL}}{\gamma_{LV}} \tag{2.5}$$

where γ_{SV}, γ_{SL} and γ_{LV} represent the surface tensions of the solid-vapour solid-liquid, and liquid-vapour interfaces respectively. While fundamental debates about the exact nature of the forces involved in the wetting process are still on-going, the possibility of manipulating and directly observing liquid behaviour under nanometre scale confinement has opened an exciting new chapter in the study of wettability.

In 1805 Young established a relationship between the contact angle (CA) of a drop of liquid and the interfacial tensions at the three-phase contact line between a solid, a liquid, and its vapour at equilibrium. J. Willard Gibbs in 1928

subsequently derived the contact angle θ from thermodynamic quantities, and determined the surface free energies for the three interfaces (Gibbs 1928). The limits of the Young equation regarding substrate characteristics have led to the development of several modified versions to account for surface roughness and topographical or chemical in-homogeneities. Two models are commonly used to evaluate the effect of these surface characteristics on contact angles: the Wenzel model (Wenzel 1949) (Equation 2.6) and the Cassie-Baxter model (Cassie and Baxter 1944) (Equation 2.7) represented schematically in Figure 2.8.

The Wenzel model accounts for surface roughness by introducing a proportional factor between the measured contact angle θ_W, and the thermodynamic angle derived by Young for a flat, smooth surface θ_Y:

$$cos\theta_W = r\left(\frac{\gamma_{SV}-\gamma_{SL}}{\gamma_{LV}}\right) = rcos\theta_Y \tag{2.6}$$

Surface roughness, *r*, is defined as the ratio of the actual surface area to the horizontal projection of the surface area. The Cassie-Baxter model is considered for heterogeneous surfaces. In the majority of recent cases though, the Cassie-Baxter model has been utilised when the second surface is air (Equation 2.7). The interaction of the fluid with air trapped in gaps of rough (or porous) surfaces is considered alongside the liquid/solid interaction. The effect is strongest in the case of water which forms a contact angle of 180˚ with air. The Cassie-Baxter model introduces a surface fraction parameter, *f*, which represents the unit area of the wetted surface:

$$cos\theta_{CB} = fcos\theta_Y + (1-f)\cos 180 = f\ cos\theta_Y + f - 1 \tag{2.7}$$

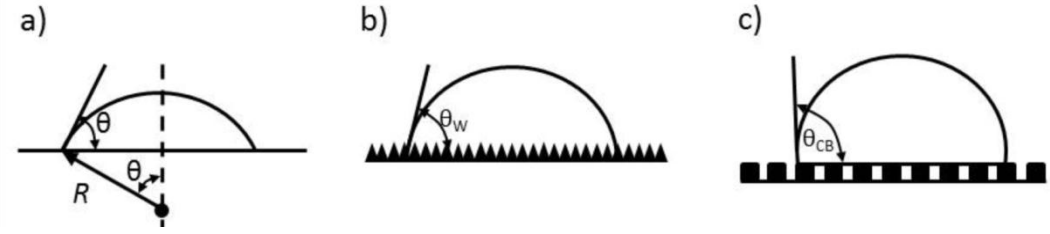

Figure 2.8 Schematic representations of contact angles on a) Young's flat smooth surface b) rough substrate, the Wenzel regime and c) rough substrate with air trapped under the drop, the Cassie–Baxter regime.

Like wetting, the flow of liquids through nanotubes has renewed interest in the area of capillary flow and nanofluidics. The fundamental equations used to describe liquid flow in capillaries and tubular structures are the Young-Laplace equation (Equation 2.8), the Hagen-Poiseuille equation (Equation 2.9), and the Washburn equation (Equation 2.10). The first describes capillary pressure difference across the interface between two fluids (such as an air/water interface). The second describes the well-developed, laminar flow of an incompressible fluid in a capillary under a pressure gradient alone. A simplified version of the third equation is used to describe the filling of an empty (horizontal) capillary by capillary pressure only, as a function of the wettability of the solid:

$$p = \frac{2\gamma_{LV}}{R} \text{ Air/water interface} \tag{2.8}$$

$$Q = \frac{\pi \Delta P R^4}{8\mu L} \tag{2.9}$$

$$L^2 = \left(\frac{R\gamma_{LV}cos\theta}{2\mu}\right) t \tag{2.10}$$

where, R is the radius of the capillary, ΔP is the pressure across the liquid-vapour interface, Q flow rate, μ viscosity, γ_{LV} the surface tension at the liquid-vapour interface, θ the contact angle, t the time elapsed to fill an empty capillary of length, L by a liquid.

The Hagen-Poiseuille equation reported above assumes a no-slip boundary condition at the capillary wall, i.e. the molecules in the fluid layer in contact with the capillary wall have zero velocity. It should be noted that this is a mathematical approximation and that there have been several reports more recently that have shown that the no-slip boundary condition cannot not apply for some systems, especially at the nanoscale. The nature and, indeed, the very existence of slip is still contentious. Several fluid flow experiments in nanometre channels showing very large slip lengths will be described later in this chapter. In these experiments, the slip length, b_0, has been calculated via the Hagen-Poiseuille equation with a slip wall boundary condition:

$$Q_{avg} = \frac{\pi \Delta P R^4}{8\mu L}\left(1 + \frac{4b_0}{R}\right) \tag{2.11}$$

A diagram of the no-slip/slip boundary condition can be seen in Figure 2.9.

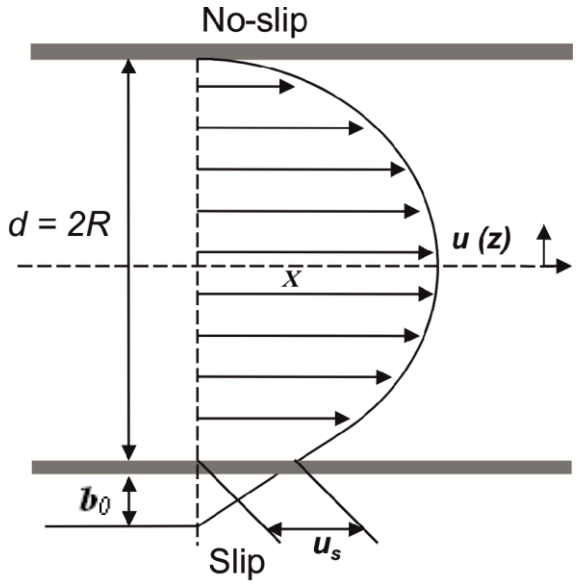

Figure 2.9 Shape of meniscus inside a nanochannel representing no slip and slip at the channel wall.

It is important to note that although surface tension and contact angle are not explicitly found in the Hagen-Poiseuille equation, there is substantial evidence that the wettability of the channel wall has an effect on slip (Whitby and Quirke 2007; Mattia and Gogotsi 2008). Several models linking slip length to the characteristics of both the tube wall and the liquid have been suggested (Blake 1990; Huang et al. 2008; Mattia and Calabrò 2012). Indeed, the interpretation of large slip values observed in certain experiments or theoretical models is complicated by the potential influence of a large number of parameters, such as the surface chemistry and structure of the channel, the type of fluid confined within the channel (i.e. polar or non-polar, its viscosity), and the height or diameter of the channel. Further to calculating theoretical slip lengths to highlight flow rates faster than expected, enhancement factors have been utilised. The flow enhancement factor, ε, is a measure of the deviation of experimental results from the no-slip Hagen-Poiseuille equation:

$$\varepsilon = \frac{Q_{exp}}{Q_{HP}} \tag{2.12}$$

where Q_{exp} is the numerically or experimentally observed volumetric flow rate and Q_{HP} the no-slip Hagen-Poiseuille predicted flow rate.

Such a result was observed for the flow of both polar and non-polar liquids in carbon nanotubes (Majumder et al. 2005). This effect has been attributed to the ordering effects of the liquid molecules at the wall. The slip boundary condition for the Navier-Stokes equation considers the wall surface as a whole, as do the Wenzel and Cassie-Baxter models for wetting. Several molecular dynamics (MD) simulations have looked at local changes of wall surface chemistry and structure, leading to local increases in slip length, which result in macroscopically larger slip lengths (Thompson and Robbins 1990; Sun and Ebner 1992; Barrat and Bocquet 1999; Voronov et al. 2006; Falk et al. 2010).

2.2.1 Wetting Properties and Transport in CNTs

From an applications point of view, the macroscopic behaviour of surfaces is crucial. It must be asked, for instance, whether they are hydrophilic or hydrophobic, and whether there is the possibility of switching between these two behaviours (Meng et al. 2005; Guo et al. 2007; Li et al. 2008; Su et al. 2009). This has been explored in Chapter 5. Understanding how individual nanostructures, composed of different materials, are wet at the nanometre scale is key to obtaining surfaces with controlled wetting behaviour. The appearance of carbon nanotubes in the early 1990s led almost immediately to investigations of the wetting behaviour of liquids under nanoscale confinement. The infiltration of molten metals and salts was used to prove that carbon nanotubes were indeed hollow soon after their discovery in the early 1990s (Ajayan and Iijima 1993; Dujardin et al. 1994; Gogotsi et al. 2001).

In more recent years attention has shifted to studying the flow of liquids through nanochannels and nanotubes by both theoretical and practical means (Supple and Quirke 2003; Majumder et al. 2005; Whitby and Quirke 2007; Mattia and Gogotsi 2008). Supple and Quirke were the first to use molecular dynamics simulations to assess the imbibition of fluids into a single wall carbon nanotube (SWCNT) (Supple and Quirke 2003). They observed much faster imbibition of decane molecules into the SWCNT (of diameter 1.764 nm) than that predicted by the

macroscopic Washburn equation (Equation 2.10). Further to this, Supple and Quirke presented molecular dynamic simulations for SWCNTs of different diameters (Supple and Quirke 2004). For the SWCNT with diameter 2.62 nm the simulations revealed that the tube filled in layers where the layers next to NT wall surface filled first. This was attributed to the convex geometry of the inner tube surface (the outside of the tube was found to wet 30 times slower). The next step was to visualise the wetting and filling behaviour of carbon nanotubes with low molecular weight fluids (such as water) which occurred in the soon after with the first direct images of water confined inside carbon nanotubes (Figure 2.10) (Mattia et al. 2007).

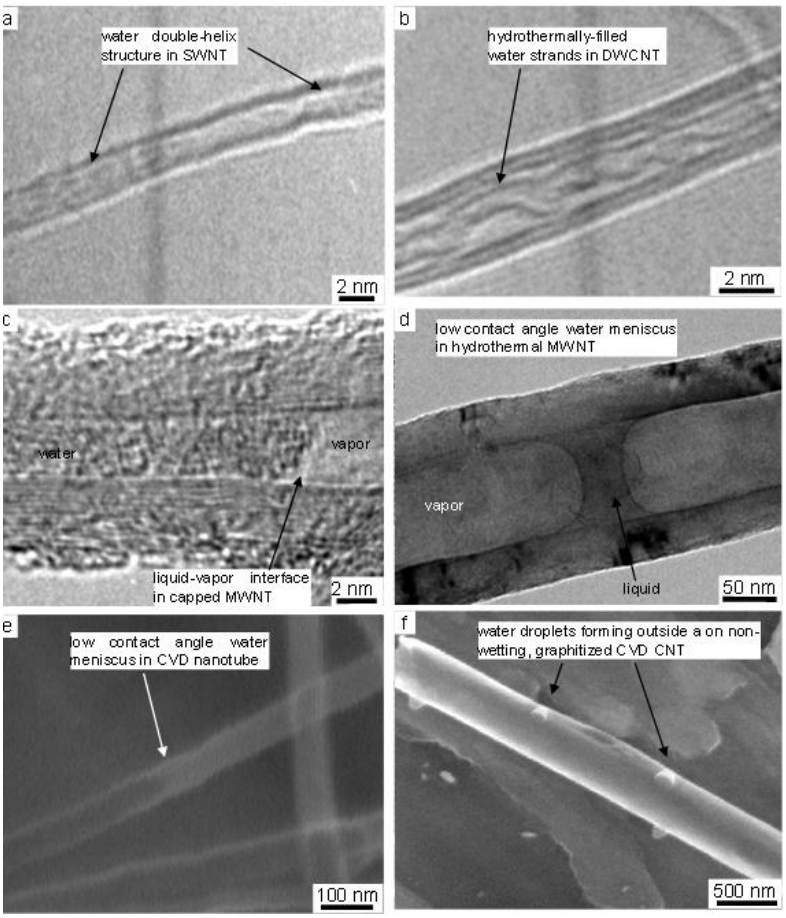

Figure 2.10 TEM and SEM images of water inside carbon nanotubes: TEM micrographs of double–helix water strands in (a) SWNT and (b) DWNT. c) TEM micrograph of the interface between water molecules and vapour in a capped MWNT. d) TEM micrograph of a low contact angle liquid meniscus between 2 vapour bubbles in a hydrothermal MWNT. e) Water-filled CVD MWNT in the environmental SEM. f) Water droplets forming outside a graphitized CVD nanotube in the environmental SEM (Mattia et al. 2007).

Molecular dynamics (MD) simulations have so far played a vital role in understanding the wetting properties of individual tubes and CNT arrays or

membranes. A key (and much debated) aspect of MD simulations is the choice of the water-carbon interaction potential. One study has correlated the wetting of water on graphite with different values of the water-carbon interaction potential, obtaining contact angle values varying from 0° to over 115° (Figure 2.11) (Mattia and Gogotsi 2008).

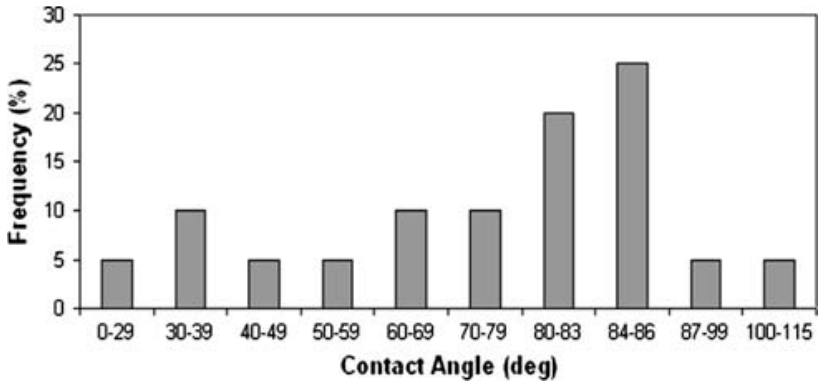

Figure 2.11 Frequency of contact angle values of water on graphite reported in literature; both experimental results and numerical simulations (Mattia and Gogotsi 2008).

Another molecular dynamics simulation of contact angles in CNTs with diameters ranging from 2.5 - 7.5 nm carried out in 2001 reported wetting behaviour contrary to that observed experimentally by Gogotsi et al. (Gogotsi et al. 2001). They found non-wetting behaviour of pristine (defect-free) CNTs at room temperature as the majority of the CAs were > 100°. Many of the discrepancies between numerical and experimental results concerning liquid behaviour inside CNTs discussed above can be attributed to the presence of surface defects or functionalities on the tube walls, or to the structure of the tube walls (Zhou et al. 1994). In reality, CNTs can exhibit defects which could dramatically change their potential as building blocks for nanofluidic devices, as the defects could impede on the fast fluid flow properties observed from the molecular dynamic simulations. A recent study has been able to use MD to simulate water transport through SWCNTs (diameters of 0.96 nm) with defects (introducing vacancy sites - i.e. removing carbon atoms) (Nicholls et al. 2012). Indeed, they found a dramatic reduction in fluid velocity compared to pristine SWCNTs. However, the fluid flow still exceeded that predicted by continuum expectations, with enhancement factors of ~ 200 with 20% of defects.

This section has been titled '*Wetting Properties and Transport in CNTs'* because the two are inter-related. If the wetting properties of these materials is more fully understood then the natural progression is to use this to research and exploit the properties for applications, such as liquid flow, and water filtration in particular (Corry 2011). Therefore, just as several publications were reporting CA measurements in CNTs (both experimentally and theoretically), there were also several publications being published on the simulation and experimentation of flow in CNTs (in the family of carbon materials discussed in Section 2.1.2.1). The most relevant studies (for the present work) have been summarised in Table 2-3.

At the beginning of the 2000s, water conduction through a CNT was simulated by molecular dynamics, where Hummer et al. showed spontaneous filling of NTs with a 1D ordered chain of water molecules (Hummer et al. 2001). They also reported the movement of water through the NT to be 'pulse-like'. This seminal paper presented the possibility that CNTs could be unique molecular channels for water and protons, due to their almost spontaneous empty-to-filled state.

Table 2-3 Selection of experimental and simulation results for water flow enhancement in CNTs.

	References	Materials Description	CNT(s) diameter (nm)	Flow Enhancement, ε (-)
Experimental Measurements	Majumder et al. (2005)	Graphitic MWCNT membranes	7.0	77018 - 53860
	Holt et al. (2006)	Graphitic DWCNT membranes	1.3 - 2.0	8400 - 560
	Whitby et al. (2008)	Turbostratic CNT membrane	44.0	34
	Du et al. (2011)	Superlong graphitic CNT membrane	10.0	388710
	Qin et al. (2011)	Superlong CNT	0.8 - 1.6	882 - 51
Molecular Dynamics Simulations	Joseph and Aluru (2008)	Single CNT	2.17	2052
		Single Silicon NT	2.17	155
	Thomas and McGaughey (2008)	Single CNT	1.66 - 4.99	433 - 47
	Thomas and McGaughey (2009)	Single CNT	0.81 - 1.66	6500 - 433
	Nicholls et al. (2012)	Single CNT (with defects)	0.96	850 - 200

The first experimental example of the 'ballistic' type of flow (Striolo 2006) observed in several simulations was reported by Majumder et al. where enhanced flow rates compared to that of classical models were observed in CNTs with pore

diameters ~ 7 nm (Majumder et al. 2005). Flow rates of four to five orders of magnitude faster were reported and these found that the more polar the liquid (water or ethanol compared to hexane or decane) the bigger the increase in flow rate. This result was further supported by the research completed by Holt et al. where gas and water flow measurements were made through CNT membranes with diameters < 2 nm. Both the gas and water flows exceeded the predictions of the Knudsen diffusion and continuum hydrodynamic models, respectively. Again these results were several orders of magnitude greater than expected. These ground-breaking papers were built upon by many other research groups as they sought to explain and exploit the flow properties of CNTs.

Towards the end of the decade there was a revival of simulations and experimental publications on CNTs. Joseph and Aluru looked to answer the question of why CNTs are such fast transporters of water, using MD simulations of water flow in CNTs with inner diameter of 2.17 nm. They observed the layering of the water which was also observed and discussed earlier. But they also concluded that there was a velocity 'jump' in a depletion area at the water-nanotube interface and that water molecule orientation and hydrogen bonding at the water-nanotube interface significantly affected flow rates (Joseph and Aluru 2008). To arrive at this conclusion, the material surface chemistry was changed, from carbon, to silicon, to boron nitride NTs. With the more hydrophilic surfaces (such as silicon) they found the enhancement in fluid flow was greatly reduced due to the decreased number of 'free' OH bonds in the depletion layer compared with the CNT.

Thomas et al. returned to the topic and, whilst still reporting flow enhancement factors larger than expected from continuum models, these were much less than had been previously reported (Thomas and McGaughey 2008). The authors suggested that there was miscalculation in previous studies, where enhancement factors ranged from 560 to 100 000. The findings from Thomas et al. were able to fully explain the enhancement factors of 47 to 433 using continuum fluid mechanics, contrary to what had previously been suspected. They proceeded to look at the structure of water in CNTs at this scale, to establish whether there is a transition from continuum to subcontinuum transport (Thomas and McGaughey 2009). It was found that in CNTs with diameters < 1.39 nm subcontinuum flow

occurred and that below 0.9 nm the enhancement factor was four magnitudes higher than expected (Figure 2.12).

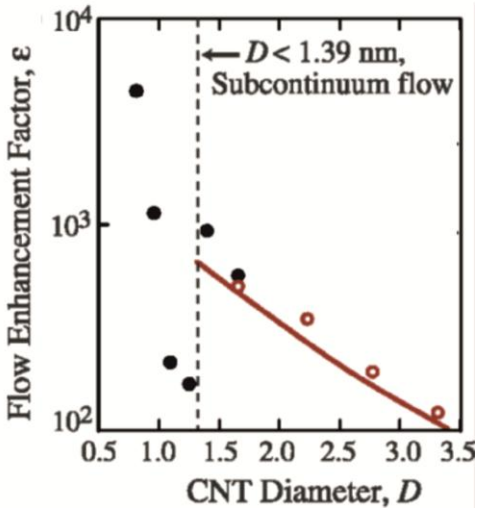

Figure 2.12 Variation in flow enhancement ε with CNT diameter *D* (Thomas and McGaughey 2009). The dashed line between CNT diameter 1.25 and 1.39 nm delineates continuum and subcontinuum. The line is the model developed from Thomas et al. (Thomas and McGaughey 2008).

One of the most recent publications to consider the high flow rates exhibited in the experimental and simulation experiments with CNTs has developed a model which links the enhanced flow rates of CNTs to the solid-liquid interactions (mentioned earlier) at the wall surface (Mattia and Calabrò 2012). The proposed model uses the Hagen-Poiseuille equation but incorporates the solid-liquid molecular interactions via the macroscopic quantities of work of adhesion and surface diffusion. They were able to predict the effects that CNT diameter, wall surface chemistry, and structure had on flow rates. The versatility of this model makes it suitable for other systems and materials (e.g. silicon carbide (SiC), NPAMs and boron nitride nanotubes (BNNTs), provided that the work of adhesion and surface diffusion can be measured or calculated independently (Mattia and Calabrò 2012).

2.2.2 Wetting Properties and Transport in Hydrophilic Nanotubes

Whilst carbon nanotubes are the first materials whose wetting behaviour has been extensively investigated, the more recent availability of nanochannels of different compositions has renewed interest in wetting at the nanometre scale. Although the

number of publications on wetting inside more hydrophilic nanotubes (metal oxides like alumina and silica etc.) is not as high as those for CNTs, interesting observations have been made regarding wetting properties and transport at the nanoscale.

One study looked at the filling characteristics of hydrophilic silica nanochannels of sizes down to 27 nm (Han et al. 2006). The liquids ethanol, isopropanol, water, and a mixture of water and ethanol were used to investigate the filling properties of nanochannels. All liquids were in accordance with the Washburn equation (Equation 2.10) filling kinetics in terms of the moving liquid meniscus being proportional to the $\sqrt{t}$. For the binary mixtures of water and ethanol, however, the filling of the nanochannel was much faster than expected. This was attributed to chemical selectivity of the nanochannels towards water rather than ethanol, but it was also suggested that the deviation may be due to the dynamic contact angle of the mixture being smaller than that of pure water or ethanol. The possibility of slip was not considered in this work.

More recently, there has been a study of water enhancement in NPAMs, which are hydrophilic in nature. A range of pore diameters were studied, with membranes with pore diameters of 20 to 100 nm. The smallest channels exhibited water permeability more than double than predicted by the Hagen-Poiseuille equation (Lee et al. 2012). The authors highlight that even though the enhancement is not on the scale shown in CNTs it is still important to acknowledge the effect of surface chemistry and diameter at the nanoscale. They proceed to compare the enhancement factors of NPAMs with pore diameters of 40 nm with the enhancement factor of similarly produced CNT membranes (Whitby et al. 2008). The calculations showed the alumina to be approximately one order of magnitude lower than the CNTs. This was in agreement with a recent MD paper that related the occurrence of hydrodynamic slippage (and hence the flow enhancement effect) to the magnitude of solid-liquid molecular interactions (Ho et al. 2011). Furthermore it supported the conclusion that the proximity of preferential adsorption sites on channel walls promotes migration of water molecules from one to the next (Ho et al. 2011).

Another relatively recent MD simulation studied the transport and structural properties of water in cylindrical silica nanopores of 0.475 to 2.5 nm in size (Zhang et al. 2009). These silica pores (close to the size of water molecules) were simulated with water by equilibrium molecular dynamics and found, due to the severe confinement effect, that the diffusion of water in the silica nanopores was slower than that expected from bulk diffusion. In the 0.475 nm pores, the confinement causes the water molecules to locate in the centre of the pores whereas for the larger pores the water located towards the wall (due to the hydrophilic nature of the wall surface). In between these values, the silica nanopore studied with a diameter of 0.951 nm showed a competing relationship between confinement effects and the hydrophilic nature of the silica walls. To date, the work completed by Zhang et al. and Joseph and Aluru (discussed earlier) are the only studies of water transport and confinement in such small hydrophilic nanopores (Zhang et al. 2009; Qiao and Aluru 2003).

2.3 Electroosmosis

The movement of fluids adjacent to charged surfaces due to the effects of the electrical properties of solid-liquid interfaces can be described as electrokinetic phenomena (EKP). Types of EKP include electrophoresis, streaming potential, streaming current, and electroosmosis (EO). This section gives an account of the development of studies in EO to date, and discusses how this phenomenon has been utilised by several research areas and groups thus far.

Electroosmosis (briefly introduced in the first section of the chapter) is the motion of a liquid through a porous plug, capillary or membrane, in response to an applied external tangential electric field around a system where an electric double layer (EDL) is established (see Section 2.3.1). A Coulomb force ($f = \rho_E E_{\text{ext}}$, where ρ_E is the free charge density and E_{ext} the external electric field) in the EDL induces fluid flow that is approximately uniform outside the electrical double layer (Kirby 2010). This induces the movement of ions towards the electrode of opposite polarity. The motion of fluid near a wall transfers momentum via viscous shear forces between the solvated ions and surrounding solvent molecules, into the bulk liquid inside the charged capillaries/pores. The theoretical velocity

profile for EO is shown in Figure 2.13; the theoretical 'plug'- and 'laminar'-flows are also represented.

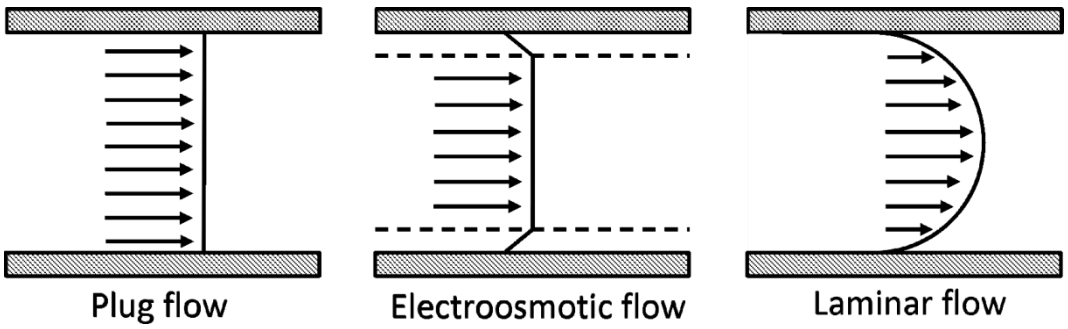

Figure 2.13 Schematic representations of the three different theoretical velocity profiles of plug, electroosmosis and laminar flows. The arrows represent the direction of flow and the dashed line indicated the EDL.

2.3.1 Electric Double Layer

Scientific works raising the question of the causes of the electric double layer (EDL) appeared in the mid-1860s after its discovery by Reuss in 1809. Quincke observed electroosmosis with glass capillaries and studied the phenomenon more systematically than had been done previously (Quincke 1861). Helmholtz adopted Quincke's idea and proposed the double layer theory, which related the electrical and flow parameters for electrokinetic transport introduced above (Helmholtz 1879) and this lead to the first derived equations for EO. In deriving the relevant expression, uniform pores were assumed. Dielectric permittivity was not included in these equations until Smoluchowski developed an expression with the permittivity term incorporated. The expression (now known as the Helmholtz-Smoluchowski equation) was written as (Smoluchowski 1903):

$$u = -\frac{\varepsilon_r \varepsilon_0 \zeta E}{\mu} \tag{2.13}$$

where u is the EO velocity, E the electric field, ζ the zeta potential, μ the dynamic viscosity, ε the dielectric permittivity and ε_0 the permittivity of vacuum.

The Helmholtz layer model, described the EDL as being made up of solvated ions which positioned themselves along a charged solid surface but a small distance away from the surface due to their hydration shells. The Gouy-Chapman model,

developed in the early 1900s, described the EDL as a diffuse double layer which took into account the disordering effect of thermal motion, unlike the Helmholtz layer model.

In the Gouy-Chapman model the local concentrations of co-ions and counter-ions within the boundary layer differ from their bulk concentrations (Figure 2.14a). Ions charged oppositely to the surface charge (counter-ions) cluster close to the charged surface, and ions with the same charges as the surface (co-ions) are repelled from it (Figure 2.14). A model which combined the two was developed by Stern and is now known as the Stern model (Figure 2.14).

The Gouy-Chapman model gave rise to an important parameter characterising the thickness of the diffuse layer:

$$\lambda_D = \left[\frac{\varepsilon_r \varepsilon_0 k_b T}{\sum_i (c_i)_0 z_i^2 e_0^2}\right]^{\frac{1}{2}} \tag{2.14}$$

Here $(c_i)_0$ is the bulk concentration of the i:th ion in the bulk phase and z_i is its valency and where ε_r and ε_0 are the relative permittivity of the electrolyte and the vacuum permittivity, respectively. λ_D has dimensions of length and is known as the Debye length. The Debye length has fundamental importance in the theory of electrokinetic phenomena (Wall 2010) and is often considered in conjunction with particle radius or cylindrical/pore radius. The latter is particularly important for the present study.

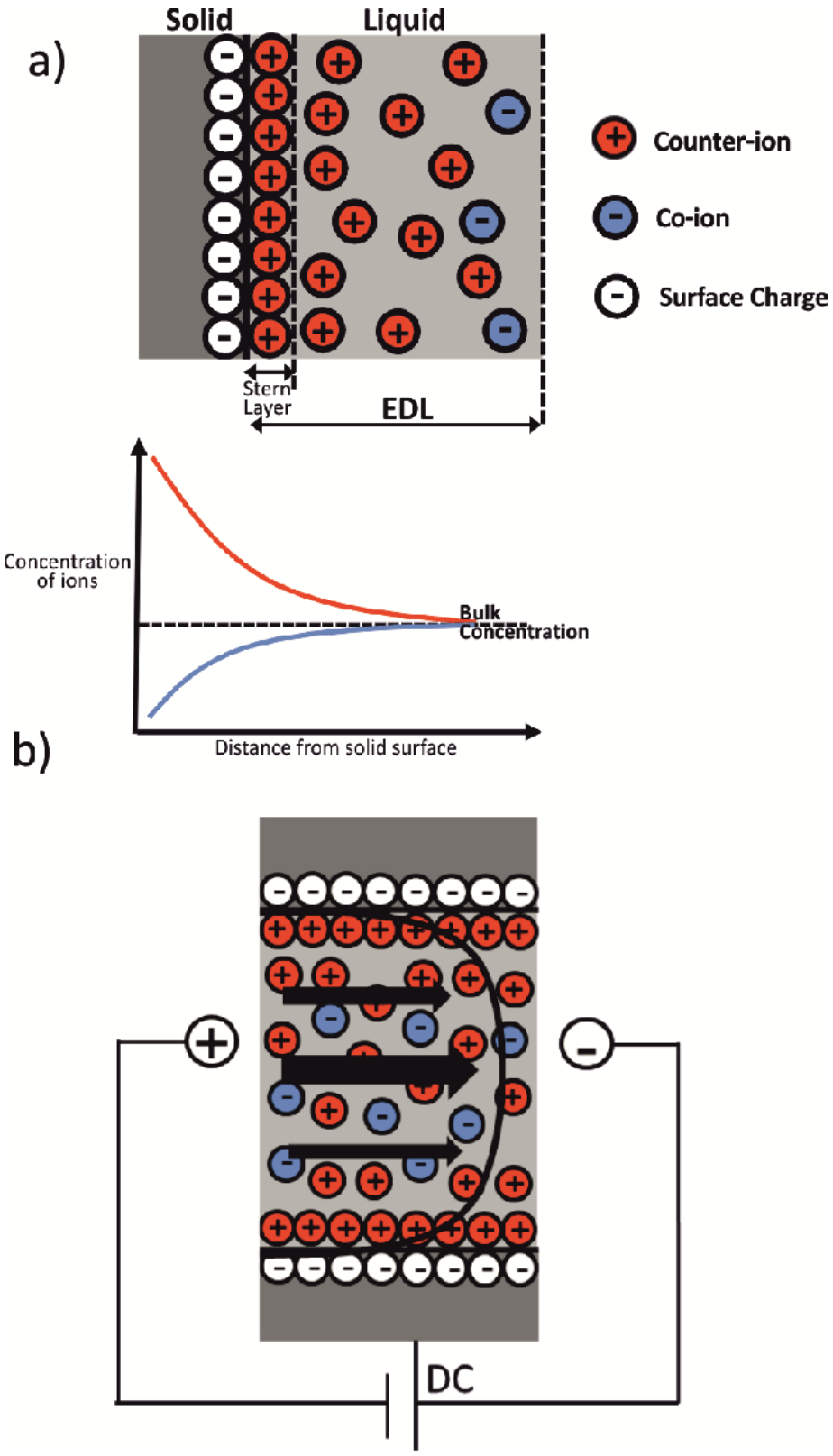

Figure 2.14 Schematic representation of a) the EDL structure where counter-ions in the liquid accumulate in the vicinity of the charged surface and b) EO flow caused by viscous drag when an externally applied electric field causes motion of counter-ions that shield a negative surface charge. The (typically nanoscale) thickness of the EDL is exaggerated for the purposes of the figure.

The effect of Debye length in electroosmosis is a contentious area, especially when applied to nano-systems. The established theory states that as a channel radius approaches the magnitude of the Debye length, theoretical velocity profiles return to that of laminar flow (a parabolic shape). Consider the plot in Figure 2.15 of a normalised EO flow profile against the radius of a channel a. When $\lambda_D/a = 1$ (i.e. the Debye length ≥ the channel diameter) the velocity profile is parabolic. This is due to Debye layer overlap in the centre of a channel which prevents maintenance of a charge neutral bulk fluid with the result that EOF is suppressed.

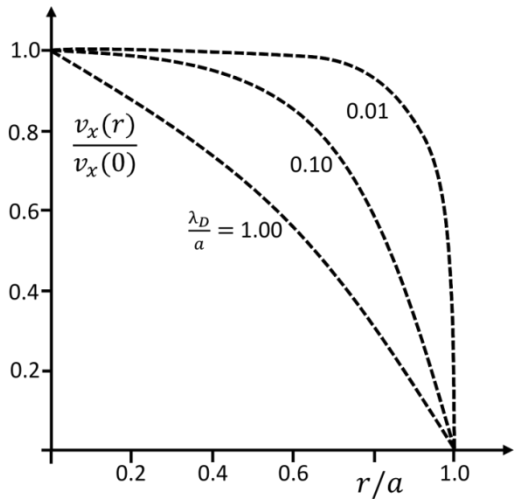

Figure 2.15 The normalized EO flow profile $v_x(r)/v_x(0)$ for a cylindrical channel of radius a with three different values of Debye length: nearly constant ($\lambda_D/a = 0.01$), rounded ($\lambda_D/a = 0.1$), and parabolic ($\lambda_D/a = 1$) (Bruus 2007).

This assumption has been challenged for nanofluidics systems, and a theoretical model for EOF at the nanoscale was recently developed to better understand transport phenomena in nanofluidic channels (Taylor and Ren 2005). The model applied the Nernst equation for ionic distribution in nanometre scale cylindrical channels. It was used to determine the effects of excess counter-ions outside the EDL layer on the velocity field of electroosmotic driven flow and significant reductions in area-average velocity were still observed.

2.3.2 Streaming Potential and Zeta Potential

Instead of applying an external electric field to induce liquid movement through a capillary or porous plug, a transmembrane voltage can be measured when a pressure gradient is applied to a porous system. Some solid surfaces become

charged when in contact with liquids of a certain pH, for example alumina becomes negatively charged when in contact with a liquid of pH > 8. When a pressure gradient is applied to a porous (membrane) system, excess charges near the wall are carried along the channel/capillary and accumulate down-stream. A steady-state is quickly established and the transmembrane voltage difference can be measured. This is known as the streaming potential (Rutgers 1940; Hunter 1981). Closely related to the streaming potential is the zeta potential. As in almost all electrokinetic systems a liquid moves with respect to a solid surface. The analysis of forces on the solid or liquid can be carried out in terms of electrostatic potential, where the average potential in the surface of shear can be calculated. This is the zeta potential, which is another fundamental quantity in electrokinetics (Rutgers 1940). Zeta potential, ζ, can be calculated using the Helmholtz-Smoluchowski equation for the streaming potential:

$$\frac{dV}{d\Delta P} = \frac{\varepsilon}{\mu\kappa}\zeta \tag{2.15}$$

where dV is the streaming potential and κ the conductivity of the liquid. For a full review on how pH, temperature, counter-ion valency, and size affect the zeta potential, refer to Kirby et al. (Kirby and Hasselbrink 2004).

2.3.3 Electroosmotic Pumps

Although electroosmosis has been known for almost two centuries, its application to miniaturized devices (and pumps in particular) for the generation of fluid flow has received increasing interest over the past few decades. More recently, electroosmosis has found application as a pulse-free, no-moving-parts pumping method for lab-on-a-chip and microfluidic applications (Chuan-Hua and Santiago 2002; Takamura et al. 2003; Prakash et al. 2006). To increase the total flow-rates and pressure capabilities of EO pumps a parallel channel configuration has been used (Bruus 2007), in other words a membrane. The flow rate through a porous membrane with cylindrical pores under an applied electric field and pressure gradient (exerted in the same direction) can be expressed as (Rice and Whitehead 1965; Vajandar et al. 2007):

$$Q_T = \frac{\phi}{\tau} A_{eff} \left(\frac{\pi D_P^2}{32 \mu L} \Delta P \pm \frac{\varepsilon \zeta}{\mu L} \Delta V_{eff} \right) \quad (2.16)$$

where ϕ is the porosity of the porous membrane, τ the tortuosity of membrane pores and A_{eff} the effective membrane area. ΔP is the applied pressure difference across the membrane, D_P the pore diameter; L the thickness of the membrane; $\varepsilon = \varepsilon_r \varepsilon_0$; ζ is the zeta potential; ΔV_{eff} is the effective voltage drop across the membrane and μ the viscosity.

Nanochannels, normally with only one dimension on the nanoscale (e.g. height of a channel), were the first materials to be fabricated for investigation into EO pumping. The first instance of using electroosmosis to drive fluids was reported by Pretorius et al. in the mid-1970s (Pretorius et al. 1974). This study used EO for thin-liquid chromatography and was on a larger length scale (than nano-EO pumps) and used higher applied voltages than the research reported throughout this thesis. Pretorius used a column with an inner diameter of 1 mm packed with polydisperse silica particles (1 - 20 μm) and applied voltages of 25 kV. EO velocities of 0.2 mm s^{-1} were reported. For studies of this kind, the Debye length (discussed above) was greater than the diameter of the channel/column (1 mm) and so the classical electroosmotic flow models hold (Equation 2.13). A year later Theeuwes patented an EO pump which utilized a porous porcelain plug with an average pore diameter of 0.1 μm, 21% porosity, and a 0.2 cm thickness, generating a flow rate of 0.3 ml hr^{-1} at 50 V (Theeuwes 1974).

2.3.3.1 EO Pumps at the Micro- and Nano-scale

Due to an increased interest in replicating biological systems for new applications in healthcare and water treatment (something which has coincided with the development of new materials to meet urgent needs in these areas) the past decade has seen the publication of numerous experimental and theoretical studies striving to further understand the fundamental science of EO pumps. The development of both NPAMs and CNTs serve as perfect materials for fundamental studies in this area whilst also offering the possibility of applied solutions in the two areas noted above. The controlled and ordered pore sizes of NPAMs (and therefore CNT membranes from the CVD process) allow the study of EO at the nanoscale.

Therefore over the past decade there have been several studies combining the two: nanoporous materials and EO, especially for low-voltage DC EO pumps. The results of these are discussed below and summarised in Table 2-4.

Between 2003 and 2007 there were several publications on EO pumping at the sub-micrometre scale. It is important to note here that the term 'nanoscale' has been used quite broadly, for example in some publications the pore diameters have been reported to be ranged from ~ 20 nm to up to 700 nm. Furthermore, in the majority of cases, these are average pore diameters and have large pore size distributions. For example high flow/high pressure EO pumps were reported using silica and alumina frits, with pore diameters ranging from 25 nm to 1 μm. The porous structure of the frits (due to the manufacturing process) results in large pore size distributions and in this case these frits were not characterised in-house but relied on the manufacturers' specifications (Prakash et al. 2006). This could lead to discrepancies in EO flow analysis. However, flow rates of 0.1 ml s^{-1} and actuation pressures in excess of 0.1 MPa were reported. Similar results have been obtained for EOF of borate buffer through glass frit discs (Yao et al. 2003). Here maximum flow rates of 33 ml min^{-1} at an applied potential of 100 V were achieved. This study fully characterised the glass frit discs and observed pore sizes on the order of 1 μm (Figure 2.16).

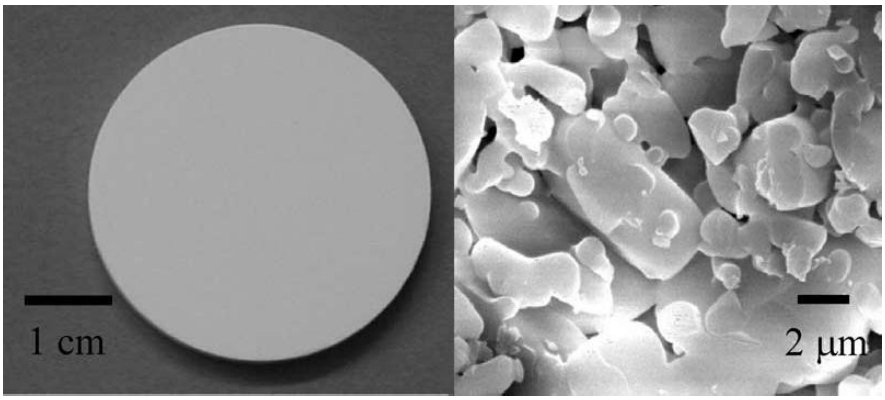

Figure 2.16 Porous glass disc (the frit) of diameter 40 mm and 5 mm thickness (left) and a SEM of the porous glass structure (right) (Yao et al. 2003).

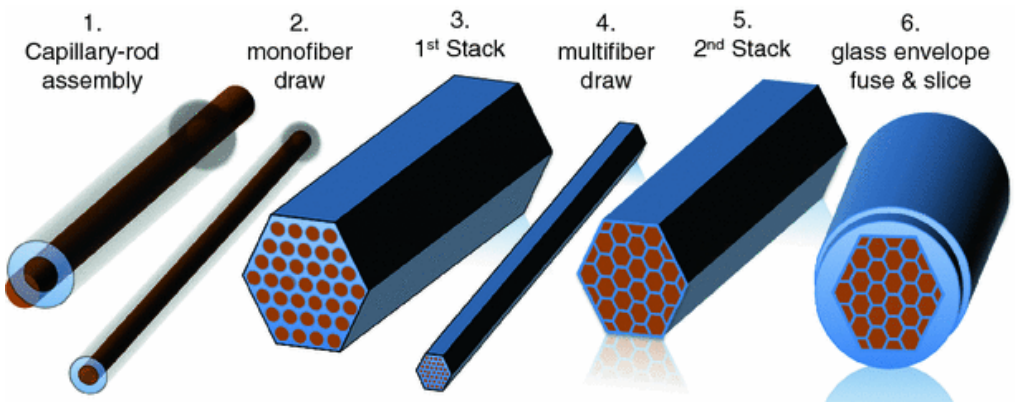

Figure 2.17 Key process steps involved in the microfabrication of MCP (Cao et al. 2012).

So-called microchannel glass plates (MCP) have also recently been reported, which contain millions of fused glass capillaries with micrometre diameters. In comparison with the glass frits discussed above, the use of capillaries means that the membranes have a uniform structure with straight channels (Figure 2.17), similar to that provided by NPAMs but at the micrometre scale (Cao et al. 2012).The MCP pumps achieved a maximum of ~ 0.2 ml min^{-1} cm^{-2} V^{-1}.

Research into EO pumps was continued by the same group which completed the work by Yao et al. discussed above. This study moved away from the glass frit to a silicon material with micrometre pore size (1 - 3 μm) which had a pore geometry nearing-unity tortuosity with hexagonally packed pores of very narrow pore distributions (again with a likeness to NPAMs but at the microscale). The maximum flow rate per applied external electric field was reported to be 0.13 ml min^{-1} cm^{-2} V^{-1}. This value was five times larger than that they had demonstrated previously with porous glass EO pumps (Yao et al. 2003; Yao et al. 2006).

Recent EO measurements using KCl as an electrolyte and commercial alumina membranes considered the effect of pore diameter (20, 100 and 200 nm) on flow rate, with slight increases in flow rate with decreasing pore size (Chen et al. 2008). These results are questionable as the authors assumed the membranes had uniform pore diameters throughout the membrane thickness, whereas the membranes used (Whatman™ Anodisc®) were asymmetric, meaning that one side had an average pore size of 200 nm and the other side an average of 20 or 100 nm. This is for approximately 1 μm out of a total 60 μm thickness. This

change in pore diameter was obtained through significant pore branching, yielding significantly different porosities for each membrane, though this was not stated in the publication. In 2010, the same group published a paper on EO using the Whatman™ Anodisc® with constant pore diameter (approximately 200 nm) throughout the whole membrane thickness, modifying the surface chemistry by H_2O_2-treatment and silanization (Chen et al. 2010). Only DI water (no buffer) was used for all of the EO experiments performed in the paper. The time scales reported for EO pumping seem unlikely for DI water as the degree of hydrolysis caused by the applied electric field > 1 V would drastically change the local pH of the electrolyte and cause excess hydrogen bubbles, retarding flow rates. It is generally accepted that this is one of the main reasons why EO pumps have not yet been used as pumping devices on a larger scale. The delicate balance needed for effective EO flows at longer time scales is difficult to maintain. This has been discussed in greater detail below (Section 2.3.4).

Table 2-4 Literature Values for EOF in silica, glass and alumina membranes.

Q_{max} (10^{-3} m^3 s^{-1} $V^{-1}m^{-2}$)	Material	Pore size (nm)	ψ	τ	Concentration (10^{-3}M)	ΔV_{eff} (V)	ΔV_{app} (V)	ref.
1.3	silicon	1 - 3·10^3	0.4	~1	$Na_2B_4O_7$, 1.0	30		Yao et al. 2006
0.5	sintered glass	550	0.24	1.45	$Na_2B_4O_7$, 1.0	50		Yao et al. 2003
0.0125	silica	600	0.4	1.25	NaCl, 2.0		200	Prakash et al. 2006
0.02	SiO_2-coated NPAM	70	0.5	~1	$Na_2B_4O_7$, 2.5	7		Vajandar et al. 2007
0.003	NPAM	80						
0.0015	Anodisc	200/100	0.31	~1	KCl, 10^{-4}		80	Chen et al. 2008
0.016	Anodisc	200	0.5	~1	DI Water, 10^{-2}		5	Ai et al. 2010

The effect of surface charge on EOF was also observed with a two-orders-of-magnitude increase in maximum flow rate for SiO_2-coated NPAMs compared to the uncoated NPAMs using a borate buffer (Vajandar et al. 2007). Furthermore, a recent study has looked at the effect of three different NPAM pore sizes (achieved by pore widening) on ion transport and found that ion diffusion coefficients decrease with decreasing pore size for ions with the same charge as the pore wall (Romero et al. 2012).

The majority of experimental results described so far have been conducted for short periods of time, approximately 10 minutes. This is due to one of the main challenges regarding the practical use of EO pumping, namely the long-term stability of the electrolyte and membrane due to electrolysis and material degradation (Brask et al. 2005). Progress in this area has been obtained by dramatically reducing applied voltages from the kV range to double or single-digit voltages. Other major obstacles include concentration polarization, fouling and fluctuating pH (Strickland et al. 2010; Suss et al. 2011).

2.3.3.2 Electroosmosis in Carbon Nanotube Membranes

The same group that developed the template synthesis method were the first (and have been the only group until now) to assess electroosmosis in the template prepared CNT membranes (Miller et al. 2001; Miller and Martin 2002). Miller et al. used commercial alumina membranes as templates for the preparation of CNT membranes. The CVD parameters differed from those discussed above in Section 2.1.2, as the templates were heated under a stream of argon up to 670 °C. At this temperature the Ar stream was terminated and ethylene (C_2H_4) introduced to the reactor (therefore there was no He:C_2H_4 mixture as in most previously reported methods). The deposition was continued for 5.5 hours, after which the C_2H_4 stream was terminated and the Ar stream resumed. This resulted in ~ 40 nm thick carbon walls inside ~ 200 nm pore diameter of the commercial alumina membranes. From zeta potential measurements performed during the studies the as-synthesised CNT membranes had anionic surface charge (i.e. the cation of the buffer makes up the EDL and drives the direction of the EO). This was due to the oxidation of the surface after the samples were left in air post-synthesis which resulted in acidic sites on the CNTs (García et al. 1997; Bismarck and Springer 1999; Miller et al. 2001).

To increase the surface charge of the CNT membranes, electrochemical derivatization was used to attach carboxylate groups to the nanotube walls. Two molecules were grafted on to the walls. One of which increased the negative surface charge of the wall from the as-synthesised CNT membrane ζ potential value of – 20.8 mV to – 30.6 mV, and the other rendered the tube wall positively charged with a zeta potential value of + 13.2 mV. By manipulating the surface

charge, the EOF rate and direction could be controlled (Miller et al. 2001; Miller and Martin 2002). This group continued the theme of manipulating surface charge on CNT membranes as a few years later a study of EOF in CNT membranes after coating the nanotubes in a thin layer of the redox polymer poly(vinylferrocene) (PVFc) was conducted (Miller and Martin 2004). The purpose of grafting a redox-active polymer onto the nanotube surfaces was to enable a switching capacity when investigating EO. This meant that the charge of the material could be electrochemically switched from neutral to polycationic. The novelty of this method comes from its ability to control the surface charge when applying an external electric field to the redox-coated CNT membranes. The magnitude of the external electric field would fully oxidise, partially oxidise or fully reduce the PVFc on the CNT membranes. On applying a current density to the membrane (to induce EO) they found that the magnitude of the EO was much larger for the fully oxidised PVFc-CNT membranes than the fully reduced PVFc-CNT membranes. These studies confirm the necessity of surface charge for effective EOF and they also develop a possible switching method using redox-active molecules to do so. As the diameter of the CNT membranes is ~ 120 nm, the EDLs do not come into contact. The works completed by Miller et al. (discussed above) are the only studies until now that have used CNT membranes produced by CVD in alumina to study EO. The results presented in Chapter 8 of this thesis are the first to use CNT membranes in engineered NPAMs of different pore diameters, allowing the effect of pore diameter and EDL overlap on EO to be studied.

EOF in CNTs was not returned to experimentally until 2011, when Wu et al. presented results which suggested highly efficient EO in CNT membranes. The CNT membranes were very different from those discussed above. These membranes were produced using a previous method developed by Hinds et al. where aligned MWCNTs were incorporated across a polymer film (Hinds et al. 2004). A year later the same group performed permeability measurements on these membranes and observed four to five times faster flow rates in 7 nm diameter MWCNTs (Majumder et al. 2005). To fully utilise the fast fluid transport observed in CNTs, the Hinds group investigated EOF and noted that the combination of the transport properties and EO could be relevant for drug delivery applications (Wu et al. 2011; Hinds 2012). Wu et al. functionalised the CNT membranes (similar to Miller et al.) by diazonium grafting and found the EOF

was more efficient with grafting than without, as the surface charge density of the CNTs was increased. It is difficult to fully compare the results of the as-synthesised CNT membranes presented by Miller et al. and Wu et al. as the CNTs have different carbon structures (i.e. degree of graphitization) and vastly different pore diameters. For example, the diameters of the CNTs in Wu et al. may exhibit EDL overlap where at the Miller et al. studies have pore diameters considerably larger than the EDL thickness.

2.3.4 Electroosmotic Pumping – Challenges

Electroosmotic pumping does not come without challenges, particularly in achieving stable and prolonged pumping. This section will discuss the main obstacles that affect the longevity of EO pumps: concentration polarisation, pH effects, double layer overlap, and efficiency.

2.3.4.1 Concentration Polarization and pH Effects

A group at Stanford University has completed some of the most coherent work regarding EO pumps and what affects their performance. The first series of papers reviewed the electrolyte chemistry for microfluidic electrokinetic studies and highlighted the effect of pH and the importance of understanding the buffer system used for experimental set-ups. They also stated the necessity for publications to fully report the buffer systems employed (Persat et al. 2009a; Persat et al. 2009b). As highlighted by Mani et al. complex behaviours emerge in electrokinetics when nano- and micro-channels are employed, one of the main being concentration polarization (CP) (Mani et al. 2009). CP was observed in nanochannels by Pu et al. (Pu et al. 2004) where depletion and enrichment zones of ions were observed when an electric field was applied across a channel, the extent of which was due to the degree of double-layer overlap. This means that as the EDL thickness decreased (by increasing electrolyte concentration) the depletion and enrichment effects were negligible. However, for much lower concentrations of electrolyte where the EDL thickness was much greater and most probably overlapped there was severe ion depletion/enrichment. This finding was further supported by the group in Stanford where concentration fields in a millichannel around a microporous silica frit (shown earlier in Figure 2.16) were

visualized using pH sensitive Fluorescein dye (Suss et al. 2011). Concentration polarization was observed, with depletion and enrichment zones of ions at the electrode and frit surface (Figure 2.18). Furthermore, this was also coupled with the concentration of the electrolyte. This topic was pursued a year earlier by the same group, again supporting the conclusion that CP is one of the key factors determining EO pump performance (Strickland et al. 2010).

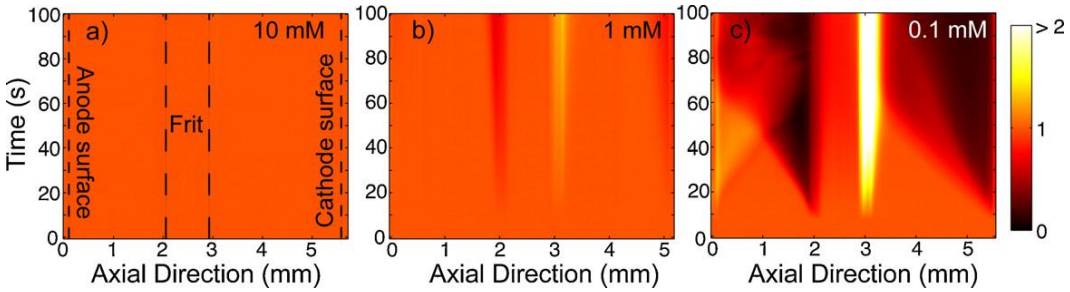

Figure 2.18 Experimental visualizations of concentration fields in a millichannel between the silica frit (225 nm mean pore radius). The x-axis represents axial position along the borosilicate millichannel which houses the frit. The colour map represents the concentration enrichment factor a) at 10 mM borate, no CP is observed. The frit and electrode boundaries are shown as dashed lines b) at 1 mM, CP zones observably form but remain local to the frit surfaces c) at 0.1 mM, CP fronts clearly propagate from the frit (Suss et al. 2011).

2.3.4.2 Efficiency

The efficiency of EO pumps has long been one of the biggest obstacles in terms of using these systems at larger scales. To date, the most efficient EO pump reported was a micro-pump with an efficiency of approximately 5.6% (Reichmuth et al. 2003). But the majority of achieved efficiencies lie between 0.01 - 1.5% (Chen et al. 2008). For example Gan and colleagues reported an EO pump flow injection analysis system and applied it in the determination of chromium (VI) traces in waste-water (Gan et al. 2000). Several electrolytes with varying concentrations were investigated in the EO pump, which consisted of a porous core made from boric glass powder. The porous core was 35 mm in diameter, 13 mm thick and had a pore size of 2 - 5 µm inner diameters. The highest efficiencies reported in this study were ~ 1.0% when 500 V was applied (this potential was applied in all cases throughout the study).

The low efficiencies are mostly due to the voltage drop from the applied V_{app} to effective voltage V_{eff}, which is the voltage directly inducing EO flow. Yao et al. proposed a simple model which more accurately related the DC applied voltage delivered by the power supply to the V_{eff} supplied to the pump (Yao et al. 2003):

$$V_{eff} = V_{app} - V_{dec} - 2R_d I \tag{2.17}$$

where V_{dec} is the decomposition potential associated with the electrode reactions at the electrode/electrolyte surfaces, R_d the resistance of the region between each electrode and the frit/membrane surface and I is the system current. When the voltage drop is calculated, the value of V_{eff} is substantially lower than that of V_{app} in the majority of cases. This was supported by the findings of Vajandar et al. who reported voltage drops of 9 to 41 V (for V_{eff} of 1 - 9 V when V_{app} ranged from 10 - 50 V). It is also further supported by the results discussed in Chapter 7 of this thesis. The lack of efficiency also lies with the magnitude of voltage applied. When voltages of more than 1 V are applied, electrolysis of the electrolyte occurs and in the majority of cases (when platinum, Pt electrodes are used) hydrogen bubbles are formed (Equation 2.18 and Figure 2.19). The gas generation can retard EO flow rates as bubbles can block the channels of the membranes.

$$2H_2O \rightarrow 2H_{2\,(g)} + O_{2\,(g)} \tag{2.18}$$

Figure 2.19 A magnified view of Pt electrode chamber of the EO pump. A hydrophilic fibre mesh (not visible) was inserted between the spiral shaped Pt electrode and the membrane support mesh in order to prevent the visible bubbles from blocking the current (Brask et al. 2005).

More recently there has been a report of more efficient EO flows through functionalised CNT membranes. These CNT membranes were discussed earlier in Section 2.2.1 and 2.3.3.2. They showed that by utilising the CNT membrane properties with inner diameters of 7 nm and 1.5 nm and diazonium grafting (to increase the surface charge density) the electroosmotic mobility was increased by 90%, resulting in 25 to 110 times improved efficiencies in comparison to previously reported EO pumps (the comparisons were mainly made with nanoporous alumina) (Wu et al. 2011).

2.4 Summary

This chapter has introduced and discussed crucial techniques and phenomena which have been employed throughout this thesis. The first section of the current chapter, *Material Development and their Characteristics*, introduced and discussed in detail the fabrication of NPAMs and proposed growth mechanisms for self-organised pore structures observed in NPAMs. This section also explained how NPAMs can be employed as templates for the production of nanotubes made of a variety of materials, in particular for the production of CNTs for CNT membranes.

The second section, *Wetting Properties and Transport at the Nanoscale*, discussed the importance of considering wetting properties of materials with their transport properties at both the macro- and nanoscale. This section also highlighted unique flow properties observed in CNTs (experimentally and theoretically) but also discussed how assumptions at the macro-scale may not always be applicable at the nanoscale. The third main section of the chapter, *Electroosmosis*, presented a historical background in the discovery of EO and how this developed over the last two centuries to the applications of EO pumps seen today. It also discussed the challenges EO presents in application-based devices. In addition to this, it presented critical questions regarding EO which still remain unanswered, particularly with regard to EO flows at the nanoscale when EDLs overlap.

The following chapters of this thesis will first, fully characterise the materials utilised throughout the present work. They will then move on to the wetting properties of hydrophilic and hydrophobic nanostructures. This will be followed

by chapters which present work on the transport of water in hydrophilic NPAMs with pressure-driven flow. The final chapters will present research on EO in NPAMs and CNT membranes.

Chapter 3

Materials and Methods

Porous membranes have generated significant scientific and technological interest because of their large surface area to volume ratio, which offers a number of advantages and opportunities. Nanoporous alumina membranes, for instance, provide an ideal platform for the systematic study of pore diameter, surface chemistry, and wetting properties at the nanoscale. These studies can only be conducted accurately if the material structure is highly controlled. The anodization of aluminium is therefore an attractive method since it produces ordered and consistent pore diameters in a cost-effective process. The engineering of nanoporous alumina membranes in this study has been optimized for the investigation of their properties as both membranes and templates.

3.1 Nanoporous Alumina Membranes by One- and Two-Step Processes

Aluminium anodization was introduced and discussed in Chapter 2 Section 2.2, where the following were considered in detail: the oxide growth mechanism, optimized anodization parameters, and the relationship between the structural parameters of porous alumina and the applied anodization voltage first discovered by Keller et al. (Keller et al. 1953). In the first section of this chapter, the materials used for the fabrication process of porous alumina are discussed in detail along with the methods and procedures of the fabrication process itself.

Prior to the work of Masuda et al. the anodization of aluminium (using a range of electrolytes) was primarily carried out through a one-step process. This process (described in the literature review) uses anions from acidic electrolytes (sulfuric acid, H_2SO_4, and oxalic acid, $C_2H_2O_4$. and in some cases phosphoric acid, H_3PO_4) and an applied potential to oxidise the aluminium to aluminium oxide (also referred to as alumina). This process produces nanopores and, after a time, nano-channels, of micro-scale thickness. These will be referred to in what follows as nanoporous alumina membranes (NPAMs).

3.1.1 Materials

Flat aluminium sheets of 99.999% purity were purchased from Alfa Aesar in two thicknesses: 0.1 mm and 0.25 mm. Oxalic acid, $C_2H_2O_4$ (anhydrous 99%), and phosphoric acid, H_3PO_4 (85+%), were obtained from Fisher Scientific (UK). Sulfuric acid, H_2SO_4 (5.0 M) was purchased from Sigma Aldrich (UK). Each chemical was made up to the desired electrolyte concentration for the anodization process. Perchloric acid, $HClO_4$ (60 - 62%), and ethanol, CH_3CH_2OH (96%), were purchased from Alfa Aesar and Sigma Aldrich respectively for the electropolishing process. Hydrochloric acid, HCl (37%), and copper (II) chloride, $CuCl_2$ (98+%), were obtained from Fisher Scientific (UK) for the aluminium removal process.

3.1.2 Anodization of Aluminium

The aluminium sample was first cut into 13 mm diameter discs and annealed in a Carbolite CWF 1100 furnace at 500°C for 1 hour flattened by a 1 kg weight. Before anodization, the aluminium was degreased in acetone (99.8%, HPLC grade) for 10 minutes. The first step in preparation for anodization was electropolishing and the result of this process was critical to the outcome of the end product. Electro-polishing of the aluminium was carried out by submersing the chosen area of the aluminium in a mixture of perchloric acid and ethanol. The importance of this step has been described in Chapter 2. Following the investigation of others, the electropolishing solution used throughout the experiments was a 4:1 mixture of 96% ethanol and 60 - 62% perchloric acid. A potentiostatic value of 20 V was applied for 15 minutes with constant monitoring. This was conducted at a temperature of $– 77 \pm 4$ °C using dry ice (solid CO_2) in an acetone bath (Figure 3.1). It was important to ensure that the time between the electropolishing process and the anodization process was as short as possible. This is due to the rapid formation of an oxide layer on the surface of the aluminium, something which could prevent the initial structure barrier layer from forming as homogenously as desired.

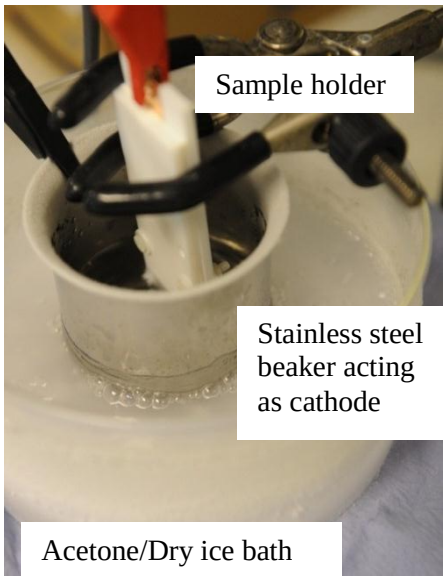

Figure 3.1 Pre-treatment of the aluminium surface - electropolishing set-up.

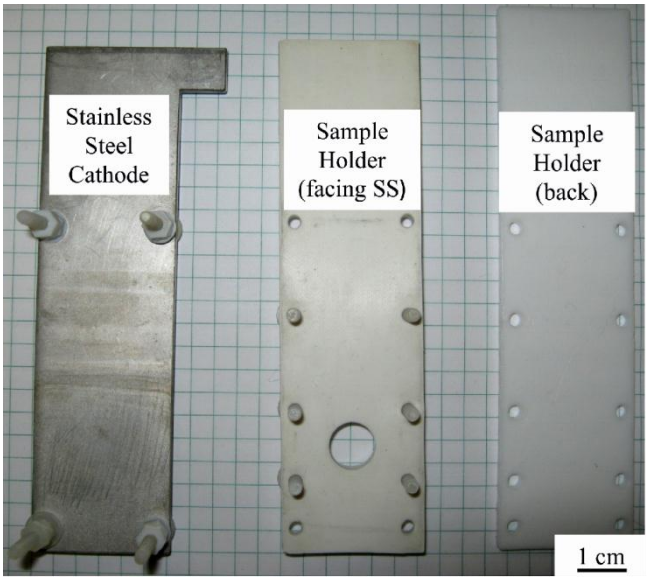

Figure 3.2 Anodization sample holder.

The two-step process first described in 1995 (Masuda and Fukuda 1995) was a variation on the one-step method that came before it and has been described in detail in Chapter 2. The two-step method, used throughout this research, is identical to the one-step process with the difference that the anodization is carried out in two steps with an alumina removal step between. When the first step (of between 15 minutes and 3 hours) was completed, the alumina layer which had formed in the first step was removed by submersion in a 1:1 solution of 1.8 wt.% chromic acid and 6 wt.% of phosphoric acid heated to 60 °C for a time equivalent to the first anodization step. The sample was then rinsed thoroughly with

deionised water (as the chromic acid solution was extremely aggressive) so as not to contaminate the second anodization process. The sample was then re-submersed in the same electrolyte solution and the anodization process started again with the same parameters as the first step but for an extended period of time. The custom-made anodization sample holder and set-up for the anodization procedure are shown in Figure 3.2 and Figure 3.3 respectively. Full details of the anodization parameters for each membrane have been summarised in Table 3-1.

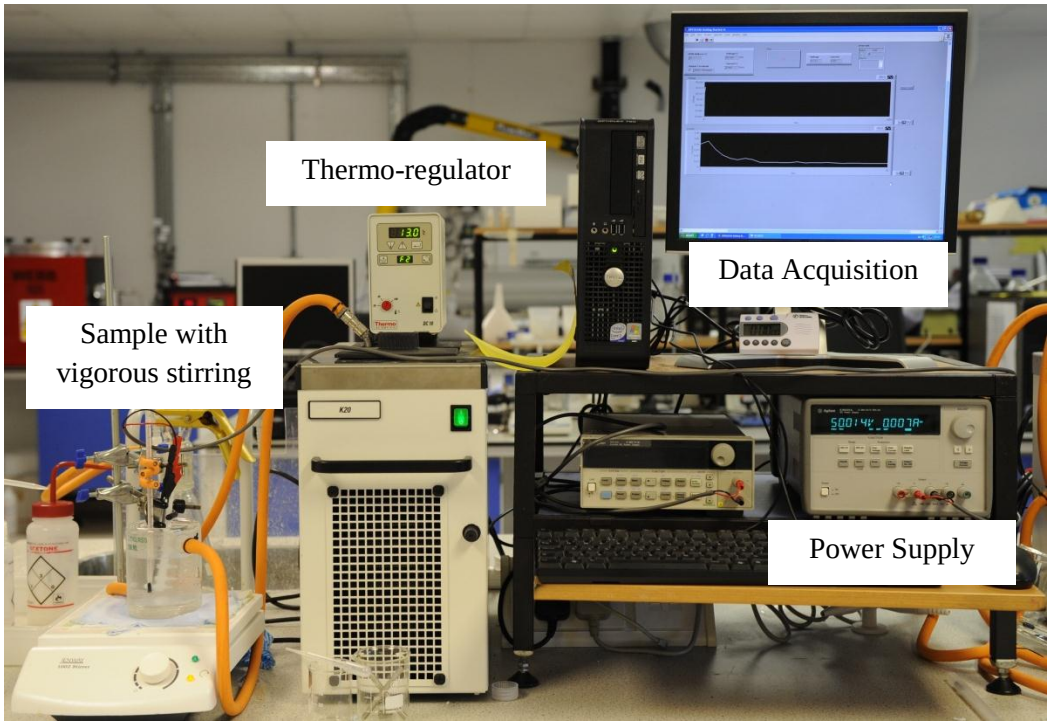

Figure 3.3 Nanoporous alumina membrane production set-up; temperature controlled anodization of aluminium with constant applied voltages and data acquisition.

After 5 to 6 hours at 0 °C or 10 to 12 hours at 14 °C (for 0.5/1.0 M sulfuric and 0.3 M oxalic acid respectively) the anodization process was terminated. After anodization a fully oxidised layer was visible. As only one side of aluminium had been exposed to the electrolyte, an aluminium back layer remained. One side of the aluminium was protected from exposure to the acid in order to avoid the pore branching and misalignment of pores which would have resulted if both sides were anodized.

The next and penultimate step was the removal of the remaining aluminium back layer. A 1:1 solution of 0.2 M copper (II) chloride ($CuCl_2$) in 20% hydrochloric acid (HCl) was used in this process. With a successful electropolishing and

anodization procedure, the aluminium removal took approximately 20 minutes. The sample was submersed in the solution at ambient temperature. After removal and thorough rinsing the sample was a translucent material.

Table 3-1 Anodization parameters and the resulting structural characteristics of the membranes.

Voltage (V)	Electrolyte	Pore Diameter, D_P (nm)[a]	Interpore Distance, D_C (nm)[a]	Oxide Layer Thickness, B (nm)	Porosity, ϕ (-)
10	1.0 M H_2SO_4, 0 °C	13±2	33±3	8	0.11
15		18±3	37±3	10	0.10
20	0.5 M H_2SO_4, 0 °C	25±4	54±4	12	0.11
25		30±4	64±5	23	0.15
30	0.3 M $C_2H_2O_4$, 14 °C	32±3	94±3	29	0.23
40		44±2	113±2	35	0.18
50		52±5	140±3	46	0.17
60		59±3	163±6	58	0.11
70		99±6	219±7	69	0.32
80		115±5	238±8	81	0.11
110	0.1 M H_3PO_4	130±15	220±20	-*	0.30
150		220±20	-*	-*	0.42

[a] Error standard deviation of SEMs in several places from at least three membranes. *Accurate measurement prevented by fragmentation, branching, and high porosity structure.

3.1.3 Pore Opening Detection

The growth mechanism of alumina (fully described in Chapter 2) discussed the barrier oxide layer. To obtain working NPAMs and templates with open-through morphology this layer must be removed. Wet chemical etching with phosphoric acid (H_3PO_4) was utilised to achieve this. Because the whole membrane is susceptible to etching by H_3PO_4 (including the already porous side, which would be vulnerable to over-etching), a pore opening detection set-up was developed following the method of Lillo and Losic (2009). This method successfully electrochemically detected the dissolution of the barrier oxide layer and thus prevented over-etching. Using this method of control, the pore opening process resulted in optimum through-hole morphology of the membrane. This process was achieved using 0.1 M (6 wt.%) H_3PO_4. The procedure resulted in consistent measurements of the pore opening process. Figure 3.4 shows a schematic of the pore-opening set-up. The already open porous side (top-side) of the membrane was exposed to 0.2 M potassium chloride (KCl) to protect the pores from over-etching, and the barrier oxide layer was exposed to hot (50 °C) H_3PO_4. A constant

voltage was applied (2.5 V) and the current and time recorded. When the barrier oxide layer started to be etched away, the circuit was complete and a value for the current was observed. The resulting pore-opening profile will be discussed in greater detail in Chapter 4. An overall summary of the anodization procedure is shown in a flow chart (Figure 3.5).

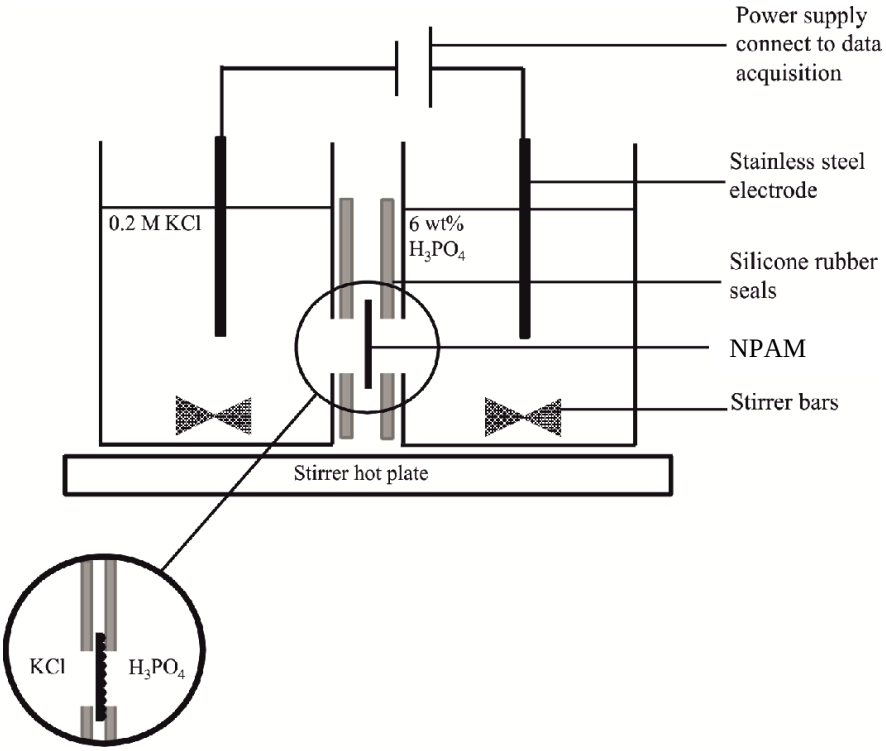

Figure 3.4 Schematic diagram of pore opening detection set-up.

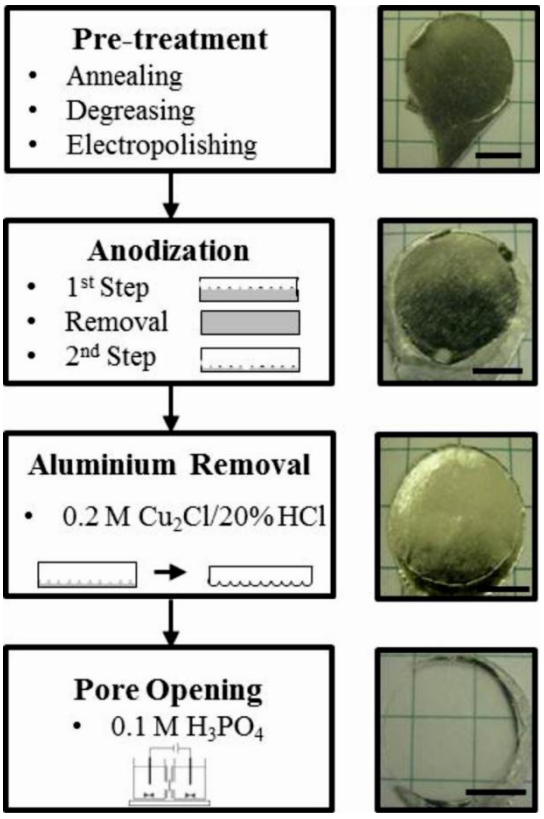

Figure 3.5 Flow chart of anodization procedure and equivalent digital images of the aluminium anodization at each stage (scale bar 5 mm).

3.2 Contact Angle Measurements on Porous Anodic Alumina

Porous anodic alumina (PAA) was fabricated using the anodization method described above but in this case the oxide barrier was not etched away. The PAA nomenclature is therefore used to distinguish between NPAMs (open-through pore network) and PAAs (porous alumina with barrier layer intact). The pores were closed throughout the contact angle measurements in order to assess the wetting properties of the nanostructured porous alumina. Contact angle measurements were made using the sessile droplet method in air at 20 °C with 5 μl droplets of de-ionized (DI) water as solvent. The alumina substrate was washed with DI water and HPLC grade ethanol and then thoroughly dried with an argon stream. The alumina substrate was then placed on the goniometer and still images were obtained using a Discovery VMS-001 USB microscope (Veho). Each measurement was repeated at least 6 times, within the error ± 2°.

3.2.1 Silanization of PAAs

In order to assess and develop a model for the wetting properties of the PAA their surface chemistry was modified with a monolayer coating of fluoro-octyltrichlorosilane (FOTS) (Figure 3.6). A simple and effective method developed by Aran et al. (Aran et al. 2011) was optimised for this process: 40 μl of FOTS were dropped into 40 ml of n-hexane (Fisher Scientific, UK). Each PAA sample was placed inside the FOTS-hexane solution for 1 hour with gentle agitation. The PAAs were then taken out of the solution, rinsed and placed in an oven at 100 °C for 1 hour. The samples were subsequently rinsed with acetone and left to dry.

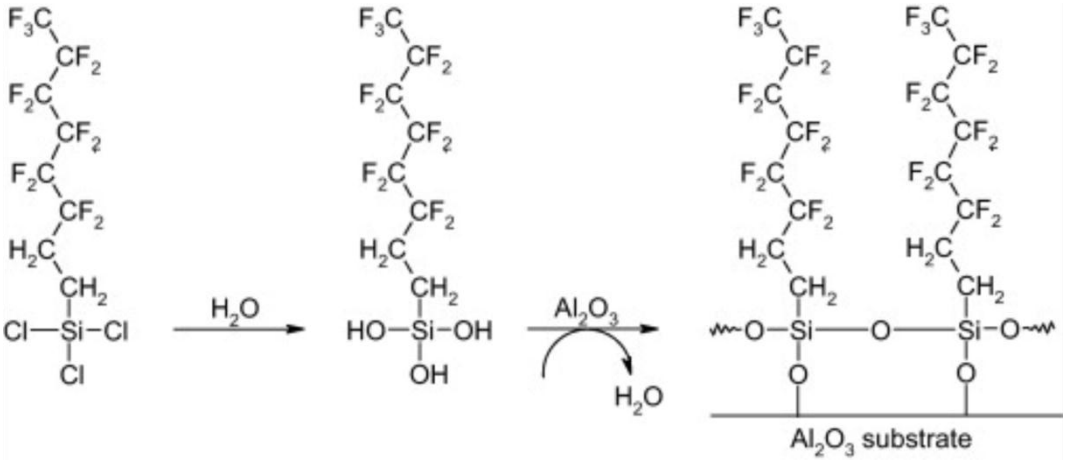

Figure 3.6 Schematic representation of the surface modification of Al_2O_3 using FOTS (Aran et al. 2011).

3.3 Hydrothermal Treatment of Alumina

Hydrothermal treatment of NPAMs results in a swelling of the microcrystalline surfaces (Patermarakis et al. 1999). It was applied in order to shrink the pore diameters and thereby achieve a more robust membrane with very small and highly ordered pores (< 10 nm). During anodization, as discussed earlier, electrolyte anions are incorporated into the porous alumina structure, the largest proportion accruing in the barrier oxide layer and surface walls of the pores. During hydrothermal treatment this oxide layer is hydrated: chemisorbed OH^-, H^+, and H_2O add to the microcrystalline surface and physically adsorbed H_2O is added to the layer of chemisorbed species, thus swelling the structure. The

electrolyte anions are, at the same time, removed from the microcrystalline surfaces (Murphy 1967). Three methods of hydrothermal treatment were applied in this research.

1. Electrochemical detection of pore shrinkage: 0.5 M KCl was heated to 90 °C in the same set-up as the pore-opening detection method (Figure 3.4) but in this case KCl on both sides of the membrane. 2.5 V was applied across the membrane which was sandwiched between the two vessels. At first there was a large current (20 mA) as expected and over time this value reduced. The results of this are discussed in full detail in Chapter 4.
2. Membranes were submersed in boiling water: approximately 200 ml of DI water was boiled in a Pyrex beaker and covered to reduce evaporation. The membranes were submersed in the boiling water for 1 hour.
3. Steam treatment: First an incision was made in a bung seal in order to insert an inverted tube (Figure 3.7). This tube was connected to an adapted sample holder holding the membrane. DI water was boiled in a conical flask and the steam driven through the tube onto the sealed membrane surface. Steam was observed flowing out of the membrane. The steaming process was carried out between 5 to 40 minutes to shrink the pores.

The results of the hydrothermal treatments have been discussed in detail in Chapter 4. AFM and SEM were utilised to track hydrothermal treatment over time and observe the limits of the process. Pore shrinkage was observed as expected. However, at a certain threshold, a matt growth of fibres nucleated.

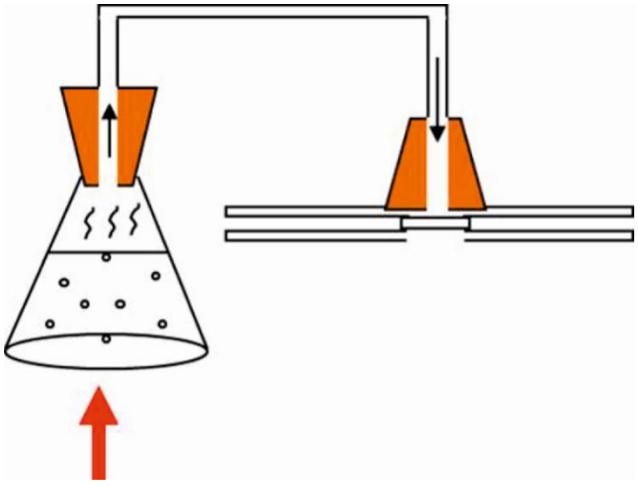

Figure 3.7 Hydrothermal treatment by steam set-up.

3.4 Chemical Vapour Deposition in the Production of CNT Membranes

In 1994 Martin and his group were the first to propose using nanoporous membranes as a template for the synthesis of nanomaterials (Martin 1994). One of the most successful membranes they used as a template was of nanoporous alumina. Since then membranes have been used to produce a plethora of different nanomaterials. Examples include nickel (Yin et al. 2001) and silver nanowires (Choi et al. 2003), polymer nanotubes (Steinhart et al. 2002), SiC (Cheng et al. 2005), BNNTs (Bechelany et al. 2007), CNTs (Miller et al. 2001; Mattia et al. 2006; Rossi 2007), and many more. Here NPAMs have been utilised for the production of CNT membranes.

3.4.1 Annealing of Alumina

Pre-treatment of the alumina membrane was necessary before non-catalytic chemical vapour deposition (CVD) because alumina produced by electrochemical oxidation is amorphous. Annealing enabled phase change in alumina for this purpose. Alumina undergoes several phase transformations in the annealing process: from amorphous (as produced) to γ-alumina (~ 900 °C) to α-alumina (~1200 °C) (Mardilovich et al. 1995). When heated too rapidly the NPAMs curled under thermal stress and the volume expansion (Jessensky et al. 1998) caused by the annealing process and phase transformations. However, by slowly annealing the alumina membrane to above the temperature necessary for CVD the deformation of the membrane was eliminated and the membrane could then be heated quickly during the CVD experiment itself. The NPAMs were therefore placed between quartz slides and annealed in air for 4 hours at 700 ºC at a heating rate of 1 °C min^{-1} in a Carbolite CWF 1100 furnace.

3.4.2 Non-Catalytic Chemical Vapour Deposition

CNT membranes were synthesised with a non-catalytic CVD method. This process was preferable because it does not rely on the presence of metal catalyst particles within the nanotube and therefore produced no blockages in the nanotube bore. Figure 3.8 shows a schematic of the CVD set-up with the tubular Carbolite 1200 furnace which was employed in the process. The system was first purged

with argon to remove any air present in the system. The deposition was then carried out under a 70:30 vol% mixture of He and C_2H_4 (ethylene) in a custom-made quartz tube (Chemglass) of 1 m length and 2.5 cm outer diameter. Omega FMA5400/5500 mass flow controllers were used to monitor Ar, He and C_2H_4 flow rates and this was controlled with a LabView interface. The substrates (i.e. the membranes) were heated under He to 670 °C. Because the membranes needed to be perpendicular to the gas flow they were placed in a custom-made quartz boat. The furnace was initially heated at a rate of 20 °C min^{-1} to 670 °C. C_2H_4 was then introduced into the furnace and the temperature was held for 2 to 6 hours depending on the flow rates. Table 3-2 summarizes the parameters used in the CVD process. As soon as the deposition time was complete, and before the temperature of the furnace began to drop, the C_2H_4 was turned off. The furnace was left to cool to ambient temperature under argon flow, resulting in a glossy carbon nanotube membrane within the alumina template.

Non-catalytic CVD was performed on a range of NPAMs with pore diameters from 10 - 100 nm. However for the flow experiments after annealing, membranes with D_P < 25 nm curled and/or cracked during the CVD process (even with a slow ramp). Therefore, to obtain smaller pore diameters and a mechanically durable membrane suitable for further fluid flow experiments, the CVD deposition time had to be increased. Therefore to obtain smaller pore diameters the CVD deposition time had to be increased, to obtain a mechanically durable membrane which would withstand flow. Therefore the most reliable NPAM in terms of structure (the membranes produced at an anodization voltage between 35 and 40 V) were used to deposit a thicker layer of carbon on the surface and within the channels of the NPAM template. The deposition time for the CVD process was up to 8 hours at 120 sccm (standard cubic centimetre per minute) in a NPAM with D_P ~ 42 nm to obtain an unblocked working membrane with D_P ~ 15 nm.

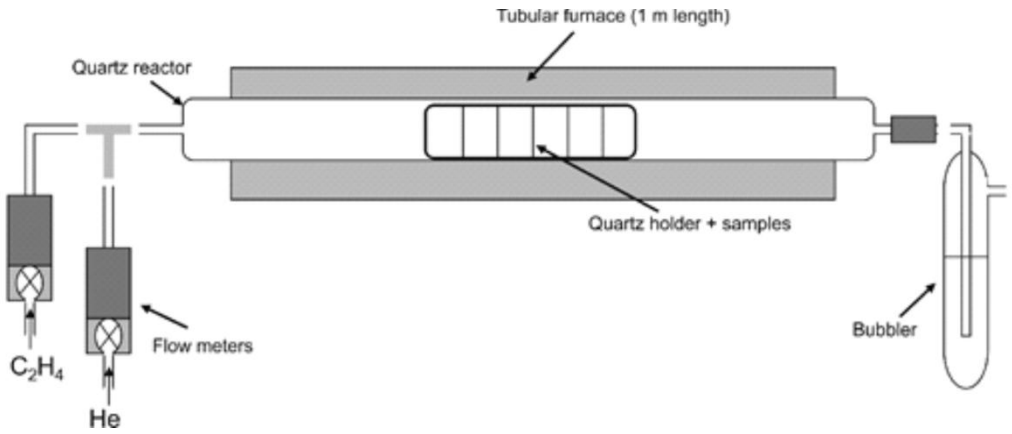

Figure 3.8 Schematic of non-catalytic CVD set-up; the He and C_2H_4 flowed perpendicular to the porous membranes.

Table 3-2 Chemical vapour deposition parameters.

Flow Rate (sccm)	Ratio of He:C_2H_4	Temperature (°C)	Deposition time (h)
20	14:6	670	6
60	42:18	670	2
100	70:30	670	3
120	84:36	670	3-8
140	98:42	670	3
160	112:48	670	3-6

3.4.3 Carbon Nanotube Release from Template

The CNTs were released from the alumina template for full characterization. In order to release the CNTs from the template the membranes were crushed and refluxed in 1.0 M sodium hydroxide, NaOH. The NaOH reacted with the alumina template to produce aluminium hydroxide, leaving the CNTs in a suspension caused by their now (after treatment with NaOH) hydrophilic nature (Mattia et al. 2006). Following this procedure the CNTs could be graphitised to change their surface chemistry.

3.5 Pressure-Driven Flow Experiments

In order to investigate water flow rates through varying pore diameters in the hydrophilic NPAMs, pressure-driven flow measurements were conducted. Two approaches were used: (a) the permeability of the membranes was measured by varying the flow rate applied to the membrane via a syringe pump and (b)

dynamic force measurements were taken using atomic force microscopy (AFM) to detect flow within the pores.

3.5.1 Flow Measurements in NPAMs

In order to conduct fluid flow measurements through the NPAMs, each membrane was clamped in a custom-made membrane holder. These consisted of two stainless steel flanges with silicone rubber annuluses (with a 5 mm inner diameter effective area). The annuluses ensured effective sealing (preventing slippage of water around the membrane) and prevented membrane fracture. The membrane holder was connected to a fluid flow measurement apparatus constructed with Swagelok® stainless steel quarter inch tubing parts (Figure 3.9). Pressure transducers (Swagelok industrial standard, ± 5kPa error) were placed before and after the membrane holder, recording pressure loss across the membrane. Since viscosity is temperature-dependent, a thermocouple (Omega, Type T) was attached to the rig. Several precautions were taken to ensure accurate measurements. Ultrapure water (Milli-Q, 18.2 MΩ cm^{-1} at 25 °C) in a stainless steel syringe of 225 ml capacity was driven by a high force syringe pump (Nexus 6000). Before starting a flow measurement, the system was pre-filled with water and air bubbles were purged. To check the effectiveness of the sealing, the NPAMs were placed in the membrane holder prior to oxide barrier layer dissolution.

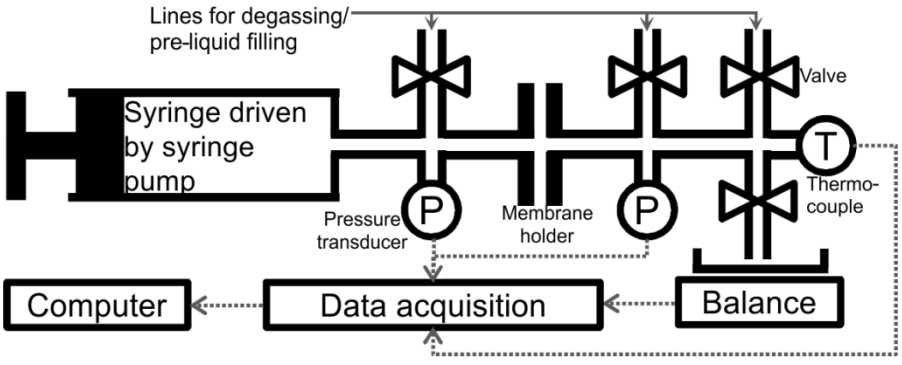

Figure 3.9 Schematic of pressure-driven fluid flow measurement rig.

The key variable measured in the fluid flow experiments was the steady-state pressure difference across the membrane at an imposed water flow rate. For each membrane four flow rate settings were tested and each run was continued for at

least 45 minutes after the pressure had stabilized. The water permeate was collected in a beaker on a high precision balance (Mettler Toledo, MS304S/01, sensitivity up to 0.1 mg). The beaker was pre-filled with oil in order to minimise water loss by evaporation. All real-time measurements (pressure, temperature, and mass of water permeate) were recorded via a data acquisition system.

3.5.2 AFM Force Measurements on NPAMs

In order to conduct dynamic force measurements on the nanoporous alumina membranes an AFM with silicon nitride tipless probe cantilevers was utilised. Cantilever spring constants, *K*, were determined by the method of Hutter and Bechhoefer (Hutter and Bechhoefer 1993) in the range 0.10 - 0.15 N m^{-1}. The AFM measurements were performed on an Asylum MFP-3D AFM equipped with a linear variable differential transformer (LVDT) sensor in the Z-movement direction in order to allow direct detection of cantilever Z-position during force measurements. This has been shown to be vital for accurate force-displacement measurements because the AFM Piezo drive is not linear with the input voltage within the required tolerance (Manor et al. 2008). The force on a colloidal particle is measured by the deflection of the cantilever which is monitored with a laser. The laser diode is directed on to the back side of the cantilever and the signal recorded by a Position Sensitive Detector (PSD). As the cantilever goes down (and undergoes deflection), the signal of the PSD changes and this is measured in volts. This change in voltage is directly proportional to the slope position of the cantilever at the point where the laser is positioned, and therefore directly proportional to the force on the cantilever (Butt et al. 2005). The optical lever system is calibrated by a proportionality constant between voltage and deflection which is determined by measuring the deflection of the cantilever on a hard surface. When the solid cantilever end is pressed against the hard surface, the deflection is equal to the Piezo displacement and the measured slope of the linear plot gives the detector sensitivity in m V^{-1}. The calibration of the cantilevers must be performed in situ before the proceeding experimental measurements. This is mainly due to the fact that the PSD signal is very sensitive to the position of the laser on the cantilever.

The tipless cantilevers were loaded with approximately 15 μm diameter silica particles. To do this the V-shaped cantilevers were mounted onto the cantilever holder with the aid of a high-magnification optical microscope (Nikon TE2000). As the view was from below, care had to be taken to focus at the top surface so as not to crash the probe into the glass surface. The silica particles were distributed onto a glass slide alongside the glue Araldite®. The tipless probe ends were dipped into the Araldite® and then moved and lowered to pick up a silica particle. It was important to ensure that only one particle was attached to the probe (smaller particles could become attached onto the end or the side of the cantilever for instance) so that accurate force measurements were could be taken. Once the particle-probes had been left to dry, their structure was confirmed by observing the cantilever on its side under an optical microscope. The cantilever was then mounted back into the cantilever holder. The cantilever holder had a skirt of Viton® to protect the Piezo and electronics from the fluids in the cell.

A range of NPAMs with varying pore diameters (as described in Table 3-1) were produced for the dynamic force measurements. A control experiment of alumina with no surface features was also conducted. Comparisons of the force curves between closed and open pores were investigated. There was a considerable difference between the force curves of the closed NPAM system and the open-through NPAM system and this has been discussed in detail in Chapter 6. To ensure that there was no blocking of flow through the pores in the case of open NPAMs the membranes were suspended across two glass cover slips and placed into a glass petri dish (Figure 3.10). To guarantee there was no movement of the membrane when the measurements were taking place (i.e. when the probe was driven into the surface) the coverslips were adhered to the bottom of the petri dish with nail varnish. The membranes were also secured to the coverslips using this method. The measurements were performed in a 1 mM NaOH, pH 10 solution and several areas of each membrane were tested at several different velocities (from 20 - 100 μm s^{-1}).

The Asylum MFP-3D measures force in 0.6 mV increments. For force measurements conducted with particles in this thesis the spring constant range

was 100 - 400 pN nm^{-1} and the detector sensitivity range was 70 - 120 nm V^{-1}. This equates to a force measurement accuracy of ± 0.005 - 0.05 nN.

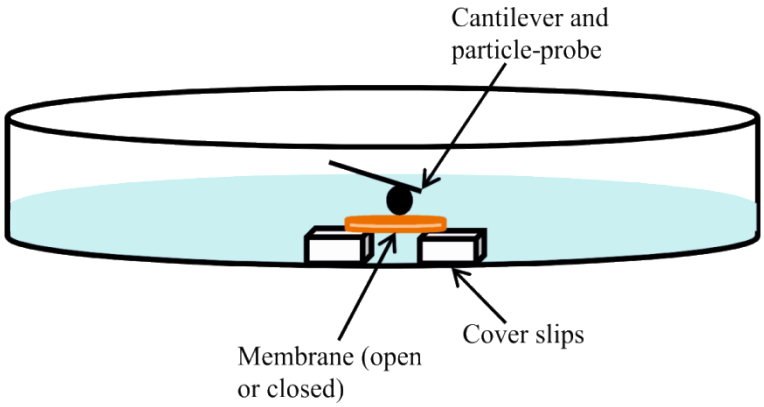

Figure 3.10 Schematic of experimental set-up for dynamic force measurements.

3.6 Electroosmotic Pumping Experiments

Electroosmotic pumping at the nanoscale has been investigated using several approaches. NPAMs were used to observe the effect of pore diameter on electroosmotic flow rates. The surface chemistry of the membrane materials were also varied (i.e. alumina and carbon) in order to observe their effect on electroosmotic flow. These processes required much optimisation, leading to further investigations into the effect on electroosmosis of different electrolytes and different concentrations of electrolytes/buffers. Further investigation was conducted regarding the concentration polarisation which was observed in all experiments in which hydrolysis at the platinum electrodes was taking place. The next sections will describe in detail the methods used to conduct these experiments.

3.6.1 Electroosmotic Experimental Set-Up

Electroosmotic flow measurements through NPAMs were conducted using a custom-made rig and membrane holder. The membrane holder was made of two polycarbonate and acrylic flanges with 60 ml chambers on either side to hold the buffer solution (Figure 3.11). The membrane holder is a second generation design: some of the preliminary EO results from the first generation membrane holder

have been presented in Appendix B. NPAMs were placed between the two vessels with an 8 mm effective diameter. To ensure effective sealing the membrane was clamped between silicone rubber annuluses. Platinum mesh (Advent, 99.99%, 52 mesh per inch) was used for the electrodes. These were clamped both sides of a NPAM and sealed by more silicone annuluses to ensure that an electrical connection was possible through the membrane pores but not between the meshes. The holder was then connected to the custom-made rig for the electroosmotic flow measurements. Pressure transducers (Swagelok industrial standard®, 0.05 Bar error) were placed before and after the membrane holder (and chambers) in order to measure pressure drop across the membrane. A reservoir was placed at the feed side of the membrane which could be pressurized when higher pressure was necessary for the flow measurements. A thermocouple was also inserted in the rig to monitor the temperature of the liquid. A high precision mass balance (Fisherbrand, FB73650, 0.1 mg sensitivity) recorded the droplet rate and through this the flow rate was calculated. A layer of oil was added to the collection beaker to prevent evaporation. Sodium tetraborate $Na_2B_4O_7$, pH 9.2, was used as a buffer during the experiments. The concentration of the aqueous electrolyte was varied from 2 to 10 mM and the applied voltage for the electroosmotic measurements ranged from 10 to 40 V using an Agilent power supply (Agilent Technologies, 6645A). This was recorded by a computer using automated data acquisition equipment (Semaphore Systems, ADAM-4017) and LabView software. Each measurement was repeated at least three times. The experiments continued for at least 30 minutes and the longest electroosmotic pumping time was 2 hours, achieved with D_P = 65 nm and 5 mM sodium tetraborate buffer. Generally, after 20 to 40 minutes, the electroosmotic pumping rate would decrease to laminar flow or less. It is believed that this is due to fouling, concentration polarization and buffer depletion. This will be discussed in detail in Chapter 7.

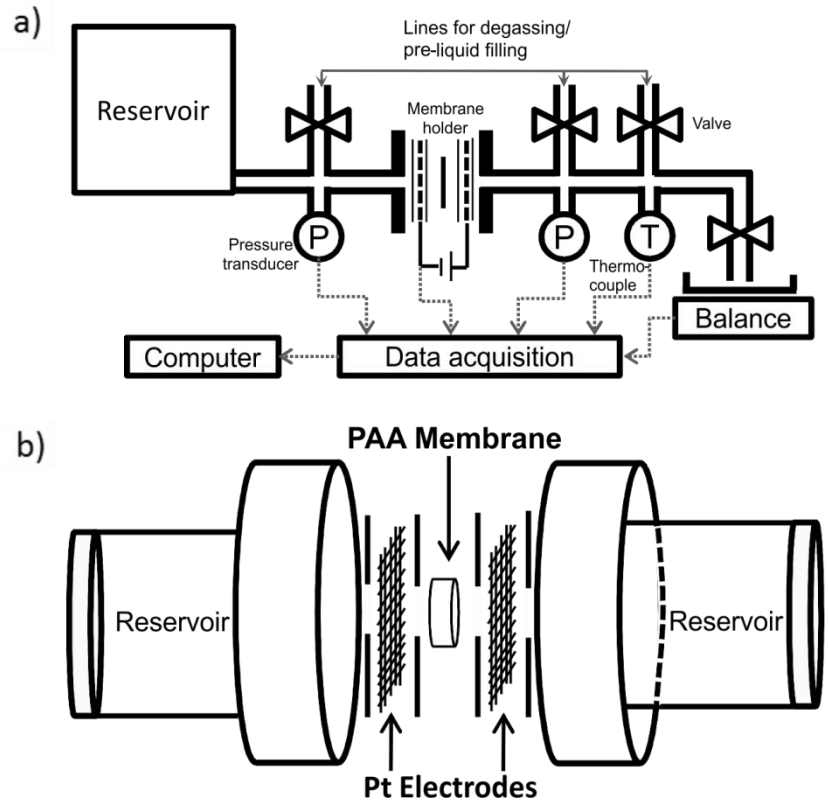

Figure 3.11 Schematic of a) the EO rig and b) the membrane holder design.

3.6.1.1 Pressure-Driven and EO Experiments in CNT Membranes

Pressure-driven and EO flow experiments were conducted on CNT membranes (for CVD procedure and parameters see Section 3.4) in the custom-made rig described in Section 3.6.1. Due to the decreased wettability of the membranes, larger pressures were required for measureable flow rates. A series of pressures were applied to CNT membranes with different pore diameters (from 15 - 65 nm) using the pressurised reservoir cylinder discussed above. The flow rates were recorded via the data acquisition LabView software which logged the time, mass, pressure and temperature every two seconds. This enabled results for the effect of flow with pore diameter, which in turn made it possible to assess whether fluid flow enhancement was observed.

For the EO experiments in CNT membranes, sodium tetraborate, $Na_2B_4O_7$ (pH 9.2) and sodium chloride, NaCl (pH 6.8) were used as electrolytes. EO was measureable in the CNT membranes unlike the NPAMs (which has been discussed in Appendix B). Similar to the NPAM EO experiments, the external applied electric field was introduced after the pressure-driven flow rate had been

recorded. This was to make sure a steady flow was detected through the membrane. This enabled a check that there were no defects/cracks in the membrane and no slippage of liquid around the membrane. As a further control measure, a membrane with closed pores was tested under fluid flow. No flow was detected at > 500 kPa, which confirmed that there was no slip of fluid around the membrane (and effective sealing of the membrane holder). This also confirmed membrane mechanical stability. They were strong and stable under this mechanical stress. To compare and contrast to the NPAMs and observe any effects of pore diameter variation, the applied voltage was kept at 10 V for all experiments.

3.6.2 Streaming Potential Measurements

Streaming potential measurements were carried out in the electroosmotic rig in Figure 3.11 in order to calculate zeta potential. No voltage was applied across the membrane but the transmembrane voltage was recorded using a Keithley 179 RMS Digital multimeter when a sequence of pressures was applied. The linear relationship of transmembrane voltage and applied pressure allowed the zeta potential of the membrane to be calculated (Equation 2.15). The concentration of the electrolyte and the pH was constant for all the measurements for zeta potential calculations. The change in zeta potential was therefore due solely to the range of pore sizes.

3.7 Material Characterisation Techniques

As flow measurements on the alumina and carbon nanotube membranes were dependent on their structure and surface chemistry, it was crucial to accurately measure the dimensions of the membranes in order to accurately calculate pore size and porosity. Accurate measurements allowed for the comparison of experimental measurements to theoretical values calculated from continuum models (for example the Hagen-Poiseuille equation). Therefore, multiple characterisation techniques were exploited in this process.

3.7.1 Scanning Electron Microscopy

The main characterisation method was scanning electron microscopy (SEM). This was primarily Field Emission SEM (FESEM) due to the high resolution achievable with this apparatus. The majority of SEM images were taken in Microscopy and Analysis at the University of Bath using a JEOL JSM 6330F FESEM. Samples were also analysed using a CrossBeam® FIB/SEM system, Carl Zeiss XB1540, through the Nanoaccess Programme offered by the EPSRC at Cardiff University. The alumina was not coated as an accurate conductive coating was not guaranteed and this would have compromised the accuracy of pore diameter and porosity measurements. Charging was experienced due to the non-conductive alumina, but at low kV (2.5 kV) and relatively small working distance (15 - 5 mm), good quality images were achievable. For the CNT membranes (coated NPAMs) the accelerating voltage was increased to 5 - 10 kV and the samples were imaged at a working distance of ~ 13 mm.

3.7.2 Focus Ion Beam

The focus ion beam (FIB) was utilised to study the internal structure of the alumina, both the barrier layer and the porous structure. The CrossBeam® FIB/SEM Carl Zeiss XB1540 system at the MEC, University of Cardiff, was used to deposit Pt onto a selected area of the sample. This ensured a cleaner cut through the material when Ga^+ ions were focused to etch the area selected.

3.7.3 Atomic Force Microscopy

Imaging and material characterisation was conducted with a Digital Instruments Nanoscope IIIA Atomic Force Microscopy in the Microscopy and Analysis Suite at the University of Bath. This sensitive technique allowed the surface morphology of the materials to be observed. Both tapping and contact modes were used for imaging the surfaces of the nanomaterials.

An Asylum MFP-3D AFM at the Department of Biochemical and Chemical Engineering at the University of Melbourne, Australia, was used for dynamic

force measurements. In this process, silica particles were glued to the end of tipless silicon nitride V-shape cantilevers.

3.7.4 Raman Spectroscopy

Raman spectroscopy was performed using a Renishaw 2000 micro-spectrometer from Renishaw Inc. The spectrometer had three lasers with wavelengths of 532, 633, and 788 nm. The green laser (532 nm) at 10% power was used to characterise CNT membranes. Typical scans were in the range of 900 - 2400 cm^{-1}, 5 seconds, 10 accumulations per area. For each CNT membrane at least 5 areas around the sample were analysed.

3.7.5 Transmission Electron Microscopy

Transmission electron microscopy (TEM) was performed on CNTs embedded within the alumina template and on CNTs which had been released from the template (see section 3.4.3). TEM was performed using a JEOL JEM1200EXII provided by the Microscopy and Analysis suite at the University of Bath. This is a standard tungsten filament TEM operated at 120 kV up to magnifications of 500k. Micrographs were recorded using a high resolution Gatan Dualvision Digital Camera.

3.8 Characterisation of NPAMs: Porosity and Pore Diameters

3.8.1 SEM Image Analysis

ImageJ is public software used for image processing and analysis. It enables the user to edit, analyse, and process images. Using ImageJ, micrographs were converted from a greyscale image into a binary (black and white) image (Figure 3.12a-b). The software identified each pore and quantified their area, perimeter, Feret's diameter, and circularity. To calculate porosity, the pores at the edges of the bracketed area were included (Figure 3.12c). For pore diameter, however, pores at the edges of the bracketed area were excluded (Figure 3.12d). Table 3-1 displays data obtained from ImageJ on pore diameter and porosity using this method. Because the Feret's diameter represents the longest distance between any

two tangents contacting the pore boundary, ImageJ overestimated effective pore diameter. Thus, the Feret's diameter was compensated by circularity to obtain the effective pore diameter. This gave values in agreement with previous literature and will be discussed in greater detail in Chapter 4.

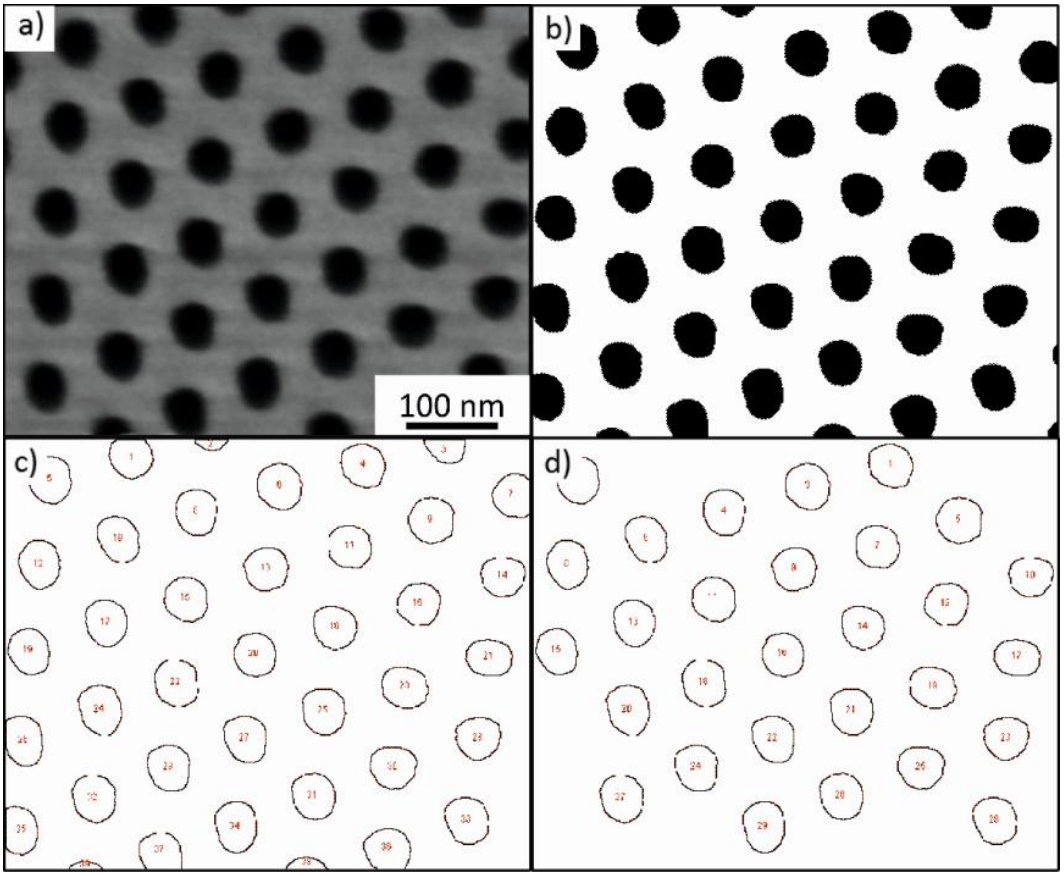

Figure 3.12 ImageJ analysis tool to calculate pore diameter and porosity of NPAMs and CNT membranes a) FESEM of 40 V oxalic acid anodization procedure, b) the binary imaged created by the software using the threshold technique, c) outlines of the identified pores for calculation of porosity and d) outlines of pores for calculation of pore diameter - edges excluded only whole pores used to calculate pore diameter.

3.8.2 AFM Image Analysis

Gwyddion is a modular programme for scanning probe microscopy (SPM) and is used primarily to analyse AFM data. There are two modes: tapping and contact mode. Both modes were utilised for imaging the nanodomes and pores in this study. The tapping mode is a less invasive method; the probes merely ‘tap’ the surface of substrate by oscillating up and down. Contact mode is more invasive and can damage parts of the substrate. It can, however, result in sharper images.

Images from either technique can be used within Gwyddion, where they can be made sharper and statistical measurements can be analysed.

3.9 Statistical Analysis and Reproducibility

Over 900 membranes were fabricated in total, of which 70% were utilised for fluid flow, electroosmosis and wetting investigations (the remaining 30% either failed at anodization or were discarded due to poor porous structure or membrane fracture). Each NPAM and CNT sample was subject to SEM analysis for pore diameter, pore size distribution and porous structure. The SEM analysis method discussed in Section 3.8 was employed to calculate the standard deviation (SD) of the pore diameter and interpore spacing using Microsoft Excel's internal functions. All error bars associated with pore diameter and alumina structure provided throughout the present work are attributed to the standard deviation of several areas of a membrane ($3 \leq n \leq 6$). Each plot, including error bars concerning fluid flow, electroosmosis and wetting properties, has been explained within the caption. At least three measurements ($n = 3$) were performed and in some cases up to five repeats were necessary (e.g. for the smallest pore diameter membranes produced due to membrane fragility).

3.10 Summary

This chapter described the experimental systems employed throughout the following chapters, detailing the experimental procedures for the production of nanoporous alumina and CNT membranes as well as for the subsequent studies of fundamental nanofluidic behaviour. The chapter contained experimental details of (i) hydrothermal treatments, (ii) wettability studies, (iii) pressure-driven flows (iv) AFM force measurements and (v) electroosmotic experiments in NPAMs and CNT membranes.

Chapter 4

Characterisation of Nanoporous Alumina

The anodization of aluminium and the applications of nanoporous alumina have been discussed in detail in Chapter 2. This chapter will evaluate the outcomes of aluminium anodization by fully characterising the materials. It will also discuss the limits of the anodization process, which were observed in the production of some of the smallest pore sizes yet fabricated. The findings support the conclusion that pore diameter, interpore spacing, and barrier layer thickness are all dependent on the applied anodization voltage, and that the thickness of the whole membrane is dependent on anodization time. SEM and AFM were the main characterisation techniques used to analyse pore diameter, porosity, and the structure/morphology of alumina. The final part of this chapter presents findings from the hydrothermal treatment of alumina, a process which resulted in shrinkage of the pores.

4.1 Anodization of Aluminium

This first section presents the size range of NPAMs produced and characterised for fluidic studies. It will compare one- and two-step anodization processes and highlight why the two-step procedure was required to obtain high quality materials. It will also compare commercial Anodisc^{TM} and Synkera© membranes with engineered in-house membranes, and justify why, throughout this work, membranes produced in-house have been favoured.

4.1.1 One- versus Two-Step Anodization

Chapters 2 and 3 discussed in detail the development and procedure of one- and two-step processes for the anodization of aluminium. Figure 4.1 indicates a stark difference in the quality of membranes produced by the one- and two-step processes. Membranes produced via the anodization process display what will be referred to as ‘top’ and ‘bottom’ surfaces. The top surface faces the electrolyte continuously throughout anodization. The bottom surface is covered by the remaining aluminium after anodization is complete (this is subsequently removed

as discussed in Section 3.1.2). The membrane shown in Figure 4.1a and c was produced with the one-step process; the anodization was potentiostatic at 40 V (in 0.3 M oxalic acid, 14 °C) and the current and time was recorded. Figure 4.1a shows the top side of a NPAM. The degree of pore branching and pore distribution is greater than that observed in the two-step anodization process as shown in Figure 4.1b. The images in Figure 4.1b and d show a NPAM produced via the two-step process under the same conditions as the membrane shown in Figure 4.1a and c. It is clear that the quality of the membrane is far greater: the pore size distribution is much narrower and the degree of pore branching has been substantially reduced. Figures 4.1b and d show a bottom surface after the removal of the barrier oxide layer. There is very little difference between the two membranes. What is important to note here is that an extremely ordered top structure with no branching is necessary for the subsequent fluidic and CVD experiments.

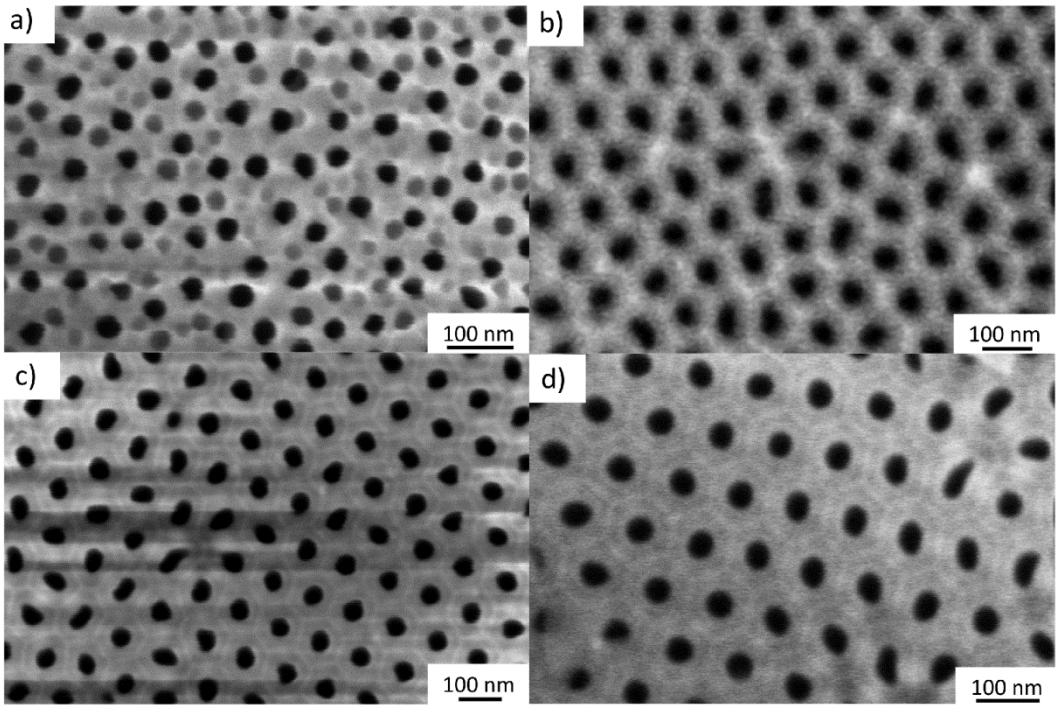

Figure 4.1 FESEM of NPAM produced via 40 V anodization in oxalic acid a) one-step anodization *top* surface with visible branching b) *top* surface of NPAM produced by a 2-step process c-d) similar structure observed for the bottom surfaces in one- and two-step anodization processes.

The two commercial NPAMs mentioned in the introduction to this chapter were Whatman® Anodisc™ inorganic membranes and Synkera© membranes. Both materials are made of alumina. Anodisc™ membranes are mainly used for

filtration purposes, but their pore size and structure are much larger and less ordered than those of the in-house membranes used in this study (Figure 4.2). This research has probed the effect of pressure-driven flow and electroosmotic flow at the nanoscale and so a highly controlled process has been necessary. Large pore sizes with large standard deviations (which the Anodisc^{TM} exhibit) were thus inappropriate for this research. Although the Synkera© membranes offer a larger range of pore sizes (compared with the Anodisc^{TM}) their top surface exhibits a higher degree of branching (Figure 4.3), similar to that of the one-step process shown above. Consequently, when using Synkera© membranes during CVD, pore blocking was observed and flow rates were greatly reduced. All the experiments throughout this research have therefore used NPAMs fabricated in-house.

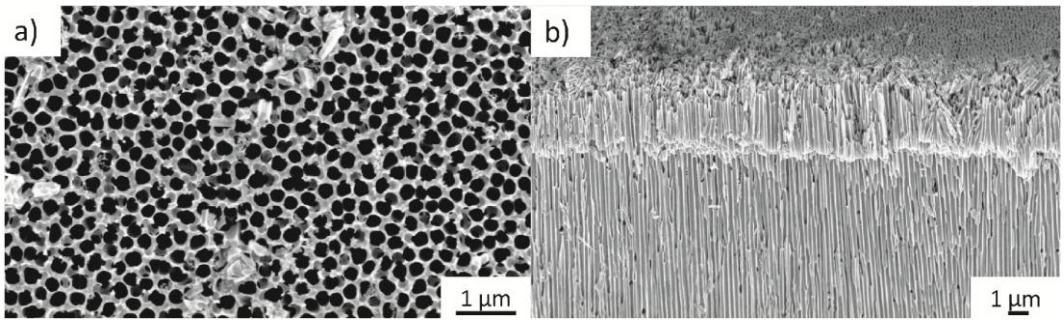

Figure 4.2 FESEM of commercial Whatman® Anodisc^{TM} membranes a) highly branched surface b) cross section with branching channels.

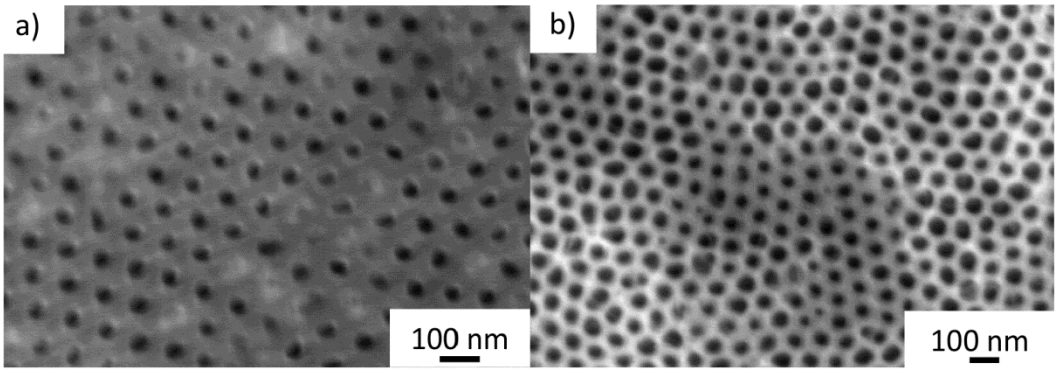

Figure 4.3 FESEM of Synkera© NPAMs a) ordered pores after barrier oxide layer removed b) *top* surface exposed to electrolyte throughout anodization - larger pore size distribution and branching.

4.1.2 Pore-Opening Detection

The pore-opening detection set-up used throughout this work was further developed from the initial publication by Lillo and Losic (2009). It was vital to maintain a narrow pore distribution for all following experiments (flow and EO flow measurements and CNT synthesis) and the pore-opening detection set-up enabled this. Several publications (Redon et al. 2007; Whitby et al. 2008; Romero et al. 2012) have utilised 'pore-widening' in which pores of alumina membranes are widened after anodization and pore opening processes. Unwanted pore-widening usually occurs when there is limited control of the pore opening process, unlike the control provided by the electrochemical detection used in this study. If uncontrolled, the pore-widening process can substantially change the structure of the membranes, resulting in either increased porosity or the breaking up of the structure (Figure 4.4). The deformed 'nest'-like structure observed in Figure 4.4b has been observed previously in a study of the hydrophilicity and super-hydrophilicity of alumina (Ye et al. 2009). By using the pore-opening set-up the risk of this deformation was eliminated as the already porous top surface was only exposed to KCl and the barrier oxide layer only exposed to hot H_3PO_4 for etching (see Chapter 3 Figure 3.4).

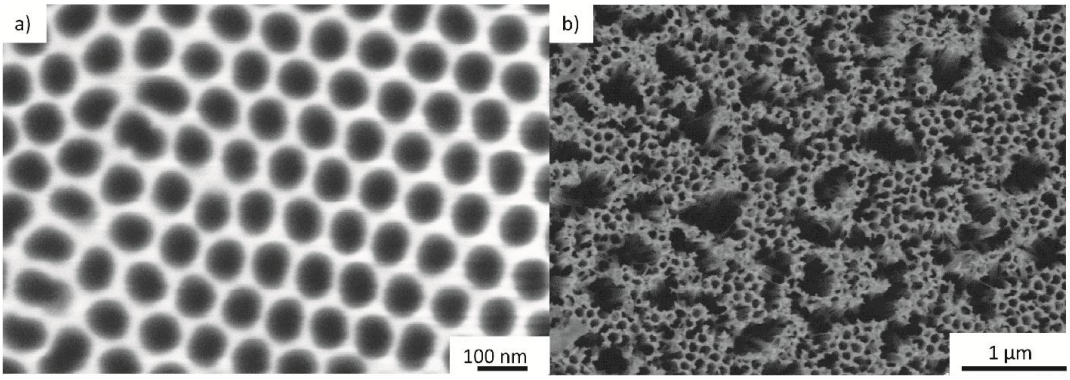

Figure 4.4 FESEM of a) increased porosity for over-etched NPAMs by wet chemical etching and b) extreme wet chemical etching results in a break-up of the structure.

Figure 4.5 displays an example of a current-time plot recorded during the etching of the barrier oxide layer using pore-opening detection. The first section of the plot (A) detects no current; this is due to a thicker barrier oxide layer being etched away. As the pores start to open (B), a current is detected between the two electrodes and this steadily increases until pores are fully opened, something

indicated by a plateauing of the current (Figure 4.5, section C). When the process was prolonged the pores were continually etched and the destruction of the porous structure was obvious (Figure 4.4b). The process was therefore stopped as soon as a plateauing current was observed. This method was used for all NPAMs produced, guaranteeing a greater degree of control over the integrity of the structure.

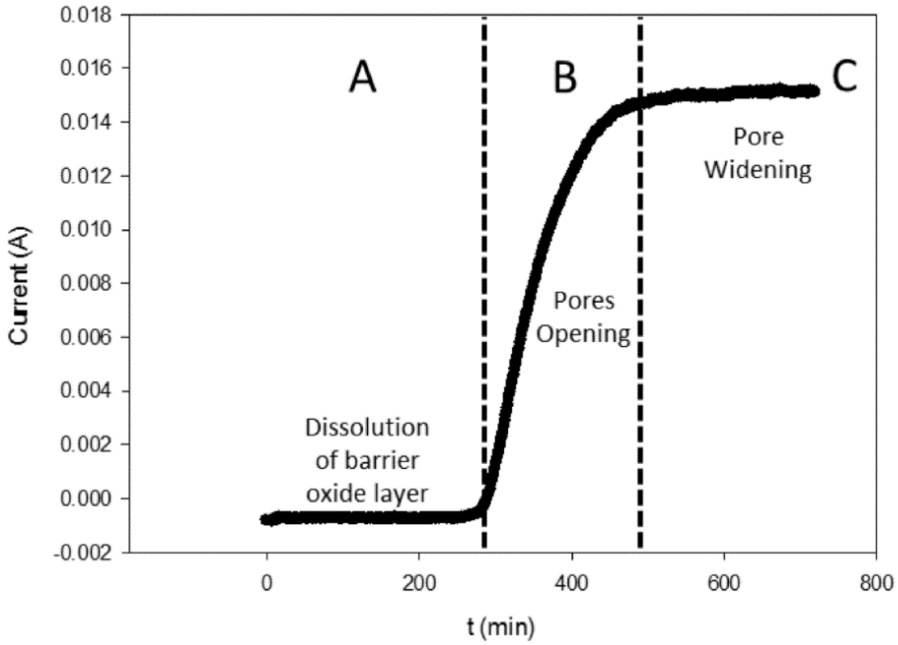

Figure 4.5 Current-time plot for pore-opening detection A - dissolution of barrier layer B - when the pores start to open and C - prolonged etching can result in pore widening.

4.1.3 Relationship between Anodization Voltage and Pore Diameter

That the size of structures in porous alumina is determined by anodization voltage was first identified by Keller et al (1953). Since then, with the optimisation of anodization conditions and characterisation techniques, the proportionality between anodization voltage and pore diameter, interpore spacing and barrier oxide layer thickness has been observed. The linear dependence for anodization voltage and pore diameter is shown in Figure 4.6. The proportionality constant was found to be ~ 1.25 nm V^{-1} with little deviation within the samples analysed, something which supports published literature values (Sulka 2008). Figure 4.7a presents another set of data for the relationship between anodization voltage and pore diameter, but also includes the linear dependence of interpore spacing and barrier oxide thickness with applied anodization voltage. The proportionality

constant between anodization voltage and interpore spacing was ~ 2.5 nm V^{-1}. A recent publication challenged the 1.25 nm V^{-1} rule discussed above observing a pore diameter limit of 6 - 10 nm between 1 and 10 V applied potentials (Ding et al. 2010). Whether this is the case for alumina is still inconclusive; at such small applied potentials (< 10 V) it was difficult to obtain a membrane mechanically stable enough for any analysis that could have supported the conclusions of the publication.

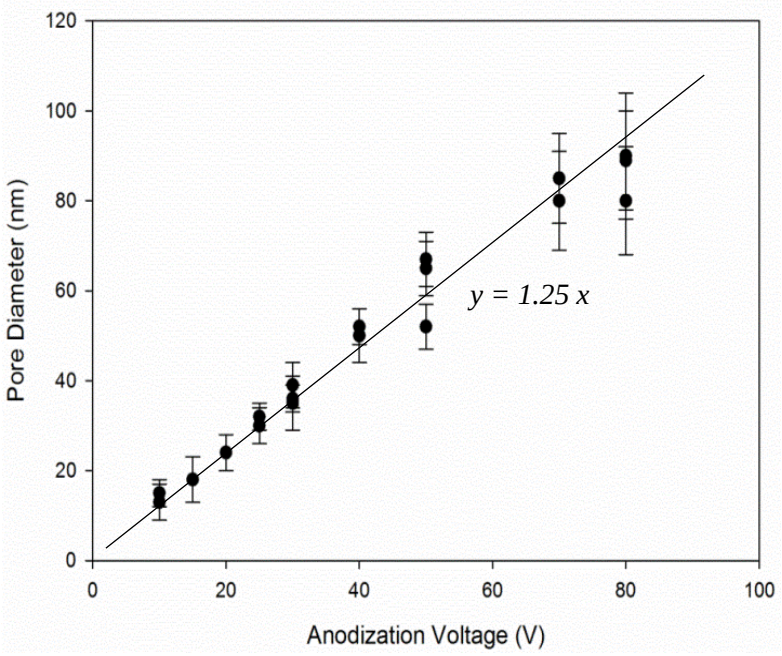

Figure 4.6 Linear relationship between applied anodization voltage and pore diameter of porous alumina - approximately 1.25 nm V^{-1}. Error bars: SD from SEM analysis (see Section 3.8 and 3.9) n = 3 and R^2 = 0.96.

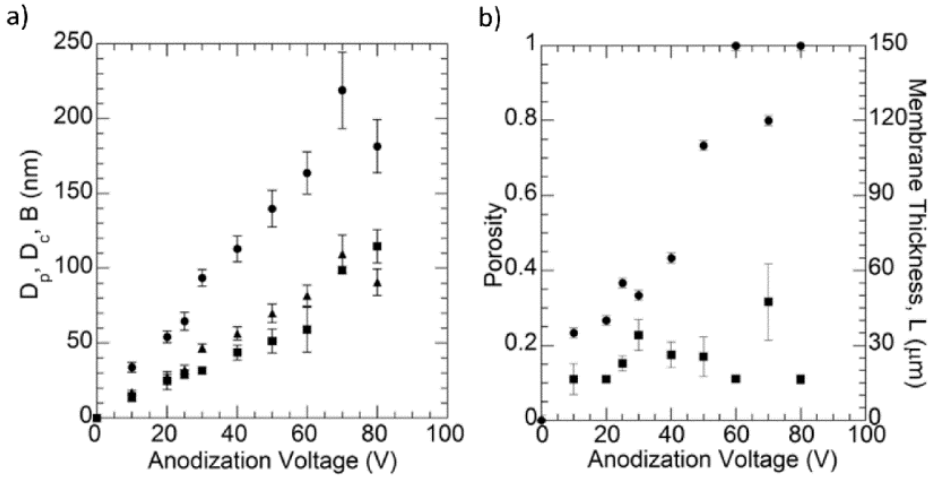

Figure 4.7 Dependence of anodization voltage on porous alumina structure a) (■) for pore diameter D_P, (●) interpore spacing D_C, and (▲) barrier oxide layer thickness B and b) (●) for membrane thickness and (■) for porosity. Error bars: SD from SEM analysis (see Section 3.8 and 3.9) n = 3.

It was observed throughout analysis of all SEMs and AFMs that porosity was independent of anodization voltage (Figure 4.7b), which differs from other structure parameters of alumina. The increased porosity observed in other reported research was due to the pore-widening explained above. In fact the as-produced alumina has quasi-constant porosity due to the exponential relationship between the number of pores and pore diameter (i.e. the number of pores for the same area increased for the smallest pore diameters) (Figure 4.8). This has been an important point to consider when assessing the wetting properties of nanostructured PAAs as some previous wetting models have used solid surface fractions (in the case of alumina this is $1 - \phi$ (porosity)). As the value for porosity was found to be quasi-constant, previous models were found to be inadequate, something explained in detail in Chapter 5.

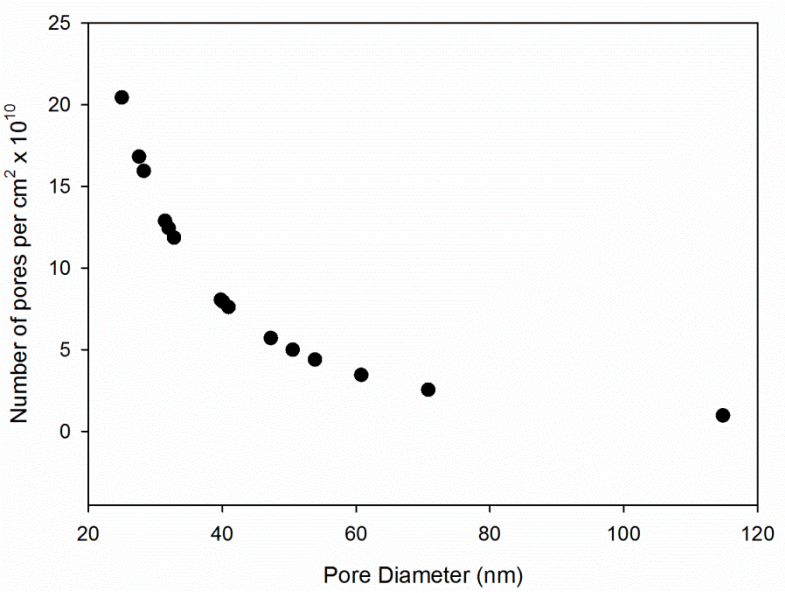

Figure 4.8 Relationship between pore diameter and the number of pores of nanoporous alumina membranes - which supports the quasi-constant porosity of alumina membranes of between 10 and 20%.

4.1.4 Annealing of Alumina

In the case of alumina the annealing process changes the as-produced (i.e. after anodization) amorphous phase to a more crystalline phase. Alumina goes through several phase changes with heat treatment, from amorphous- to γ- to α-alumina (Stumpf et al. 1950). Figure 4.9 presents the phase diagram for hydrated alumina (i.e. alumina comparable to that of NPAMs produced via anodization). During

annealing NPAMs also experience volume expansion. Heated too quickly, internal stresses caused by volume expansion caused the NPAMs to curl and crack.

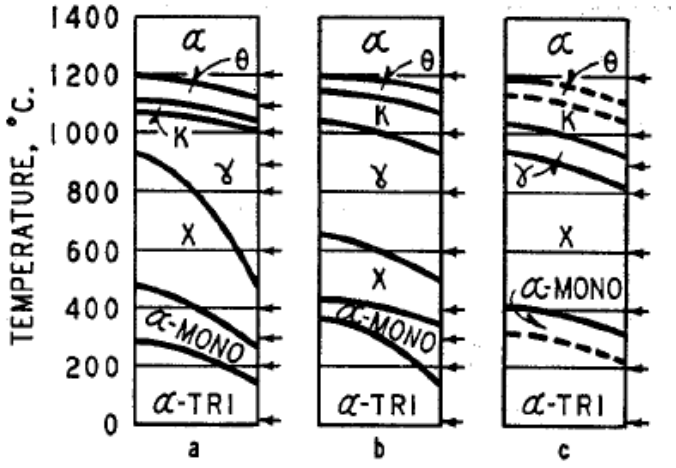

Figure 4.9 Bayer process hydrate heated (a) 1 hour in dry air, (b) 1 hour in steam, (c) fine particle hydrate heated 1 hour in dry air. A horizontal line at any temperature shows nature and relative amounts of phases present at 200 °C. 75% α-trihydrate and 25% α-monohydrate are present in (a) (Stumpf et al. 1950).

It was particularly important to anneal NPAMs before CVD treatment. For CVD, NPAMs were annealed to 700 °C, and there were also attempts to anneal CNT membranes (once NPAMs had been coated with carbon) to > 1200 °C in order to fully graphitise the carbon. For this the alumina was annealed to 1250 °C to change the crystalline phase to α-alumina (Figure 4.10). Unfortunately the mechanical stability of the membrane consistently failed. Thus, even though the structure of carbon had been changed from amorphous to a more graphitic structure, the membrane was fractured and no longer useful. Consistent membrane fracturing can be attributed to the different thermal expansion coefficients of alumina and carbon. The literature reports values for the thermal expansion coefficients, α_{exp}, of alumina to be between $5.4 \cdot 10^{-6}$ and $10.7 \cdot 10^{-6}$ K^{-1} (Huntz et al. 2006), whereas for carbon it is approximately $0.5 \cdot 10^{-6}$ K^{-1} (Jiang et al. 2004). As the coefficient for carbon is smaller than that of alumina it is therefore inevitable that thermal stresses will cause cracks to the membrane (i.e. because alumina expands faster than carbon).

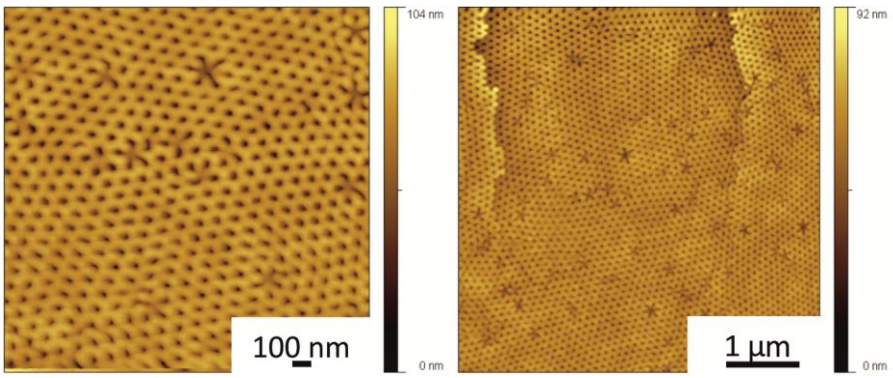

Figure 4.10 AFM of a 40 V oxalic acid produced NPAM after annealing at 1200 °C but not carbon coated.

4.2 Hydrothermal Treatment of NPAMs

Although pore diameters close to 10 nm were achieved in the anodization of aluminium, the mechanical stability of the material in the majority of cases was too low to withstand the pressures applied during fluid flow experiments. Three variations on hydrothermal treatments were therefore used to shrink the pore sizes of more mechanically stable NPAMs (40V oxalic acid NPAMs). Although this method was not used throughout the research (for reasons discussed below) it was important to investigate and understand the technique. Potentially, this technique could be utilised in future research where superhydrophilic surfaces and tuning the wettability of surfaces may be necessary.

4.2.1 Electrochemical Detection of the Hydrothermal Treatment

This first method utilized an electrochemical detection technique similar to the pore-opening detection discussed in Section 3.3 and 4.1. The idea was to replicate the process of pore opening in the opposite direction (from opened pores to smaller pores). One could open pores from the barrier oxide layer by a small amount, resulting in very small pore diameters (which has been explored in Chapter 7). This would not be the diameter of the cylindrical channels, and the aim was to achieve shrinking throughout the entire channel diameter.

Membranes were heated to 85 - 90 °C in vessels (see Chapter 3 Figure 3.4) filled with 0.5 M KCl in order to detect a current. Current-time plots for the experiments were recorded and Figure 4.11 presents the results of this process. The results have been displayed in one plot though the pore opening of the barrier oxide

layer. The hydrothermal experiments were conducted separately because (as discussed earlier) pore-opening requires H_3PO_4. The plot shows a clear decrease in current as the membrane was heated constantly for ~ 30 minutes. Indeed, the current dropped to almost zero. It was assumed that pore/cylindrical shrinking had occurred but it was uncertain by how much and what effect the treatment had had on the structure of the membranes. Figure 4.12 presents the resulting SEMs from the process discussed from Figure 4.11. This shows that the pores had not shrunk. They were in fact blocked by fibrous structures shown in Figure 4.12a. Figure 4.12b shows the nucleation of fibrous bundles which were observed across the whole surface. Interestingly, the hexagonal porous structure was maintained and the interpore distance was consistent with that of as-produced NPAMs. Although the electrochemical detection method produced an interesting structure it did not present the control it was originally believed to have.

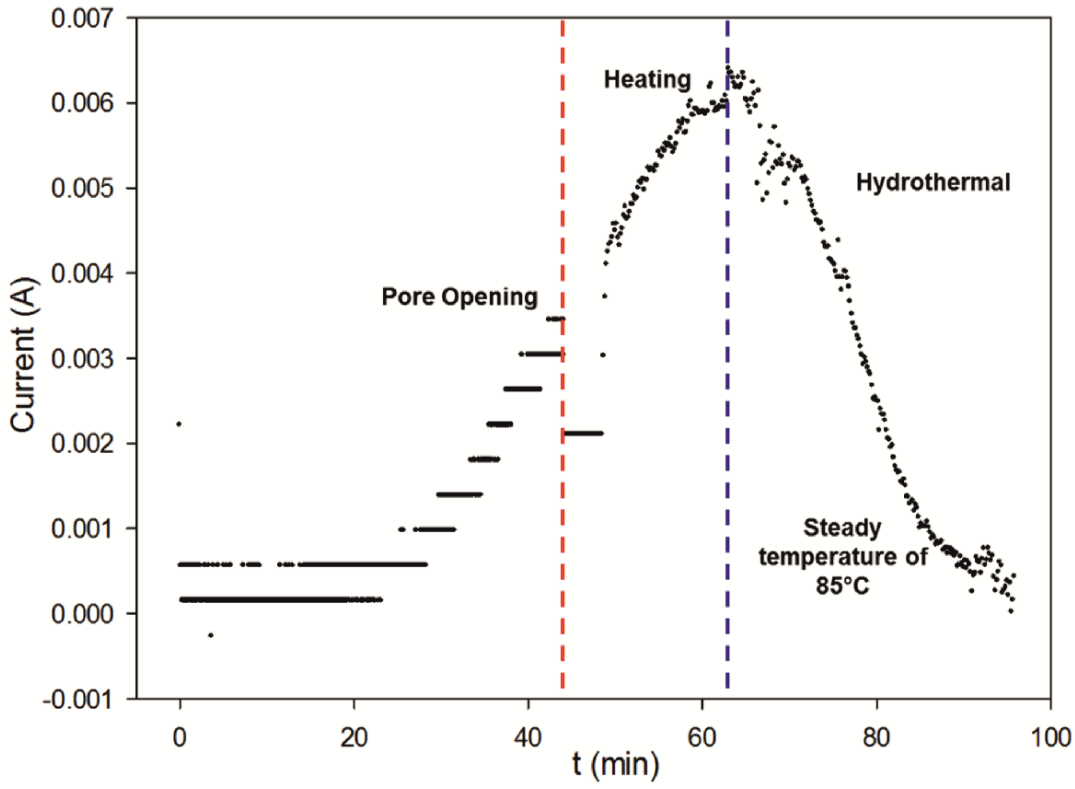

Figure 4.11 Current-time plot for the electrochemical detection of NPAMs during hydrothermal treatment.

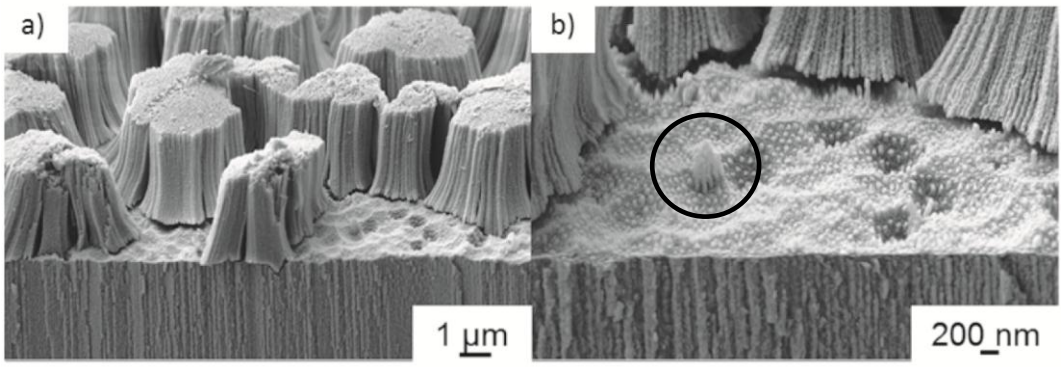

Figure 4.12 FESEM of NPAMs after hydrothermal treatment heated in salt conditions for electrochemical detection a) no shrinking of pores but bundles of fibres on surface of NPAMs and b) nucleation of a fibrous bundle (circled).

4.2.2 Hydrothermal Treatment - Boiling Water Method

Previous studies have only performed hydrothermal treatment on porous alumina with the barrier layer intact (Patermarakis and Papandreadis 1993; López et al. 2006; Boisier et al. 2008; Takmakov et al. 2006). Therefore the present section (along with the previous and following sections) present the first hydrothermal treatments completed on porous alumina with open-through pores. Previous studies used boiling water in their hydrothermal treatment, performed from periods of 1 minute to 1 hour. These studies suggested several mechanisms for hydrothermal treatment which in most cases resulted in pore blocking. Figure 4.13 presents a mechanism proposed from López et al. for pore blocking. This study used both hydrothermal sealing (HTS) and cold sealing to observe a mechanism for the hydrothermal treatment of alumina. They proposed an initial dissolution of the channel wall which resulted in pore widening. With continual treatment, hydrated alumina precipitated throughout the channel resulting in channel swelling and eventual blocking.

Figure 4.14 shows two AFM images from the present study, where open-through alumina was submersed in boiling water continuously for 30 minutes to 1 hour. It was evident that the pore surface swelled (from Figure 4.14a to b), but it was inconclusive from SEM cross-sections whether this occurred throughout the entire channel. It is more likely that swelling only occurs at the pore openings as shown in Figure 4.14c.

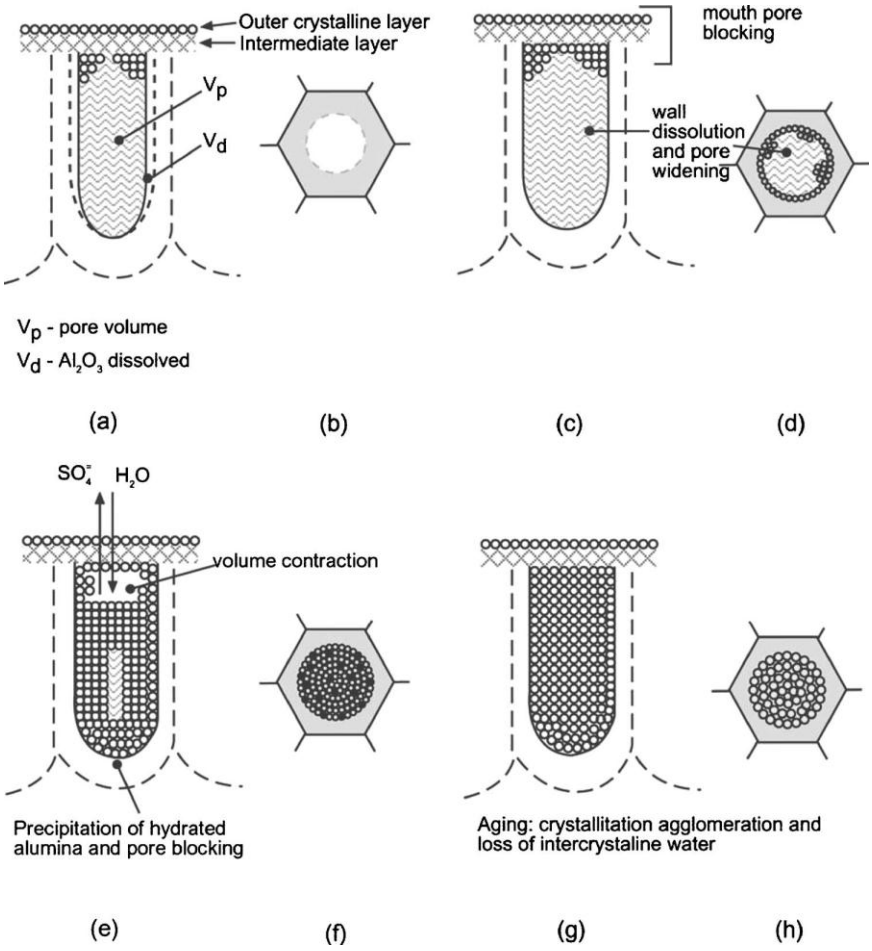

Figure 4.13 Sealing mechanism: (a) and (b) Filling of pores with sealing solution, plugging of the pore mouths, and formation of acicular and intermediate layers (c) and (d) dissolution of the walls and widening of the pores. (e) and (f) Saturation of the hydroxide gel, precipitation with contraction of volume and plugging of the pore along its entire length by diffusion of water through the plug and repetition of stages (c)-(f). (g) and (h) Agglomeration, reduction of surface energy, and great increase in porous layer resistance, R_p (López et al. 2006).

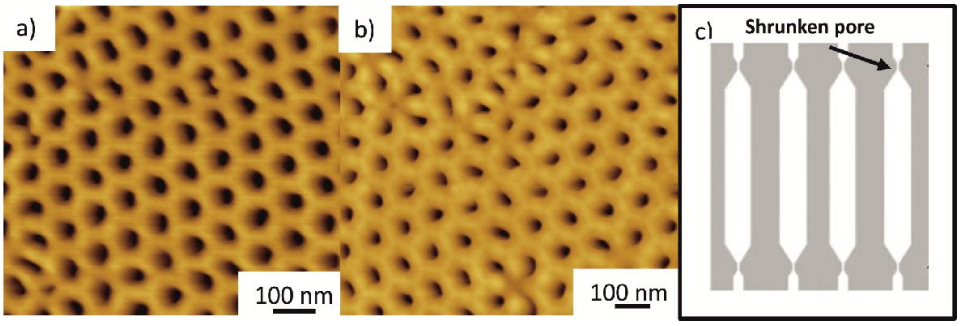

Figure 4.14 AFMs of a) before hydrothermal treatment D_P ~ 50 nm b) after 30 minutes of hydrothermal treatment in boiling water D_P ~ 38 nm and c) schematic representation of pore shrinking at surfaces.

4.2.3 Steam Treatment of NPAMs

In order to achieve a hydrothermal treatment in which the shrinking was as uniform and efficient as possible, a final method was devised: steam treatment. This became the preferred hydrothermal method as it proved the most consistently successful. Steam was driven through pores of alumina using the set-up shown in Figure 3.6. Two characterisation methods, AFM and SEM, were used to monitor the degree of shrinking, and these results are discussed below.

4.2.3.1 Results via AFM analysis

AFM effectively characterised steam treatments on the same membrane. Samples were treated for a total of 20 minutes but the process was stopped at 10, 13 and 16 minutes respectively to monitor changes in pore diameter and surface structure. It was possible to track pore shrinkage over time and Figure 4.15 presents an example of such a process. Figure 4.15a represents an AFM image of an as-produced 40 V oxalic acid NPAM with an average pore diameter of ~ 40 nm. Figure 4.15b shows the resulting morphology after 10 minutes of steam treatment. The average pore diameter was reduced to ~ 30 nm and the sample also increased in roughness, suggesting a swelling of the solid surface. Figure 4.15c-d display two resulting AFMs after 13 and 16 minutes of steam treatment respectively (time associated to Figure 4.15a being 0 minutes). The average pore diameter of Figure 4.15d was ~11 nm; the convoluted pore shape being due to the shape of the AFM tip rather than the shape of the pore. This was the result of the pore being too small to allow full access of the AFM tip. From images like those shown in Figure 4.15c and d it was also clear that the roughness had increased substantially. As ~ 11 nm was the limit achieved via anodization (for mechanically usable NPAMs) the sample was treated for a further 4 minutes to reduce pore diameter as much as possible. Every time this was attempted, topography as shown in Figure 4.15e was obtained. There was a limit at which steam/hydrothermal treatment no longer resulted in reduced pore size; at this activation point, fibres started to grow across the surface. This might be expected, as not only the material around the pore, but also the whole solid surface of alumina hydrates during treatment. SEM was also utilised to follow pore shrinkage and treatment limits. These results are discussed in the next section.

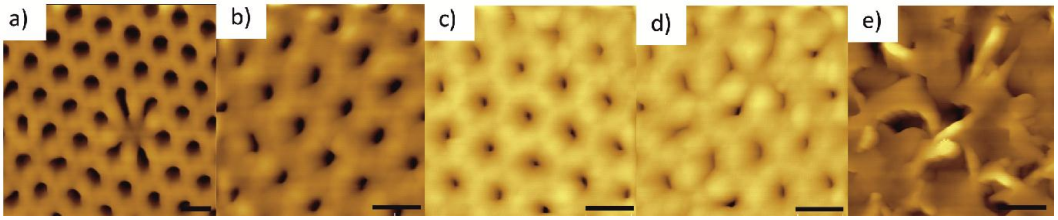

Figure 4.15 Series of tapping-mode AFM micrographs (for a NPAM produced at 40 V in oxalic acid) during and after steam treatment a) as-produced NPAM b) after 10 minutes of steaming pores have swelled slightly c-d) 13 and 16 minutes of steam treatment, respectively with an average pore diameter ~ 11 nm and e) after 20 minutes swelling of pores had reached the limit and growth of fibres ensued (all scale bars 100 nm).

4.2.3.2 Results via SEM analysis

SEM was also useful in tracking pore shrinkage and the nucleation of fibre growth. Due to the results from AFM (which showed fibre growth at 20 minutes of exposure) exposure length to steam was reduced for the following experiments to < 15 minutes without interruption. It was assumed that the result would be the same if samples were treated continually rather than incrementally.

Figure 4.16 show two SEMs before and after treatment. Figure 4.16a has a high porosity and larger than expected average pore diameters due to over-etching of the alumina surface. Before treatment the average pore diameter was 85 ± 8 nm, but after 12 minutes of steam treatment (Figure 4.16b) the SEMs showed reduced pore diameters of 44 ± 4 nm, a reduction of approximately 48%. These results were promising: if the initial sample had not been over-etched, the pore diameter would have been even smaller. By contrast the SEM of the as-produced NPAM in Figure 4.17a shows that this sample was not over-etched. This time steam treatment was applied for 14 minutes in order to obtain the smallest possible pore size. Because the average pore diameter was 57 ± 4 nm, the length of treatment (14 minutes) passed the threshold of pore swelling, and fibres again grew across the surface (Figure 4.17b). What is believed to be the nucleation of fibrous structures has been shown in Figure 4.18a. Fibres start to grow at defect points in the alumina surface; these tendril-like structures ‘reach’ out from defect points and a net of fibres masks the whole surface (this was also observed in the AFM images in the previous section). These fibrous structures are confined to the outer

surfaces of NPAMs, as cross sections still exhibited very straight channels after analysis with the focus ion beam (FIB) (Figure 4.18b).

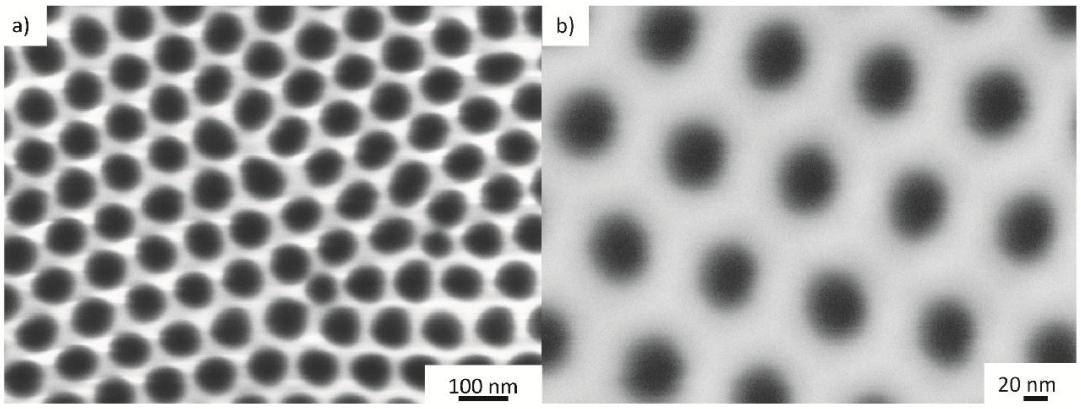

Figure 4.16 FESEM of a) average pore diameter before steam treatment ~ 85 ± 8 nm (note pores are over-etched for this case) and b) pore diameter post steam-treatment (12 minutes) ~ 44 nm resulting in a reduction of ~ 51%.

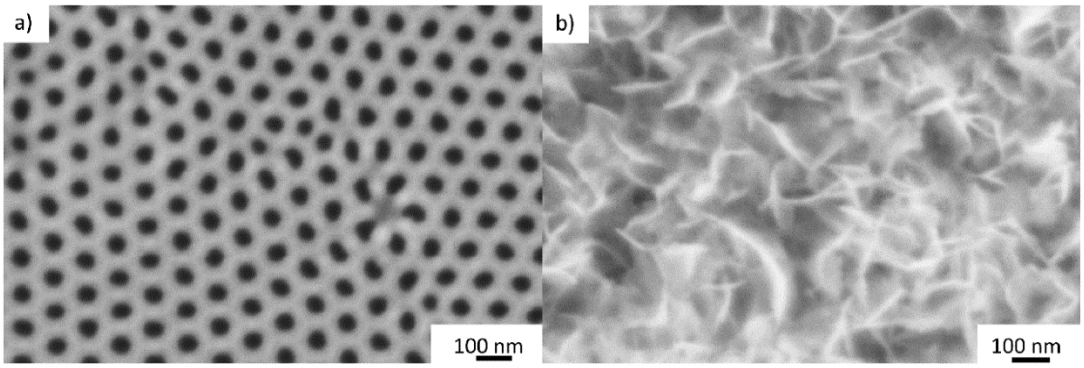

Figure 4.17 FESEM of a) average pore diameter before steam treatment ~ 57 ± 4 nm and b) no visible porous structure as surface covered in alumina fibres after 14 minutes of steam-treatment.

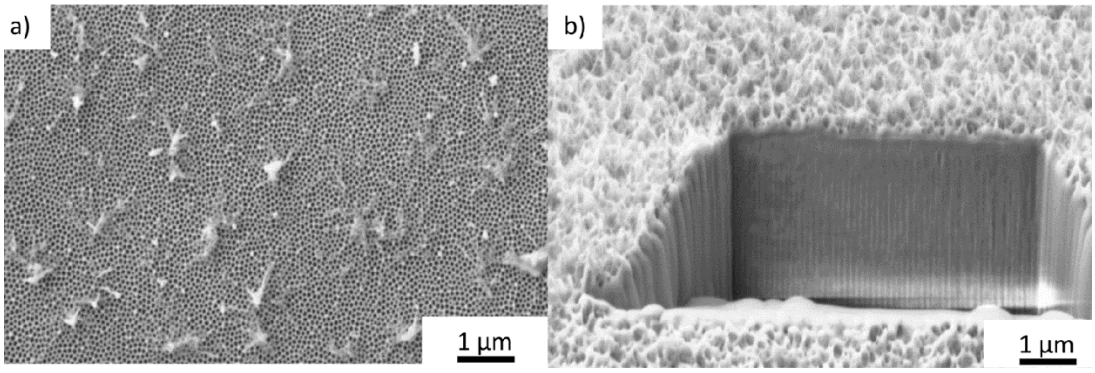

Figure 4.18 FESEM of a) tendril-like alumina fibre growth from defects in alumina surface and b) FIB cross-section of fibrous structure - cylindrical channels remain integral to structure but surface covered in fibres.

4.2.3.3 Summary of Steam Treatment Analysis

Of the three methods investigated for hydrothermally treating alumina, steam treatment was the most successful for its consistency and the reduction in pore size it produced. But there was a limit to the degree of pore shrinkage/swelling before fibres started to grow. The smallest pore diameters obtained using these methods was from ~ 40 nm to 11 nm (imaged using AFM). The limit of pore reduction for samples analysed via SEM was ~ 30 nm. As discussed above, this may have been due to a step-wise method utilised for AFM imaging. The plot in Figure 4.19 has summarised the findings from AFM and SEM for steam-treated NPAMs. The analysis implies a negative linear relationship between pore shrinkage and time, but it becomes negligible when fibres appear. The limit to pore reduction caused by fibre growth meant that, ultimately, it was not advantageous to use this method for the subsequent research, as the same pore dimensions were still achievable by anodization.

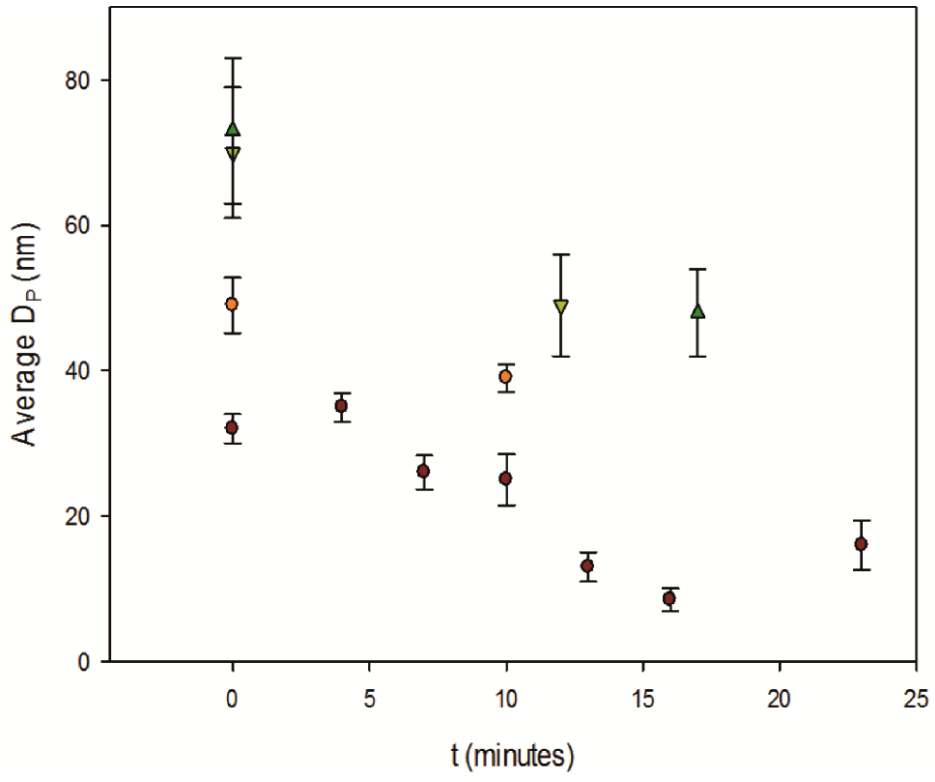

Figure 4.19 Plot of pore shrinkage with steam treatment analysed by (●) AFM and SEM (●) after steamed for 10 minutes, (▼) after steamed for 12 minutes and (▲) after steamed for 17 minutes. Error: SD from SEM and AFM analysis($3 \leq n \leq 6$).

4.3 Summary

The aim of this chapter has been to explain and fully characterise nanoporous alumina, from commercial alumina membranes to membranes engineered in-house. To do this, SEM and AFM were utilised to confirm current structure models for alumina. The relationship of applied anodization voltage to the structural parameters of alumina was discussed in detail. The 1.25 nm V^{-1} rule for pore diameter to anodization voltage was corroborated, but it was also demonstrated that anodization voltage determined interpore spacing, barrier oxide layer thickness, and the thickness of membranes. The chapter also discussed the quasi-constant porosity observed in NPAMs and the reasons for this. The effect of porosity on wetting models, which was highlighted earlier, will be discussed in detail in the next chapter (Chapter 5). The later sections of this chapter discussed the effect of annealing and hydrothermal treatments of alumina. Hydrothermal treatments were adopted to further control the pore diameter of alumina following anodization. This was successful to a point but there was a limit to the degree that pores could be swollen before fibrous growth covered the structure. Although this method was not used throughout, it did increase the hydrophilicity of the macro contact angle. In future these methods could prove useful for applications which require hydrophilic surfaces to attain superhydrophilicity.

Chapter 5

Wetting Properties of Porous Anodic Alumina

This chapter investigates the effects of surface structure and surface chemistry on the wetting properties of nanostructured porous anodic alumina (PAA) Previous chapters have used the abbreviation 'NPAM' to refer to porous alumina in the form of membranes. This chapter will use the abbreviation 'PAA' to refer to porous alumina with the barrier layer intact. The majority of this work has recently been published in *Colloids and Surfaces A*: *Physicochemical and Engineering Aspects* (Leese et al. 2013).[1] The wetting properties of alumina nanodomes (the barrier oxide layer) are also discussed in this chapter. SEM and FIB were performed at the MEC at Cardiff University under the EPSRC Nanoaccess scheme.

5.1 Introduction

As discussed in Section 2.2.1, an understanding of the macroscopic wetting behaviour of materials with nanostructured surfaces is crucial for their potential material application. Hydrophilic nanostructures which result in the decreased wettability of macro surfaces have come under particular scrutiny (Li et al. 2008; Lai et al. 2008). Wetting properties are also of concern in industry. Apple Inc. ©, for example, anodize their materials to protect product surfaces. From a filtration point of view, it is important to identify the contact angle between the surface and liquid and establish and how much pressure would be needed to fully wet membrane pores.

PAAs make ideal substrates for systematic studies in which the influence of nanostructures on macro-surface wettability is analysed. Measurements of equilibrium apparent contact angles (APCA) were taken on as-produced hydrophilic nanoporous PAAs with a range of pore diameters from 10 to 170 nm (some Anodisc^{TM} PAAs were also tested with pore diameters ~ 200 nm). These

[1] All data has been re-plotted. The text has been modified and extended.

yielded an increase in contact angles from 10 to 100°. The PAAs were also coated with a monolayer of fluorosilane in order to render them hydrophobic. The same trend was observed here as with the hydrophilic PAAs, but contact angles increased from 106 to 150° for pores sizes ranging from 10 to 200 nm. These results have probed the limits of current wetting models such as the Cassie-Baxter and Wenzel equations for nanostructured materials. A geometric model has been developed using the equation proposed by Marmur (Marmur 2003) to account for the wetting properties of bare- and silanized-PAAs.

5.2 Wetting Models

The crucial wetting models for this study, the Cassie-Baxter and Wenzel equations have already been discussed in Section 2.2. Over the past decade they have come under increasing scrutiny, with a surge in citations observed in 2004 (see Figure 5.1) (Gao and McCarthy 2007). Equations 5.1 and 5.2 represent the Cassie-Baxter and Wenzel equations, respectively. The Cassie-Baxter model considers a heterogeneous wetting regime, with two or more species with differing contact angles. When the second species is air, the cosine of the apparent contact angle (APCA) can be represented by the following equation:

$$\cos\theta_{CB} = f(cos\theta_Y + 1) - 1 \tag{5.1}$$

where θ_{CB} is the Cassie-Baxter contact angle, θ_Y the Young contact angle on a flat smooth surface, and *f* the surface fraction of a solid wet by the liquid. The Wenzel model accounts for the effect of surface roughness on the APCA with a roughness factor, *r*, which constitutes a ratio of the actual surface to its flat smooth projection:

$$cos\theta_W = rcos\theta_Y \tag{5.2}$$

In the Cassie-Baxter regime, liquid droplets sit above a solid surface and air pockets. In the Wenzel regime, water penetrates the crevices of the rough surface. Subsequent research has adapted these models to account for the dimensions of solid structures, line tension, and contact line pinning (Kwon et al. 2010; Bormashenko et al. 2007).

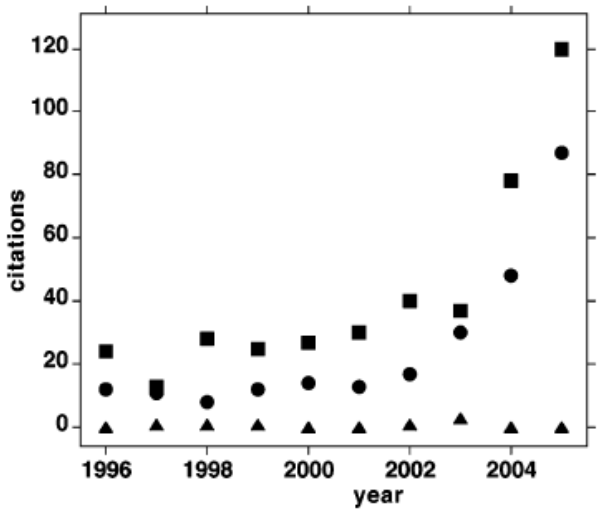

Figure 5.1 Citations versus publication year: (■) Wenzel, R. N. Ind. Eng. Chem. 1936, 28, 988, (●) Cassie, A. B. D.; Baxter, S. Trans. Faraday Soc. 1944, 40, 546, (▲) Pease, D. C. J. Phys. Chem. 1945, 49, 107 (Gao and McCarthy 2007).

In this chapter the equation proposed by Marmur (Equation 5.3) has been adapted for modelling the wetting of PAAs as an intermediate between the Cassie-Baxter and Wenzel models. That there are intermediates between the two models has been recognized in recent research. This chapter suggests that the wettability of PAAs can be accounted for through the same intermediate models. The base of the model proposed in this work stems from Equation 5.3, which reduces to Equation 5.1 for a non-porous rough surface (*f = 1)* when the second species is air, and to Equation 5.2 for a non-rough, porous surface (r_f *= 1)* where r_f is the roughness ratio of the wet area.

$$\cos\theta = r_f f cos\theta_Y + f - 1 \tag{5.3}$$

5.3 Characterisation of PAAs

SEM micrographs of the porous structure are shown in Figure 5.2a - c. A regular pore structure was observed in all samples, with limited branching observed only in the samples with smallest average pore diameters (Figure 5.2a). Cross-sections of membranes were obtained via FIB sectioning, which confirmed the regularity of the pore structure along the membrane thickness and that the pore channels were capped at one end (Figure 5.2d - f). From results obtained using the SEM

and AFM micrographs the average pore diameter and porosity have been related to anodization voltage (see Chapter 4). Porosity varied between 10 - 20% for all membranes, as reported in literature (Nielsch et al. 2002) and highlighted in Chapter 4. Numerical values for all the quantities measured have been reported in Table 5-1.

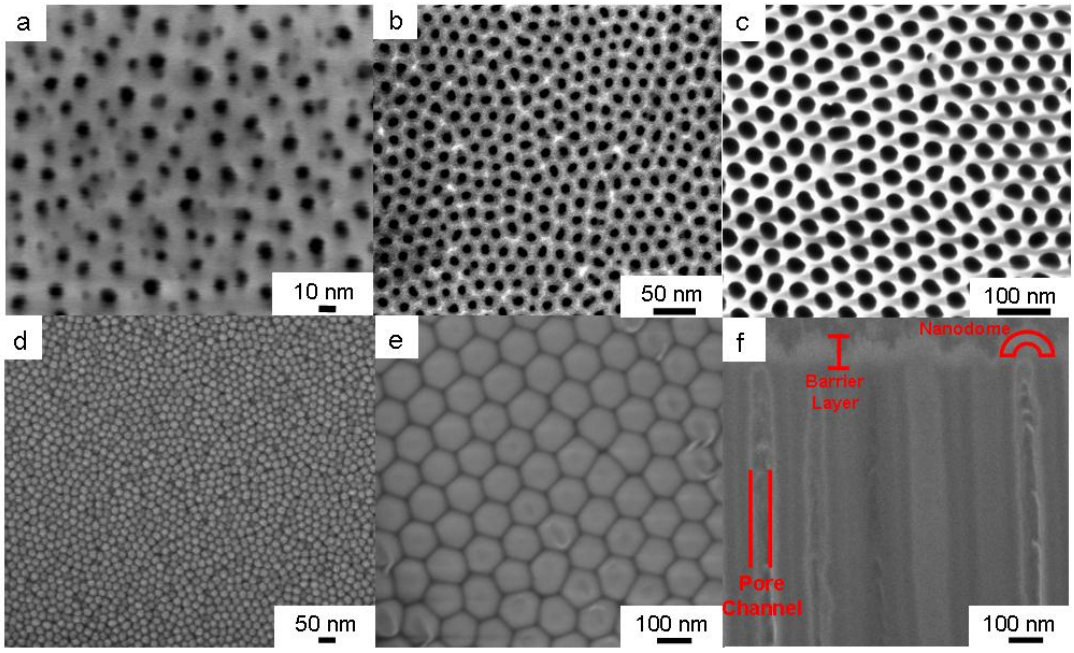

Figure 5.2 FESEM image of ordered PAAs *top* surface a) average D_P = 13 nm (10 V, 0.5 M H_2SO_4, 0 °C); b) average D_P = 30 nm (25 V, 0.5 M H_2SO_4, 0 °C); c) average D_P = 44 nm (40 V, 0.3 M oxalic, 14°C); d-e) FESEM of capped PAAs bottom surface; f) cross section of PAA and barrier oxide layer.

Table 5-1 Anodization conditions for template preparation and values of the pore diameter, D_P, inter-pore spacing, D_C, barrier oxide layer thickness, B and porosity for varying anodization voltage. This was a two-step anodization process, after the first step the thin oxide layer was removed using a mixture of 6wt% H_3PO_4 and 1.8wt% H_2CrO_4.

Voltage (V)	Electrolyte	D_P[a] (nm)	D_C[a] (nm)	B (nm)	Porosity, ϕ (-)
10	0.5 M H_2SO_4, 0 °C	14±2	33±3	0	0.11
20		25±4	54±4	12	0.11
25		30±4	64±5	23	0.15
30	0.3 M $C_2H_2O_4$, 14 °C	32±3	94±3	29	0.23
40		44±2	113±5	35	0.18
50		52±5	140±6	46	0.17
60		59±3	163±6	58	0.11
70		99±6	219±7	69	0.32
110	0.1 M H_3PO_4, 12 °C	170±20	240±13	-	0.30
150		190±15	380±30	-	0.31
Anodisc™		230±25	-	-	0.40

[a] Error: SD from SEM analysis, n =3.

5.4 Modelling the Wetting Properties of PAAs

The equilibrium APCA of water on PAAs increases linearly with pore diameter in the range investigated (10 - 100 nm) up to approximately 100° for the bare alumina and 150° for silanized PAAs (Figure 5.3). Extrapolation of the contact angle data for $D_P = 0$ (i.e. for a solid smooth surface) yields a contact angle of ~ 13° for bare-PAAs and ~ 103° for silanized-PAAs. The extrapolated values are in agreement with previously published data (Megias-Alguacil et al. 2011) and contact angle measurements performed on a slab of bare (12 ± 2°) and silanized (103 ± 2°) alumina. The data in Figure 5.3 demonstrates that the contact angle increases linearly with pore diameter until a critical value, D_P*, after which the contact angle increase plateaus. The plateauing of CA increase is more apparent for silanized surfaces than for bare PAAs. A dashed line has been used to indicate D_P* for each of the surfaces.

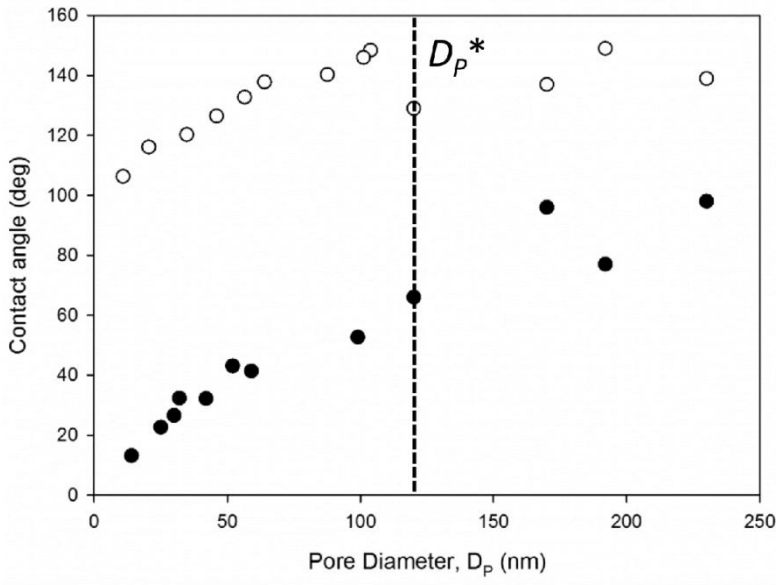

Figure 5.3. Water APCA on bare-PAA (●) and silanized-PAA (○) as a function of the average pore diameter, (error ± 2°). Dashed line represents D_P* for bare- and silanized-PAAs.

For $D_P < D_p$* both curves in Figure 5.3 have the same slope ~ 0.4° nm^{-1}, yielding the following relationship between the cosine of the APCA and pore diameter:

$$cos\theta_{exp}^{i} = \alpha^{i}\theta_{Y}^{i} + \beta^{i}D_P \qquad (5.4)$$

where θ_{exp} is the experimental contact angle, θ_Y the Young's contact angle (CA) on a flat surface (i.e. flat alumina), α and β are derived experimentally, and i = bare- or silanized-PAA. The equation shows that the contribution to the contact angle of the surface structure can be decoupled from the surface chemistry contribution, given by the Young contact angle for the bare and silanized surfaces. The surface chemistry represents a constant contribution to the contact angle whereas the changing pore diameters result in a variable contribution to the contact angle (i.e. the smaller the structure the closer the contact angle is to the Young's contact angle). The combination of both of these factors ultimately increases the contact angle of both the hydrophilic and the hydrophobic nanostructures. For $D_P > D_P$* it appears that the APCA for silanized surfaces becomes constant around or just below 150°. After crossing the 90° threshold, the contact angle increase for the bare surface diminishes. However, it should be noted that the position of D_P* (i.e. the transition between the linear relationship of pore diameter and contact angle and plateau) could be contested. For example, a straight line could be drawn for the relationship between contact angle and pore diameter for bare-PAAs (i.e. without any plateau) when taking into account the error of the contact angle measurements and pore diameter for $D_P > 150$ nm shown in Figure 5.3. If this were the case then one would assume a Wenzel wetting regime for bare-PAAs. This, however, does not fully explain the wetting of the bare-PAAs (see Figure 5.6). Therefore, having adapted Marmur's model and also observing the same relationship with different surface chemistry (but same nanostructure) the discussion below provides a model for the findings expressed in Figure 5.3.

As the APCA increases with increasing pore diameter, the Cassie-Baxter equation for porous, non-rough surfaces, appears to be the obvious way to model the experimental data. However, the solid surface fraction f, from the Cassie-Baxter model alone (calculated by $1 - \phi$, porosity for PAAs) is not sufficient to explain the increase in contact angle. The reason for this is as follows. PAAs have a quasi-constant porosity of approximately 10 - 20% (Nielsch et al. 2002). This is due to the fact that as pore diameter increases, the number of pores decreases exponentially, leaving porosity quasi-independent of anodization voltage (see Section 4.1.3). Several adapted Cassie-Baxter models have been developed, but

all still depend on the solid surface fraction varying when the structures size increases which is not the case for PAAs (Larsen and Taboryski 2009).

If porosity alone is not responsible for the increase in contact angle, then it must be associated with a larger interaction of the liquid with the solid (i.e. some penetration of the liquid inside the pore has to occur). This phenomenon has been observed for both hydrophilic and hydrophobic porous surfaces (Lafuma and Quere 2003). The extent of penetration is given by a balance of the Laplace pressure of the macroscopic liquid drop on the substrate surface $2\gamma_{LV}/r$ (Bormashenko et al. 2007; Raspal et al. 2012) and the resistance to compression of the air in the pores (assuming that it behaves as an ideal gas and that no air escapes from the pores):

$$p_1 V_1 = p_2 V_2 \tag{5.5}$$

where $p_1 = p_{atm}$ and,

$$V_1 = \frac{\pi D_P^2 L}{4} \tag{5.6}$$

When the liquid is partially filling the pore (Figure 5.4), then:

$$p_2 = p_1 + \frac{2\gamma_{LV} cos\theta}{r} \text{ and } V_2 = \frac{\pi D_P^2 (L-\delta)}{4} \tag{5.7}$$

where δ is the pore filling depth (i.e. how deep the droplet goes into the pore - full penetration would yield $\delta = L$). All other symbols are described in Figure 5.4a. For simplicity, this model considers the bottom of the pore to be flat. However, in reality it has the shape of a spherical cap of radius $D_P/2$ (due to the barrier oxide layer). Given that $L/D_P > 10^3$, the error associated with this is in the order of 0.1%. The Laplace pressure exercised by the droplet is significantly different for the two surfaces, given their different wetting properties (Figure 5.4b). In fact, it somewhat mirrors the APCA behaviour shown in Figure 5.3. It should be noted that since the drop diameter for the lowest contact angles for bare alumina is larger than the capillary number for water, the height of the liquid films was used in lieu of the radius to calculate the Laplace pressure (Lafuma and Quere 2003).

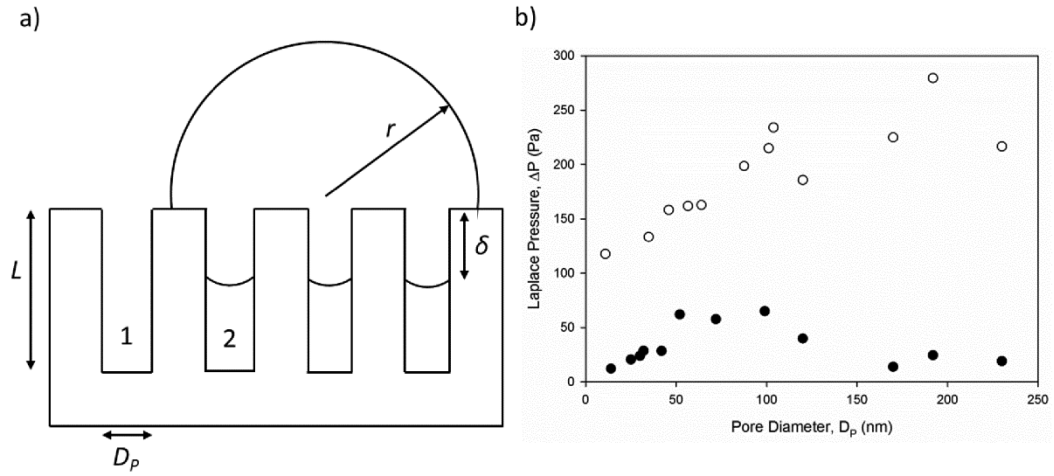

Figure 5.4 a) Schematic of water droplet penetration inside cylindrical channels of length, L and diameter D_P, for a silanized, hydrophobic PAA. The liquid penetrates inside the pores by a depth $\delta \leq L$, as a function of water drop diameter, r and pressure of air trapped inside the pore and b) Laplace pressure of water droplets on silanized (○) and bare (●) PAAs as a function of pore diameter.

For $D_P < D_P^*$ the dependency of cosine of the APCA on the pore diameter can be modelled using the inhomogeneous wetting regime (Equation 5.3). Comparing Equation 5.3 and 5.4, one finds that:

$$f = 1 - \beta D_P \tag{5.8}$$

$$r_f = \frac{\alpha}{1-\beta D_P} \tag{5.9}$$

As r_f is defined as the ratio between the actual wet surface and its smooth projection, in the case of the PAAs it is defined as (Marmur 2003):

$$r_f = 1 + \frac{4\phi\delta}{(1-\phi)D_P} \tag{5.10}$$

where the porosity $\phi = \left(\sum_{i=1}^{n} \pi D_p^2/4\right)/A_S \cong n\pi D_p^2/4A_s$. Here n is the number of pores and A_S the drop-solid contact surface for each value of D_P. The second relation is only valid when pore size distribution is narrow, as is the case for the PAAs used here (Lee et al. 2012). This expression for r_f results in an excellent agreement with the experimental data for $D_P < D_P^*$ (Figure 5.5).

As can be observed in Figure 5.5, f decreases with increasing pore diameter, ideally down to 0 when $D_P = 1/\beta$, where β is obtained experimentally from

Equation 5.3. The fact that *f* decreases might appear to contradict the experimental evidence that pore filling increases with increasing pore diameter. However, the effect of the reduction of the drop-solid surface also has to be taken into account, and this value is significantly larger than the increase given by liquid filling the pore. As such, *f* can be defined as:

$$f = (1 - \phi)\frac{A_S}{A_0} \tag{5.11}$$

where A_0 is the droplet area on a flat, smooth surface where $\theta = \theta_Y$. When $\delta = 0$, $r_f = 1$, and $f = 1$, it corresponds to a flat, smooth surface, $A_S = A_0$. On the other hand, when $D_P = 1/\beta$ then $f \sim 10^{-8} = 0$. This is because the macroscopic droplet size would ideally coincide with a single pore diameter, with no liquid in contact with the PAA surface except for the (small) area of pore wall wet by the liquid. This state is never reached however, as can be seen in Figure 5.5, where the values for r_f and f obtained using Equation 5.10 and 5.11 deviate from experimental data. The reason for this behaviour is discussed below. The inflection point corresponds with $D_P = D_P^*$, as in Figure 5.3. Behaviour for $D_P > D_P^*$ is discussed below separately for silanized- and bare-PAAs. By substituting the expressions for r_f and f in Marmur's model (Marmur 2003), a good correlation with experimental data is obtained (Figure 5.6, with the Cassie-Baxter and Wenzel equations for the silanized PAAs drawn in bold dashed lines).

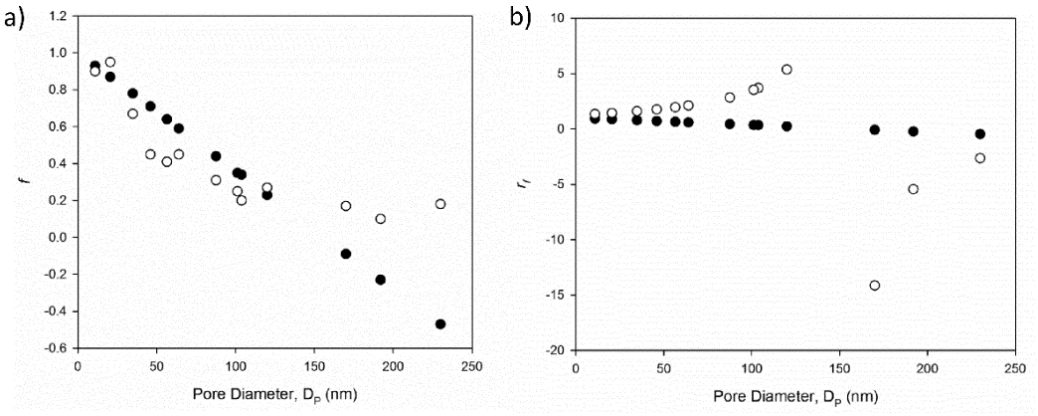

Figure 5.5 a) parameter (●) $f = 1 - \beta D_P$ and (○) $f = (1 - \phi)A_s/A_0$; b) (●) $r_f = 1 + (4\phi\delta/(1 - \phi)D_P)$ and (○) $r_f = \alpha/1 - \beta D_P$ for silanized PAAs as a function of pore diameter. The behaviour is similar for the bare PAAs.

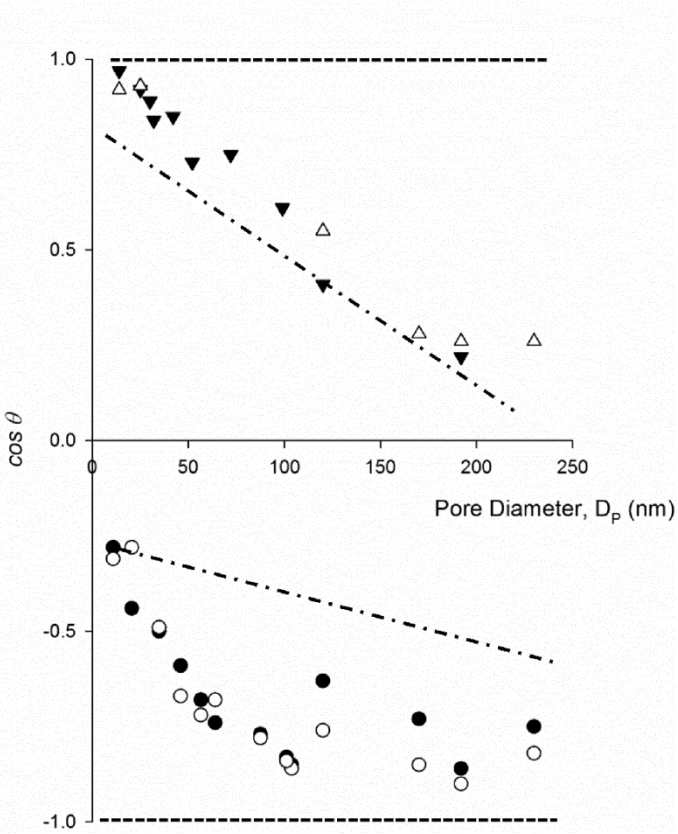

Figure 5.6 Cosine of the APCA for experimental data (●), (▼) and model data (○), (Δ) data for the silanized and bare PAAs derived from Equation 5.3, respectively. The Cassie-Baxter (- - -) and Wenzel (— · — · —) models are shown as dashed lines, based on Equation 5.1 and 5.2, respectively.

5.4.1 Wetting of Silanized (Hydrophobic) PAAs

For silanized PAAs, Laplace pressure first increases linearly starting from a value as low as 32 Pa, followed by a quasi-constant value around 100 Pa. Previous experiments in the literature have shown that pressure can induce a wetting transition from Cassie-Baxter to Wenzel-type behaviour (Lafuma and Quere 2003; Bormashenko et al. 2007). It is quite clear that for the smallest pores there is little to no penetration of liquid inside the pores of silanized PAAs, consistent with Cassie-Baxter behaviour. In fact, the Laplace pressure of the water droplet formed in PAAs with the smallest pore size is below the 50 - 100 Pa threshold for inducing penetration, as reported in literature (Lafuma and Quere 2003; Bormashenko et al. 2007). As the APCA increases, the Laplace pressure increases and penetration of water inside the pores occurs, leading to a Wenzel-like behaviour. Above D_P*, however, the cosine of the APCA is approximated – 0.8, somewhat short of the – 1 value that one would obtain if the whole pore were to

be filled with water in ideal Wenzel behaviour. This is attributed to the fact that the pore is not completely filled. The pore filling depth, δ, is a function of not only the PAA geometric characteristics: pore diameter and pore length, but also of the Laplace pressure of the overlaying droplet. A full Wenzel case ($\delta \equiv L$, $r_f \equiv r \gg 1$) could indeed be achieved by applying further external pressure, as shown in the literature (Lafuma and Quere 2003). It should be noted that this could occur only if all the air present in the pores were to be replaced by water. While the evolution of air bubbles out of hydrophilic PAA pores through a liquid droplet has been observed (Ran et al. 2008), the same behaviour appears unrealistic for hydrophobic surfaces.

5.4.2 Wetting of Bare (Hydrophilic) PAAs

As can be seen in Figure 5.3, contact angle increase for bare PAAs is more linear than that for silanized PAAs. It could also be argued that it is fully linear and that no slow-down is observed, within the margin of error of the experimental data. The shape of the Laplace pressure curve suggests the latter within experimental error, though the overall value of the pressure is much lower; at or below the threshold for the liquid penetration of hydrophilic surfaces reported in the literature (Bormashenko et al. 2007). It should be noted, however, that since bare PAAs are hydrophilic, there is capillary pressure for the liquid to enter the pore. Although the resistance presented by air trapped in the pores prevents full wetting of the pores, liquid can still enter the pores. The reason for the APCA change with pore diameter is here opposite to that of silanized substrates: the pores are initially penetrated by water and, as the pore size increases, so does the amount of air trapped in the pores, leading to a higher contact angle. As discussed in the introduction, a previous study considered the wetting behaviour of bare PAAs with pores in the 100 - 450 nm range (Ran et al. 2008), with a wetting transition from the Wenzel to Cassie-Baxter regime above 250 nm. This was justified by assuming the Young contact angle for alumina to be $\theta_Y = 85°$. This is a high value for alumina, which is a high energy solid (de Gennes et al. 2004). Moreover, as suggested earlier, literature data of the contact angle of water on alumina is more closely aligned with the 10 - 12° value reported here. The experimental results from (Ran et al. 2008) have been combined with those reported in this paper (Figure 5.7, (○) and (●), respectively), showing good agreement in a linear

correlation between contact angle and pore diameter. These results challenge the model proposed in (Ran et al. 2008), as the transition between Wenzel and Cassie-Baxter regimes starts for much smaller pores than those previously analysed. The results can be explained by combining the inhomogeneous wetting regime in Equation 5.3 with the parameters in Equation 5.10 and 5.11.

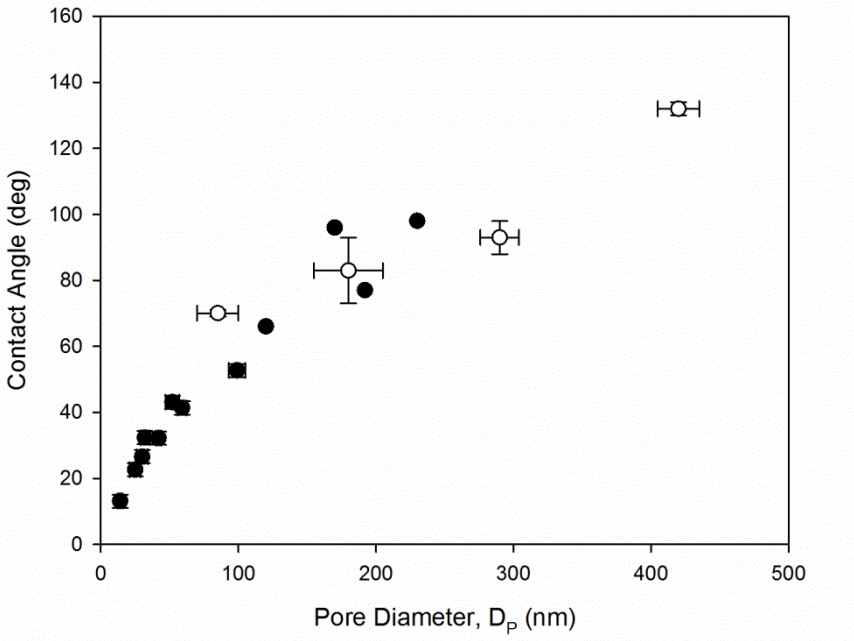

Figure 5.7 Comparison of contact angle values for water on bare, hydrophilic PAAs: this study (●, error ± 2°), and (○, error bars from paper) Ran et. al. (Ran et al. 2008).

Finally, it should be noted that the linear variation of contact angle with increasing pore diameter (and anodization voltage) in Figure 5.4 is conserved in samples anodized in sulfuric, oxalic, or phosphoric acid (Table 5-1). While it is well-known that anions from electrolytes are incorporated into the alumina during the anodization process (Sulka 2008), they do not significantly affect the contact angle. This is because the presence of anions does not significantly alter the charge state of the alumina surface (Megias-Alguacil et al. 2011; Franks and Meagher 2003).

5.5 Wetting of Nanodomes

Further to the wetting properties of nanoporous alumina, the barrier oxide layer (referred to here as 'nanodomes' and highlighted in Section 5.3) present another controlled nanostructured surface for systematic study. In this section the wetting properties of alumina nanodomes are discussed. In addition to this, the nanodomes were also utilised in an on-going collaboration with Dr Wuge Briscoe and his research group at the University of Bristol. This work utilised AFM and force measurements to assess friction at the nanoscale and interrogate the validity of continuum models. Information of the two papers which emerged from this collaboration (Pilkington et al. 2011) can be seen in Appendix A.

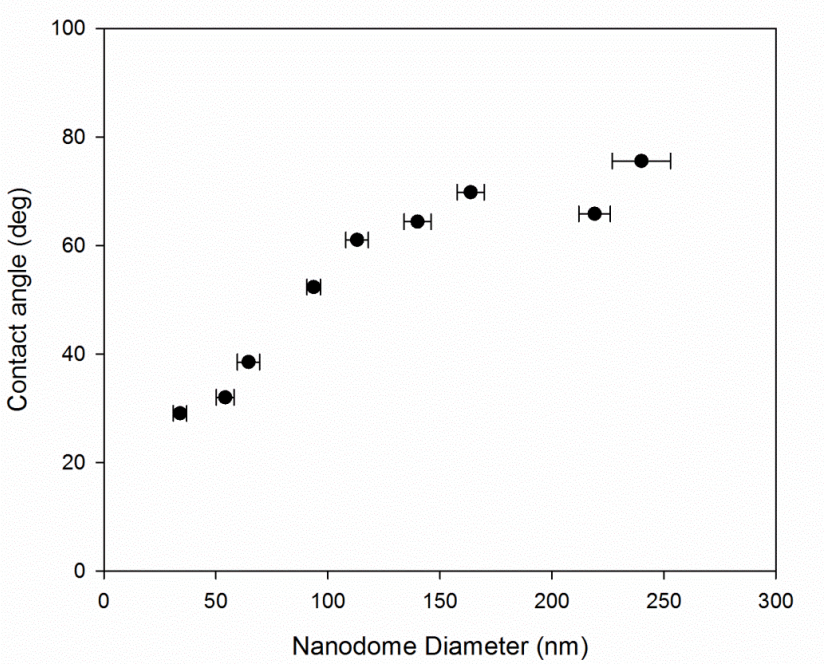

Figure 5.8 APCA of water with change in nanodome diameter (CA error ±2°). The slope is approximately 0.24 nm deg^{-1}.

Contact angle measurements were performed on bare (untreated) nanodomes. The APCA on alumina nanodomes produced a similar trend to that observed in the case of nanoporous alumina (see Figure 5.8). The structures of the nanodomes have been shown in Figure 5.2d - f. As discussed earlier, barrier oxide layer thickness and structure is dependent on anodization voltage, and here the nanodome diameter is equivalent to the interpore spacing, D_C. The proportionality constant between nanodome diameter and CA is approximately 0.24 nm deg^{-1}.

This value is approximately half of that observed for nanoporous alumina. However, if the values of CA were plotted against pore diameter it would yield the 0.4 nm deg^{-1} observed earlier (see Figure 5.3).

The wetting behaviour of nanodomes is similar to that of nanoporous alumina. Instead of a surface of circular pores, however, it is assumed here that the areas of nanodomes likely to increase roughness and/or trap air are the approximately equilateral-triangular areas between the nanodomes themselves (Figure 5.9). The error of this assumption has been calculated to be < 10%. If the triangular 'pores' shown in Figure 5.9a and the area filled in red in Figure 5.9b are taken to be equilateral, the length, *l*, of each side is approximately equal to the pore diameter, D_P. The wetting model proposed by Marmur (Equation 5.3) has been utilised again, as both the Wenzel and the Cassie-Baxter regimes need to be reconsidered for nanodomes. To calculate the solid surface fraction the area of the triangles A_t, needs to be calculated. The area of one triangular pore can then be multiplied by the total number of triangular pores; nA_t, where n is the number of triangular pores. Porosity can then be calculated as $\phi = 1 - (nA_t/A)$, where ϕ is porosity and A is the total surface area. The solid surface fraction, $f = 1 - \phi$, discussed earlier is represented:

$$A_t = \frac{D_P^2\sqrt{3}}{4} \tag{5.12}$$

As for nanoporous alumina, the porosity of nanodomes is both constant and independent of anodization voltage. These are the values for f considered in Equation 5.3. The r_f and f values shown in Figure 5.10 clearly show a decreasing r_f value and a constant f. This indicates that at the smallest dome diameters there is almost full Wenzel wetting of the nanodomes and the triangular pores due to the larger r_f value. As this value tends to 1 for increasing dome diameters, there is a transition to a partial Wenzel wetting regime. This is due to fact that the larger triangular pores have a large volume of trapped air.

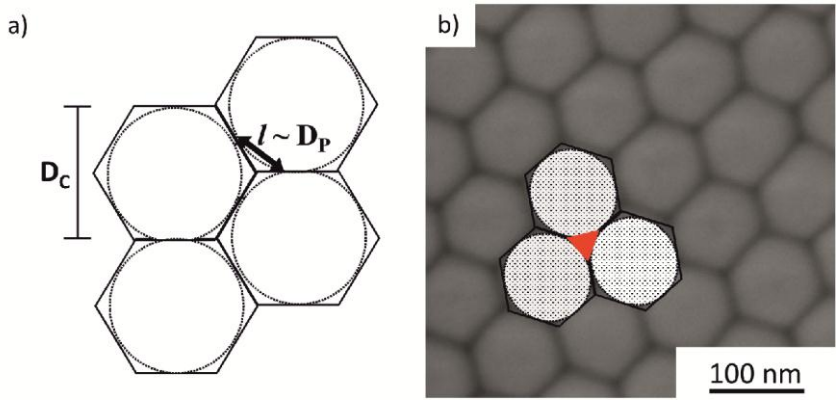

Figure 5.9 a) Simplified schematic of the hexagonal geometry of nanodomes, the interpore spacing D_C, is equivalent to nanodome diameter and b) the schematic super-imposed onto an SEM of the nanodomes, the triangle in red highlight the equilateral triangle of $l \equiv D_P$.

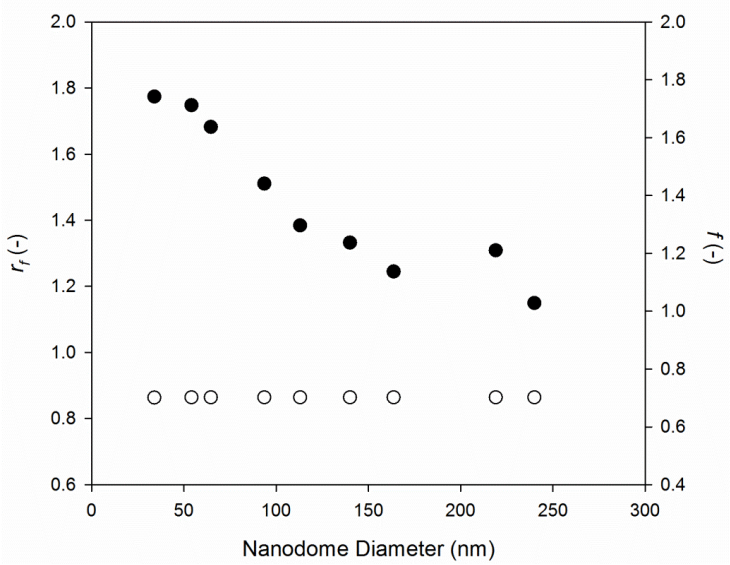

Figure 5.10 Parameter r_f (●) and f (○) as a function of nanodome diameter. The r_f values decrease with increasing nanodome diameter due to the fully Wenzel case (for the smallest diameters) and partial Wenzel at larger nanodome diameters. It is clear that the f term is constant (i.e. supporting again that the structure parameters of alumina either on porous or barrier oxide side the porosity remains constant).

5.6 Summary

This chapter has exploited the structure of nanoporous alumina (fabricated by aluminium anodization) for studying the effect of nanostructures on the macro wetting properties of surfaces. Systematic contact angle measurements were taken on bare- and silanized-PAAs with pore diameters varying from 10 to 240 nm. In both cases, the CA increased with increasing pore diameter. For hydrophilic bare-PAAs the CA was raised by 90°, from ~ 10 to 100° with pore diameters from

10 to 240 nm. For the hydrophobic silanized-PAAs with the same range of pore diameters the CA increased from 106 to 150°. In both cases the relationship between contact angle and pore diameter was 0.4° nm^{-1}.

In the first instance, the Cassie-Baxter and Wenzel models were used to try and explain the wetting regime of the nanostructured materials. These models proved inadequate as an intermediate state between the Cassie-Baxter (no water penetration inside the pores) and Wenzel (full wetting of the porous structure/roughness) was in fact controlling the wetting behaviour; i.e. there was penetration of liquid inside the pores as well as trapped air. An equation proposed by Marmur was sufficient to model the findings when the parameters r_f and f were modified for the PAA structure.

The Cassie-Baxter equation was found to be insufficient in modelling the experiment results from this study owing to the solid surface fraction value which the model depends on. It is the first time that a range of pore diameters at this scale have been probed in this way. The fact that the porosity was quasi-constant has served to expose a limitation of the Cassie-Baxter model. Indeed, quasi-constant porosity finds the solid surface fraction parameter in the Cassie-Baxter model inadequate for explaining the wetting regime in hydrophilic and hydrophobic PAAs.

Finally, experimental measurements on the barrier oxide layer (‘nanodomes’) were taken. The same dependence on nanostructure size and resulting CA was observed as in the case of the nanoporous alumina. Marmur’s modified equation was utilised as well. It is believed that a transition from a partial wetting regime to Cassie-Baxter regime occurs for the smallest to the largest nanodomes. This is due to trapped air between the nanodomes in the case of larger nanodomes, whereas roughness directs the wetting properties of the smallest nanodomes (i.e. less or no air was trapped between the domes in the case of the smallest domes). The next chapter will explore the flow properties of NPAMs using atomic force microscopy (AFM) force measurements.

Chapter 6

Pressure-Driven Flow in Nanoporous Alumina Membranes by AFM

The previous chapter investigated the effect of nanostructures on material wetting properties. This chapter will follow this by discussing the effect of pore diameter on pressure-driven flow through NPAMs. The first section will outline work completed in collaboration with Mr Kah Peng Lee in which flow enhancement was observed through NPAMs. This work has recently been published in the journal *Nanoscale* (Lee, Leese and Mattia 2012)[1]. The main part of the chapter will discuss work completed in collaboration with the Particulate Fluids Processing Centre at the University of Melbourne, Australia. The experimental findings gained from this collaboration (which involved a visit by the candidate to Melbourne) have been modelled by Mr Chu Wu. The manuscript for this work is currently in preparation for publication in *Langmuir*.

6.1 Flow Measurements in NPAMs

This first section discusses recent work completed by Lee et al. which observed flow enhancement in hydrophilic nanochannels. The methods described in Chapter 3 Section 3.5.1 were used to carry out flow measurements of NPAMs by imposing set flow rates. The methods described in Chapter 3 Section 3.8.1 were adopted for membrane characterisation and theoretical volumetric flux J_{HP}, was calculated using Equation 6.1. In order to identify whether there was any deviation from the theoretical values (and therefore flow enhancement) the J_{HP} was compared to the experimentally measured volumetric flux J_{exp} (Equation 6.2).

$$\frac{J_{HP}}{\Delta P} = \frac{\phi D_p^2}{32\tau} \tag{6.1}$$

$$\varepsilon = \frac{J_{exp}}{J_{HP}} \tag{6.2}$$

[1] All the data in Figure 6.1 and 6.2 have been referenced and re-plotted.

No enhancement (i.e. no-slip) was observed (ε ~ 1) in NPAMs with average pore diameters of 100 nm. This corroborates a publication by Cheng and Giordano, where no-slip was observed in pressure-driven flow experiments of water in rectangular channels coated with a photoresist of hydraulic diameter ~ 84 nm (Cheng and Giordano 2002). However, in the research presented here, flow enhancement was observed in NPAMs with pore diameters < 100 nm. Figure 6.1 displays the flow enhancement factors with mean pore diameter. It is clear that the enhancement factor increases with decreasing pore diameter. Further to this, Figure 6.2a shows the change in enhancement factor with the distribution of pore diameter. In recent studies, the length of CNTs has been shown to have an effect on the observed enhancement factor. Thus, when one divides the enhancement factors by the thickness of the NPAMs the distribution of pore diameters collapse into one line (Figure 6.2b). As discussed in Chapter 2 Section 2.2.1, flow enhancement factors have previously been used in the discussion of fluid flow in CNTs, but flow in hydrophilic nanochannels has received little attention. From the results presented in this chapter it is clear that there is also an enhancement from the expected flow rate for hydrophilic nanochannels (compared to the continuum fluid mechanics no-slip Hagen-Poiseuille model). This is further supported by results obtained by AFM, analysis of which will form the main part of this chapter.

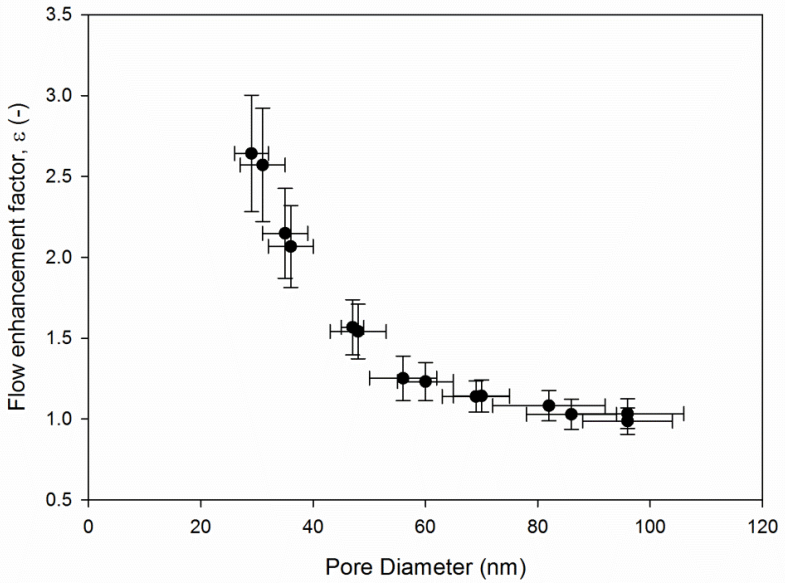

Figure 6.1 Plot of flow enhancement against pore diameter of each NPAM based on the mean pore diameter with error span (Lee et al. 2012). Error of pore diameter and enhancement factor are the SD of statistical analysis from SEM micrographs and repeated measurements ($3 \leq n \leq 5$), respectively.

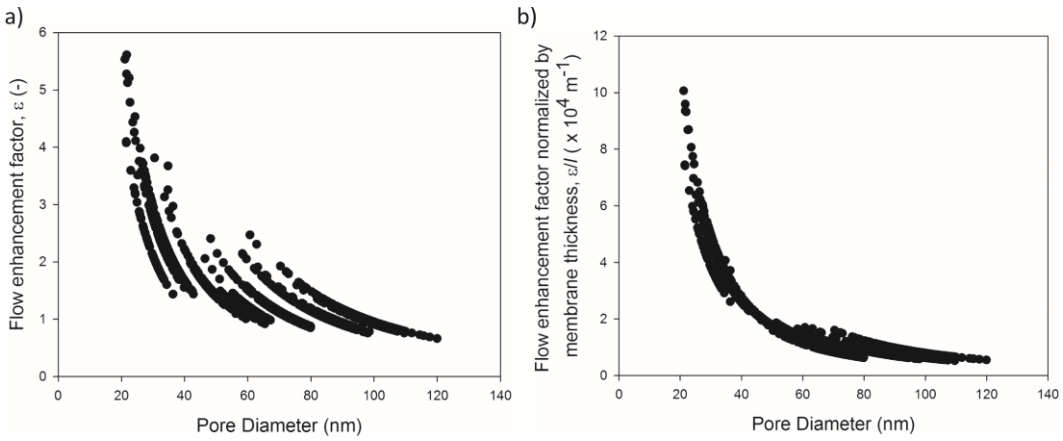

Figure 6.2 Plot of flow enhancement factor a) with the distribution of pore diameter and b) normalized by membrane thickness against pore diameter of each NPAM based on the distribution of pore diameter (Lee et al. 2012).

6.2 Detecting Slip and Drainage by AFM Force Measurements

AFM force measurements were performed on NPAMs in order to assess fluid flow at the membrane surface. This follow the work presented in Section 6.1. In addition to assessing fluid behaviour in the NPAM channels, however, it also considers flow behaviour between two solid surfaces (i.e. the surface of the membrane and the surface of a solid particle). 'Closed' and 'open' pore systems were used (see Figure 6.3) to compare differences in force measurements. The ultimate aim here was to establish whether the no-slip boundary condition was valid and whether flow through the 'open' pores could be detected using AFM. The first part of this second section will introduce the principles of the atomic force microscope (AFM) and resulting force measurements. It will then explain how this technique was used to analyse no-slip boundary conditions and drainage on and through NPAMs.

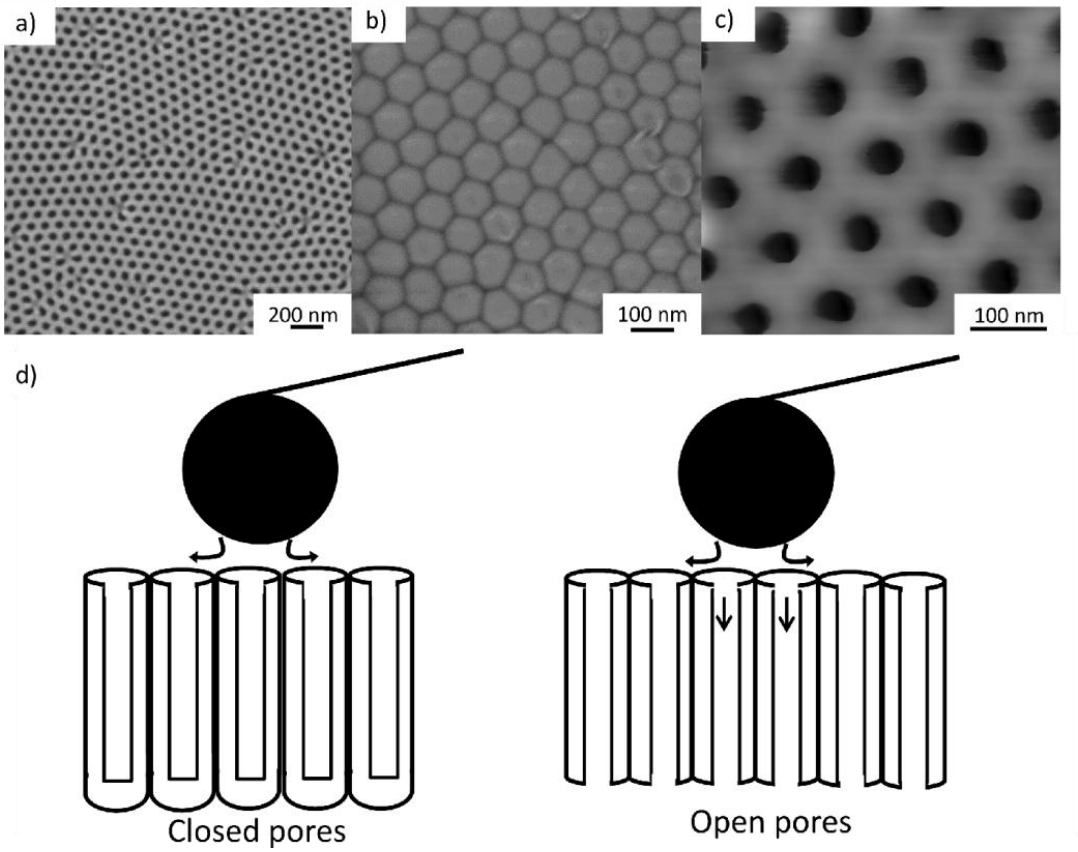

Figure 6.3 FESEM images of a) the porous top surface of alumina (D_P = 48 ± 5 nm) which the particle was driven into for the 'closed' and 'open' pores b) the barrier oxide layer of the alumina which blocked the channels in the case of the 'closed' pores and c) an AFM image after the removal of the barrier oxide layer (shown in b) in the case of 'open' pores, d) is a schematic cross section of the 'closed' and 'open' pore systems (not to scale). The arrows present the hypothesis of liquid movement at the surface for each case.

The no-slip boundary condition, which assumes that fluid velocity at the surface is equal to surface velocity, has been used successfully to model Couette and Hagen-Poiseuille flow as well as other hydrodynamic and engineering systems on the macroscopic scale. It has also successfully been used to model systems that generate a Hagen-Poiseuille flow of deformable surfaces at the nanoscale (Chan et al. 2011). However, deviations from the no-slip Hagen-Poiseuille model have been observed, and this can be described as 'slip'. The slip condition assumes that fluid velocity at the surface is different from that of the surface itself (see Figure 6.4). It has been argued that slip occurs for Newtonian fluids, and it has recently been observed at the micro- and nano-scale (Lee et al. 2012; Mattia and Calabrò ; Neto et al. 2005; Bonaccurso et al. 2003; Chan and Horn 1985).

Establishing the boundary conditions that apply to fluid flow in confined geometries provides further understanding of fundamental flow behaviours at the

micro- and nano-scale. It also improves our understanding of a number of industrial and technological processes, such as flow in porous media, microfluidic and nanofluidic devices, electroosmotic flow, and lubrication (Neto et al. 2005).

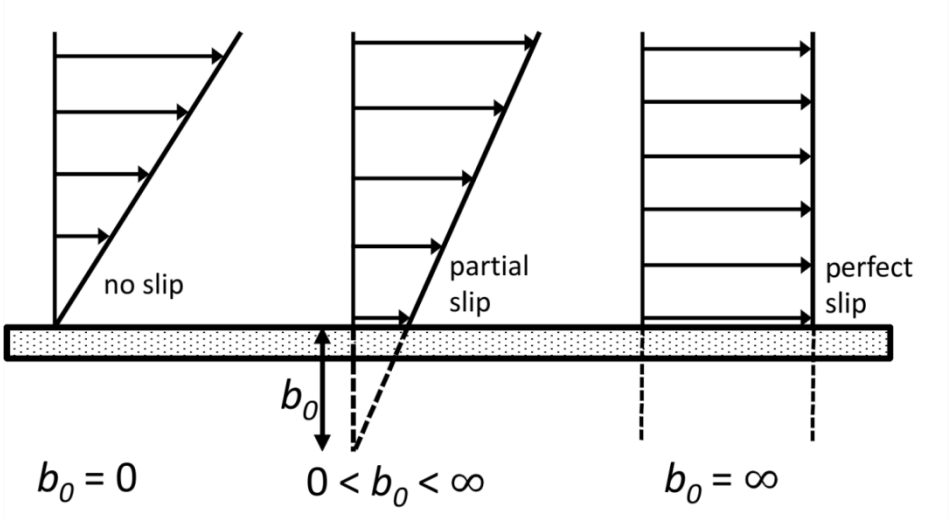

Figure 6.4 Schematic of slip flows on a stationary solid surface, with slip length b_0. Redrawn from (Holt 2009).

In order to extend the work discussed in Section 6.1, the atomic force microscope (AFM) has been utilised to observe fluid flow at the membrane surface. In the past few decades AFM has been developed for sophisticated dynamic force measurements. It is therefore possible to experimentally investigate fluid flow at membrane surfaces and thus establish whether the no-slip boundary condition applies. The force measurements were conducted using what is known as solid-probe AFM force measurements. Solid-probe measurements are amongst the most useful techniques for dynamic force measurements as the probes can be driven into surfaces at relatively high velocities, thus allowing the measurement of hydrodynamic forces.

The idea of a hydrodynamic slip boundary condition in which the tangential velocity of the fluid at an interface is proportional to tangential stress was first proposed by Navier in 1823 (Navier 1823a; Navier 1823b). This idea has been revived as a convenient model to account for complex flow conditions at surfaces that arise from surface structures or fluid granularity. For example, Bonaccurso et al. examined hydrodynamic slips using AFM between a colloidal probe and surfaces with systematically increasing surface roughness (Bonaccurso et al. 2003). Hydrodynamic slip was proposed as a way to capture deviations between

experimental data and the simple model of a smooth, solid, no-slip surface. Zhu et al. used AFM to study the hydrodynamic interaction between a smooth octadecyltrichlorosilane (OTS)-coated silicon wafer and a borosilicate particle in di-n-octylphthalate fluid (Zhu et al. 2011b). Deviations from the no-slip model in this unusual fluid/solid system were attributed to a slip length in the range of 24 - 31 nm at approach velocities of 10 - 80 μm s^{-1}.

As well as examining interactions on the smooth surfaces discussed above, 'controlled roughness' can also be introduced in the form of ordered pore structures. This is extremely important for the wetting of materials and flow behaviour because these conditions are usually observed in practical settings. Gupta et al. made direct force measurements between surfaces with structured cylindrical posts in a hexagonal array using a surface force apparatus (SFA). They modelled the hydrodynamic drainage behaviour in terms of a deviation function from the no-slip model and employed scaling analysis to describe the separation which was the onset of the deviation (Gupta and Fréchette 2012).

The present study utilised a model which was developed and solved in MATLAB (conducted by Mr Chu Wu). This incorporated hydrodynamic forces with slip effects, cantilever drag forces (due to the relatively high velocities used in the experiments), and Derjaguin and Landau, Verwey and Overbeek (DLVO) forces (consisting of van der Waals and the electric double layer (EDL)). Hydrodynamic forces in the case of 'open' pores have been adjusted to accommodate the possibility of flow through the channels. The developed model uses AFM LVDT experimental data as well as measured parameters - particle radius and cantilever spring constants. The slip lengths (see Figure 6.10a) and initial separation values are adjusted to fit the model with the AFM data (for full derivation see Appendix D).

6.2.1 Atomic Force Microscopy - Force Measurements

AFM was invented by Binnig et al. and was first reported in 1986 (Binnig et al. 1986). It has traditionally been used for imaging substrate topography using the optical detection of deflection of a cantilever traversing the surface. It has now

become common practice to use AFM for force measurements utilising the same cantilever deflection measurements which were originally developed for imaging.

6.2.1.1 Force on a Particle and AFM Kinematics

The objective of AFM force measurements is to obtain force as a function of Piezo displacement. For solid systems this can then be converted to force as a function of surface separation (the distance between the solid particle and the solid surface). The Piezo displacement is measured by the AFM in voltage and converted to length through an internal system calibration which gives the relative displacement as a function of time ($\Delta X(t)$). The model for the experimental results can be derived by first considering the force balance on the cantilever particle (Figure 6.5). It is expected that the particle will experience forces from three main sources: the force from the spring (F_K), DLVO forces (F_{DLVO}), and hydrodynamic forces (F_H). The Reynolds number for this system is very low so inertial effects can be neglected. Summing up these forces yields Equation 6.3.

$$F_K = F_H + F_{DLVO} \tag{6.3}$$

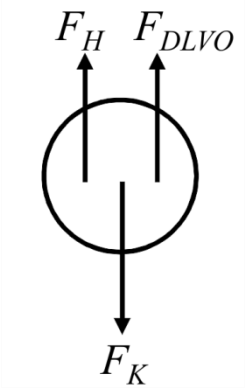

Figure 6.5 Free body diagram of the particle.

Figure 6.6 is a schematic of an AFM, where $h_0(0)$ is the initial separation, $h_0(t)$ is the separation of the particle centre to the surface, D is the particle diameter, ΔS the cantilever deflection, $X(0)$ the initial LVDT (linear variable differential transformer) position, $X(t)$ the position of the LVDT after time t, and V_t is the LVDT velocity. AFM experiments were conducted at fairly high velocities of around 10 to 20 μm s^{-1}. As a result the cantilever experienced drag. Cantilever

deflection is therefore caused by a combination of cantilever drag and force on the particle. AFM thus measures an apparent force (F_{app}) consisting of the force on the particle and a force due to drag. For this model it is assumed that drag is directly proportional to cantilever velocity (Dagastine et al. 2010), where *C* shown in Equation 6.4 is the drag constant.

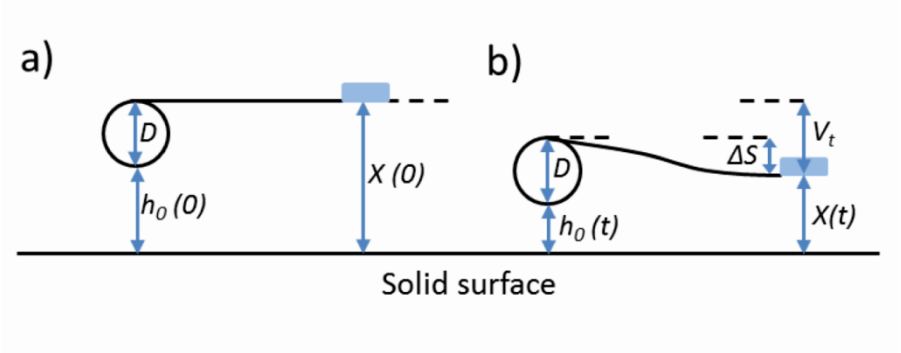

Figure 6.6 Schematic of the atomic force microscope a) cantilever particle in static position and b) cantilever in motion being driven to the surface.

The apparent force can be related to the cantilever deflection ΔS through Hooke's Law and using Figure 6.6. The force experienced by the particle can be related to the AFM parameters through Equation 6.4, where μ is the viscosity.

$$F_K = K(h_0(t) - h_0(0) + V_t) - C\mu\frac{dX}{dt} \tag{6.4}$$

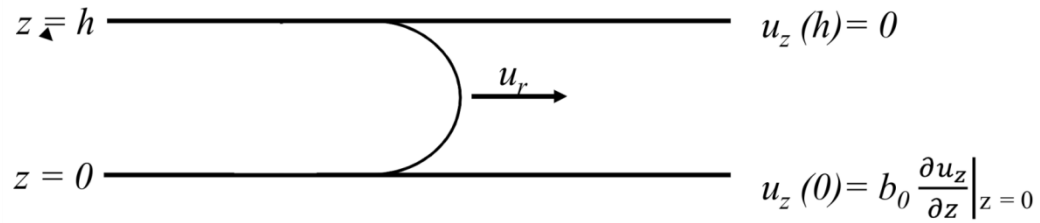

Figure 6.7 Flow between two solid plates with the upper plate and lower plates experiencing no-slip and slip boundary conditions respectively.

Flow between the silica particle and membrane surface can be modelled as flow between two flat plates. Both plates have zero velocity though it is assumed that the membrane surface experiences slip. The finite-slip boundary condition is therefore applied to the bottom surface (Figure 6.7), whilst it is assumed that the silica particle experiences the no-slip condition. The system is very similar to Couette flow with pressure gradient, albeit both surfaces have zero velocity.

Nonetheless, starting with the Navier-Stokes equation for Couette flow in the r-direction:

$$0 = -\frac{\partial P}{\partial r} + \mu \frac{\partial^2 u_r}{\partial z^2} \tag{6.5}$$

Integrating the above equation twice with respect to z will yield:

$$u_r = \frac{1}{2\mu}\frac{\partial P}{\partial r} z^2 + c_1 z + c_2 \tag{6.6}$$

Where c_1 and c_2 are determined from applying the boundary conditions in Figure 6.7. This gives the result:

$$u_r = \frac{1}{2\mu}\frac{\partial P}{\partial r}\left[z^2 - \frac{h^2(z+b_0)}{h+b_0}\right] \tag{6.7}$$

The volumetric flow rate between the plates can be found by integrating the velocity in Equation (6.7) from $z = 0$ to $z = h$ which will give:

$$Q = \int_0^h u_r \, dz = -\frac{h^3}{12\mu}\left(\frac{h+4b_0}{h+b_0}\right)\frac{\partial P}{\partial r} \tag{6.8}$$

6.2.2 DLVO and Hydrodynamic Forces

The DLVO component consists of both EDL and van der Waal (vdW) forces, which are modelled through Derjaguin's approximation as shown in Equation 6.9.

$$F_{DLVO} = 2\pi R W_{EDL} + 2\pi R W_{vdW} \tag{6.9}$$

where R is the radius of the particle and W_{EDL} and W_{vdW} are the interaction energies of the EDL and the van der Waals, respectively.

Force for the hydrodynamic pressure was found by solving the Stokes-Reynolds equation as expressed in Equation 6.10. The heterogeneity of the system (i.e. the solid surface and liquid due to the pores of the membrane being filled with water) suggests that the no-slip boundary condition may no longer be applicable here.

The H term represents no-slip, finite-slip, and full-slip. Analytical solutions to Equation 6.10 were found and Equation 6.11 provides a general expression in which a correction factor, λ, depends on whether the system satisfies no-slip, finite-slip, or full-slip conditions.

$$\frac{dh}{dt} = \frac{1}{12\mu r}\frac{\partial}{\partial}\left(rH\frac{\partial P}{\partial r}\right) \tag{6.10}$$

$$F_H = 6\pi\mu R^2\frac{dh}{dt}\lambda \tag{6.11}$$

6.2.3 Force Measurements of the 'Closed Pore' System

Control experiments were conducted on flat alumina with no pores. The no-slip boundary condition was applied here and the solution is shown as the red curve in Figure 6.8. The main plot shows the force against separation as the cantilever approaches the surface. The inset plot represents the same for the retraction of the cantilever. The no-slip closed pore model fits experimental data for the approach of the cantilever very accurately, though there are some deviations on retraction, especially around the force minimum. This may be caused by unknown surface features, such as localised surface roughness, which the particle may have interacted with.

An example of the experimental force curves in the case of 'closed' pores (PAAs) is shown in Figure 6.9. This is for a PAA with D_P = 48 ± 5 nm. To reiterate, in these systems the pores are closed at one end so that water fills the pores but cannot pass through them (see Figure 6.3d). A comparison of the no-slip, slip, and full-slip models has also been shown. The experimental results lie between the no-slip and full-slip models, suggesting that a model with a finite-slip length will match the experimental data. The blue curve represents the model result using a slip length of 80 nm and this closely matches the experimental data of both approach and retraction. However, as the alumina membrane consists of pores filled with liquid it is likely that the calculated slip length results from the no-slip boundary condition no longer applying due to the heterogeneous surface (i.e. the solid particle interacting with a solid and a liquid surface). In order to investigate

this, calculated slip lengths were plotted as a function of pore diameter to observe any correlation.

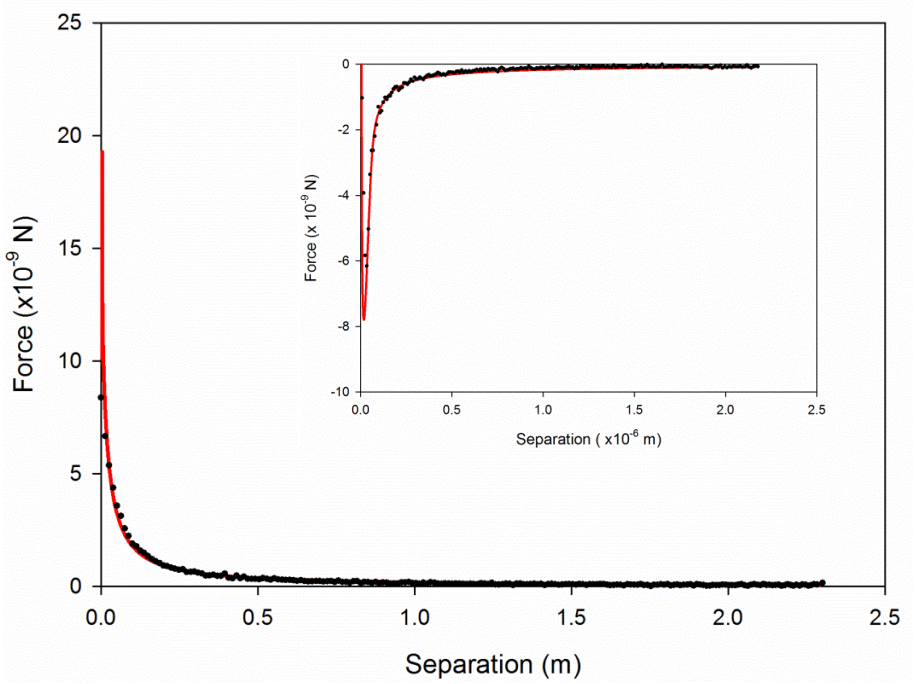

Figure 6.8 Force as a function of surface separation for the control experiment on a flat non-porous alumina surface (●) experimental data and (—) the model. Inset: force curve on retraction.

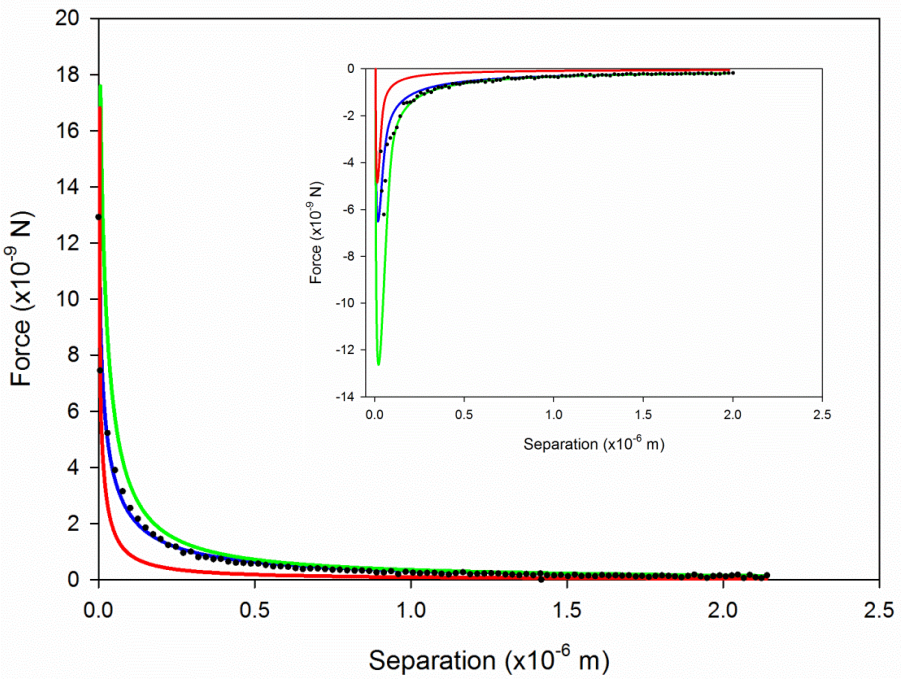

Figure 6.9 Force as a function of separation for a closed pore system of NPAM with D_P ~ 48 nm (●) experimental, (—) model for slip, (—) no-slip, and (—) full-slip. Inset force curve on retraction.

The incorporation of a slip length into the developed model provides a simple but appropriate way to summarise the variations of the measured hydrodynamic force for membranes with different surface structures. Clearly an *ab inito* prediction of hydrodynamic flow conditions under the differing surface morphologies of the membranes used is a challenging task. The goal is to seek simple relationships between membrane morphology and flow conditions.

This relationship is highlighted in Figure 6.10a where large pore diameters have corresponding larger slip lengths. There is, however, some variability in the model slip length and the range of acceptable lengths used in the model to approximate different NPAMs. In part, this is due to uncertainties in the pore diameter, and the error bars in Figure 6.10a show the diameter and slip length values that lie within the acceptable error tolerances. There appears to be an acceptable linear correlation between the slip length and pore diameter, with the line passing through the origin that corresponds to the no-slip boundary condition. This is expected to hold for NPAMs without pores (Figure 6.8). However the pore diameter is considerably smaller than the slip lengths used in the modelling and this disparity in length scales suggests that there may be unknown factors contributing to the slip-like behaviour. Nonetheless an *ab initio* derivation of this system will be extremely difficult and using the slip model provides a reasonably accurate description of the system. From this analysis it does appear that the porous surface has an effect on fluid flow at the surface. It might be thought that porosity would therefore also have an effect on fluid flow at the surface. However, as discussed in Chapter 4 Section 4.1.3, porosity does not depend on anodization voltage (as with the other structural parameters) and is quasi-constant. No correlation was therefore observed between the modelled slip lengths and the porosities of membranes with varying pore diameter.

It is of interest to compare the slip lengths calculated here to those results discussed in Section 6.1, which solely considered slip within NPAM channels (presented as flow enhancement in Section 6.1). The slip length values shown in Figure 6.10b were calculated using Equation 2.11, which was discussed in Chapter 2. The calculated slip length values in Figure 6.10b are much smaller than those shown in Figure 6.10a, and display a different trend. This is further evidence

that the findings of fluid flow behaviour in the case of the AFM force measurements is mainly due to the fluid behaviour between the solid particle and surface, especially as the data in Figure 6.10a is for the closed pore system and the slip lengths presented in Figure 6.10b are for the fluid flow measurements presented in Section 6.1.

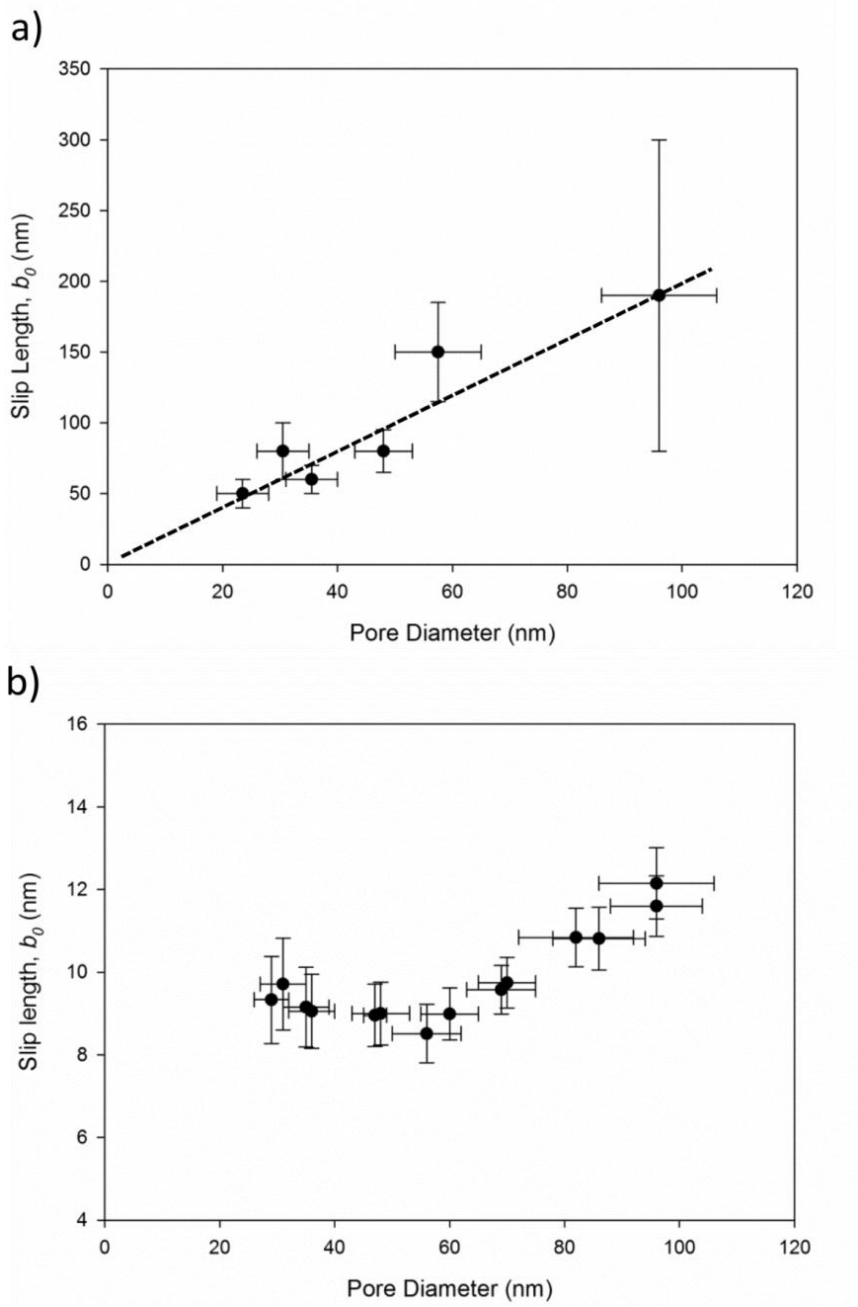

Figure 6.10 Plot of slip length against pore diameter for a) NPAMs fabricated at different anodization voltages b) for the equivalent flow enhancement factors presented in Section 6.1. Error: standard deviation of at least three repeats.

6.2.4 Force Measurements of the Open Pore System

For the open pore system, the possibility of drainage through the channels had to be accounted for. Figure 6.11 therefore presents a comparison of the no-slip and full-slip perturbation solution for open pores with the corresponding no-slip and full-slip closed pore solution (Equation 6.11). The difference between the open pore perturbation solution and the 'closed' pore solution is negligible, the only observable difference being the slight deviation around the force minimum. This deviation is likely to be caused by drainage through the pores. Since the deviation for the perturbation solution for the no-slip and full-slip models differ little compared to the closed model, the closed finite-slip solution (Equation 6.11) can be used in the case of open pores.

Figure 6.12 shows the breakdown of the different pressures acting at the centre of the AFM particle. The total pressure reaches approximately 170 kPa but most of this is due to the electric double layer. As the particle approaches the surface the velocity drops due to the increasing DLVO forces. So according to Equation 6.11 the hydrodynamic force must drop as the DLVO forces rise. The hydrodynamic pressure is of the order of approximately 10 to 20 kPa and may not be sufficient to cause significant fluid flow through the pores. In Lee et al. (2012) the experiments were conducted at ~ 100 kPa before flow was established through the membrane, though lower pressures have also been observed (see Chapter 7). Whilst it is possible that flow was established through the open pores, the small generated hydrodynamic pressure suggests that flow through the channels was not a large contributor to the experimental results.

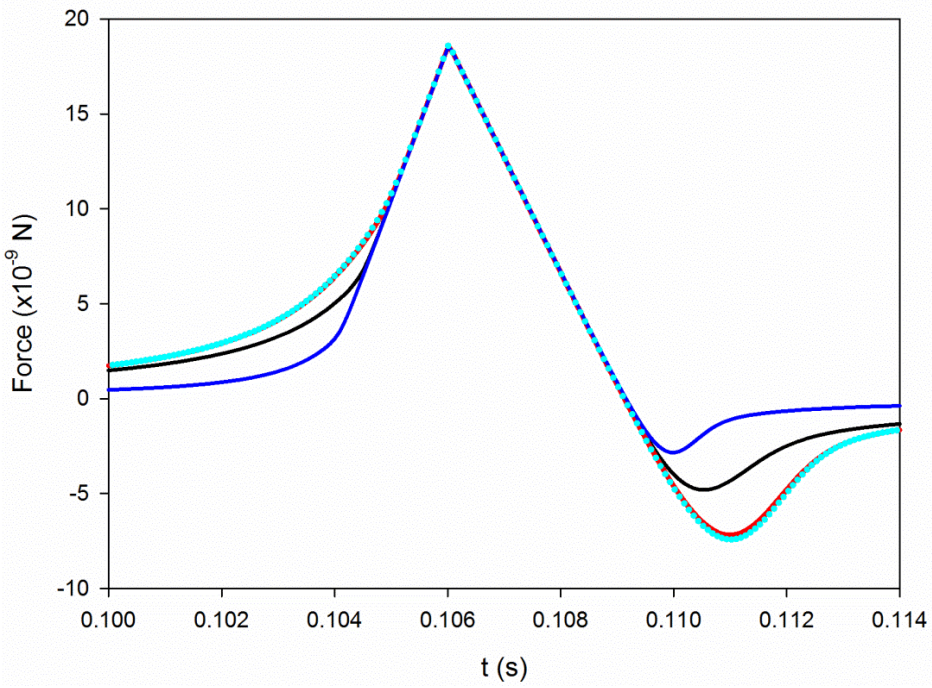

Figure 6.11 Force as a function of time for an open pore system of NPAM with D_P ~ 32 nm, experimental and models overlap (●) closed-pore no-slip, (—) no-slip with drainage, (—) finite slip, and (—) full-slip with drainage.

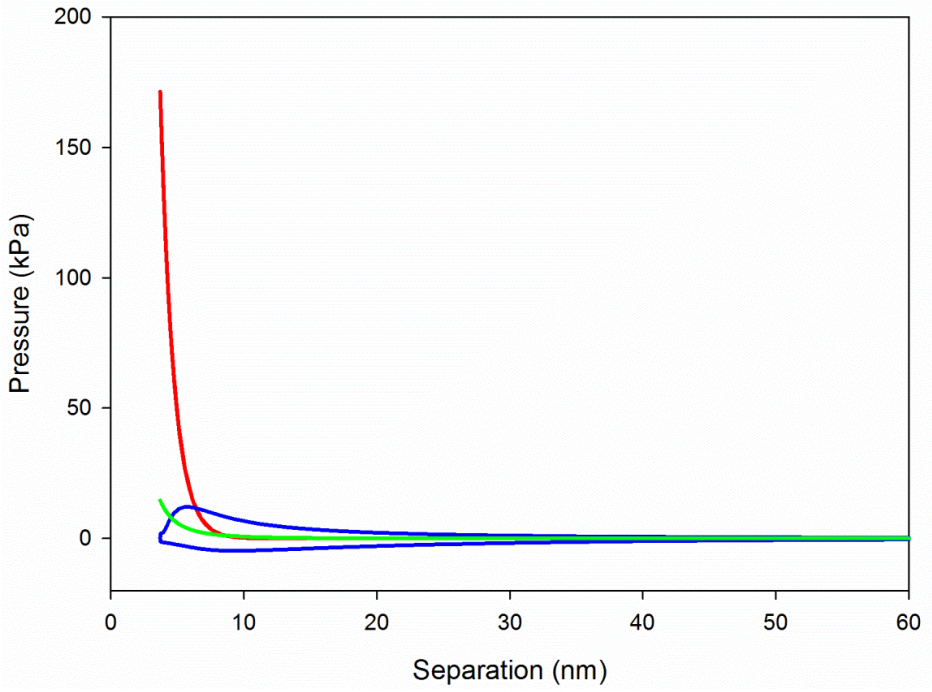

Figure 6.12 Breakdown of the pressures exerted by the particle on the surface with separation (—) hydrodynamic pressure, (—) electric double layer, and (—) van der Waals.

The experimental results for open pores can be separated into two groups. Figure 6.13 shows experimental results for open pore systems which resemble that of the

closed pores. The experimental results lie between the no-slip and full-slip perturbation models. Again this suggests that some form of slip length can be used in the modelling. In this case a closed pore slip model with slip length of 20 nm was used. This model fitted the experiment better than the perturbation solution but does not account for the force minimum on retraction (similar to Figure 6.6). This could have been caused by adhesion of the particle to the surface, itself caused by local roughness on the surface. This, however, is speculative.

The second group (which consisted NPAMs of large pore diameters) of experimental data for the open pore system is shown in Figure 6.14. Here the experimental results lie below both the no-slip and full-slip perturbation solutions. Unlike the force curves discussed above, the results presented in Figure 6.14 remain flat until the particle is very close to the surface. At this point the force curves spike before the particle retracts. The overall flatness of the force curves suggests that no film is forming between the surfaces (the stationary solid and the particle), as the rise observed in previous force curves was caused by the hydrodynamic force. This could be due to fluid escaping the interaction region between the particle and the surface via the open channels of the membrane. This is presented with caution however because, given the small hydrodynamic pressure generated (as seen in Figure 6.12), it is unlikely that drainage through the pores is the major contributor to the observed results.

An alternative explanation is that the open pore membranes are rough. Roughness would prevent the particle from making full contact with the surface, thus presenting the particle with a smaller interaction region. As the particle is non-deformable, it could also have been that its interaction region was too small to allow film formation. This could be explained by the etching procedure used to open the pores, which may have increased the surface roughness of the membrane surface. It is suspected that surface roughness is proportional to anodization voltage. Interestingly, the no-film formation occurs only for open pore membranes and for NPAMs produced at anodization voltages greater than 40V. It is concluded that this is the result of two factors: (i) drainage through the pore channels due to the large pore diameters, and (ii) the surface roughness. Indeed, the latter may be the overriding determinant of the force curves in Figure 6.14.

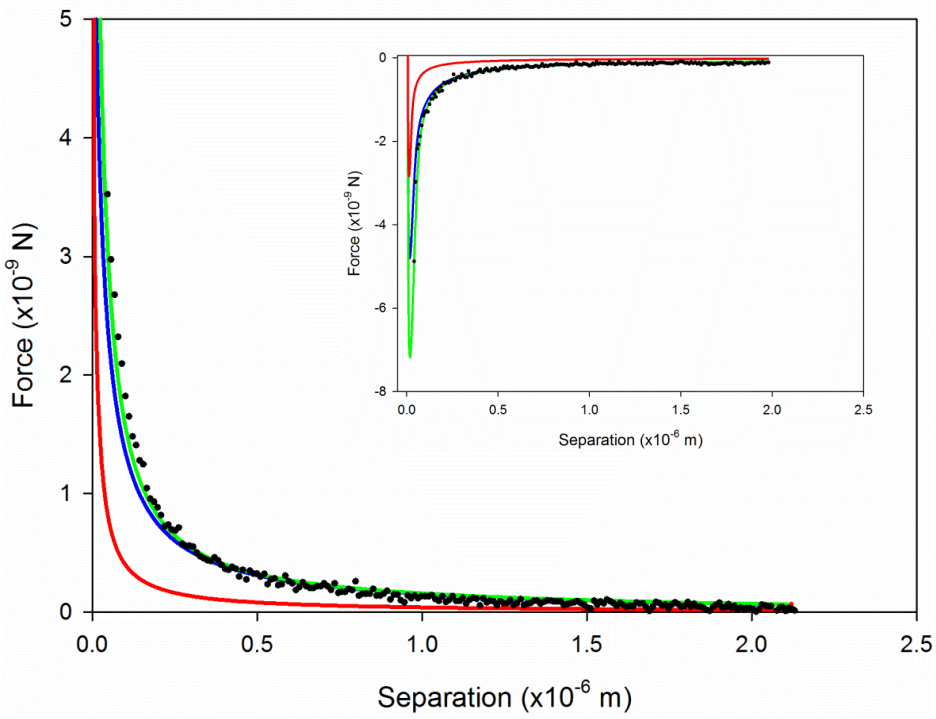

Figure 6.13 Force as a function of separation for an open system of NPAM with D_P ~ 32 nm (●) experimental, (—) model for slip, (—) no-slip, and (—) full-slip. Inset force curve on retraction.

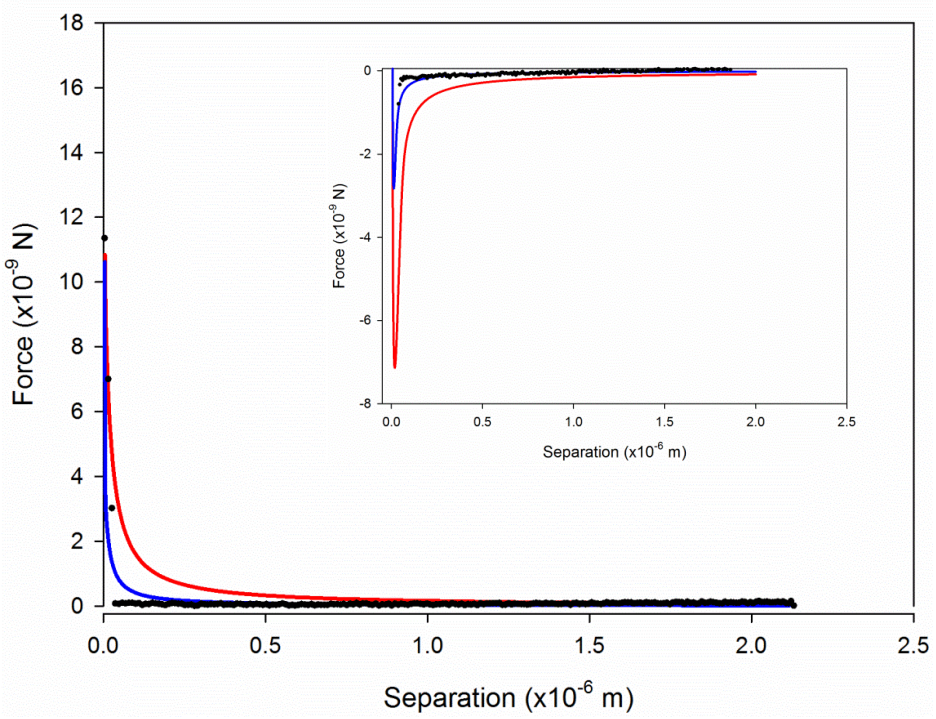

Figure 6.14 Force as a function of separation for an open system of NPAM with D_P ~ 52 nm (●) experimental, (—) full-slip perturbation, (—) no-slip perturbation. Inset force curve on retraction.

6.3 Summary

This chapter has considered the behaviour of fluid through and around nanoporous alumina. The first section introduced the topic through recent work completed by Lee et al. which observed enhanced flow rates through nanoporous alumina membranes. This led into the main section of the chapter which presented experimental findings with AFM regarding fluid flow between two solid surfaces (the solid particle and the membrane surface) and drainage through nanoporous alumina (both closed and open pore NPAM systems). Collaboration with the University of Melbourne enabled modelling of the experimental results. The theoretical model incorporated hydrodynamic effects, DLVO forces (electric double layer and van der Waals), and cantilever drag. As drainage effects were considered to be small compared to finite-slip, the open pore system was modelled with the finite-slip model for closed pores (Equation 6.11).

The fluid flow enhancement discussed in Section 6.1 was measured through pressure-driven experiments on NPAMs. Slip lengths were calculated to be between 8 and 13 nm. These values are smaller than the slip lengths calculated from the AFM force measurements discussed in Section 6.2. This is due to the fact that the latter incorporated a ‘slip’ on the surface as well as within the cylindrical channels. The no-slip boundary condition is no longer applicable here, however, as the surface is not wholly solid but a mixture of fluid and alumina. By assuming slip, it is possible to correlate the theoretical model with experimental results. The slip lengths were found to be proportional to NPAM pore diameter and the no-slip boundary condition is expected to hold for a completely flat, featureless surface. In the absence of an *ab initio* model to quantify the hydrodynamic complexities of such porous membranes, the slip model provides the most suitable way to summarise the main hydrodynamic characteristics.

Chapter 7

Electroosmosis in Nanoporous Alumina Membranes

Capitalising on the versatility of nanoporous alumina for controlled and systematic investigations at the nanoscale, this chapter presents a study of electroosmosis (EO) in nanoporous alumina membranes. Electroosmosis at the nanoscale was introduced in Chapter 2 Section 2.3, where an understanding of wetting properties, flow properties, and surface chemistry, were seen to be crucial. This was supported by findings presented in the previous chapters. Much of this work in the present chapter has been submitted for publication in the journal *Microfluidics and Nanofluidics*.

7.1 Introduction

This chapter discusses electroosmotic pumping with a sodium tetraborate buffer in nanoporous alumina membranes (NPAMs) with inner pore diameters from ~ 8 to 100 nm. The first section presents findings regarding the effect of pore diameter on EO pumping, in which the applied voltage and buffer concentrations were kept constant. For the smallest pore diameters (~ 8 to 25 nm) electroosmotic flow (EOF) was up to five times that of the pressure-driven flow. Contrary to theoretical predictions, electroosmotic pumping was still observed when the electric double layer overlapped (although the magnitude dropped). The second part of the chapter discusses the lifetime of EO pumps and the limitations of EO pumping for long periods of time. This research has developed EO pumps with lifetimes of up to 2 hours, one of the longest continuous EO pumps reported to date. This was also reproducible, as the EOF was regenerated from one run to another (therefore the same NPAM-EO pump worked for 4 hours in total after regeneration). In some cases, however, a severe reduction in flow rate was observed, and the cause of this, concentration polarization (CP), has also been discussed in detail. A simple model has been developed to characterise the thickness of the δ_{cp} layer. The final sections highlight the effect of electrolyte concentration and applied voltages on NPAM EOFs. In line with other reports, the

applied voltage was significantly different from the effective voltage, and this will also be discussed later. It should be noted here that, as the efficiency of EO pumps relies on the effective voltage being similar to that of the applied voltage, EO pumps have only achieved efficiencies of between 0.05 and 5.8% (Yao et al. 2003; Reichmuth et al. 2003).

Several studies have addressed the effect of electric double layer (EDL) overlap on electroosmosis at the nanoscale, the majority of which have been theoretical. One study assessed the effect of EDL overlap on EO in packed-capillary columns and found that EO decreased with higher porosity, particle diameter (in the packed columns), and electrolyte concentration (Wan 1997). A more recent study developed a model to accurately predict electro-kinetic phenomena at the nanoscale, especially for EDL overlap (Huang and Yang 2007). In this case, concentration variations were used to investigate EDL overlap and a parabolic profile was predicted when the EDLs overlapped. The majority of theoretical and numerical investigations have predicted that as EDLs approach each other and overlap, the entire channel becomes charged and the expected 'plug-like' velocity profile reduces to that of a parabolic profile (Bruus 2007; Rice and Whitehead 1965). Furthermore, one study simulated EO in 6.5 nm diameter channels and found that ions in the stern layer were not fixed to the walls and that viscosity increased by a factor of 6 in the nanometre closest to the wall (Freund 2002). Simulations of EO in nanotubes with high surface charge densities found that both the thickness of the EDL and the peak height of the counter-ion density increased with surface charge density (Chen et al. 2008b). This is supported by previous AFM findings (Besteman et al. 2004).

A recent experimental study produced a carbon nanotube (CNT) membrane with diameters of 1.5 and 7 nm and found that, when CNTs are functionalized, EOFs with much greater efficiency could be obtained (Wu et al. 2011). It is likely that the EDLs were overlapped in this study as the concentrations of buffer would produce Debye lengths of ~ 5 - 10 nm. It should be noted that efficiency in this publication is referred to as a ratio of the transport of neutral caffeine molecules compared to the transport of ions in comparative studies (the power consumption is expressed as power per nanomole). To see improved efficiencies is encouraging, since it presents the possibility of translating these pumps into

applied processes. In the present research, the thermodynamic efficiency, η, is defined as the useful work applied to the EO pump over the total power consumption:

$$\eta = \frac{\Delta PQ}{V_{app} I} \tag{7.1}$$

where I is the current of the system. The efficiency of EO pumps will be analysed in further detail below.

7.2 NPAM Characterisation and Streaming Potential Measurements

Streaming potential measurements were carried out in the electroosmotic rig shown in Section 3.6, Figure 3.11 in order to calculate zeta potential. Zeta potential, ζ, defined as the average potential in the surface of the hydrodynamic shear, can be calculated using the Helmholtz-Smoluchowski equation from experimental data:

$$\frac{dE}{d\Delta P} = \frac{\varepsilon_0 \varepsilon_r}{\mu \kappa} \zeta \tag{7.2}$$

where E is the streaming potential, ε_0 is the vacuum permittivity, ε_r the dielectric constant of the electrolyte and κ the conductivity of the liquid.

The non-zero intercepts in Figure 7.1 arise from asymmetries in the electrodes and have no subsequent effect on evaluating zeta potentials (Burns and Zydney 2000). The non-zero intercept has also been observed previously (Prakash et al. 2006; Burns and Zydney 2000). No voltage was applied across the membrane, but the transmembrane voltage was recorded using a Keithley 179 RMS Digital multimeter when a sequence of pressures was applied to the membrane. The linear relationship of transmembrane voltage and applied pressure enabled the zeta potential of the membrane to be calculated (see Chapter 2 Equation 2.15).

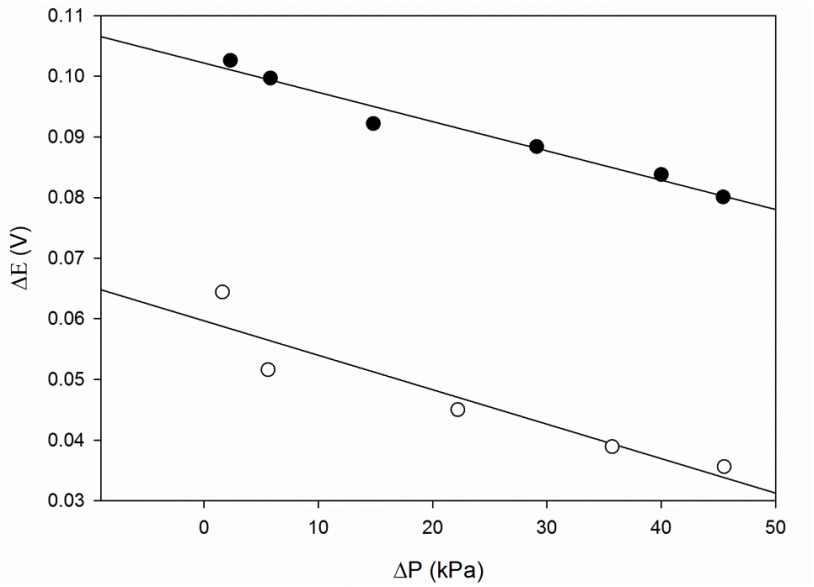

Figure 7.1 Streaming potential data for two different NPAMs (●) D_P = 67 ±7 nm and (○) D_P = 48 ±6 nm at pH 9.2 in 5 mM ionic concentration.

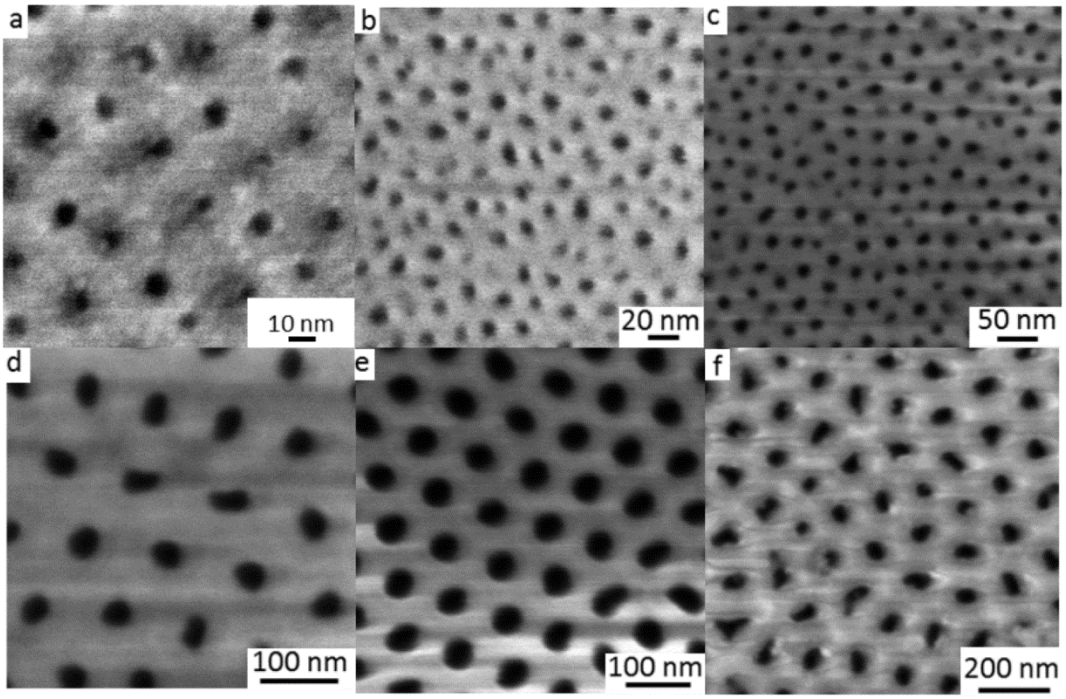

Figure 7.2 FESEM of NPAMs under different anodization conditions of a) 0.5 M H_2SO_4, V_I = 24 V, V_F = 5 V, ~ 8 nm b) 1.0 M H_2SO_4, 10 V, D_P ~ 13 nm; c) 0.5 M H_2SO_4, 20 V, D_P ~ 24nm; d) 0.3 M $C_2H_2O_4$, 30 V, D_P ~ 36 nm; e) 0.3 M $C_2H_2O_4$, 40 V, D_P ~ 52 nm; f) 0.3 M $C_2H_2O_4$, 50 V, D_P ~ 67 nm.

Electrolyte concentration and pH were constant in all measurements for zeta potential calculations. The change in zeta potential was therefore due solely to the range of pore diameters. A regular pore structure was observed in all NPAMs tested, with a narrow pore size distribution (Figure 7.2). This finding, which is consistent with previous work (Lee et al. 2012), has been reported throughout the present research and highlighted in particular in Chapter 4. Table 7-1 presents pore diameter, porosity, and thickness data of all membranes tested.

Table 7-1 Summary of Pore Diameters, Thickness and Porosities of the NPAM range tested.

Anodization Voltage (V)	Pore Diameter (nm)	Thickness (μm)[a]	Porosity, ϕ (-)
80	80±12	85	0.25
80	90±14	90	0.28
80	89±11	90	0.29
70	80±11	55	0.30
70	85±10	55	0.25
70	85±10	55	0.21
50	67±6	45	0.18
50	67±6	45	0.18
50	65±6	70	0.19
50	52±4	60	0.20
40	52±4	60	0.18
40	52±4	60	0.16
40	50±6	80	0.15
30	35±6	50	0.11
30	39±5	45	0.13
30	36±3	40	0.12
25	32±3	30	0.13
25	32±3	30	0.15
25	30±4	30	0.15
20	24±4	25	0.12
15	18±5	20	0.10
15	18±3	20	0.11
10	15±3	15	0.09
10	13±4	15	0.11
10	15±3	15	0.11
24_5[b]	9±3	20	0.09
24_5[b]	6±3	20	0.08
24_5[b]	5±3	20	0.07
24_5[b]	5±3	20	0.07
24_5[b]	8±3	20	0.09
24_5[b]	8±3	20	0.09

[a] error ± 5 μm

[b] $V_{initial}$ = 24 V and V_{final} = 5 V

Table 7-2 Zeta potentials of NPAM as a function of pore size.

Anodization Voltage (V)	Pore Diameter (nm)	Zeta Potential (mV)
15	18±5	-16±1
20	24±4	-19±1
30	38±6	-10±1
40	48±6	-17±1
50	67±7	-33±1

Metal oxides such as alumina are amphoteric (capable of gaining or losing protons). Their surface charge therefore changes when exposed to acidic or basic conditions (Hunter 1981):

$H^+ + —Al—OH \rightarrow —Al—OH^{2+}$

$—Al—OH \rightarrow Al—O^- + H^+$

The isoelectric point of alumina has been reported to be between pH ~ 8 (Chen et al. 2008; Tang et al. 2004) and pH 9.1 (Hunter 1981). In this study the alumina was therefore negatively charged in the more basic solution of the borate buffer (pH ~ 9.2). The counter ions (i.e. the Na^+) of the borate buffer were attracted to the pore wall of the alumina building up the EDL. When an electrical potential was applied across the membrane the excess (diffuse) counter-ions in the EDL moved towards the counter-electrode, dragging the bulk of the liquid and resulting in a net (plug-like) flow (Bruus 2007).

Streaming potential measurements were performed on NPAMs with different pore diameters in order to calculate the zeta potential according to Equation 2.15 in Chapter 2. An example of the streaming potential measurements for two NPAMs with different pore diameters has been shown in Figure 7.1. Results show that zeta potential varies with pore diameter (Table 7-2). While a clear trend is not obvious, there is an overall reduction in zeta potential with decreasing pore diameter, approaching the thickness of the EDL. This is consistent with previous findings (Prakash et al. 2006).

7.3 Electroosmotic Flow Rates and Pore Diameter

Flow measurements for all membranes tested under an external pressure gradient show a decrease with decreasing pore diameters, in line with previous results (Lee et al. 2012) (also see inset of Figure 7.3). When an external electric field was applied perpendicular to the membrane, EOF was superimposed onto the pressure-driven flow (Equation 7.3), resulting in an overall higher flow rate. This equation, which was introduced in Chapter 2 Section 2.3.3, combines pressure-driven and electroosmotic flow (Rice and Whitehead 1965).

$$Q_T = \frac{\phi}{\tau} A_{eff} \left(\frac{\pi D_P^2}{32 \mu L} \Delta P + \frac{\varepsilon \zeta}{\mu L} \Delta V_{eff} \right) \tag{7.3}$$

The contribution of EOF to total flow rate became more significant for the smallest pore diameters, as discussed below. The measurements in Figure 7.3 present all points of the tested membranes, with measurements normalized to the same applied pressure (20 kPa), the same applied voltage (10 V), and the same concentration of electrolyte (5 mM sodium tetraborate). Minimum pressure gradients were exerted across the NPAMs (18 - 50 kPa) in order to overcome the pressure necessary to wet all pores of the membranes. This allowed full analysis of pressure-driven flows as well as a full assessment of the effect of EO. The cumulative error was 5% for flow measurements for each data point (y-axis). Contributions to this include applied voltage, pressure gauge error, and the standard deviation of repeat runs. This 5% does not include the pore diameter errors which have been reported in Table 7-1. As discussed in Chapter 3 Section 3.6, experiments were carried out for at least 20 minutes and to a maximum of 2 hours. In several cases, there was clear evidence of a severe reduction in EO flow rate after approximately 20 - 40 minutes.

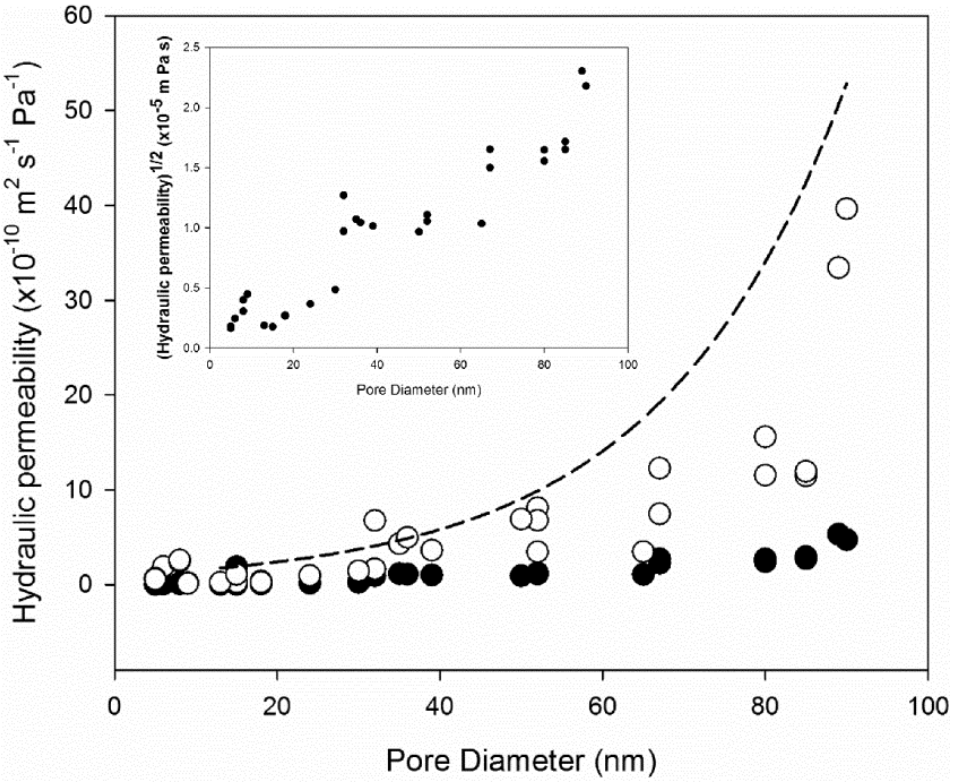

Figure 7.3 Effect on hydraulic permeability with increasing pore diameter (●) for pressure-driven flow only and (○) when V_{app} = 10 V was superimposed to the pressure driven flow (conditions of electrolyte concentration and applied voltage are the same for all points; the data has been normalized for effective area, thickness of the membrane and pressure). Dashed line: theoretical Q_T (calculated from Equation 7.3) Inset: square root of permeability with pore diameter.

A dramatic increase in flow was apparent during experiments when the EO-driven flow was imposed on pressure-driven flow, especially for the smallest pores tested (~ 8 to 25 nm). As the membranes have different thicknesses as well as pore diameters, flow rate data points were normalized by the applied pressure in order to directly compare results between different membranes. This resulted in a clear trend in which the ratio $Q_{eo}/Q_{\Delta P}$ (Q_{eo}, electroosmotic flow rate and $Q_{\Delta P}$ pressure-driven flow rate) was found to be a function of pore diameter (Figure 7.4). The dashed black line in Figure 7.4 represents the EDL overlap ($2\lambda_D$ ~ 9 nm) for a 5 mM borate buffer which was used for all NPAMs tested. These findings suggest that, in this experimental scenario, EO occurs when EDLs overlap (black points to the left of the dashed line in Figure 7.4). The value for Debye length was calculated using Equation 2.14 in Chapter 2. The smallest pore diameter achievable was between 7 and 9 nm and this was in the region of EDL overlap (see black dashed line Figure 7.4). EOF was measurable even for the smallest

pore diameters tested and although the overall flow rate decreased with decreasing pore diameter, pressure-driven flow decreased much more rapidly, leading to the behaviour in Figure 7.4. Attempts at using a lower borate buffer concentration to obtain a larger Debye length were frustrated by a severe reduction in EOF rate due to concentration polarization and electrolysis. It was for this reason that the NPAM produced via anodization ramping was utilised (Lee and Mattia 2013). There is a trade-off between obtaining stable and accurate EOF and lowering the ionic concentration of the electrolyte in order to increase the thickness of the EDL. The anodization procedure here was therefore manipulated to produce NPAMs with pore diameters < 10 nm.

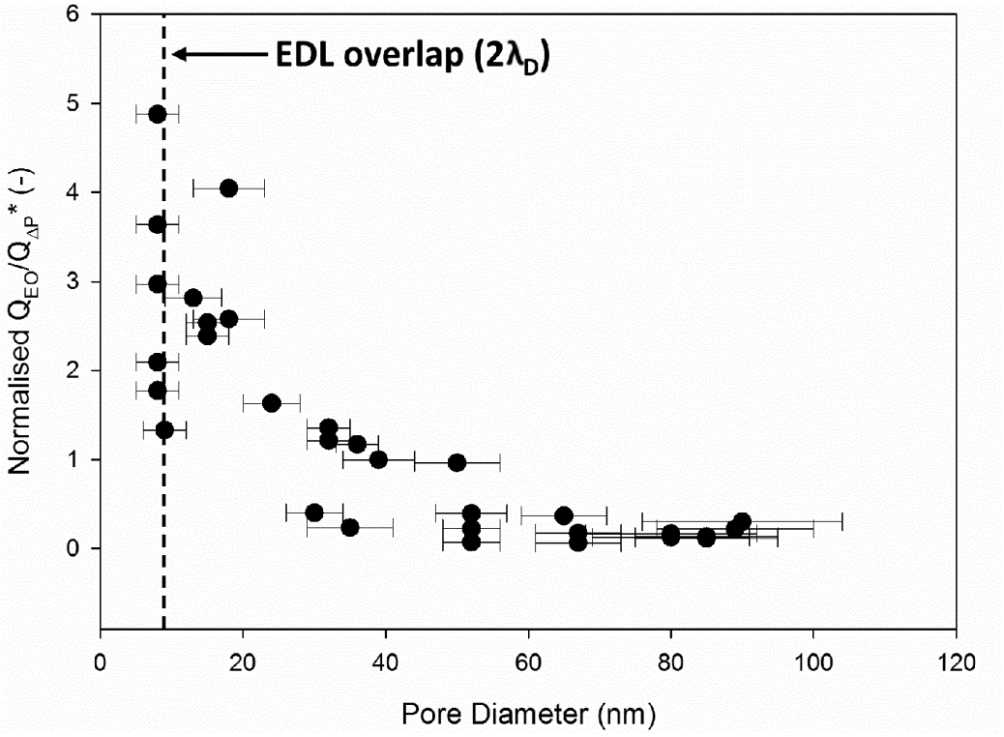

Figure 7.4 Factor of increase in flow ($Q_{EO}/Q_{\Delta P}$) with pore diameter; the dashed line indicates Debye layer (EDL) overlap. Error: SD from image analysis of SEM micrographs.

EOF results for the smallest pores in the EDL overlap region (Figure 7.4) are contrary to theoretical and previous experimental findings. A recent experimental investigation on EOF-induced ion-rectification in conical nanopores (similar to the asymmetric NPAMs fabricated to obtain the smallest pore diameters) observed a larger than expected rectification factor for pores approaching the dimensions of the EDL (Yusko et al. 2010). However, unlike our results, a breakdown of EOF induced ion-rectification was observed for almost complete EDL overlap.

In the case of asymmetric NPAMs, the smallest pore diameters faced the bulk fluid movement which determined flow rate. The asymmetry of the system has therefore been discussed to understand why EOF was still detected in the region of EDL overlap. It has previously been proposed that an asymmetric distribution of ions form along the length of the pore cylinder, resulting in reduced or enhanced permeability of conducting ions through the pores depending on the direction of the electric field (Cervera et al. 2007). In the present study, the NPAM is negatively charged. Therefore an increased conductance is observed when (i) the narrow opening faces the anode (which in this case it does) and (ii) the net flow of cations (the counter-ions, Na^+) are directed to the side of the membrane with larger pore diameters (in the direction of flow away from the anode). This has been discussed in recent work (Yusko et al. 2010) and supports our analysis that an increase in pore conductance due to the asymmetry of charge caused by asymmetrical pore channels enhances the permeability of ions through the membrane. Contrary to Yusko et al. (2010) the present research still observed EOF at the scale where EDL overlap should occur (pore diameter ~ 8 nm).

7.4 Effect of Concentration Polarization

In order to assess the degree of CP a ratio known as the Dukhin number was first utilised. This is the ratio of surface to bulk conductivity (Zangle et al. 2009; Strickland et al. 2010). For binary electrolytes and NPAMs this can be expressed as:

$$Du = \frac{z_1 v_1 (s/l)}{F c_0 (z_1^2 v_1 + z_2^2 v_2)} \tag{7.4}$$

where surface charge density, *s*, was assumed to be spatially uniform, parameter *l* is the ratio of total electrolyte volume in the NPAM to pore surface area, c_0 is bulk concentration, *v* is ionic mobility, *z* is ionic charge, and *F* is Faraday's constant. Subscripts represent the counter-ion (Na^+) and co-ion (borate) respectively. Surface charge density and ionic mobility were derived from literature (Hernandez et al. 1995; Corti et al. 1980). When the Dukhin number > 1,

CP effects become noticeable. The Dukhin number is > 1 for all membrane pore diameters examined (Figure 7.5). As such, CP effects cannot be ignored.

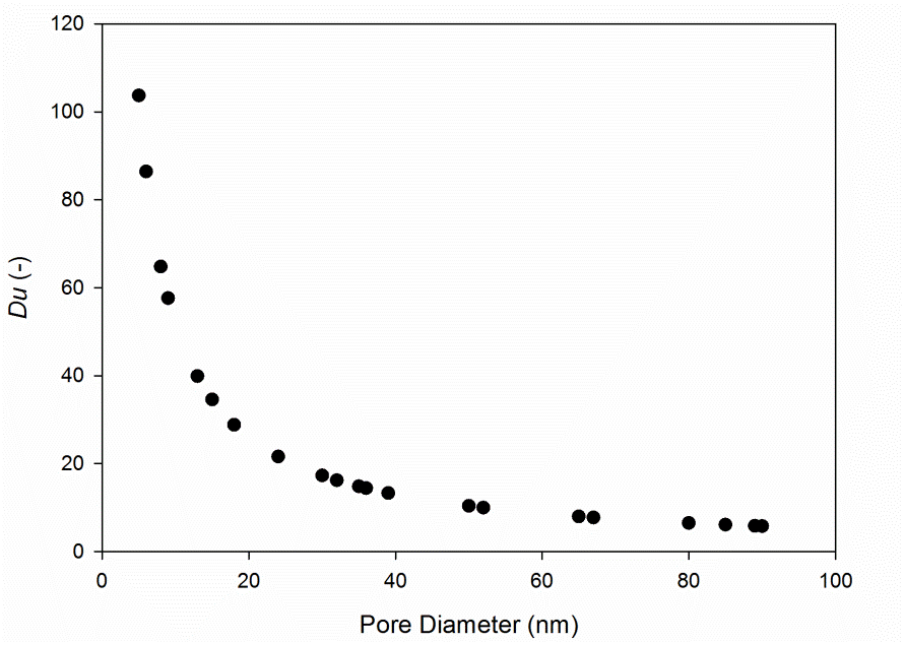

Figure 7.5 Dukhin ratio with pore diameter indicates concentration polarization propagating within the system. Dukhin numbers > 1 indicate that CP propagates current shocks.

Several recent studies have examined reduction in flow rates using the same buffer solution as the present study (Strickland et al. 2010; Suss et al. 2011). By using a fluorescein solution, these studies observed ionic build-up (concentration polarization) at both the membrane surface and the electrodes. This proved that local concentration changes were caused by ion depletion zones within the system (Suss et al. 2011; Strickland et al. 2010; Pu et al. 2004). Most successful EO pumps at this scale have used borate buffer (as in the present study) since this has given the most stable EOF. The buffer capacity of borate is large enough to neutralize the effect of the hydronium ions released into the electrolyte from reactions at the electrodes caused by the inert Pt electrodes. This is shown in the following reaction schemes:

Anode: $2H_2O \rightarrow 4H^+ + 4e^- + O_2$,

Cathode: $2H^+ + 2e^- \rightarrow H_2$

The buffer capacity aims to limit the fluctuating pH values from electrolysis at the platinum electrodes. However, current shocks were also observed due to the buffer capacity (Suss et al. 2011; Mani et al. 2009). Indeed, shocks were observed in all EO experiments, accounting for some of the instabilities observed in flow (for example the slight deviations from steady state shown in Figure 7.6). Figure 7.6a presents a comparison of a steady state pressure-driven flow and stable pressure-EO-driven flow over time for a 67 nm pore diameter membrane and 5 mM ionic concentration with V_{app} = 10 V. With these conditions EO was stable for up to 2 hours. Figure 7.6b is an example of the reduction in flow rate observed after less than 20 minutes of EO pumping for a 36 nm pore diameter membrane and 5 mM ionic concentration with V_{app} = 10 V. The reason for this reduction has been attributed to CP, which is discussed in greater detail below.

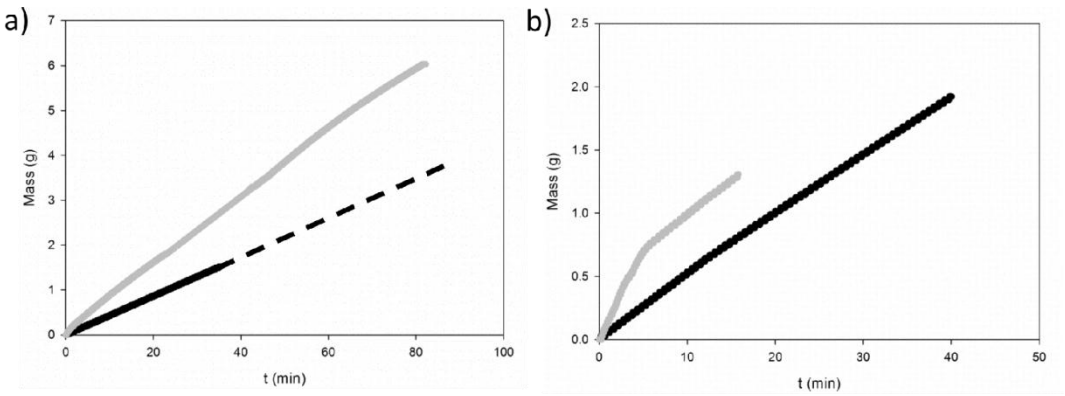

Figure 7.6 Mass versus time plots for two NPAMs (●) when no voltage is applied (i.e. pressure-driven flow only) and (●, gray line) when V_{app} = 10 V is superimposed onto the pressure-driven flow: a) shows a steady EO pump for almost 2 hours with a 67 nm average pore diameter NPAM b) shows a short-lived EO pump for a 36 nm average pore diameter NPAM where the flow rate gradient reduces to the ΔP gradient after a matter of minutes (conditions of electrolyte concentration and applied voltage are the same in both cases).

The high initial current induces a large increase in flow rate (see Figure 7.7a) which decreases over time, something also observed by Suss et al. (2011). In this case, however, it was observed throughout the nanochannels. Sharp spikes in current were observed in the first and following runs for regenerated EOF as shown in Figure 7.7b. This supports the findings of Mani et al. (2009) and Suss et al. (2011), who predicted and experimentally observed current shocks due to CP (in micro-nano-micro-channels) as well as the recombination of ion enriched and ion depleted zones.

A simple model is proposed here to quantify the extent of concentration polarization over time. Experimental data shows that V_{eff} is constant during the experiment. $V_{eff} = V_{app} - V_{dec} - 2R_dI$ (as discussed in Chapter 2 Section 2.3.4.2) can therefore be generalised as follows:

$$V_{eff} = (\Delta V_{app} - \Delta V_{dec}) - R_{tot}I \tag{7.5}$$

where $R_{tot} = R_{cp} + 2R_d$ is the total resistance of the EO process and R_{cp} is the resistance arising from concentration polarization. By substituting $V_{eff} = V_{app} - V_{dec} - 2R_dI$ into Equation 7.3, the time dependence of R_{tot} can be obtained from experimental data. The total resistance increases with time, with the sudden current shocks leading to a decrease in R_{tot}, (Figure 7.7b) the resistance then restores until the next current shock (which have comparable slopes). The sharp spikes in current were observed in the first and repeated runs of the regenerated EOF. Although R_d cannot be measured directly, its value can be estimated by the value of R_{tot} at the start of the EO experiment. This yields $R_d \sim 70\ \Omega$. As no weakening or thinning of the membrane was observed after more than 2 hours of operation, R_d was assumed to be constant during the experimental time. The resistance given by the concentration polarization can then be calculated and, from this, the propagation of the CP enrichment layer can be estimated as $\delta_{cp} = \kappa A R_{cp}$, where δ_{cp} is the concentration polarization layer thickness, κ the conductivity of the electrolyte and A the area of the membrane. The membrane area coincides with the cross-section of the sample holder zone closest to the membrane. This section is approximately 1.6 cm long, ensuring that A can be considered constant. Although the electrical conductivity in the concentration polarization domain will vary due to local changes in the electrolyte concentration, the large reservoir volume (60 ml, see Chapter 3 Figure 3.11) will eventually account for any localized change. In the first approximation, therefore, the electrical conductivity can be considered constant, yielding a total peak thickness of the CP layer equal to 0.7 mm (see Figure 7.8), with a propagation velocity of ~ 0.09 μm s^{-1}. These values are comparable to those obtained for a rectangular cross-sectional channel (Suss et al. 2011). An exact variation of the electrical conductivity as a function of local electrolyte concentration cannot be

estimated using well-known models such as the Debye-Hückel or Onsager-Fuoss, due to the high concentration of the starting electrolyte (Wright 1988). Unfortunately no local measure of the electrolyte concentration near the membrane surface was possible in this study (see Chapter 9 Section 9.2.3).

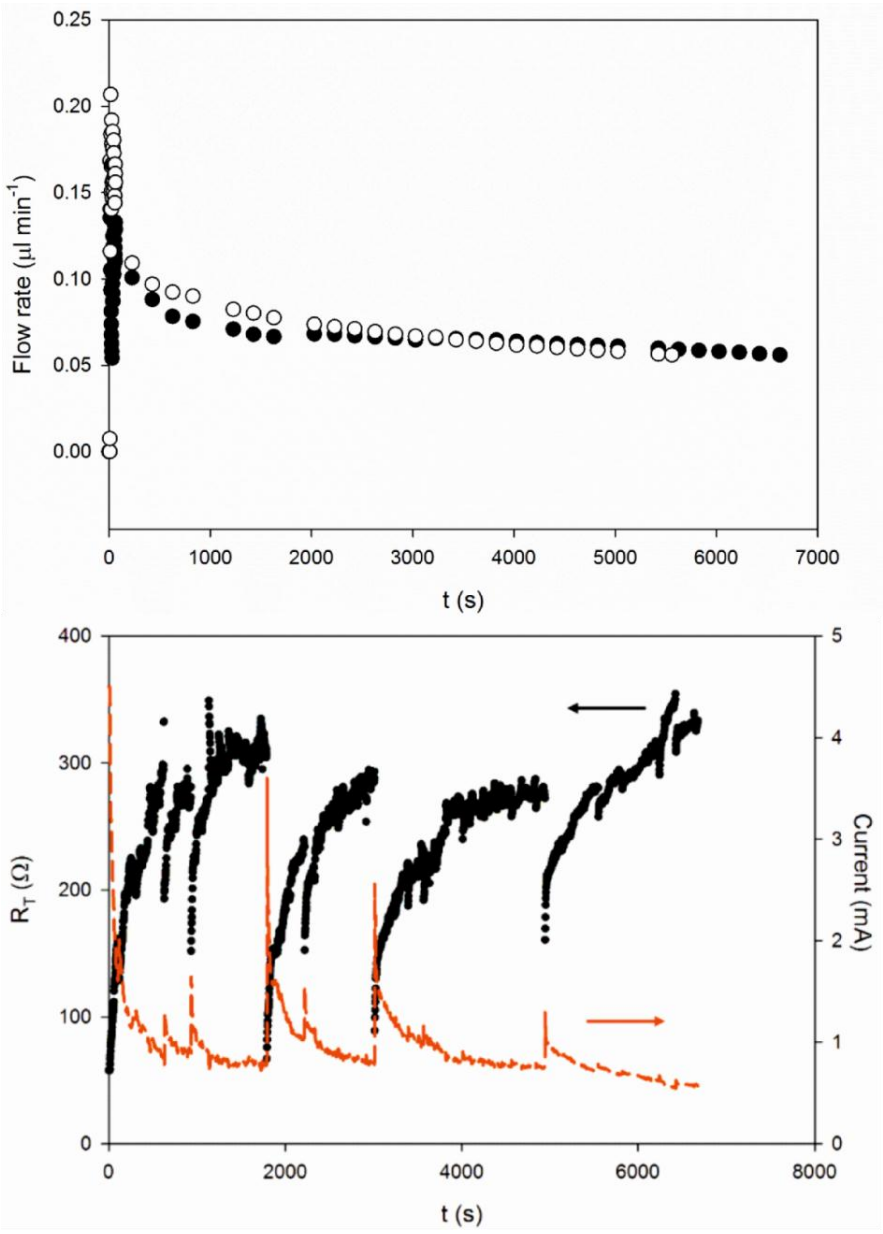

Figure 7.7 a) Flow rate with time (●): A sharp initial increase followed by a steady decrease in flow rate from a fresh run, and (○) a repeated second run. The flow rate with time is similar to that of the first run indicating EOF was regenerated (data recorded every 2 s therefore some data points have been removed). Inset: initial surge in flow rate zoomed in and b) is the R_T vs. time (●) and current vs. time plot (—, red line) represents total resistance of the system over time and the current shocks (the steep peaks) which are visible throughout.

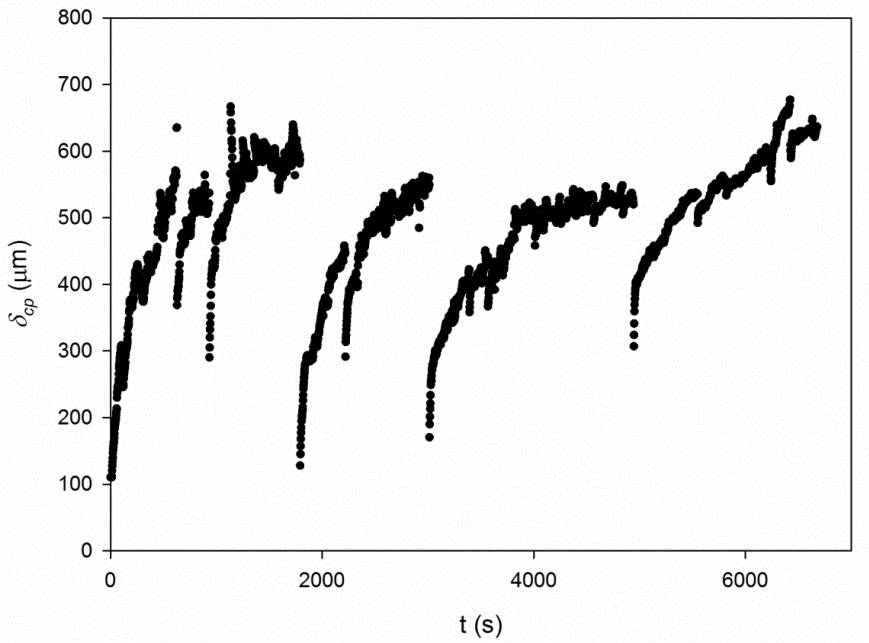

Figure 7.8 Thickness of concentration polarization layer over time.

In order to further establish and overcome the concentration polarization effect (and therefore successfully regenerate EOF), further experiments were undertaken. Instead of reversing the electrodes to change the direction of EOF (thereby dislodging ion build-up at the membrane surface) the membrane holder was physically turned around and pressure-driven flow applied to the 'fresh' side of the membrane. It was expected that this would dislodge the bulk of ions which had built up on the surface of the membrane and redistribute the ions within the buffer solution. After this process the membrane holder was turned back to the original position to repeat the EO measurement. It can be clearly seen in Figure 7.9 that with this procedure the EOF was able to recover its original flow rate, though the lifetime of the EO pump was reduced slightly. It should be noted here that the EO pump lasted for 2 hours; a considerable improvement on EO pump lifetimes achieved in previous studies (and 4 hours if second run is included). Similar results have been obtained for membranes of all pore diameters, including the smallest pore diameters tested. This indicates that the reduction in flow rate was caused by concentration polarization at the membrane surface and that this can be overcome by sweeping the accumulated ion layer away from the membrane surface.

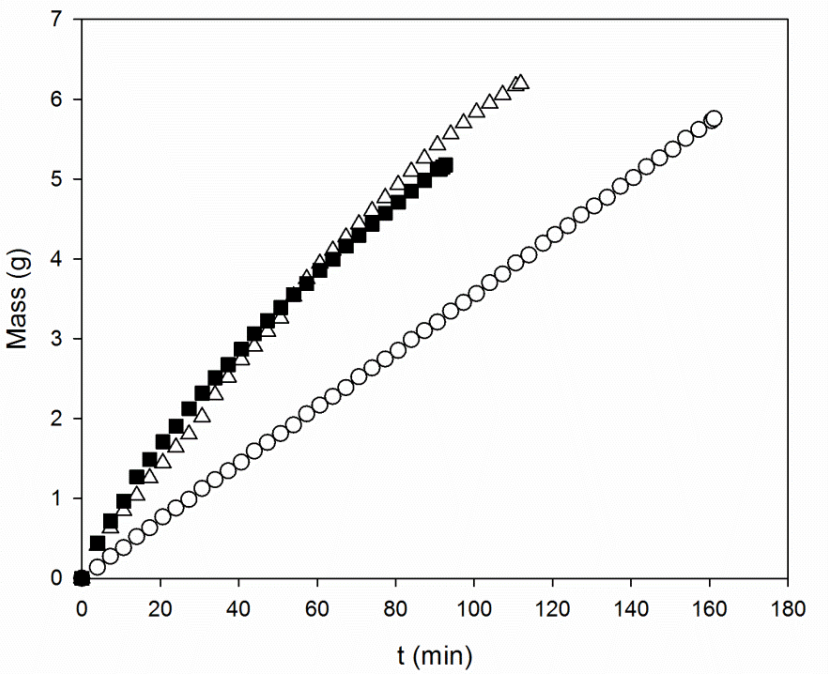

Figure 7.9 Mass versus time plots for an NPAM demonstrating concentration polarization for a 67 nm average pore diameter NPAM, (○) when no voltage is applied, (Δ) when V_{app} = 10 V is superimposed onto the pressure-driven flow for the first run and (■) when V_{app} = 10 V after the build-up of ions has been flushed from the surface of the membrane.

7.5 Effect of Buffer Concentration on EOF Rates

EOF rates were found to vary according to the concentration of borate buffer (for constant V_{app}= 10 V) for three different membrane pore sizes (Figure 7.10). For all membranes, an increase in EOF was observed with increasing buffer concentration. The Debye lengths for 2, 5, 8 and 10 mM were calculated using the Debye Hückel approximation (Equation 2.14) and found to be 6, 4.5, 3.5 and 3 nm, respectively. In a comparable investigation, which varied borate buffer concentration for a NPAM of fixed pore size, a linear relationship between EO flow rates and increasing electric fields for the highest buffer concentrations (5 to 7.5 mM) was also observed. However, it also observed a plateau of EO flow for the lowest concentrations (0.1 to 2 mM) (Vajandar et al. 2007). This deviation from the expected linearity, which was observed in (Vajandar et al. 2007), might be attributed to buffer capacity and concentration polarization, which supports the findings in this present work. Vajandar et al. also observed plateauing EO flow rates for the lowest concentrations when increasing electric field strength (i.e. with increased applied voltage). This might be attributed (i) to ion depletion in the

buffer following electrolysis reactions at the electrodes and (ii) concentration polarization at the membrane. A similar limitation was observed where unstable EOF occurred at lower ionic concentrations (due to the reasons discussed above). The present study therefore supports the findings of Vajandar et al. Thus far, this has prevented us from obtaining accurate EO data at lower concentrations when an overlap of the EDL would be predicted for NPAMs with larger pore diameters. In short, a balance must be found between obtaining stable and accurate EO flow and lowering the ionic concentration of the electrolyte in order to increase the thickness of the EDL.

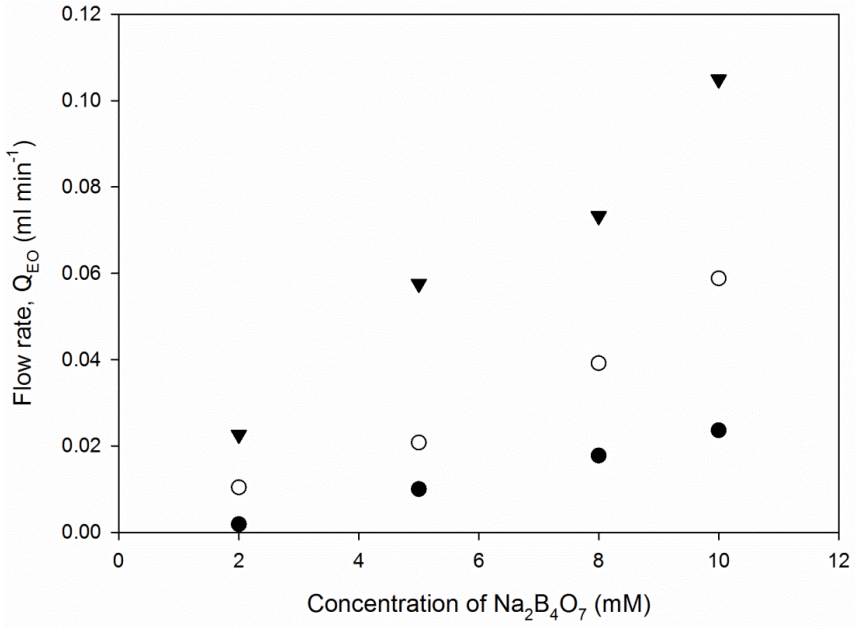

Figure 7.10 Effect of concentration of $Na_2B_4O_7$ on electroosmotic flow rate for three different pore sizes of the NPAM (●) 24 ± 4 nm, (○) 48 ± 7 nm and (▼) 61 ± 8 nm with V_{app} = 10 V for all cases.

7.6 Effect of Voltage and Efficiency of EO Pumps

The electrical potential felt by the membranes (i.e. the effective voltage, V_{eff}) differs from the applied electrical potential V_{app} as described earlier. The V_{eff} can be calculated using Equation 2.17 (discussed in Chapter 2) or by using Equation 7.3 with experimental EOF rates, pore diameter, membrane thickness, and zeta potential values. In both methods, V_{eff} was significantly smaller than V_{app} (Figure 7.11) for membrane pore diameters of 24, 52 and 67 nm. This difference in V_{app} and V_{eff} explains the low efficiency of DC EO pumps; significant loss can be

attributed to the resistance of the electrodes and the membrane as well as to decomposition reactions taking place at the cathode and anode (i.e. hydrolysis of water). In most previous publications efficiencies have been reported between 0.01% and 5.6%, consistent with the findings presented here. One of the most efficient EO pumps was recently reported in (Wu et al. 2011). This showed that by utilising CNT membranes with inner diameters of 7 nm and 1.5 nm with diazonium grafting (in order to increase surface charge density), electroosmotic mobility was increased by 90%, resulting in 25 to 110 times improved efficiencies compared with previously reported EO pumps (Wu et al. 2011). The present study applied a negative bias of – 300 mV in order to obtain the highest fluxes. When a positive bias of up to + 300 mV was applied a lower flux was observed. This was attributed to back pressure flow in the opposite direction to the applied electric field. Applied voltages used in this study were well below that needed for the hydrolysis of water when using Pt electrodes (2.0 V) (Erlandsson and Robinson 2011).

The results presented in this chapter show that EO flow rate through NPAMs for all pore diameters is much higher than pressure-driven flow rates, especially for the smallest pore diameters. When this is translated into power consumption, however, the efficiency of the EO pump suffers, with efficiencies reported here between 0.05% and 1% depending on the pore size of the NPAM (Figure 7.12). A major challenge for potential EO applications at a larger scale is therefore to reduce the disparity between effective and applied voltages. If V_{app} was equal to V_{eff} the thermodynamic efficiency of EO pumps would be equivalent to (indeed slightly higher than) modern mechanical pumps.

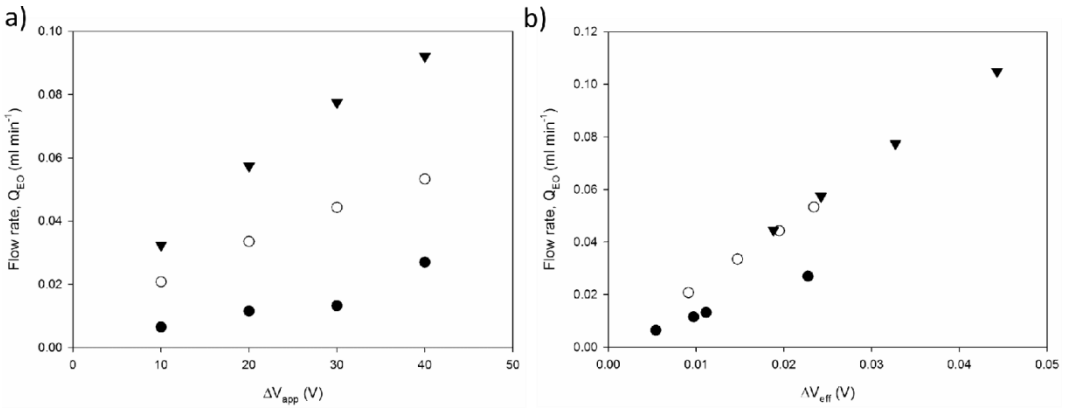

Figure 7.11 Electroosmotic pumping performance for three NPAMs (● D_P = 24 ± 4 nm, ○ D_P = 52 ± 5 nm, ▼ D_P = 67 ± 7 nm) a) with applied voltage, V_{app}, and b) with effective voltage, V_{eff}.

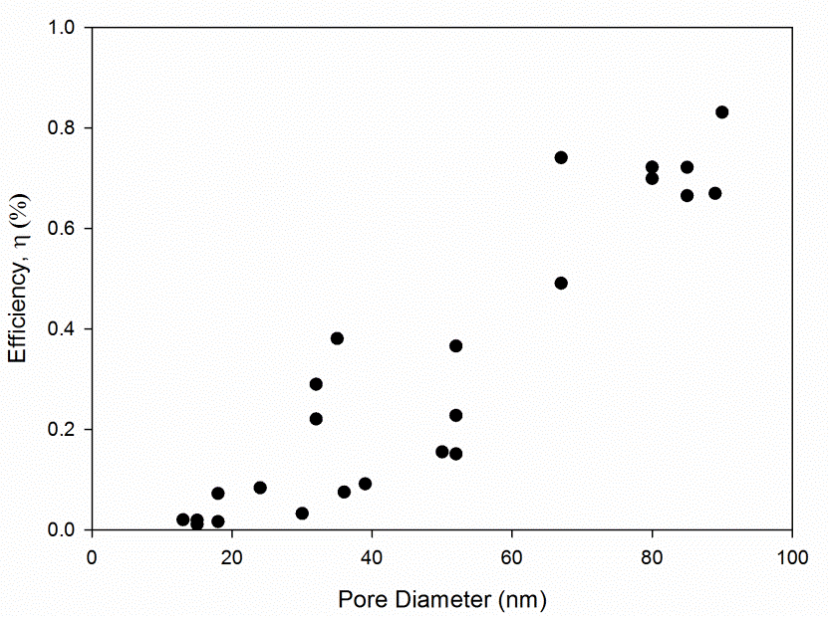

Figure 7.12 Thermodynamic efficiency of EO pumping, η, as a function of NPAM pore diameter.

7.7 Summary

This chapter investigated EO at the nanoscale using nanoporous NPAMs whose pore diameters had been accurately controlled through electrochemical aluminium anodization. The first section discussed the full characterisation of the NPAMs used in the study through SEM and streaming potential measurements. It then discussed the enhanced flow observed for EOF rates compared with pressure-driven flow rates. This was found to be most significant (up to 5 times) for the smallest pore diameters tested (~ 8 to 25 nm), where pore diameter approached

EDL overlap. The following sections discussed the limitations of EO pumps and their causes. The effect of pore diameter, buffer concentration, and applied voltage were each investigated in order to determine the main limiting factor: concentration polarization. EOF was found to increase with increasing buffer concentration but achieving stable EOF at lower ionic concentrations proved challenging due to concentration polarization and ion depletion of the buffer. After optimisation, stable EOF for up to 2 hours was achieved and this was also recoverable. This presents a much longer lifetime than those reported for a majority of EO pumps. A significant difference between applied and effective voltage was also found to be responsible for low thermodynamic efficiency (0.05 to 1.0%), in line with previous findings. Following these results it might be observed that, whilst EO pumps cannot be used in continuous processes, they could be used (with the smallest pore sizes tested) in current lab-on-a-chip systems or perhaps to support mechanical pumps in larger scale applications.

Chapter 8

Pressure-Driven and Electroosmotic Flow in Carbon Nanotube Membranes

This final results chapter will discuss the optimisation pathway for the template-assisted synthesis of CNT membranes necessary for the study of fluid flow. It will identify the importance of gas flow rates and deposition times for the CVD process and discuss how the quality of NPAMs affects flow rates. Both the gas flow rates in the CVD process and the quality of NPAMs were of paramount importance to successful fluid flow and electroosmotic experiments. The effect of NPAM quality on fluid flow was also discussed earlier in Chapter 4. The first section will discuss the characterisation of CNT membranes and later sections will present findings for pressure-driven and electroosmotically driven flow through CNT membranes. It will primarily discuss the effect of pore diameter on flow.

8.1 Introduction

In order to take full advantage of the properties of nanostructured materials, a fundamental understanding of the properties which affect their performance at the nanoscale and macroscale is imperative. This represents the first step towards the future fabrication of successful and reliable nanofluidic devices, whether these are lab-on-a-chip devices or industrial scale filtration processes. So far this thesis has highlighted the effect of pore diameter, surface chemistry, and surface structure on wetting properties and the flow of NPAMs in particular. The present chapter furthers this by utilising NPAMs as templates in order to produce CNT membranes with a different surface chemistry (i.e. more hydrophobic than NPAMs). It also probes the effect of pore diameter on flow rates in order to identify the magnitude of flow enhancements compared to hydrophilic NPAMs and CNT enhancements reported in literature. Similar methods to the EO experiments conducted in Chapter 7 and reported in Chapter 3 Section 3.6 were also conducted on CNT membranes.

8.2 Characterisation of CNT Membranes

Several techniques were applied to fully characterise all pore diameters and ensure the high quality of CNT membranes and CNT structure. It should be noted that all CNTs were produced at the same temperature (670 °C), as described in Chapter 3, Section 3.4. As discussed in Chapter 4 Section 4.1.4, attempts to anneal CNT membranes to graphitise the carbon resulted in mechanical failures of the membrane (cracks and, in some cases, complete fragmentation). This was attributed to the different thermal coefficients of alumina and carbon. Raman spectroscopy was therefore used to identify any differences caused by the different parameters of the CVD process.

8.2.1 Characterisation of CNT Membranes by SEM

In the first instance CNT membranes were produced through procedures reported in literature. However, as all flow measurements were taken before full CNT characterisation, the structure of the carbon formed on the NPAM was unknown. In subsequent fluid flow experiments, very low flow rates were observed. Indeed, in some cases, unexpectedly, no flow at all was detected through the pores at pressures > 500 kPa. A review of the literature revealed that previous studies of CVD in NPAMs had, despite mutual citation, employed markedly different experimental CVD methods (different flow rates, carrier gas, carbon source, and deposition times). The present study therefore attempted to identify the effect of each of these variables in turn.

Samples produced at lower flow rates were metallic grey and shiny in appearance, whereas those produced at higher flow rates were jet-black and either matt or glossy. Furthermore, SEM analysis revealed why little or no flow was observed. Figure 8.1 shows SEMs of a NPAM after CVD at 670 °C, with a flow rate of 14:6 sccm He:C_2H_4 for 4 hours. Figure 8.1a is a micrograph of the top surface where no porous features were identified due to a layer of carbon covering the surface of the membrane. Figure 8.1b and c display the cross section of the NPAM under these conditions, and approximately 300 nm layer of carbon on top of the template. This is due to the low flow rate of both carrier gas and carbon source which resulted in a coating of the inner channels of the template as expected, but

also resulted in a layer of carbon on the top surfaces. It would be expected that carbon deposits would form on the surface as well as in the channels, as the solid surface is also alumina. To overcome the unwanted layer of carbon produced when using a low total flow rate, F_T, a series of higher flow rates were used to optimise the CVD process. The ratio of $He:C_2H_4$ (70:30) and deposition temperature (670 °C) were kept constant.

Figure 8.2a is a resulting SEM of a NPAM post-CVD, which was also performed at F_T = 20 sccm but for a reduced time of 2 hours. Though deposition time is an important factor, Figure 8.2a makes clear that the low total flow rate still caused problems. The dashed white line in Figure 8.2a represents a cleaved area of the membrane (left) and top surface (right). The pores were visible in the cleaved region but it was not possible to focus on the top surface due to a thin layer of carbon blocking and covering the pores. Figure 8.2b and c show CNTs pointing upwards out of the NPAM template, which were produced at F_T = 60 sccm for 3 hours. The white arrows in Figure 8.2b indicate pores filled with CNTs and empty pores, respectively. The empty pores (those not containing CNTs) could be empty for two reasons: either (i) the channel was blocked at some point (this will be discussed below) or (ii) CNTs were dislodged during preparation for characterisation.

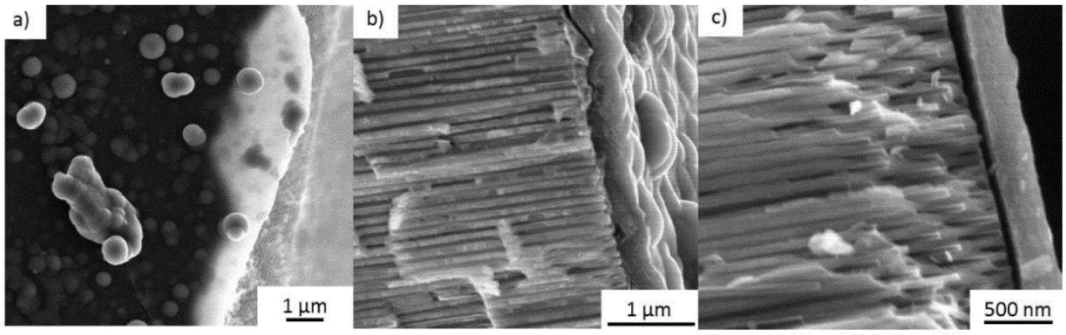

Figure 8.1 FESEM of NPAM post-CVD (parameters: 670 °C, F_T = 20 sccm, 4 hours) a) top surface structure completely coated and blocked by a glassy carbon layer b) and c) cross-sections of NPAMs coated in a layer of carbon approximately 300 nm thick.

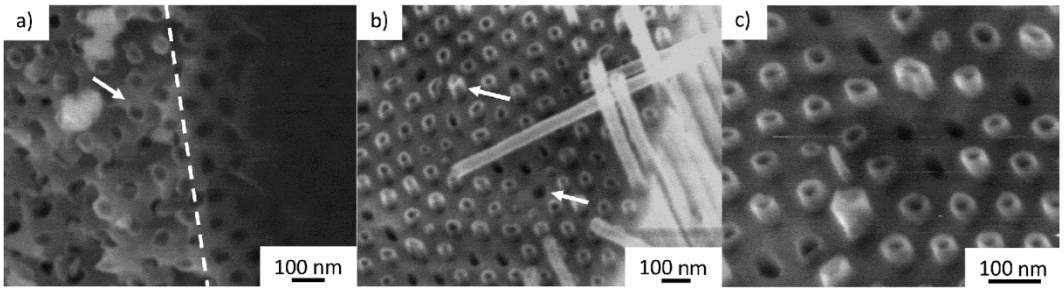

Figure 8.2 FESEM of NPAM post-CVD a) the white arrow indicates a cleaved area, and the dashed line separates the cleaved area from the top surface – it was not possible to focus as pores were covered/blocked in a layer of carbon (CVD parameters: 670 °C, F_T = 20 sccm, 2 hours) b) and c) show cleaved areas of the CNT membranes with CNTs pointing upwards out of the template. Some pores are filled with CNTs and others are empty (indicated by white arrows and CVD parameters: 670 °C, F_T = 60 sccm, 3 hours).

In order to overcome this blocking, the F_T was increased in the 60 - 160 sccm range, following the work completed by Whitby et al. (Whitby et al. 2008). Results for the fastest flow rates are shown in Figure 8.3a, c, and e, showing SEMs of the top surfaces of NPAMs post-CVD at 120, 140, and 160 sccm, respectively. Figure 8.3g shows a micrograph of a CNT membrane which had D_P ~ 48 nm before CVD. To obtain smaller channel diameters, in the case of Figure 8.3g, CVD deposition time was extended to 8 hours at F_T = 120 sccm (in order to ensure there was not a large build-up of carbon on the surface). This produced channel diameters of ~ 16 - 20 nm. Unlike Figures 8.1 and 8.2, the porous structures here are free of blocked or covered pores. At these high total flow rates little difference between the qualities of carbon coating was observed. Therefore 120 sccm was used in the majority of cases. Figure 8.3b, d and f are the resulting CNTs released from the NPAMs in Figure 8.3a, c and e respectively. Figure 8.3h represents a cleaved section of a CNT membrane produced at 120 sccm. All the channels here are clear of blockages and no branching (i.e. the formation of two pore channels) was visible, suggesting a high quality NPAM. The CNTs fall in different directions due to the mechanical stress imposed on the membrane in the preparation of the samples, but it is clear that the CNTs are long, straight, and uniform, indicating a homogeneous coating of carbon along NPAM channel walls. In the majority of cases the highest CVD total flow rates were most successful in subsequent fluid flow and electroosmotic experiments. After optimisation the flow rates and deposition times were adjusted depending on the pore diameter required and the initial pore diameter of the NPAMs. Table 8-1 has summarised the main CVD parameters in the optimisation process.

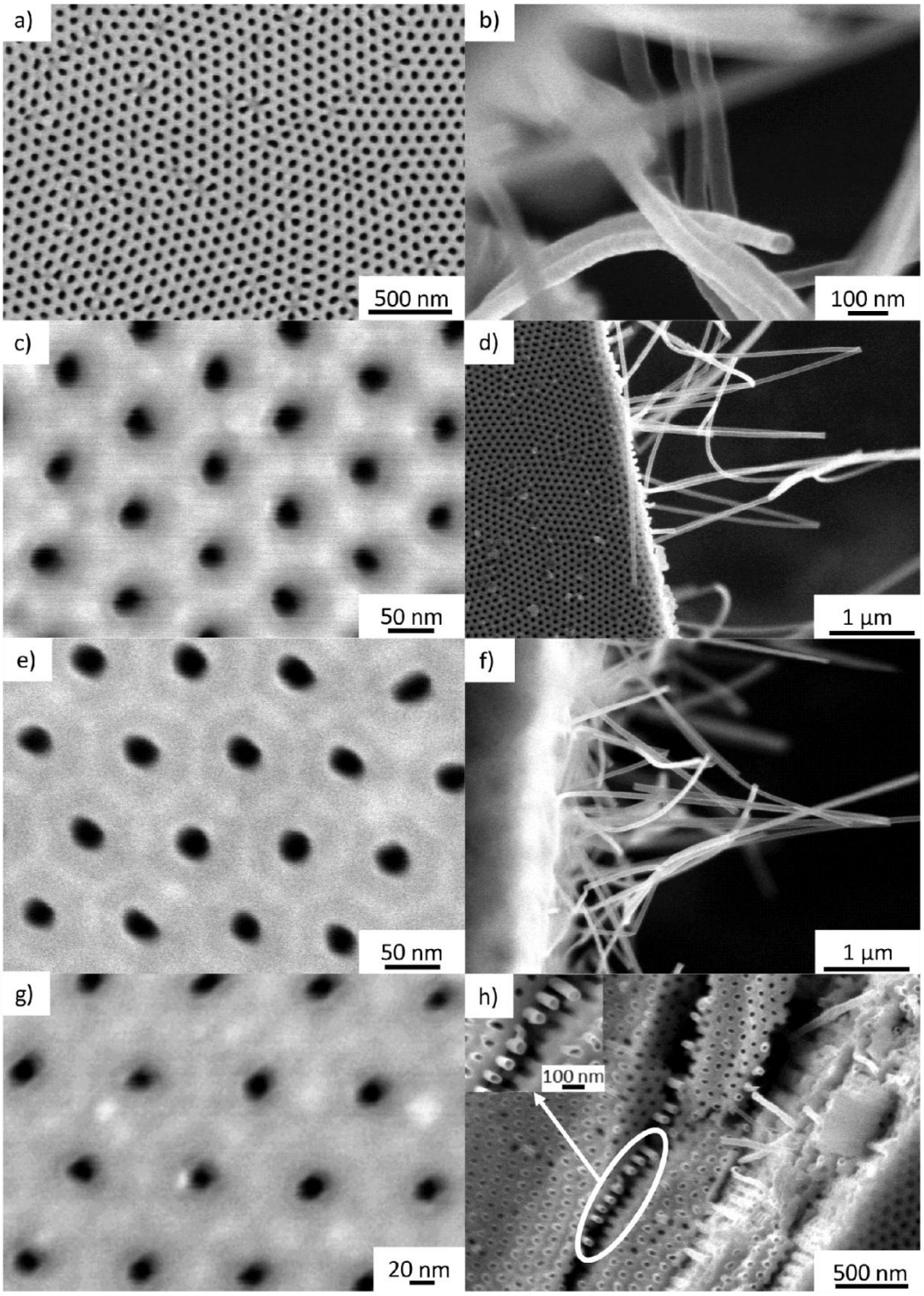

Figure 8.3 FESEM of NPAMs post-CVD a-b) average D_P = 70 ± 5 nm with CVD parameters: 670 °C, F_T = 120 sccm, 3 hours and CNTs released from the template c-d) average D_P = 28 ± 2 nm with CVD parameters: 670 °C, F_T = 140 sccm, 3 hours and CNTs released from the template show from cleaved edges, e-f) average D_P = 25 ± 1 nm with CVD parameters: 670 °C, F_T = 160 sccm, 3 hours and CNTs released from the template show from cleaved edges g) average D_P = 16 ± 2 nm, CVD parameters: 670 °C, F_T = 120 sccm, 8 hours and h) a cleaved area with CNTs protruding from the template with no visible branching.

Table 8-1 Summary of CVD parameters which resulted in detected flow rates or no flow

Total Gas Flow Rate, F_T (sccm)	Deposition time (h)	Water flow rate detected?
20	2 - 6	N
60	3 - 6	Y (reduced)
100	3	Y
120	3	Y
140	3	Y
160	3 - 8	Y

8.2.2 Characterisation of CNT membranes by TEM

To further characterise the differences between CNTs embedded inside NPAM templates with different CVD parameters, TEM was utilised. It was not possible to look at the wall structure (i.e. the turbostratic structure) due to the limitations of the instrument, but as the carbon was not annealed a random structure would be expected. However it was possible to identify wall thickness and the quality of CNTs. Figure 8.4a shows a CNT produced via the CVD process discussed above (670 °C, 120 sccm, and 3 hours). The walls of the tube are only a few nanometres thick (2 - 8 nm). This was also observed in Figure 8.4b. These were produced with the same CVD parameters but in a NPAM with smaller pore diameters, resulting in smaller pore diameters of the CNTs. The images in Figure 8.4 suggest there is a certain roughness in the CNT walls and an almost 'wavy' structure. It is not clear whether this is due to the quality of the template or the sample preparation process. It could be the preparation process, however, because the CNTs are no longer supported by the template and the SEM images show that the CNTs tend to bend (as seen in Figure 8.3b, d and f). As was discussed at the beginning of the chapter, both the CVD flow rates and the quality of the NPAM template were vital for measuring flow rates successfully. Regarding the template quality, branching has been described as a hindrance and can be the cause of reduced flow rates. Figure 8.4g is a TEM of a branched channel, which, when coated in carbon results in a blocked pore (see white circle in Figure 8.4g). Branching occurs within the NPAM template either when there has been a problem in the two-step anodization process (i.e. poor electropolishing and/or first-step anodization) or the anodization voltage used (< 20 V or > 50 V) produced a poor structure. Figure 8.5 presents an amalgamation of several TEM micrographs to piece together an image of the whole length of a CNT. A broken end of the CNT is also visible, similar to that shown in Figure 8.4a (area pointed to by the white arrow). This could also be

attributed to alumina still encasing the CNT. A possible crystallised meniscus remains near the section of template in Figure 8.5c.

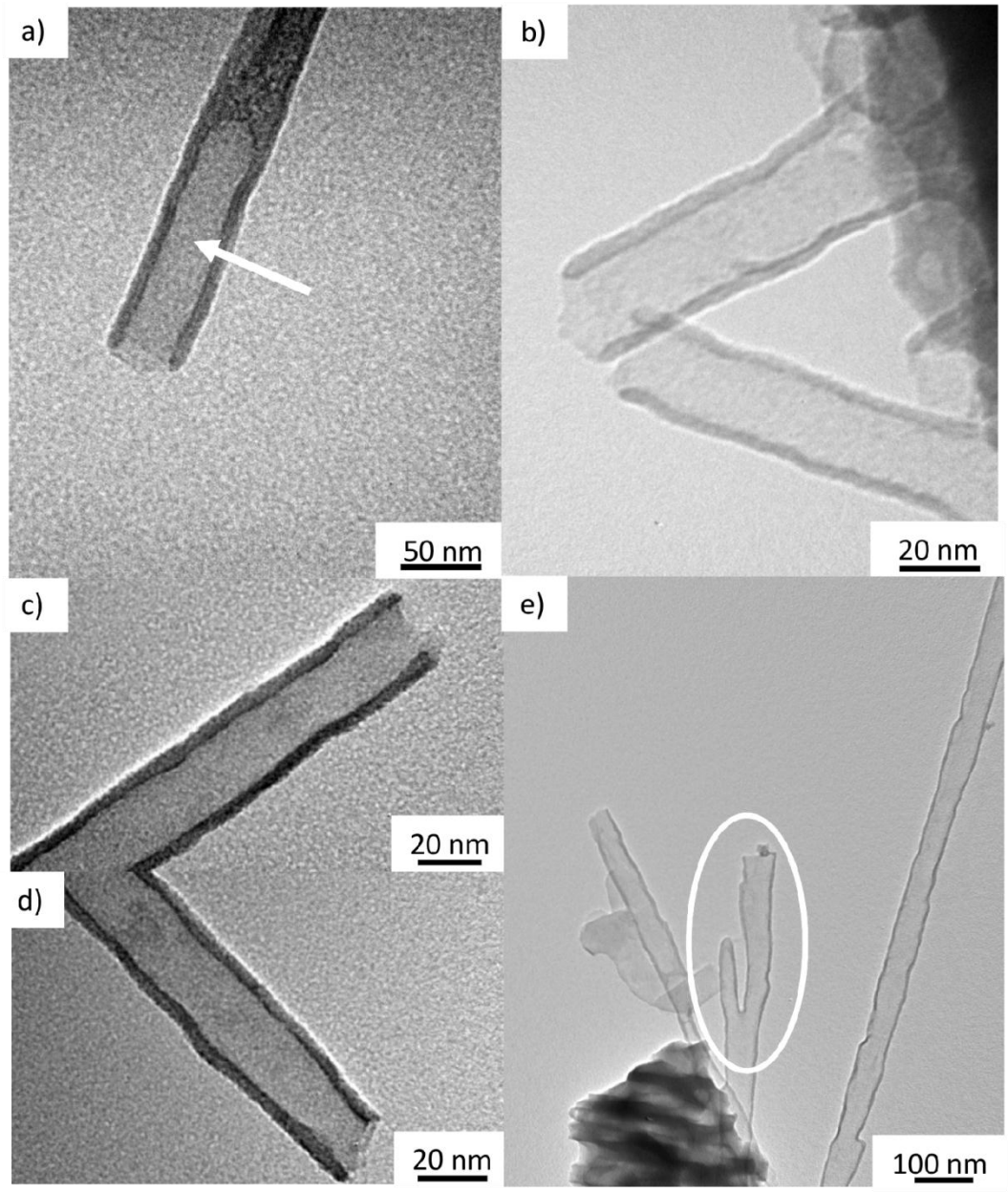

Figure 8.4 TEM micrographs of CNTs with inner diameter of a) ~ 30 nm with wall thickness of ~ 7 nm, the white arrow indicates what could be either a broken edge of the CNT or alumina still coating the CNT b) ~ inner diameter of 17 nm with wall thickness ~ 4 nm c) and d) are TEM images of individual CNTs with inner diameter < 20 nm and e) is an example of a CNT with a blocked side branch (white circle) which is the result of a low quality membrane. A membrane made of such channels resulted in reduced flow rates.

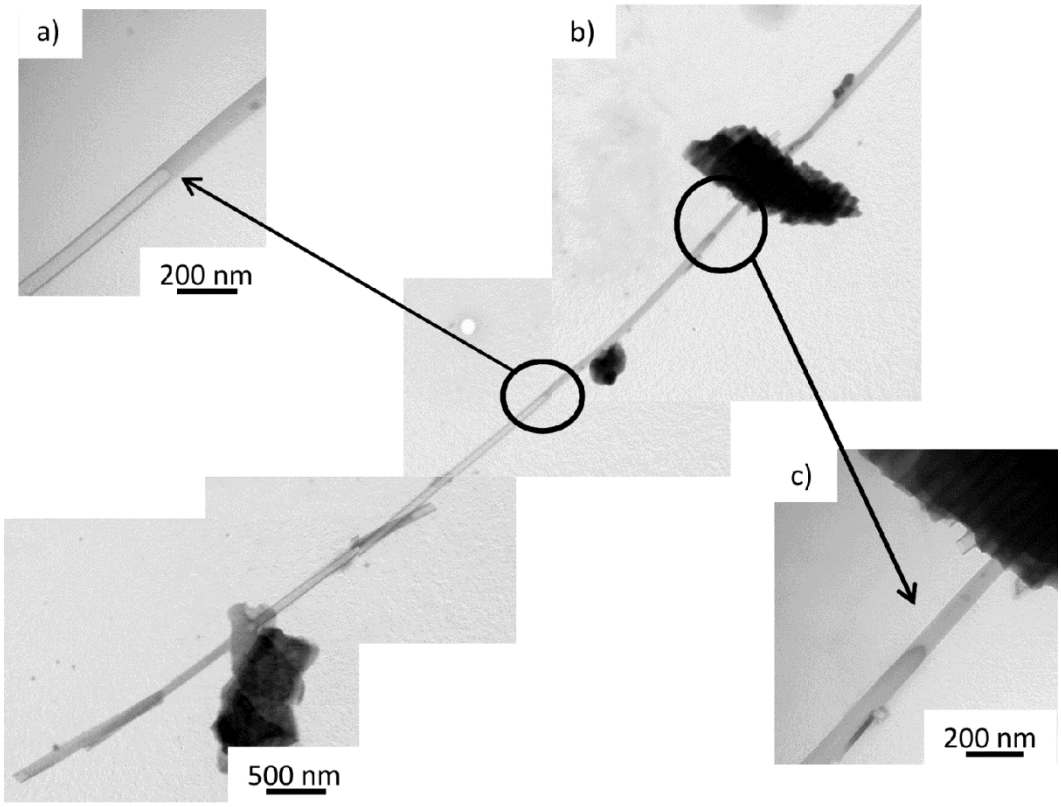

Figure 8.5 Collage of TEM micrographs showing the homogeneous structure from the template method a) a broken edge of CNT b) is part of the NPAM template remains and CNT protrudes from it and c) presents a possible crystallised meniscus, as these CNTs were characterised post EO experiments.

8.2.3 Characterisation of CNT Membranes by Raman Spectroscopy

Raman spectroscopy was utilised to further analyse the carbon structure produced under the different CVD parameters as observed via SEM and discussed in Section 8.2.1. The samples covered in a layer of carbon (as shown in Figure 8.1), and subsequent samples prepared by the parameters given in Table 8-1, were both analysed, as there was a possibility that the carbon structure would be different between the different CVD parameters. Figure 8.6 displays the normalised Raman spectra for six different $F_{T.}$ Very little difference between the samples was observed and there were no major shifts in the either the D- or G-band. All samples gave broad curvature, which is expected from the disordered structure of the carbon produced using this method. This is further supported by Figure 8.7, which displays an almost constant Raman shift of the full width half maximum (FWHM) of the disorder-induced D-band and G-band for different F_T. The I_D/I_G ratios were also calculated for the different F_T and these are shown in Figure 8.8. The I_D/I_G ratios were constant at ~ 1.8 with increasing F_T. However, at F_T = 20

sccm the I_D/I_G ratio was ~ 1.5. The samples produced at F_T = 20 sccm resulted in a layer of carbon covering the porous surface, and I_D/I_G of ~ 1.5 indicates a slightly more ordered structure of carbon compared to the other samples. It should be noted that this could also be due to the absence of a porous structure in the 20 sccm samples (due to the thick layer of carbon). In short, even though different CVD parameters had a large influence on the fluid flow experiments, Raman spectroscopy experiments confirmed that there was no large effect on the carbon structure deposited on the NPAMs.

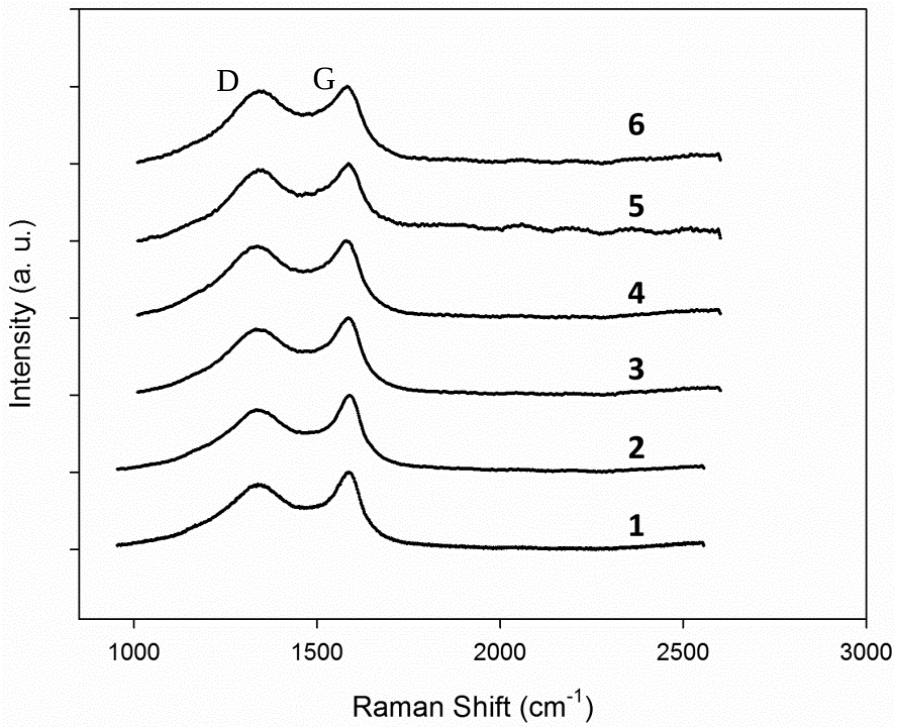

Figure 8.6 Raman spectra (green laser, wavelength - 512 nm) for CNT membranes produced at 670 °C with total flow rates of (1) 20 sccm (2) 60 sccm (3) 100 sccm (4) 120 sccm (5) 140 sccm and (6) 160 sccm.

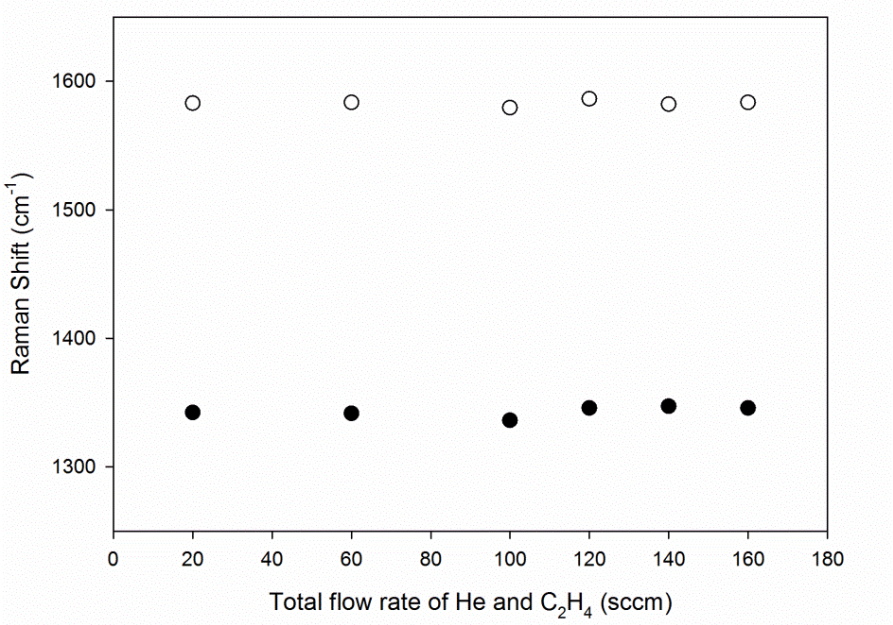

Figure 8.7 FWHM shift of the D-band (●) and G-band (○) with total flow rates on CNT membranes produced at 670 °C.

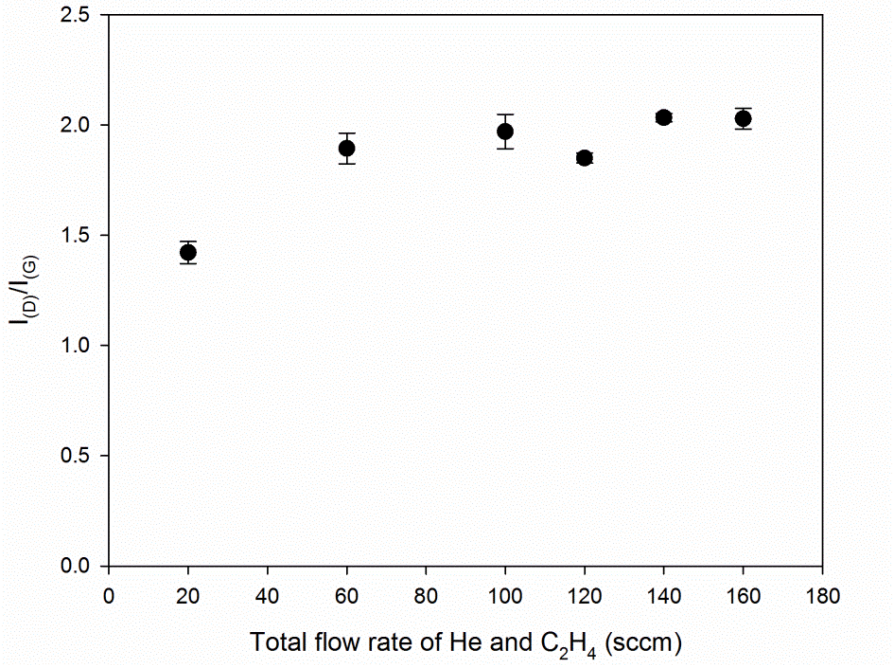

Figure 8.8 I_D/I_G ratio with increasing total flow rate of He and C_2H_4. The total flow rate was increased but the ratio of He and C_2H_4 was kept constant. Error: standard deviation of several different areas of the CNT membrane at each flow rate.

8.2.4 Wetting Properties of CNT Membranes

The wettability of CNT membranes was also investigated. The same CA methods as those in the case of alumina (presented in Chapter 3 Section 3.2) were used to observe the wetting properties of CNT membranes. The measured CAs of water

on the CNT membrane surface ranged from 70° to 90°. In the case of the CNT membrane, investigation into the wetting properties was carried out in order to establish whether the liquid would wet the surface and enter the pores of the membrane. Figure 8.9 shows digital images of CAs on a series of CNT membranes with different diameters. Figure 8.10 presents the relationship between pore diameter and contact angle, where CA increases slightly, with decreasing pore diameter. However, when taking into account the error of the contact angle measurements there is little variability of CA with pore diameter. This could be for two reasons: (i) the porosity of the membrane (and therefore the solid surface fraction - discussed in Chapter 5) varied due to the deposition time of the CVD, resulting in small diameters but decreased porosity or (ii) the pores/channels in the membrane were all open unlike the PAAs presented in Chapter 5.

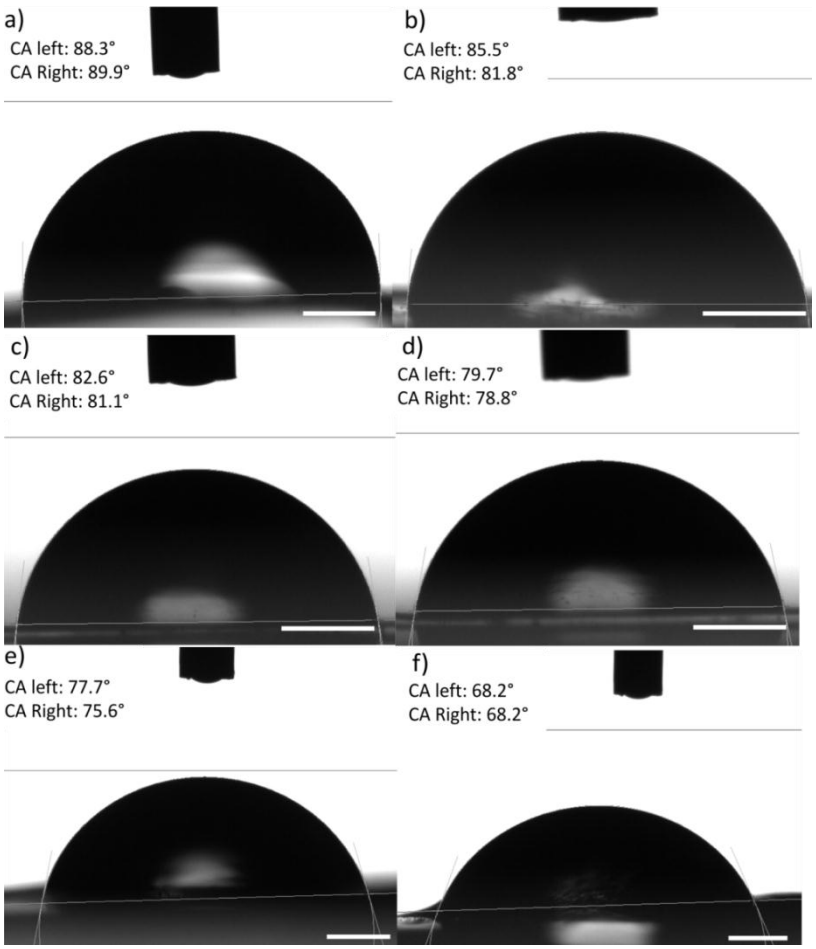

Figure 8.9 Contact angle measurements on CNT membranes for a) D_P = 18 ± 2 nm b) D_P = 20 ± 2 nm c) D_P = 25 ± 4 nm d) D_P = 34 ± 4 nm e) D_P = 42 ± 2 nm f) D_P = 50 ± 7 nm. Scale bar: 1mm.

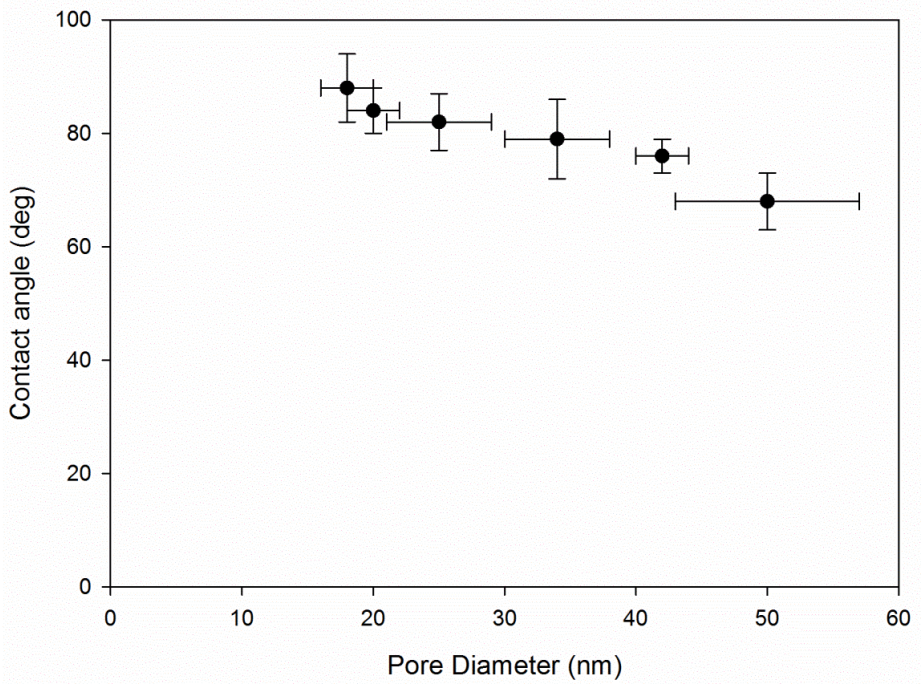

Figure 8.10 Contact angle data of water on CNT membranes with a range of pore diameters. Error: SD of each at least 3 repeat runs.

As the contact angles were < 90°, it was expected that the channels would wet by capillarity, the ability of a liquid to flow spontaneously into narrow spaces without the assistance of an external pressure, particularly in tubes with a small diameter. This was particularly expected because the channels in the membranes were fully open with no likely internal blockages, ensuring that any air within the channels could escape. Although the CAs of the CNT membranes < 90° the membrane did not appear to wet the surface unlike the alumina. Though carbon is more hydrophobic than alumina, it was expected that the surface would wet due to the open channels in the membrane surface. This, however, was not the case. The next section will discuss the results of pressure-driven flow through CNT membranes. These did, in some cases, require considerable pressure to obtain measureable flow rates.

8.3 Pressure-Driven Flow in CNT Membranes

This section will present findings regarding pressure driven flow rates in CNT membranes and discuss the effect of pore diameter on the observed flow rates. Due to the abundance of work on the enhancement of fluid flow in CNTs, the results will be compared to the literature and employ the model recently developed by Mattia and Calabrò (Mattia and Calabrò 2012). Figure 8.11a

presents the raw data of mass recorded over time for a CNT membrane with pore diameter ~ 42 nm. Figure 8.11b displays the recorded mass flow rate with increasing ΔP. The pressure was applied via the pressurised reservoir.

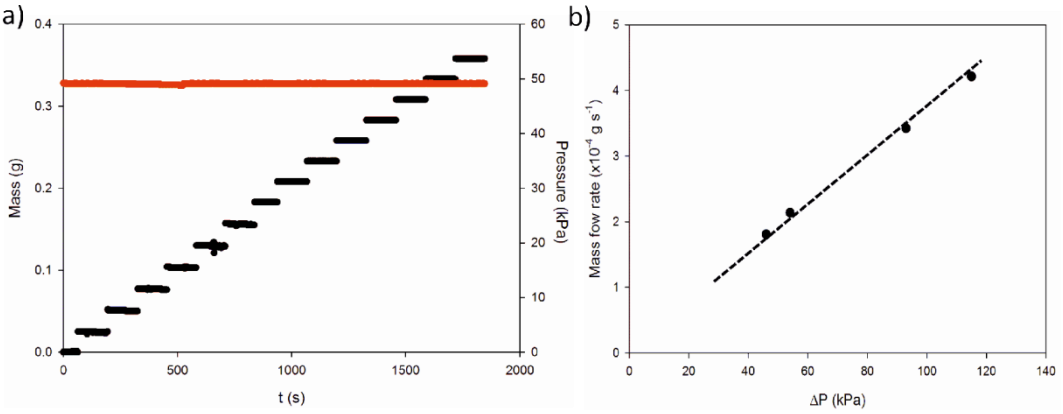

Figure 8.11 Flow data for a CNT membrane of D_P = 42 ± 6 nm, effective area of 5mm^2 a) raw data of (●) recorded mass with time and (●) constant pressure and b) measured mass flow rate of four different imposed pressures.

As discussed in the first section of this chapter, the quality of the membranes was just as important to fluid flow experiments as the CVD parameters. Therefore, due to the fragility of the membranes after annealing, the NPAMs produced at an anodization voltage between 10 to 25 V could not be used for flow measurements. Every attempt to do so resulted in membrane failure (due to cracks). Failure usually occurred during the process of sealing (which prevented liquid slipping around the membrane): when the membrane was sealed between two flanges of the membrane holder, the sample invariably snapped. To overcome this (and to ensure that there was no branching and therefore blocking within the channels) NPAMs were produced at an anodization voltage between 35 and 50 V instead. The CVD parameters were then tuned to produce thicker CNT walls in order to reduce the pore diameter (see Figure 8.3g). This resulted in a decreased porosity of the membrane which has been accounted for in further analysis. Therefore 16 - 65 nm was the range of pore diameters tested in this study. Table 8-2 presents a summary of the CNT membranes tested (over 100 membranes were fabricated for this particular study, which resulted in approximately 60 successful tests). Theoretical flow rates were calculated with the no-slip Hagen-Poiseuille equation (see Equation 8.1).

$$Q_{HP} = \frac{\phi A_{eff} D_P^2 \Delta P}{32 \tau \mu L} \tag{8.1}$$

where Q_{HP} is the Hagen-Poiseuille volumetric flow rate, ϕ the porosity, A_{eff} the effective area, D_P pore diameter, ΔP pressure difference, τ the tortuosity, μ the viscosity and L the thickness.

Table 8-2 Summary of data for CNT membranes, the ratio between the experimental and theoretical flow rate yields the enhancement factor.

No.	ϕ	D_P[a]	L[b]	$Q_{HP}/\Delta P$[c]	$Q_{exp}/\Delta P$[d]	ε[e]	b_0[f]
	(-)	(nm)	(μm)	(x 10^{-15} m^3 s^{-1} Pa^{-1})		(-)	(nm)
1	0.075	65 ± 4	50	7.23 ± 0.25	11.24 ± 0.56	1.55 ± 0.23	12 ± 2
2	0.150	60 ± 8	80	8.09 ± 0.14	9.88 ± 0.49	1.22 ± 0.13	8 ± 1
3	0.200	50 ± 9	60	9.99 ± 0.19	29.07 ± 1.45	2.91 ± 0.38	18 ± 2
4	0.130	48 ± 3	55	6.53 ± 0.08	8.29 ± 0.41	1.27 ± 0.17	7 ± 1
5	0.086	42 ± 2	125	1.35 ± 0.07	2.33 ± 0.12	1.72 ± 0.15	9 ± 1
6	0.065	40 ± 8	95	1.25 ± 0.24	2.35 ± 0.12	1.88 ± 0.19	9 ± 1
7	0.130	37 ± 2	85	2.33 ± 0.11	6.52 ± 0.33	2.80 ± 0.30	13 ± 1
8	0.089	34 ± 8	40	3.08 ± 0.11	8.86 ± 0.44	2.87 ± 0.48	12 ± 2
9	0.089	32 ± 3	80	1.27 ± 0.09	4.60 ± 0.23	3.63 ± 0.40	14 ± 1
10	0.060	31 ± 3	80	0.42 ± 0.09	1.00 ± 0.05	2.39 ± 0.26	9 ± 1
11	0.090	30 ± 3	75	1.28 ± 0.20	6.00 ± 0.30	4.70 ± 0.53	17 ± 2
12	0.100	29 ± 2	80	1.17 ± 0.13	2.96 ± 0.15	2.53 ± 0.28	8 ± 1
13	0.077	28 ± 2	70	1.03 ± 0.09	2.87 ± 0.14	2.77 ± 0.33	9 ± 1
14	0.091	26 ± 5	40	0.94 ± 0.09	1.44 ± 0.07	1.53 ± 0.26	4 ± 1
15	0.080	25 ± 3	85	0.67 ± 0.19	1.69 ± 0.08	2.52 ± 0.27	7 ± 1
16	0.065	24 ± 2	65	0.64 ± 0.13	5.95 ± 0.30	9.29 ± 1.14	28 ± 3
17	0.048	22 ± 4	65	0.20 ± 0.10	0.63 ± 0.03	3.12 ± 0.38	8 ± 1
18	0.050	20 ± 2	120	0.09 ± 0.01	0.42 ± 0.02	4.47 ± 0.40	11 ± 1
19	0.049	19 ± 3	50	0.20 ± 0.09	0.75 ± 0.04	3.73 ± 0.54	9 ± 1
20	0.052	18 ± 3	65	0.29 ± 0.08	2.81 ± 0.14	9.73 ± 1.20	22 ± 3
21	0.038	17 ± 3	130	0.09 ± 0.01	0.57 ± 0.03	6.08 ± 0.53	13 ± 1
22	0.045	16 ± 3	90	0.13± 0.07	0.68 ± 0.03	5.29 ± 0.54	10 ± 1

[a] error is the standard deviation. [b] error is 5mm from micrometre sensitivity. [c] theoretical flow rate calculated using Equation 8.1:viscosity values were corrected for temperature, error calculated from pore diameter and membrane thickness. [d] error calculated from the error of pressure transducers. [e,f] error propagation of the variables discussed above.

In almost all previous experimental investigations of fluid flow in CNTs (with diameters ranging from 1 - 44 nm) an enhancement in flow compared to that predicted by continuum fluid mechanics has been observed. The large variability in the calculated enhancement factors for this range of tube diameters arises from the different structure of the carbon. Graphitic MWCNTs, DWCNTs, and turbostratic CNTs have different carbon structures, and all have exhibited vastly different enhancements factors (see Table 2-3 in Chapter 2). The present study has produced CNT membranes with a series of pore diameters which were all produced by the same CVD method in order to ensure that the surface chemistry

of CNTs from sample to sample was consistent and thus that the effect of pore diameter could be fairly assessed.

Figure 8.12 presents flow enhancement factors, calculated from the experimental flow rates and the theoretical flow rate predicted by the no-slip Hagen-Poiseuille equation (see Equation 2.9 and 2.12) normalised by membrane thickness (L), work of adhesion (W_A) and surface diffusion (D_S), as shown in Equation 8.2. The W_A can be calculated for each membrane tested (Equation 8.3). W_A depends on surface wettability, where θ is the contact angle, π_e the film pressure of the adsorbed vapour (which here we assume to be 19 mJ m^{-2}), γ_{LV} in the liquid-vapour surface tension, and R_P pore radius. The calculated values of W_A using the experimental values of contact angle presented above varied between 95 and 145 mJ m^{-2}, close to that of typical values of W_A (~144 mJ m^{-2}) known for carbon (Mattia and Calabrò 2012). The value of D_s ~ 1·10^{-9} m^2 s^{-1} between CNT and water was also used (Park and Aluru 2010).

$$\varepsilon = \left(\frac{R_P-\delta}{R_P}\right)^4 \left(1-\frac{\mu_1}{\mu_2}\right) + \frac{\mu_1}{\mu_2}\left(1+8\mu_2 \frac{L}{{R_P}^2}\frac{D_S}{W_A}\right) \quad (8.2)$$

$$W_A = \pi_e + \gamma_{LV}(1+cos\theta) \quad (8.3)$$

The full theoretical model developed by Mattia and Calabrò was applied to the CNT membranes and theoretical values (dashed lines in Figure 8.12) were solved using MATLAB. It initially appears that the model fits the experimental data well. However, on zooming into the area of interest we see that the experimental enhancement factors lie below those predicted by the model. There are several factors which could influence this, deriving either from errors in the experimental data (including pore diameter analysis) or in the assumed values of D_S and viscosity. To see whether or not the pore diameter error was the main influencing factor in the discrepancy between experimental and theoretical results, the limits of pore diameter (which was based on the error: i.e. for D_P = 25 ± 5 nm then was taken as D_P = 20 nm) were taken to recalculate ε. This did not significantly change the results presented in Figure 8.12 and a discrepancy still remained.

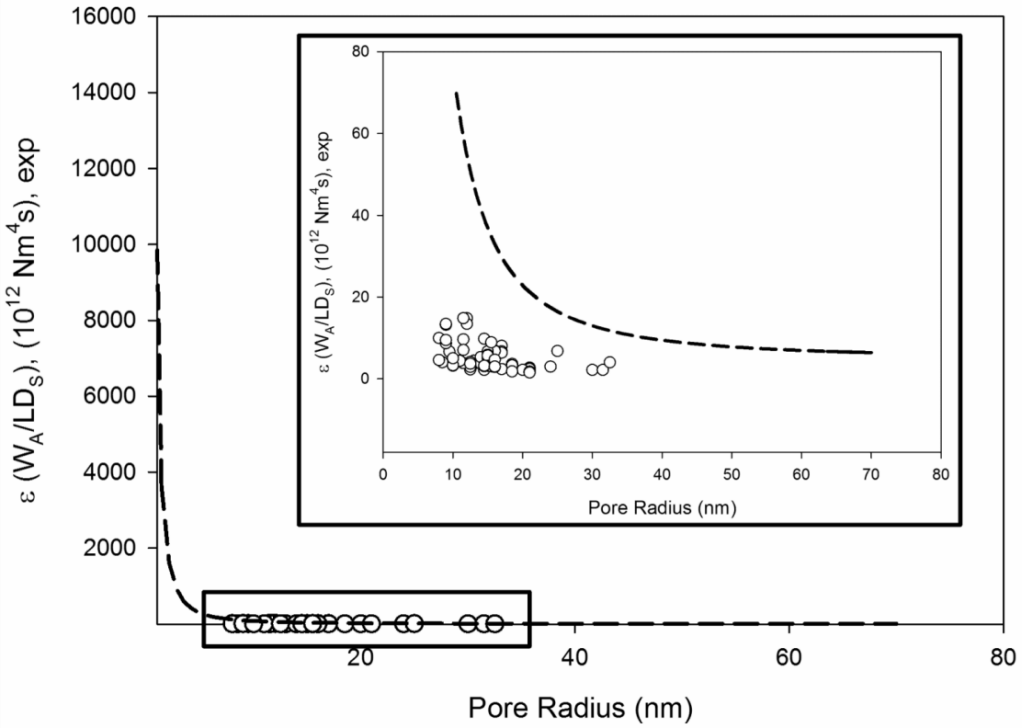

Figure 8.12 Normalised flow enhancement factors with pore diameter of CNT membranes for experimental (○) and those predicted by the model developed by Mattia and Calabró (- - -) (using MATLAB to solve Equation 8.2). Inset: zoomed in region of experimental data.

Great care was taken in the production of the CNT membranes. Branching in the membrane was carefully avoided by optimizing the anodization process and the CVD procedures were also fully optimised. Nevertheless, the measured flow rates were much lower than expected and lower than those of previous experiments. These experimental results highlight the high degree of variability in studies conducted at the nanoscale. Due to the sensitivity of experiments at this scale, even very similar procedures are capable of producing significant variations in results. Nevertheless, the present study did observe a degree of enhanced flow. It can be noted here, that there has been recent experimental work on EO in CNT membranes which (although reporting more efficient EO flow) noted no enhanced mobility of ions in CNTs of ~ 7 nm diameter, something attributed to the confined geometry presented by the pore entrance (Wu et al. 2011). This study further highlights the variability of findings in these systems. However, although the enhancement in flow is lower than that predicted by current models such as the one shown in Equation 8.1, enhancement factors of even double those predicted by continuum models would be favourable in filtration and lab-on-a-chip applications. Indeed, this would significantly reduce their energy consumption.

Several studies in Chapter 2 Section 2.2 were discussed due to the large enhancement factors observed in both experimental and molecular dynamic simulations. For example, the experimental study conducted by Majumder et al. (2005) observed enhancement factors of up to 67000 in graphitic MWCNTs with diameters of ~ 7 nm. This equates to a slip length, b_0 of 58 μm, which is over 8000 times larger than the diameter of the nanotubes. Another experimental study which performed fluid measurements in carbon nanopipes with diameters of 44 nm (which have a similar carbon structure to those investigated in the present study) observed water enhancement factors of up to 34, which equates to a b_0 of up to ~ 177 nm (Whitby et al. 2009). However, this present study has found flow enhancements much lower, between 1 and 10, for CNT diameters between 65 and 16 nm (see Table 8-2 for equivalent calculated slip lengths). This yields slip lengths much closer to the diameter of the individual CNTs.

As discussed in Chapter 2, most experimental and theoretical investigations have had degrees of disagreement. However, a recent molecular dynamics investigation which studied slip boundaries on two amorphous surfaces, namely PDMS and amorphous carbon found slip lengths to be an order or magnitude lower (Groombridge et al. 2011) than previous experimental findings (Whitby et al. 2009). Therefore, although the extent to the enhancement factors in graphitic CNTs is still disputed, there appears to be strong agreement between the enhancement factors observed for the simulated results of Groombridge et al. (2011) and the present experimental data presented here.

8.4 Electroosmotic Flow in CNT Membranes

This section will present the results of EO in CNT membranes, comparing the effect of two different electrolytes on EO and assessing the effect of pore diameter on EOF. The latter also leads to consider the possibility of EO with EDL overlap. Comparisons are drawn between NPAMs and CNT membranes.

8.4.1 Conductance of CNT Membranes

A high density of fixed surface charge on a material is crucial to the magnitude of EOF. Therefore CNTs without functionalization do not exhibit great EOF

mobility (Miller et al. 2001; Miller and Martin 2002; Wu et al. 2011). The conductivity of the CNTs produced through the method of non-catalytic CVD was therefore calculated. This was performed on CNT membranes where Pt wires were connected either side of the membrane and a series of voltages applied to record the current. Conductance was calculated from Equation 8.4, which uses the linear relationship between the current, *I*, (mA) and voltage, *V*, (V).

$$\sigma = \frac{I}{V} \tag{8.4}$$

The conductance, σ, was calculated to be approximately $1 \cdot 10^{-4}$ S, an example of the measured *I-V* curve is shown in Figure 8.13. Mattia et al. previously measured the conductance of individual annealed CNTs and reported a similar value (Mattia et al. 2006). The measurements by Mattia et al. were conducted on individual CNTs and at relatively low voltages (1 - 7 V). A breakdown voltage was observed (where the current fell to zero) to be < 3V for CNTs produced through CVD at 670 °C. The breakdown was attributed to ohmic heating and tube oxidation (Collins et al. 2001; Lee et al. 2002). It is known that disordered carbon nanostructures oxidise at lower temperatures compared with ordered carbon nanostructures (Osswald et al. 2005). Therefore the EO experiments presented in this chapter were conducted at an externally applied voltage of 10 V. It is most likely that the carbon oxidises at this voltage. However, a breakdown voltage was not recorded in the range measured in the previous study.

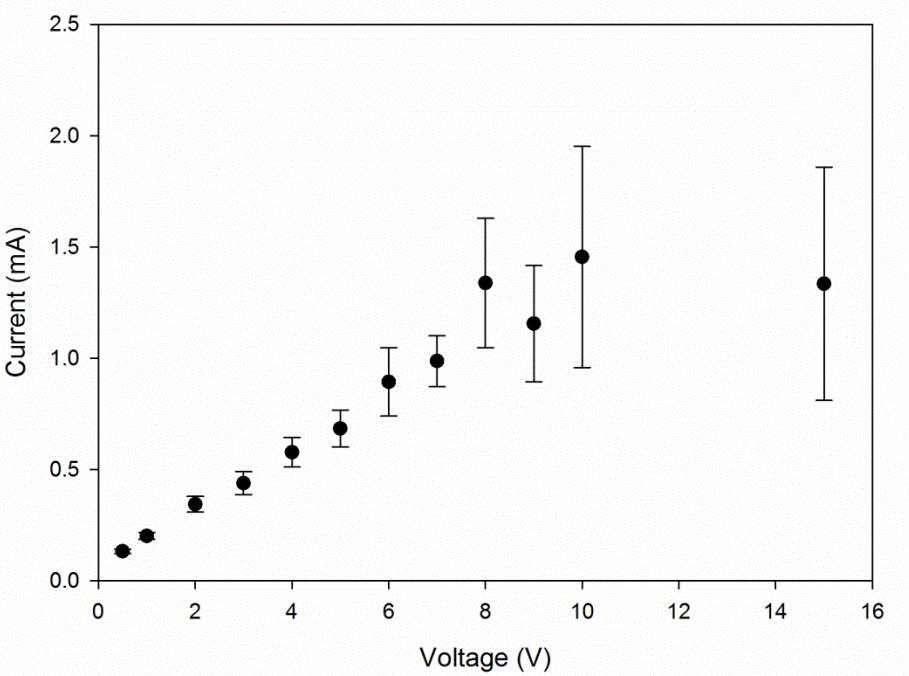

Figure 8.13 Current-voltage measurement of a CNT membrane produced at 670 °C (error bars SD of repeated runs n = 3).

8.4.2 Effect of Electrolyte and CNT Pore Diameter

Two different electrolytes were used to investigate EO in CNT membranes. The first was 5mM sodium tetraborate buffer, $Na_2O_7B_4$, the same electrolyte and concentration used to investigate EO in NPAMs. The second was 2mM NaCl as it is relevant to the potential use of using EO pumps as an aid to water filtration. These electrolytes have two different pH values: as $Na_2O_7B_4$ has pH ~ 9.2 and NaCl pH ~ 6.8. Unlike alumina both of the pH values of the electrolytes did not introduce a change in surface charge (as the isoelectric point for alumina ~ pH 8). Therefore, as discussed in Chapter 2 Section 2.3.3.2, the CNTs produced via template-assisted CVD have an anionic surface charge resulting in the Na^+ ions of both electrolytes making up the EDLs. The Debye lengths calculated from Equation 2.14 (see Chapter 2 Section 2.3.1) for 5mM $Na_2O_7B_4$ and 2mM NaCl are ~ 4.5 nm and ~ 9.6 nm, respectively.

The previous chapter suggested that EO was detected experimentally in the region of EDL overlap, in apparent contradiction to previous theoretical models and experimental findings. However due to the sensitivity of alumina to local pH changes it was not possible to measure (in this designed set-up) EO reliably with lower concentrations of $Na_2O_7B_4$ or with electrolytes pH < 8 (see Appendix B).

Therefore, to assess the effect of pore diameter on EO in CNT membranes a similar analysis to that of EO and NPAMs was applied. First the results were normalised so that membranes (which experienced different applied pressures and were of different thicknesses) could be accurately compared to one another. For all EO measurements in CNT membranes the external applied voltage was constant at 10 V to focus on the effect of pore diameter on EOF.

In this study it was of interest to compare EOF with the flow rates produced by pressure because of the possibility of integrating EO into current pumping systems. The relationship between the ratio of electroosmotic flow rates Q_{EO}, and normalised pressure-driven flow rates, $Q_{\Delta P}$* ($Q_{EO}/Q_{\Delta P}$*) with CNT pore diameters was therefore interrogated. This relationship has been shown in Figure 8.14. For both electrolytes, when the flow rate ratio between EO and pressure are compared, EO (as in alumina) becomes the major contributor to the total flow rate for the membranes of smallest diameter. The ratio $Q_{EO}/Q_{\Delta P}$* is < 1 for ~ D_P > 20 nm for experiments conducted in 5 mM $Na_2O_7B_4$ and ~ D_P > 25 nm for experiments conducted in 2 mM NaCl. This is not unexpected as it is possible that EO flow rates are the same or less than the flow rates produced at normalised pressure. If the efficiency of EO pumps were on par with the efficiency of present pressure-driven systems, EO could therefore be integrated as a support to pressure pumps for driving liquids.

From this study, it would be of particular interest to use EO in CNT membranes with D_P < 20 nm. Figure 8.14a sees a favourable increase in EOF rate (from 2 to 4 times) with D_P between 20 and 15 nm when 10 V was applied perpendicular to the pores. Due to the concentration of the borate buffer the EDL thickness is < 5 nm meaning that EDL overlap is not observed here (EDL overlap represented by dashed line in Figure 8.14a). EOF in CNT membranes on the whole was smaller when compared to EOF detected in NPAMs using the same buffer. This is most likely due to the surface charge density of the CNTs being smaller than that of alumina. The dependence on surface charge and EO was discussed in detail in Chapter 2 Section 2.3.3.2.

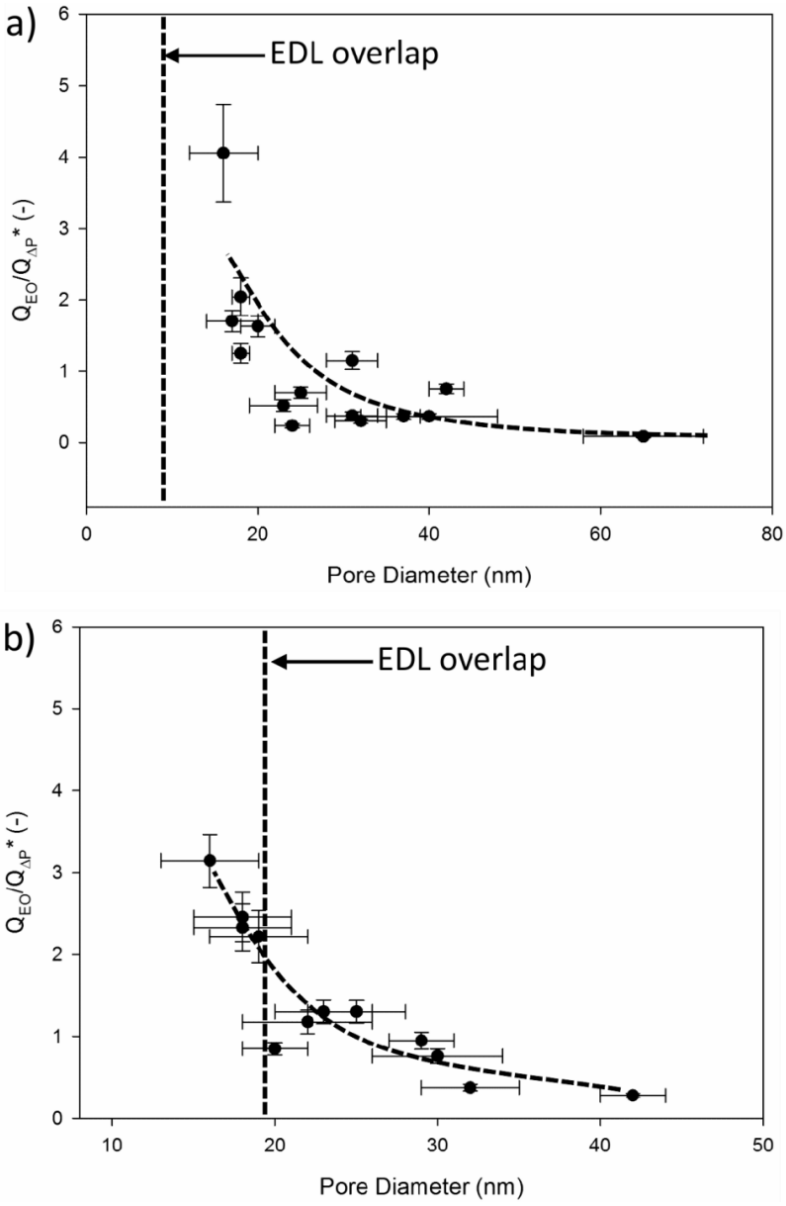

Figure 8.14 $Q_{EO}/Q_{\Delta P}$* with CNT pore diameter for a) 5 mM $Na_2O_7B_4$ and b) 2 mM NaCl - dashed lines represent EDL overlap. Error: SD of D_P and repeat EOF measurements (n = 3).

Figure 8.14b presents the data of $Q_{EO}/Q_{\Delta P}$* and CNT pore diameter with 2 mM NaCl. As mentioned earlier, the thickness of the EDL for 2 mM NaCl is ~ 10 nm. It is therefore likely that EDL overlap occurred in some of the EO experiments conducted in NaCl, as tests in CNT membranes with diameters of < 20 nm were conducted. The dashed line represents where the EDLs would theoretically overlap, and even though the magnitude of Q_{EO} is smaller than that for the borate buffer, EO is still detected with EDL overlap. A study discussed earlier, which reported highly efficient EOFs in CNT membranes, detected EO in CNT inner diameters between 1.5 and 7 nm, much smaller than the smallest CNTs tested in

this present study. Although the work does not explicitly discuss EDL overlap, it is likely that EDLs overlap in this study, as it utilised 10 mM KCl as the electrolyte solution would produce a theoretical EDL thickness of ~ 4 nm, resulting in EDL overlap for all of the EO experiments conducted in the study. A deeper theoretical assessment of EDL overlap in these materials needs to be conducted and this will be discussed in Chapter 9.

8.4.3 Concentration Polarization in CNT Membranes

As the EO experiments conducted in NPAMs were similar to those conducted in CNT membranes, similar limitations were observed in the form of EO pump lifetime due to, concentration polarization. Unlike the NPAMs system, it was possible to use a more neutral pH electrolyte to probe EO. This was not possible in the NPAMs due to the local pH becoming too acidic and, after a short time, degrading the alumina (resulting in membrane failure or highly etched pores) after a short period of time. The CNT membranes were less vulnerable to etching and it was therefore possible to successfully measure EOF using 2 mM NaCl. The externally applied voltage was kept constant at 10 V for all EO measurements in CNT membranes. At this voltage there was electrolysis at the Pt electrodes and concentration polarization at the membrane surface and electrodes as discussed previously (Strickland et al. 2010; Suss et al. 2011). It was also possible to use the EO pump at very small applied pressures (2.4 kPa - this pressure was caused by the height of the reservoir). However, the longevity of the pump would not extend beyond 15 minutes. Whilst this was still an improvement on the lifetime of some EO pumps, regeneration and improvement was desired. It was possible to regenerate the EO pump by redistributing the ions in the reservoir and this discussed below.

Figure 8.15 presents an example of a regeneration experiment. The plot presents the raw data of mass with time. This is not in an absolutely steady state owing to the reduction in EOF rate caused by concentration polarization. The current-time plot is also shown in this figure, highlighting the drop and regeneration in current. The current value recovered when a short pulse and release of pressure was applied to the membrane (50 kPa). On releasing this pressure the build-up of ions on the membrane surface were dislodged and redistributed into the reservoir

(caused by a back pressure generated on releasing the pressure). The current density then recovers, maintaining the EO pump for extended periods of time. It is not practical to apply and release pressure sequentially in these systems and so a cross-flow system has been proposed as a more practical solution to overcome CP. This has been discussed in *Proposed Future Work* in Chapter 9. This evidence of CP also supports the understanding that DC EO cannot be used in a continuous process, though it could be utilised to support mechanical pumping or in applications where pumping is only needed for very short periods of time.

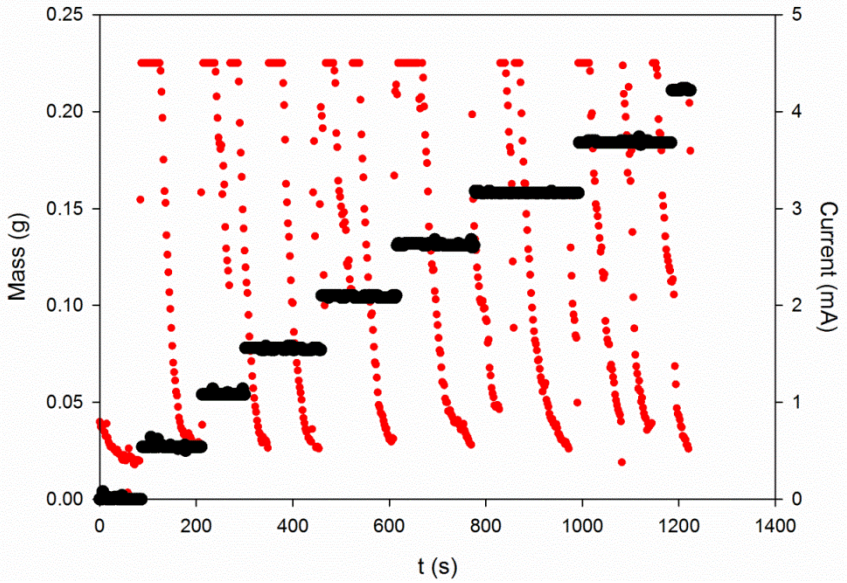

Figure 8.15 Regenerated CNT membrane EO pump with D_P = 26 ± 3 nm (the applied pressure caused by the height of the reservoir was minimal 2.4 kPa) (●) presents the mass with time when 10 V is applied to the membrane and (●) is the measured current.

8.5 Summary

This chapter has presented research conducted in CNT membranes engineered through a template-synthesis method using non-catalytic CVD. The first sections discussed results from the characterisation methods used. These included SEM, TEM, Raman spectroscopy and a discussion of wetting properties. Due to initial low flow rates through the CNTs a more in-depth study into the CVD parameters and quality of NPAMs was conducted. This found that the lowest total flow rates of gases used in the CVD process resulted in blocking of the channels and a coating of the faces of the membranes. It was also found that in NPAMs of poor quality branching resulted in pore blockage. The optimisation of CVD parameters was therefore conducted and much faster gas flow rates were used (up to

160 sccm). CNT membranes with pore diameters from 16 - 60 nm were also fabricated. The smallest pore diameters were produced by increasing CVD deposition time. The anodization process which produced the highest quality membranes was consistently used, ensuring that branching did not occur in NPAM channels.

After full characterisation and optimisation of the CNT membranes had been presented, the next section discussed the results for pressure-driven flow rates in a series of CNT membranes with pore diameters from 16 - 60 nm. This is the first study which has performed systematic studies of fluid flow in CNT membranes produced by CVD in NPAMs. Due to the abundant amount of work on fluid flow in CNTs, the experimental flow rates were compared to the no-slip Hagen-Poiseuille model and flow enhancement factors were observed. The enhancements were lower than the majority of previous experimental and theoretical results of fluid flow in CNTs. This could be for two reasons (i) the surface chemistry of the CNTs is much closer to that of a metal oxide like alumina and (ii) there are internal blockages that were not identified in the characterisation process. Over sixty samples were tested and more than a hundred CNT membranes were fabricated. The largest flow enhancement observed in all the tests was ~ 10.

The final section of this chapter discussed EOF in CNT membranes. This is the first study to assess the effect of CNT pore diameter on EOF. Two electrolytes were used: 5 mM $Na_2O_7B_4$ and 2 mM NaCl. This enabled (i) a comparison to the EO in NPAMs when using the $Na_2O_7B_4$ buffer and (ii) an increase in EDL thickness by using NaCl to assess the effect of EDL overlap. Similar to the NPAM EO pumps it was possible to compare the pressure-driven flow rates and EO flow rates as a function of pore diameter. Both the borate buffer and NaCl EO produced higher flow rates than the pressure-driven flow rates for D_P < 20 nm. It is also possible that EO was observed at EDL overlap for the EO experiments conducted in 2 mM NaCl, contrary to theoretical predictions. The theoretical EDL thickness for 2 mM NaCl was calculated to be ~ 10 nm. This finding is supported by a recent investigation by Wu et al. where EO in CNT membranes with inner channel diameters of ~ 7 nm was observed with a solution of 10 mM KCl producing an EDL thickness of ~ 4 nm. Finally, CP in CNT membrane EO pumps was discussed and a method to regenerate EOF was also presented.

Chapter 9

Conclusions and Proposed Future Work

9.1 Conclusions

The aim of the work presented throughout this thesis was to provide further understanding of fluid flow at the nanoscale by developing NPAMs and assessing the effects of pore diameter, surface chemistry and surface structure. The main focus was on pressure-driven and electroosmotic flow in nanoporous alumina and carbon nanotube membranes. Wetting properties were also investigated and slip was identified on the alumina via AFM dynamic force measurements. This final chapter will conclude the main findings from each of the results chapters and suggest possible avenues for future research.

9.1.1 Characterisation and Manipulation of NPAMs

The development and optimisation of aluminium anodization produced highly controlled and reproducible membranes with nanoscale precision. A series of membranes with controlled pore diameters were produced with applied anodization voltage, and the results supported existing accounts of the relationship between anodization voltage and the pore diameter of the resulting nanoporous alumina of ~ 1.25 nm V^{-1}. NPAMs were also manipulated using hydrothermal treatment. Three methods were utilised to hydrothermally shrink the pores of the nanoporous alumina: (i) hydrothermal treatment by electrochemical detection (ii) hydrothermal treatment by boiling water and (iii) hydrothermal treatment by steam. Though each method was successful in shrinking the pores, the most successful method was the third, which produced shrunken pores (up to ~ 50%), mechanically stable membranes with increased and robustness, and smaller pore diameters (which also decreased porosity). A limit to the degree of shrinkage was observed, (most likely due to material and size effects) whereby, at a certain activation point, fibres developed on the surface and the pores ceased to shrink. This is the first time that the hydrothermal treatment of alumina has been conducted in open-through channels, all previous studies having performed

hydrothermal treatment with the barrier oxide layer intact. Although this method was not utilised to obtain smaller pore diameters for subsequent fluid and electroosmotic flows, it will be of interest for tuning wetting properties through surface features as well as for the study of the ageing effects of alumina.

9.1.2 Wetting Properties of PAAs

This study systematically investigated two alumina nanostructures, namely porous and dome nanostructures, and the effect they have on the macro wetting properties of alumina surfaces. To further this investigation, the surface chemistry was also changed to render the nanostructures hydrophobic. This gave two surface chemistry platforms (one hydrophilic and the other hydrophobic) from which the relationship and contribution to the wetting behaviour between (i) nanostructure and wetting properties and (ii) surface chemistry and wetting properties could be separated and analysed. Nanoporous structures with a series of pore diameters from 10 to 240 nm showed an increase in water CA from 12 - 90° (for hydrophilic surfaces). The same trend was observed for hydrophobic surfaces (same structure size range), though these showed CAs from 103 - 150° due to the hydrophobicity of the solid surface. This is the first time such small surface features have been identified to have an effect on the macro wetting properties of alumina. The quasi-constant porosity of nanoporous alumina highlighted in Chapter 4 and 5 proved to be the main deviation from (and limiting factor to) the Cassie-Baxter wetting model. A model was therefore proposed, adapted from a previous model developed by Marmur, which incorporated both the Cassie-Baxter and the Wenzel equations. The structural parameters of the nanoporous alumina were crucial in deriving the solid surface fraction factors, f and r_f, and adapting and applying these to the existing model. In addition, hydrophilic nanodomes of size range 20 - 250 nm were shown to increase the macro CA from 20 - 85°. A similar wetting regime to that of the nanoporous alumina was identified, where the porosity was also constant. An increased volume of air was trapped between the dome structures and beneath the water droplet with increasing nanodome diameter, ultimately increasing the macro CA.

9.1.3 Pressure-Driven Flow in NPAMs by AFM

Chapter 6 first introduced the recent study of enhanced water flow in hydrophilic NPAMs. This is the first report of a systematic investigation on a series of hydrophilic membranes with channels from 29 to 96 nm. By comparing experimental permeability with the theoretical permeability calculated by the no-slip Hagen-Poiseuille equation, flow enhancement factors of up to 3 were found for the membranes with the smallest diameter. Enhanced flow rates were unexpected in hydrophilic systems as the main focus of flow enhancement has been on the more hydrophobic CNTs. To further investigate the possibility of slip on hydrophilic surfaces, dynamic force measurements were performed by AFM, which formed the main body of this chapter. The force measurements were performed on a series of porous alumina, one set with closed pores and the other open with pores. The closed pores were used to observe the hydrodynamics of the surface and compare these with the open pore system. By driving a colloid-particle into the alumina surface it was possible to detect flow through the pores in the open pore system. However, the pressure generated by the particle produced small amounts of drainage through the open channels. The surface features directed the main variance between samples. A model was developed by collaborator Mr Chu Wu from the University of Melbourne to support the experimental data using MATLAB. The no-slip boundary condition was no longer applicable for the closed pore samples with a porous surface. Slip lengths were also calculated for each sample and correlated with the average pore diameter of the sample. It was found that the slip length increased with increasing pore diameter. This was attributed to the interaction of the colloid particle with the solid surface and liquid (within the pores). It is this heterogeneous surface which generates a slip term. Although the overriding factor of slip observed in these systems was due to the heterogeneous surface it was also possible to investigate the hydrodynamics of these systems.

9.1.4 Electroosmotic Flow in NPAMs

Chapter 7 systematically assessed the effect of pore diameter on EOF. Pore diameters ranged from ~ 8 to 100 nm. A constant applied voltage of 10 V was used so that the effect on EOF was due solely to pore diameter. The magnitude of

EOF was more significant for the smallest diameters, especially compared to pressure-driven flow rates observed in the same pore diameters. Sodium tetraborate buffer was used as this was found to produce the most stable EO pumping. The ionic concentration was also kept constant at 5 mM for the pore diameter tests. EO was detected in the region of EDL overlap, contrary to theoretical predictions. The effect of applied voltage and the ionic concentration of the borate buffer were also investigated. Ultimately, for both increasing applied voltages and ionic strength the EOF rates increased.

In addition, this chapter also investigated the efficiency of NPAM-EO pumps and the aspects of EO which directly affect the lifetime of EO pumps. The main limitation preventing EO pumps from making more practical outputs has been their inefficiency and lifetimes. This study was able to extend the lifetime of an EO pump for up to 4 hours (including regeneration). This is a substantial improvement on existing EO pumps. To do this, an understanding of the limitations were necessary, and these were found to be (i) concentration polarization at the membrane surface, and (ii) ion depletion and enrichment zones in the buffer, which changes local pH and reduces the magnitude of the EOF. A simple model has been developed to observe the behaviour of the concentration polarization layer and the resistance it presents over time.

9.1.5 Pressure-Driven and Electroosmotic Flow in CNT Membranes

Chapter 8 sought to utilise the already enhanced flow rates observed in CNTs to produce a highly efficient EO pump, drawing on the results from NPAM-EO pumps. Optimisation for the production of the CNT membranes was first conducted, which highlighted the necessity of high quality NPAMs and fast gas flow rates in the CVD process in order to produce working membranes free from blocked channels. To analyse this, an extensive characterisation of CNT membranes was conducted using SEM, TEM, and Raman spectroscopy on the fabricated membranes. A systematic investigation into the effect of pore diameter on fluid flow was then conducted and this found flow enhancements of up to 10 (compared to the no-slip Hagen-Poiseuille model) for CNT membranes with inner diameters of 16 nm.

CNT membranes were then investigated for the effect of EOF with a series of pore diameters (16 - 65 nm). As discussed in Chapter 2 and Chapter 8, the magnitude of surface charge is dependent on EO mobility. The surface charge of the as-produced CNTs was relatively small, resulting in a similar EOF to that observed in the NPAMs. However, a similar relationship to NPAMs was observed between decreasing pore diameters and increasing EO. Due to the stability of the CNTs compared with the NPAMs it was also possible to investigate a more neutral electrolyte such as 2 mM NaCl. The EDL thickness of the borate buffer and NaCl were calculated to be approximately 4.5 and 9.6 nm respectively. For the smallest inner diameters of CNTs tested (~ 16 nm), electroosmosis was still observed at EDL overlap, which is contrary to theoretical predications. The same experimental set-up was used to assess the EO of NPAMs and CNT membranes and similar limitations of efficiency and EO pump lifetimes were observed.

9.2 Proposed Future Work

This section will discuss several ideas for possible future work, which could build on the platform provided by this thesis.

9.2.1 Further Optimisation of the Production of NPAMs

The aluminium anodization process to obtain highly ordered porous structures has been optimised in this study. However, the sample holder for anodization could be further developed. One might redesign the sample holder, for instance, to allow three membranes to be made in one anodization experiment. This would significantly increase production rate, since with the present system only one sample can be produced per anodization rig. As the anodization process (from aluminium to working membrane) takes approximately 24 hours, this would greatly increase production rates and also minimize variability between samples produced under the same conditions. The three produced membranes could be used in subsequent experiments such as filtration or EO experiments. Figure 9.1 is a design of the proposed sample holder for the electropolishing, anodization, and aluminium removal processes.

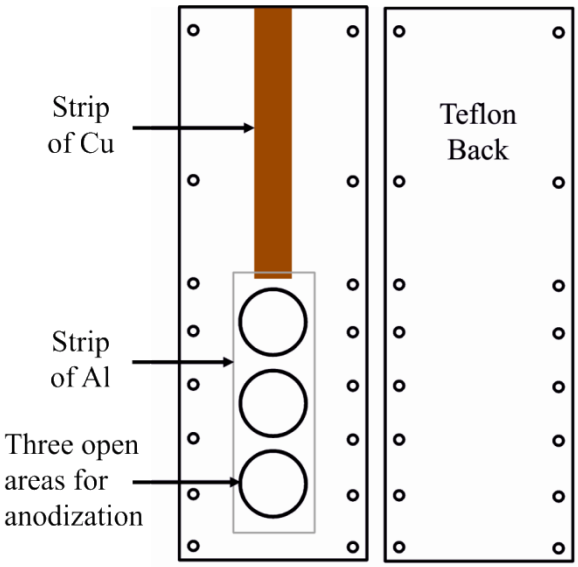

Figure 9.1 Schematic of the developed sample holder for flat sheet aluminium anodization

9.2.2 Template Synthesis of Boron Nitride Nanotubes for Fluid Flow Investigations

This thesis utilised NPAMs as templates for the production of CNT membranes. The use of NPAMs as templates for other nanotube materials was also highlighted. A project proposed here recommends using NPAMs as a template for the production of boron nitride nanotubes (BNNTs). Few publications have discussed the synthesis of BNNTs in nanoporous alumina membranes (Bechelany et al. 2007; Shelimov and Moskovits 1999), but this remains an interesting possibility. New work would need to optimise the synthesis process, as current synthesis pathways are expensive and labour intensive. Once the BNNT membranes are engineered, fluid investigations (of water in particular) could be conducted. To date, there have been no experimental investigations of water flow inside BNNTs, but molecular dynamic simulations have found similar fast flow rates to those in CNTs (Suk et al. 2008; Hilder et al. 2009a; Hilder et al. 2009b; Won and Aluru 2007). The fast flow rates and salt rejection of BNNTs suggest real potential for reducing energy intensive filtration processes. BNNT membranes are not just of interest for their fluid flow properties, however. They have also been shown to be more biocompatible than CNTs, which is not only important for water filtration but also for the development of membranes for drug delivery applications (Chen et al. 2009; Ciani and Ristori 2012). They have been shown to have anti-fouling properties which are also of paramount importance in

the longevity of filtration systems. This would be a substantial project, but one that would be of significant value to nanofluidic studies and the drive to improve membrane processes.

9.2.3 Electroosmotic Flows in NPAMs and CNT Membranes

This work observed much higher flow rates in NPAMs and CNT membranes when using electroosmosis rather than pressure-driven flows, especially with pore diameters, D_P < 25 nm. To capitalise further on this, it is proposed that a systematic study of surface-modified NPAMs and CNT membranes be conducted. This would lead the way to increasing the surface charge density of both materials, which would increase EOF rates even further. It would also be possible to inspect the effect of surface-modification on pressure-driven flow rates, especially to see the effect on flow enhancement in the membranes. Surface modification for the CNT membranes could entail using plasma treatment and electrochemical grafting of either oxidative or reductive compounds. This could add control to the direction of EOF, touched upon in a previous study (Miller and Martin 2004). In addition, the effect of pore diameter would also be investigated.

Extended studies of concentration polarization with NPAMs as EO pumps would be especially useful to further optimise the process. This could be carried out by combining two approaches: (i) by qualitatively observing CP and the ion depletion and enrichment zones by using an inverted epifluorescent microscope and fluorescein dye (Suss et al. 2011), and (ii) by developing a computational model to analyse the propagation of CP in NPAM and CNT membrane EO pumps.

For a more in-depth study of EDL overlap and its effects on EO, it would be useful to conduct a systematic study on the effect of pore diameter (of both NPAMs and CNTs) and concentration of electrolytes using impedance spectroscopy measurements. This could provide more information on the effect of EDLs under pressure-driven and EO flows as impedance spectroscopy provides information on the electronic carrier concentration at the surface as well as on the rates of interfacial charge transfer. This would also add significantly to our understanding of EOF and EDL overlap at this scale.

After the limitations of the EO process discussed in the EO chapters (Chapters 7 and 8), it is evident that EO in the current set-up cannot be a continuous process. It is therefore proposed that a cross-flow system be developed which could overcome reduction in EOF rates due to CP. The EO chapters observed (with a qualitative method) the regeneration of EO pumping by redistributing the ions of the buffer on reversing flow and creating a back pressure in the system (see Section 7.4, Chapter 7). It could be possible therefore, to develop a cross-flow membrane holder which would keep depletion and enrichment zones to a minimum and create a more continuous EO process.

Although EOF has found application in lab-on-a-chip devices, its use in larger scale processes such as water filtration has not yet come to fruition. If the efficiency and other limitations of EO could be overcome (by developing the methods discussed above) it would become possible to use the nanoporous materials developed throughout this work in a more continuous EO pumping process. If a scale-up procedure was to be pursued, the morphology of the membrane would have to change, as the anodization process of large fragile sheet membranes would be impractical. It is proposed here that this could be achieved by adapting the process of the tubular anodized alumina membranes (see Figure 9.2) developed by Lee and Mattia (2013). Cross-flow could be incorporated into such a set-up design to reduce the negative effects that concentration polarization has on EO. An example of a cross-flow EO membrane holder has been shown in Figure 9.2. The internal bore of the tubular alumina membrane is open. A cross-flow perpendicular to the pores of the membrane could therefore be driven through the internal bore. One Pt electrode would be inserted inside the bore and the other would be spiralled around the outside of the membrane. Both the inside of the membrane bore and the outer casing of the membrane holder would be filled with buffer.

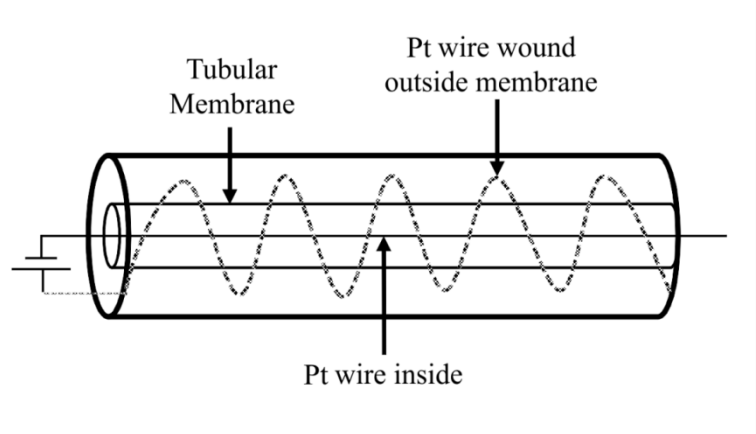

Figure 9.2 Schematic of proposed cross-flow EO membrane holder.

9.3 Concluding Remarks

This thesis has addressed fundamental questions which remain regarding electroosmotic flow at the nanoscale. It examined fluid flow behaviour at the nanoscale by systematically studying the effect of pore diameter and surface chemistry in NPAMs and CNT membranes. It also considered the effect of EDL overlap on EOF and assessed challenges to EO pumping in practical applications. Building on the research presented here, the future work proposed above would represent a significant step towards the realisation of successful nanofluidic devices for water filtration and lab-on-a-chip applications.

References

Ai, Y., Yalcin, S. E., Gu, D., Baysal, O., Baumgart, H., Qian, S. & Beskok, A. 2010. A low-voltage nano-porous electroosmotic pump. *Journal of Colloid and Interface Science,* 350**,** 465-470.

Ajayan, P. M. & Iijima, S. 1993. Capillarity-induced filling of carbon nanotubes. *Nature,* 361**,** 333-334.

Aran, H. C., Chinthaginjala, J. K., Groote, R., Roelofs, T., Lefferts, L., Wessling, M. & Lammertink, R. G. H. 2011. Porous ceramic mesoreactors: A new approach for gas–liquid contacting in multiphase microreaction technology. *Chemical Engineering Journal,* 169**,** 239-246.

Bandyopadhyay, S., Miller, A. E., Chang, H. C., Banerjee, G., Yuzhakov, V., Yue, D.-F., Ricker, R. E., Jones, S., Eastman, J. A., Baugher, E. & Chandrasekhar, M. 1996. Electrochemically assembled quasi-periodic quantum dot arrays. *Nanotechnology,* 7**,** 360-371.

Barrat, J. L. & Bocquet, L. 1999. Large slip effect at a nonwetting fluid-solid interface. *Physical Review Letters,* 82**,** 4671-4674.

Bechelany, M., Bernard, S., Brioude, A., Cornu, D., Stadelmann, P., Charcosset, C., Fiaty, K. & Miele, P. 2007. Synthesis of boron nitride nanotubes by a template-assisted polymer thermolysis process. *The Journal of Physical Chemistry C,* 111**,** 13378-13384.

Besteman, K., Zevenbergen, M. A. G., Heering, H. A. & Lemay, S. G. 2004. Direct observation of charge inversion by multivalent ions as a universal Electrostatic Phenomenon. *Physical Review Letters,* 93**,** 170802-4.

Binnig, G., Quate, C. F. & Gerber, C. 1986. Atomic force microscope. *Physical Review Letters,* 56**,** 930-933.

Bismarck, A. & Springer, J. 1999. Characterization of fluorinated PAN-based carbon fibers by zeta-potential measurements. *Colloids and Surfaces A: Physicochemical and Engineering Aspects,* 159**,** 331-339.

Blake, T. D. 1990. Slip between a liquid and a solid: D.M. Tolstoi's (1952) theory reconsidered. *Colloids and Surfaces,* 47**,** 135-145.

Boisier, G., Pébère, N., Druez, C., Villatte, M. & Suel, S. 2008. FESEM and EIS study of sealed AA2024 T3 anodized in sulfuric acid electrolytes: Influence of Tartaric Acid. *Journal of the Electrochemical Society,* 155**,** C521-C529.

Bonaccurso, E., Butt, H.-J. & Craig, V. S. J. 2003. Surface roughness and hydrodynamic boundary slip of a Newtonian fluid in a completely wetting system. *Physical Review Letters,* 90**,** 144501-4.

Bormashenko, E., Bormashenko, Y., Stein, T., Whyman, G., Pogreb, R. & Barkay, Z. 2007. Environmental scanning electron microscopy study of the fine structure of the triple line and Cassie-Wenzel wetting transition for sessile drops deposited on rough polymer substrates. *Langmuir*, 8, 4378-4382.

Brask, A., Kutter, J. P. & Bruus, H. 2005. Long-term stable electroosmotic pump with ion exchange membranes. *Lab on a Chip,* 5**,** 730-738.

Bruus, H. 2007. *Theoretical Microfluidics (Oxford Master Series in Physics)*, Oxford University Press, USA.

Burns, D. B. & Zydney, A. L. 2000. Buffer effects on the zeta potential of ultrafiltration membranes. *Journal of Membrane Science,* 172**,** 39-48.

Butt, H.-J., Cappella, B. & Kappl, M. 2005. Force measurements with the atomic force microscope: Technique, interpretation and applications. *Surface Science Reports,* 59**,** 1-152.

Bwana, N. 2008. Synthesis of highly ordered nanopores on alumina by two-step anodization process. *Journal of Nanoparticle Research,* 10**,** 313-319.

Cao, Z., Yuan, L., Liu, Y. F., Yao, S. & Yobas, L. 2012. Microchannel plate electro-osmotic pump. *Microfluidics and Nanofluidics,* 13**,** 279-288.

Cassie, A. B. D. & Baxter, S. 1944. Wettability of porous surfaces. *Transactions of the Faraday Society,* 40**,** 546-551.

Cervera, J., Alcaraz, A., Schiedt, B., Neumann, R. & Ramírez, P. 2007. Asymmetric selectivity of synthetic conical nanopores probed by reversal potential measurements. *The Journal of Physical Chemistry C,* 111**,** 12265-12273.

Chan, D. Y. C. & Horn, R. G. 1985. The drainage of thin liquid films between solid surfaces. *The Journal of Chemical Physics,* 83**,** 5311-5324.

Chan, D. Y. C., Klaseboer, E. & Manica, R. 2011. Theory of non-equilibrium force measurements involving deformable drops and bubbles. *Advances in Colloid and Interface Science,* 165**,** 70-90.

Che, G., Lakshmi, B. B., Martin, C. R. & Fisher, E. R. 1998. Chemical vapor deposition based synthesis of carbon nanotubes and nanofibers using a template method. *Chemistry of Materials,* 10**,** 260-267.

Chen, Y.-F., Hu, Y.-H., Chou, Y.-I., Lai, S.-M. & Wang, C.-C. 2010. Surface modification of nano-porous anodic alumina membranes and its use in electroosmotic flow. *Sensors and Actuators B: Chemical,* 145**,** 575-582.

Chen, Y.-F., Li, M.-C., Hu, Y.-H., Chang, W.-J. & Wang, C.-C. 2008a. Low-voltage electroosmotic pumping using porous anodic alumina membranes. *Microfluidics and Nanofluidics,* 5**,** 235-244.

Chen, Y., Ni, Z., Wang, G., Xu, D. & Li, D. Y. 2008b. Electroosmotic flow in nanotubes with high surface charge densities. *Nano Letters.,* 8**,** 42-48.

Chen, X., Wu, P., Rousseas, M., Okawa, D., Gartner, Z., Zettl, A. & Bertozzi, C. R. 2009. Boron nitride nanotubes are noncytotoxic and can be functionalized for interaction with proteins and dells. *Journal of the American Chemical Society,* 131**,** 890-891.

Cheng, J. T. & Giordano, N. 2002. Fluid flow through nanometer-scale channels. *Physical Review E,* 65**,** 031206-5.

Cheng, Q.-M., Interrante, L. V., Lienhard, M., Shen, Q. & Wu, Z. 2005. Methylene-bridged carbosilanes and polycarbosilanes as precursors to silicon carbide—from ceramic composites to SiC nanomaterials. *Journal of the European Ceramic Society,* 25**,** 233-241.

Choi, J., Sauer, G., Nielsch, K., Wehrspohn, R. B. & Gösele, U. 2003. Hexagonally arranged monodisperse silver nanowires with adjustable diameter and high aspect ratio. *Chemistry of Materials,* 15**,** 776-779.

Chu, S.-Z., Wada, K., Inoue, S., Isogai, M. & Yasumori, A. 2005. Fabrication of ideally ordered nanoporous alumina films and integrated alumina nanotubule arrays by high-field anodization. *Advanced Materials,* 17**,** 2115-2119.

Chuan-Hua, C. & Santiago, J. G. 2002. A planar electroosmotic micropump. *Journal of Microelectromechanical Systems,* 11**,** 672-683.

Ciani, L. & Ristori, S. 2012. Boron as a platform for new drug design. *Expert Opinion on Drug Discovery,* 7**,** 1017-1027.

Collins, P. G., Hersam, M., Arnold, M., Martel, R. & Avouris, P. 2001. Current saturation and electrical breakdown in multiwalled carbon nanotubes. *Physical Review Letters,* 86**,** 3128-3131.

Corry, B. 2011. Water and ion transport through functionalised carbon nanotubes: implications for desalination technology. *Energy & Environmental Science,* 4**,** 751-759.

Corti, H., Crovetto, R. & Fernandez-Prini, R. 1980. Properties of the borate ion in dilute aqueous solutions. *Journal of the Chemical Society, Faraday Transactions 1: Physical Chemistry in Condensed Phases,* 76**,** 2179-2186.

Dagastine, R. R., Webber, G. B., Manica, R., Stevens, G. W., Grieser, F. & Chan, D. Y. C. 2010. Viscosity effects on hydrodynamic drainage force measurements involving deformable bodies. *Langmuir,* 26**,** 11921-11927.

Dai, H. 2002. Carbon nanotubes: Synthesis, integration, and properties. *Accounts of Chemical Research,* 35**,** 1035-1044.

De Gennes, P. G., Brochard-Wyard, F. & Quere, D. 2004. *Capillarity and wetting phenomena: drops, bubbles, pearls, waves,* New York, Springer.

Ding, G., Yang, R., Ding, J., Yuan, N. & Zhu, Y. 2010. Fabrication of porous anodic alumina with ultrasmall nanopores. *Nanoscale Research Letters,* 5**,** 1257-1263.

Dujardin, E., Ebbesen, T., Hiura, H. & Tanigaki, K. 1994. Capillarity and wetting of carbon nanotubes. *Science,* 265**,** 1850-1852.

Edwards, J. D. & Keller, F. 1941. Formation of anodic coatings on aluminum. *Transactions of The Electrochemical Society,* 79**,** 135-144.

Erlandsson, P. G. & Robinson, N. D. 2011. Electrolysis-reducing electrodes for electrokinetic devices. *Electrophoresis,* 32**,** 784-790.

Falk, K., Sedlmeier, F., Joly, L., Netz, R. R. & Bocquet, L. R. 2010. Molecular origin of fast water transport in carbon nanotube membranes: superlubricity versus curvature dependent friction. *Nano Letters,* 10**,** 4067-4073.

Frackowiak, E. & Béguin, F. 2002. Electrochemical storage of energy in carbon nanotubes and nanostructured carbons. *Carbon,* 40**,** 1775-1787.

Franks, G. V. & Meagher, L. 2003. The isoelectric points of sapphire crystals and alpha-alumina powder. *Colloids and Surfaces A: Physicochemical and Engineering Aspects,* 214**,** 99-110.

Freund, J. B. 2002. Electro-osmosis in a nanometer-scale channel studied by atomistic simulation. *Journal of Chemical Physics,* 116**,** 2194-2200.

Gan, W.-E., Yang, L., He, Y.-Z., Zeng, R.-H., Cervera, M. L. & de La Guardia, M. 2000. Mechanism of porous core electroosmotic pump flow injection system and its application to determination of chromium (VI) in waste-water. *Talanta,* 51**,** 667-675.

Gao, L. C. & McCarthy, T. J. 2007. How Wenzel and Cassie were wrong. *Langmuir,* 23**,** 3762-3765.

García, A. B., Cuesta, A., Montes-Morán, M. A., Martínez-Alonso, A. & Tascón, J. M. D. 1997. Zeta Potential as a tool to characterize plasma oxidation of carbon fibers. *Journal of Colloid and Interface Science,* 192**,** 363-367.

Gibbs, J. W. 1928. *The Collected Works of J. Willard Gibbs - Volume I. Thermodynamics,* New Haven, Connecticut., Yale University Press.

Gogotsi, Y., Libera, J. A., Guvenc-Yazicioglu, A. & Megaridis, C. M. 2001. In situ multiphase fluid experiments in hydrothermal carbon nanotubes. *Applied Physics Letters,* 79**,** 1021-1023.

Gojny, F. H., Wichmann, M. H. G., Köpke, U., Fiedler, B. & Schulte, K. 2004. Carbon nanotube-reinforced epoxy-composites: enhanced stiffness and fracture toughness at low nanotube content. *Composites Science and Technology,* 64**,** 2363-2371.

Groombridge, M., Schneemilch, M., & Quirke, N. 2011. Slip boundaries in nanopores. *Molecular Simulation,* 37, 1023-1030.

Guo, M., Diao, P. & Cai, S. M. 2007. Highly hydrophilic and superhydrophobic ZnO nanorod array films. *Thin Solid Films,* 515**,** 7162-7166.

Gupta, R. & Fréchette, J. 2012. Measurement and scaling of hydrodynamic interactions in the presence of draining channels. *Langmuir,* 28**,** 14703-14712.

Han, A., Mondin, G., Hegelbach, N. G., De Rooij, N. F. & Stuafer, U. 2006. Filling kinetics of liquids in nanochannels as narrow as 27 nm by capillary force. *Journal of Colloid and Interface Science,* 293**,** 151-157.

Helmholtz, H. 1879. Studien über electrische Grenzschichten. *Annalen der Physik,* 243**,** 337-382.

Herderick, E. D., Tresback, J. S., Vasiliev, A. L. & Padture, N. P. 2007. Template-directed synthesis, characterization and electrical properties of Au-TiO_2-Au heterojunction nanowires. *Nanotechnology,* 18**,** 155204-6.

Hernandez, A., Martinez, F., Martín, A. & Prádanos, P. 1995. Porous structure and surface charge density on the walls of microporous alumina membranes. *Journal of Colloid and Interface Science,* 173**,** 284-296.

Hilder, T. A., Gordon, D. & Chung, S. H. 2009a. Boron nitride nanotubes selectively permeable to cations or anions. *Small,* 5**,** 2870-2875.

Hilder, T. A., Gordon, D. & Chung, S. H. 2009b. Salt rejection and water transport through boron nitride nanotubes. *Small,* 5**,** 2183-2190.

Hinds, B. 2012. Dramatic transport properties of carbon nanotube membranes for a robust protein channel mimetic platform. *Current Opinion in Solid State and Materials Science,* 16**,** 1-9.

Hinds, B. J., Chopra, N., Rantell, T., Andrews, R., Gavalas, V. & Bachas, L. G. 2004. Aligned multiwalled carbon nanotube membranes. *Science,* 303**,** 62-65.

Ho, T. A., Papavassiliou, D. V., Lee, L. L. & Striolo, A. 2011. Liquid water can slip on a hydrophilic surface. *Proceedings of the National Academy of Sciences,* 108**,** 16170-16175.

Holt, J. K. 2009. Carbon nanotubes and nanofluidic transport. *Advanced Materials,* 21**,** 3542-3550.

Holt, J. K., Park, H. G., Wang, Y., Stadermann, M., Artyukhin, A. B., Grigoropoulos, C. P., Noy, A. & Bakajin, O. 2006. Fast mass transport through sub-2-nanometer carbon nanotubes. *Science,* 312**,** 1034-1037.

Huang, D. M., Sendner, C., Horinek, D., Netz, R. R., Bocquet, L. 2008. Water slippage versus contact angle: a quasiuniversal relationship. *Physical Review Letters,* 101**,** 226101-4.

Hummer, G., Rasaiah, J. C. & Noworyta, J. P. 2001. Water conduction through the hydrophobic channel of a carbon nanotube. *Nature,* 414**,** 188-190.

Hunter, R. J. 1981. *Zeta potential in colloid science,* London, Academic Press.

Huntz, A. M., Maréchal, L., Lesage, B. & Molins, R. 2006. Thermal expansion coefficient of alumina films developed by oxidation of a FeCrAl alloy determined by a deflection technique. *Applied Surface Science,* 252**,** 7781-7787.

Hutter, J. L. & Bechhoefer, J. 1993. Calibration of atomic-force microscope tips. *Review of Scientific Instruments,* 64**,** 1868-1873.

Iijima, S. 1991. Helical microtubules of graphitic carbon. *Nature,* 354**,** 56-58.

Iijima, S. & Ichihashi, T. 1993. Single-shell carbon nanotubes of 1-nm diameter. *Nature,* 363**,** 603-605.

Iwasaki, T., Motoi, T. & Den, T. 1999. Multiwalled carbon nanotubes growth in anodic alumina nanoholes. *Applied Physics Letters,* 75**,** 2044-2046.

Jessensky, O., Muller, F. & Gösele, U. 1998. Self-organized formation of hexagonal pore structures in anodic alumina. *Journal of the Electrochemical Society,* 145**,** 3735-3740.

Jiang, H., Liu, B., Huang, Y. & Hwang, K. C. 2004. Thermal expansion of single wall carbon nanotubes. *Journal of Engineering Materials and Technology,* 126**,** 265-270.

Joseph, S. & Aluru, N. R. 2008. Why are carbon nanotubes fast transporters of water? *Nano Letters,* 8**,** 452-458.

Kalra, A., Garde, S. & Hummer, G. 2003. Osmotic water transport through carbon nanotubes membranes. *PNAS,* 100**,** 10175-10180.

Keller, F., Hunter, M. S. & Robinson, D. L. 1953. Structural features of oxide coatings on aluminum. *Journal of The Electrochemical Society,* 100**,** 411-419.

Kirby, B. J. 2010. *Micro- and Nanoscale Fluid Mechanics: Transport in Microfluidic Devices,* United States of America, Cambridge University Press.

Kirby, B. J. & Hasselbrink, E. F. 2004. Zeta potential of microfluidic substrates: 1. Theory, experimental techniques, and effects on separations. *Electrophoresis,* 25**,** 187-202.

Kong, J., Franklin, N. R., Zhou, C., Chapline, M. G., Peng, S., Cho, K. & Dai, H. 2000. Nanotube molecular wires as chemical sensors. *Science,* 287**,** 622-625.

Kwon, Y., Choi, S., Anantharaju, N., Lee, J., Panchagnula, M. V. & Patankar, N. A. 2010. Is the Cassie−Baxter formula relevant? *Langmuir,* 26**,** 17528-17531.

Kyotani, T., Tsai, L. & Tomita, A. 1996. Preparation of ultrafine carbon tubes in nanochannels of an anodic aluminum oxide film. *Chemistry of Materials,* 8**,** 2109-2113.

Kyotani, T., Tsai, L. F. & Tomita, A. 1995. Formation of ultrafine carbon tubes by using an anodic aluminum-oxide film as a template. *Chemistry of Materials,* 7**,** 1427-1428.

Lafuma, A. & Quere, D. 2003. Superhydrophobic states. *Nature Materials,* 2**,** 457-460.

Lai, Y. K., Lin, C. J., Wang, H., Huang, H. Y., Zhuang, H. F. & Sun, L. 2008. Superhydrophilic-superhydrophobic micropattern on TiO_2 nanotube films by photocatalytic lithography. *Electrochemistry Communications,* 10**,** 387-391.

Larsen, S. T. & Taboryski, R. 2009. A Cassie-like law using triple phase boundary line fractions for faceted droplets on chemically heterogeneous surfaces. *Langmuir,* 25**,** 1282-1284.

Lee, K. P., Leese, H. & Mattia, D. 2012. Water flow enhancement in hydrophilic nanochannels. *Nanoscale,* 4**,** 2621-2627.

Lee, K. P. & Mattia, D. 2013 Monolithic nanoporous alumina membranes for ultrafiltration applications: Characterization, selectivity-permeability analysis and fouling studies. *Journal of Membrane Science,* 435, 52-61.

Lee, S. B., Teo, K. B. K., Chhowalla, M., Hasko, D. G., Amaratunga, G. A. J., Milne, W. I. & Ahmed, H. 2002. Study of multi-walled carbon nanotube structures fabricated by PMMA suspended dispersion. *Microelectronic Engineering,* 61–62**,** 475-483.

Leese, H., Bhurtun, V., Lee, K. P. & Mattia, D. 2013. Wetting behaviour of hydrophilic and hydrophobic nanostructured porous anodic alumina.

Colloids and Surfaces A: Physicochemical and Engineering Aspects, 420**,** 53-58.

Li, A. P., Muller, F., Birner, A., Nielsch, K. & Gösele, U. 1998. Hexagonal pore arrays with a 50-420 nm interpore distance formed by self-organization in anodic alumina. *Journal of Applied Physics,* 84**,** 6023-6026.

Li, G. P., Chen, T., Yan, B., Ma, Y., Zhang, Z., Yu, T., Shen, Z. X., Chen, H. Y. & Wu, T. 2008. Tunable wettability in surface-modified ZnO-based hierarchical nanostructures. *Applied Physics Letters,* 92, 173104-3.

Li, J., Papadopoulos, C., Xu, J. M. & Moskovits, M. 1999. Highly-ordered carbon nanotube arrays for electronics applications. *Applied Physics Letters,* 75**,** 367-369.

Li, Y., Zheng, M., Ma, L. & Shen, W. 2006. Fabrication of highly ordered nanoporous alumina films by stable high-field anodization. *Nanotechnology,* 17**,** 5101-5105.

Li, Z. Q., Lu, C. J., Xia, Z. P., Zhou, Y. & Luo, Z. 2007. X-ray diffraction patterns of graphite and turbostratic carbon. *Carbon,* 45**,** 1686-1695.

Lillo, M. & Losic, D. 2009. Pore opening detection for controlled dissolution of barrier oxide layer and fabrication of nanoporous alumina with through-hole morphology. *Journal of Membrane Science,* 327**,** 11-17.

López, V., Bartolomé, M. J., Escudero, E., Otero, E. & González, J. A. 2006. Comparison by SEM, TEM, and EIS of hydrothermally sealed and cold sealed aluminum anodic oxides. *Journal of The Electrochemical Society,* 153**,** B75-B82.

Ma, D., Li, S. Y. & Liang, C. G. 2009. Electropolishing of high-purity aluminium in perchloric acid and ethanol solutions. *Corrosion Science,* 51**,** 713-718.

Majumder, M., Chopra, N., Andrews, R. & Hinds, B. J. 2005. Nanoscale hydrodynamics: enhanced flow in carbon nanotubes. *Nature,* 438**,** 44.

Mani, A., Zangle, T. A. & Santiago, J. G. 2009. On the propagation of concentration polarization from microchannel−nanochannel interfaces Part I: analytical model and characteristic analysis. *Langmuir,* 25**,** 3898-3908.

Manor, O., Vakarelski, I. U., Stevens, G. W., Grieser, F., Dagastine, R. R. & Chan, D. Y. C. 2008. Dynamic forcse between bubbles and surfaces and hydrodynamic boundary conditions. *Langmuir,* 24**,** 11533-11543.

Mardilovich, P. P., Govyadinov, A. N., Mukhurov, N. I., Rzhevskii, A. M. & Paterson, R. 1995. New and modified anodic alumina membranes.1. thermotreatment of anodic alumina membranes. *Journal of Membrane Science,* 98**,** 131-142.

Marmur, A. 2003. Wetting on hydrophobic rough surfaces: to be heterogeneous or not to be? *Langmuir,* 19**,** 8343-8348.

Martin, C. R. 1994. Nanomaterials: a membrane-based synthetic approach. *Science,* 266**,** 1961-1966.

Masuda, H. & Fukuda, K. 1995. Ordered metal nanohole arrays made by a two-step replication of honeycomb structures of anodic alumina. *Science,* 268**,** 1466-1468.

Masuda, H., Nishio, K. & Baba, N. 1993. Fabrication of a one-dimensional microhole array by anodic oxidation of aluminum. *Applied Physics Letters,* 63**,** 3155-3157.

Mattia, D. 2007. *Templated Growth and Characterization of Carbon Nanotubes for Nanofluidic Applications.* PhD Thesis, Drexel University.

Mattia, D., Bau, H. H. & Gogotsi, Y. 2006a. Wetting of CVD carbon films by polar and non-polar liquids and implications for carbon nanopipes. *Langmuir,* 22**,** 1789 -1794.

Mattia, D. & Calabrò, F. 2012. Explaining high flow rate of water in carbon nanotubes via solid–liquid molecular interactions. *Microfluidics and Nanofluidics,* 13**,** 125-130.

Mattia, D. & Gogotsi, Y. 2008. Review: static and dynamic behavior of liquids inside carbon nanotubes. *Microfluidics and Nanofluidics,* 5**,** 289-305.

Mattia, D., Rossi, M. P., Kim, B. M., Korneva, G., Bau, H. H. & Gogotsi, Y. 2006b. Effect of graphitization on the wettability and electrical conductivity of CVD carbon nanotubes and films. *Journal of Physical Chemistry B,* 110**,** 9850 -9855.

Mattia, D., Rossi, M. P., Ye, H. & Gogotsi, Y. Year. *In situ* fluid studies in carbon nanotubes with diameters ranging from 1 to 500 nm. *In:* 5th IASME/ WSEAS International Conference on Fluid Mechanics and Aerodynamics, 2007 Athens, Greece. 297-299.

Megias-Alguacil, D., Tervoort, E., Cattin, C. & Gauckler, L. J. 2011. Contact angle and adsorption behavior of carboxylic acids on α-Al_2O_3 surfaces. *Journal of Colloid and Interface Science,* 353**,** 512-518.

Meng, X. Q., Zhao, D. X., Zhang, J. Y., Shen, D. Z., Lu, Y. M., Dong, L., Xiao, Z. Y., Liu, Y. C. & Fan, X. W. 2005. Wettability conversion on ZnO nanowire arrays surface modified by oxygen plasma treatment and annealing. *Chemical Physics Letters,* 413**,** 450-453.

Miller, S. A. & Martin, C. R. 2002. Controlling the rate and direction of electroosmotic flow in template-prepared carbon nanotube membranes. *Journal of Electroanalytical Chemistry,* 522**,** 66-69.

Miller, S. A. & Martin, C. R. 2004. Redox modulation of electroosmotic flow in a carbon nanotube membrane. *Journal of the American Chemical Society,* 126**,** 6226-6227.

Miller, S. A., Young, V. Y. & Martin, C. R. 2001. Electroosmotic flow in template-prepared carbon nanotube membranes. *Journal of the American Chemical Society,* 123**,** 12335-12342.

Miney, P. G., Colavita, P. E., Schiza, M. V., Priore, R. J., Haibach, F. G. & Myrick, M. L. 2003. Growth and characterization of a porous aluminum oxide film formed on an electrically insulating support. *Electrochemical and Solid State Letters,* 6**,** B42-B45.

Montero-Moreno, J. M., Sarret, M. & Müller, C. 2007. Influence of the aluminum surface on the final results of a two-step anodizing. *Surface and Coatings Technology,* 201**,** 6352-6357.

Murphy, J. F. 1967. *Proceedings of the Symposium on Anodizing Aluminium,* Birmingham, Aluminium Federation.

Navier, C. L. M. H. 1823a. Mémoire sur les lois du mouvement des fluids. *Mémoires de l'Académie Royale des Sciences de l'Institut de France*, 6, 389-416.

Navier, C. L. M. H. 1823b. Mémoire sur les lois du mouvement des fluids. *Mémoires de l'Académie Royale des Sciences de l'Institut de France*, 6, 432-436.

Neto, C., Evans, D. R., Bonaccurso, E., Butt, H.-J. & Craig, V. S. J. 2005. Boundary slip in Newtonian liquids: a review of experimental studies. *Reports on Progress in Physics,* 68**,** 2859-2897.

Nicholls, W. D., Borg, M. K., Lockerby, D. A. & Reese, J. M. 2012. Water transport through carbon nanotubes with defects. *Molecular Simulation,* 38**,** 781-785.

Nielsch, K., Choi, J., Schwirn, K., Wehrspohn, R. B. & Gösele, U. 2002. Self-ordering regimes of porous alumina: The 10 porosity rule. *Nano Letters,* 2**,** 677-680.

Norinaga, K., Deutschmann, O. & Hüttinger, K. J. 2006. Analysis of gas phase compounds in chemical vapor deposition of carbon from light hydrocarbons. *Carbon,* 44**,** 1790-1800.

O'Sullivan, J. P. & Wood, G. C. 1970. The morphology and mechanism of formation of porous anodic films on aluminium. *Proceedings of the Royal Society of London,* 317**,** 511-543.

Ono, S., Saito, M. & Asoh, H. 2005. Self-ordering of anodic porous alumina formed in organic acid electrolytes. *Electrochimica Acta,* 51**,** 827-833.

Osswald, S., Flahaut, E., Ye, H. & Gogotsi, Y. 2005. Elimination of D-band in Raman spectra of double-wall carbon nanotubes by oxidation. *Chemical Physics Letters,* 402**,** 422-427.

Park, J. H. & Aluru, N. R. 2010. Ordering-induced fast diffusion of nanoscale water film on graphene. *The Journal of Physical Chemistry C,* 114**,** 2595-2599.

Parthasarathy, R. V., Phani, K. L. N. & Martin, C. R. 1995. Template synthesis of graphitic nanotubules. *Advanced Materials,* 7**,** 896-897.

Pashchanka, M. & Schneider, J. J. 2011. Origin of self-organisation in porous anodic alumina films derived from analogy with Rayleigh-Benard convection cells. *Journal of Materials Chemistry,* 21**,** 18761-18767.

Patermarakis, G., Moussoutzanis, K. & Chandrinos, J. 1999. Preparation of ultra-active alumina of designed porous structure by successive hydrothermal and thermal treatments of porous anodic Al_2O_3 films. *Applied Catalysis A: General,* 180**,** 345-358.

Patermarakis, G. & Papandreadis, N. 1993. Effect of the structure of porous anodic Al2O3 films on the mechanism of their hydration and pore closure during hydrothermal treatment. *Electrochimica Acta,* 38**,** 1413-1420.

Persat, A., Chambers, R. D. & Santiago, J. G. 2009a. Basic principles of electrolyte chemistry for microfluidic electrokinetics. Part I: Acid-base equilibria and pH buffers. *Lab on a Chip,* 9**,** 2437-2453.

Persat, A., Suss, M. E. & Santiago, J. G. 2009b. Basic principles of electrolyte chemistry for microfluidic electrokinetics. Part II: Coupling between ion mobility, electrolysis, and acid-base equilibria. *Lab on a Chip,* 9**,** 2454-2469.

Pilkington, G. A., Thormann, E., Claesson, P. M., Fuge, G. M., Fox, O. J. L., Ashfold, M. N. R., Leese, H., Mattia, D. & Briscoe, W. H. 2011. Amontonian frictional behaviour of nanostructured surfaces. *Physical Chemistry Chemical Physics,* 13**,** 9318-9326.

Prakash, P., Grissom, M. D., Rahn, C. D. & Zydney, A. L. 2006. Development of an electroosmotic pump for high performance actuation. *Journal of Membrane Science,* 286**,** 153-160.

Pretorius, V., Hopkins, B. J. & Schieke, J. D. 1974. Electro-osmosis: A new concept for high-speed liquid chromatography. *Journal of Chromatography A,* 99**,** 23-30.

Pu, Q., Yun, J., Temkin, H. & Liu, S. 2004. Ion-enrichment and ion-depletion effect of nanochannel structures. *Nano Letters,* 4**,** 1099-1103.

Qiao, R. & Aluru, N. R. 2003a. Atypical dependence of electroosmotic transport on surface charge in a single-wall carbon nanotube. *Nano Letters,* 3**,** 1013-1017.

Qiao, R. & Aluru, N. R. 2003b. Ion concentrations and velocity profiles in nanochannel electroosmotic flows. *Journal of Chemical Physics,* 118**,** 4692-4701.

Quincke, G. 1861. Ueber die fortführung materieller theilchen durch strömende Elektricität. *Annalen der Physik,* 189**,** 513-598.

Ran, C., Ding, G., Liu, W., Deng, Y. & Hou, W. 2008. Wetting on nanoporous alumina surface: transition between Wenzel and Cassie states controlled by surface structure. *Langmuir,* 24**,** 9952-9955.

Raspal, V., Awitor, K. O., Massard, C., Feschet-Chassot, E., Bokalawela, R. S. P. & Johnson, M. B. 2012. Nanoporous surface wetting behavior: The line tension influence. *Langmuir,* 28**,** 11064-11071.

Rauf, A., Mehmood, M., Asim Rasheed, M. & Aslam, M. 2009. The effects of electropolishing on the nanochannel ordering of the porous anodic alumina prepared in oxalic acid. *Journal of Solid State Electrochemistry,* 13**,** 321-332.

Redon, R., Vazquez-Olmos, A., Mata-Zamora, M. E., Odognez-Medrano, A., Rivera-Torres, F. & Saniger, J. M. 2007. Contact angle studies of anodic porous alumina. *Journal of Colloid and Interface Science,* 11**,** 79-87.

Reichmuth, D. S., Chirica, G. S. & Kirby, B. J. 2003. Increasing the performance of high-pressure, high-efficiency electrokinetic micropumps using zwitterionic solute additives. *Sensors and Actuators B: Chemical,* 92**,** 37-43.

Reis, F. D. A. A., Badiali, J. P. & Di Caprio, D. 2012. Modeling growth of organized nanoporous structures by anodic oxidation. *Langmuir,* 28**,** 13034-13041.

Reuss, F. F. 1809. Sur un Novel Effet de l'Électricité Galvanique. *Mémoires de la Société Impériale des Naturalistes de Moskou,* 2**,** 327-337.

Rice, C. L. & Whitehead, R. 1965. Electrokinetic flow in a narrow cylindrical capillary. *Journal of Physical Chemistry,* 69**,** 4017-4024.

Romero, V., Vega, V., García, J., Prida, V. M., Hernando, B. & Benavente, J. 2012. Ionic transport across tailored nanoporous anodic alumina membranes. *Journal of Colloid and Interface Science,* 376**,** 40-46.

Rossi, M. P. 2007. *Environmental scanning electron microscopy study of the interaction of carbon nanotubes with fluids.* Ph.D., Drexel University.

Rutgers, A. J. 1940. Part I.-(B) Streaming effects and surface conduction. Streaming potentials and surface conductance. *Transactions of the Faraday Society,* 35**,** 69-80.

Sadasivan, V., Richter, C. P., Menon, L. & Williams, P. F. 2005. Electrochemical self-assembly of porous alumina templates. *Aiche Journal,* 51**,** 649-655.

Saito, R., Dresselhaus, G. & Dresselhaus, M. S. 1998. *Physical properties of carbon nanotubes,* London, Imperial College Press.

Schwirn, K., Lee, W., Hillebrand, R., Steinhart, M., Nielsch, K. & Gösele, U. 2008. Self-ordered anodic aluminum oxide formed by H_2SO_4 hard anodization. *ACS Nano,* 2**,** 302-310.

Shannon, M. A., Bohn, P. W., Elimelech, M., Georgiadis, J. G., Marinas, B. J. & Mayes, A. M. 2008. Science and technology for water purification in the coming decades. *Nature,* 452**,** 301-310.

Shelimov, K. B. & Moskovits, M. 1999. Composite nanostructures based on template-grown boron nitride nanotubules. *Chemistry of Materials,* 12**,** 250-254.

Sigurdson, S., Sundaramurthy, V., Dalai, A. K. & Adjaye, J. 2009. Effect of anodic alumina pore diameter variation on template-initiated synthesis of carbon nanotube catalyst supports. *Journal of Molecular Catalysis A: Chemical,* 306**,** 23-32.

Smoluchowski, M. 1903. Contribution à la théorie l´endosmose électrique et de quelques phénomènes corrélatifs. *Bulletin de l'Academie des Sciences de Cracovie,* 8**,** 182-200.

Steinhart, M., Wendorff, J. H., Greiner, A., Wehrspohn, R. B., Nielsch, K., Schilling, J., Choi, J. & Gösele, U. 2002. Polymer nanotubes by wetting of ordered porous templates. *Science,* 296**,** 1997.

Strickland, D. G., Suss, M. E., Zangle, T. A. & Santiago, J. G. 2010. Evidence shows concentration polarization and its propagation can be key factors determining electroosmotic pump performance. *Sensors and Actuators B: Chemical,* 143**,** 795-798.

Striolo, A. 2006. The mechanism of water diffusion in narrow carbon nanotubes. *Nano Letters,* 6**,** 633-639.

Stumpf, H. C., Russell, A. S., Newsome, J. W. & Tucker, C. M. 1950. Thermal transformations of aluminas and alumina hydrates - reaction with 44% technical acid. *Industrial & Engineering Chemistry,* 42**,** 1398-1403.

Su, B., Li, M., Shi, Z. Y. & Lu, Q. H. 2009. From superhydrophilic to superhydrophobic: Controlling wettability of hydroxide zinc carbonate film on zinc plates. *Langmuir,* 25**,** 3640-3645.

Sugie, H., Tanemura, M., Filip, V., Iwata, K., Takahashi, K. & Okuyama, F. 2001. Carbon nanotubes as electron source in an x-ray tube. *Applied Physics Letters,* 78**,** 2578-2580.

Suh, J. S. & Lee, J. S. 1999. Highly ordered two-dimensional carbon nanotube arrays. *Applied Physics Letters,* 75**,** 2047-2049.

Suk, M. E., Raghunathan, A. V. & Aluru, N. R. 2008. Fast reverse osmosis using boron nitride and carbon nanotubes. *Applied Physics Letters,* 92**,** 133120-3.

Sulka, G. D. 2008. Highly ordered anodic porous alumina formation by self-organized anodizing. *In:* Eftekhari, A. (ed.) *Nanostructured Materials in Electrochemistry.* Weinheim: Wiley-VCH.

Sulka, G. D., Parkola, G, K 2006. Anodising potential influence on well-ordered nanstructures formed by anodisation of aluminum in sulphuric acid. *Thin Solid Films,* 515**,** 338-345.

Sun, J., Cole, M. T., Lindvall, N., Teo, K. B. K. & Yurgens, A. 2012. Noncatalytic chemical vapor deposition of graphene on high-temperature substrates for transparent electrodes. *Applied Physics Letters,* 100**,** 022102-3.

Sun, M. & Ebner, C. 1992. Molecular-dynamics study of flow at a fliud-wall interface. *Physical Review Letters,* 69**,** 3491-3494.

Supple, S. & Quirke, N. 2003. Rapid imbibition of fluids in carbon nanotubes. *Physical Review Letters,* 90**,** 214501-4.

Supple, S. & Quirke, N. 2004. Molecular dynamics of transient oil flows in nanopores I: Imbibition speeds for single wall carbon nanotubes. *Journal of Chemical Physics,* 121**,** 8571-8579.

Suss, M. E., Mani, A., Zangle, T. A. & Santiago, J. G. 2011. Electroosmotic pump performance is affected by concentration polarizations of both electrodes and pump. *Sensors and Actuators A: Physical,* 165**,** 310-315.

Tai, N.-H., Yeh, M.-K. & Liu, J.-H. 2004. Enhancement of the mechanical properties of carbon nanotube/phenolic composites using a carbon nanotube network as the reinforcement. *Carbon,* 42**,** 2774-2777.

Takamura, Y., Onoda, H., Inokuchi, H., Adachi, S., Oki, A. & Horiike, Y. 2003. Low-voltage electroosmosis pump for stand-alone microfluidics devices. *Electrophoresis,* 24**,** 185-192.

Takmakov, P., Vlassiouk, I. & Smirnov, S. 2006. Hydrothermally shrunk alumina nanopores and their application to DNA sensing. *Analyst,* 131**,** 1248-1253.

Tang, F., Fudouzi, H., Uchikoshi, T. & Sakka, Y. 2004. Preparation of porous materials with controlled pore size and porosity. *Journal of the European Ceramic Society,* 24**,** 341-344.

Taylor, J. & Ren, C. 2005. Application of continuum mechanics to fluid flow in nanochannels. *Microfluidics and Nanofluidics,* 1**,** 356-363.

Theeuwes, F. 1974. *Electroosmotic pump and fluid dispenser including same*. United States patent application.

Thomas, J. A. & McGaughey, A. J. H. 2008. Reassessing fast water transport through carbon nanotubes. *Nano Letters,* 8, 2788-2793.

Thomas, J. A. & McGaughey, A. J. H. 2009. Water flow in carbon nanotubes: transition to subcontinuum transport. *Physical Review Letters,* 102**,** 184502-4.

Thompson, P. A. & Robbins, M. O. 1990. Shear-flow near solids - epitaxial order and flow boundary - conditions. *Physical Review A,* 41**,** 6830-6837.

Travis, K. P., Todd, B. D. & Evans, D. J. 1997. Departure from Navier-Stokes hydrodynamics in confined liquids. *Physical Review E,* 55**,** 4288-4295.

Vaisman, L., Wagner, H. D. & Marom, G. 2006. The role of surfactants in dispersion of carbon nanotubes. *Advances in Colloid and Interface Science,* 128-130**,** 37-46.

Vajandar, S. K., Xu, D., Markov, D. A., Wikswo, J. P., Hofmeister, W. & LI, D. 2007. SiO_2 coated porous anodic alumina membranes for high flow rate electroosmotic pumping. *Nanotechnology,* 18**,** 275705-8.

Voronov, R. S., Papavassiliou, D. V. & Lee, L. L. 2006. Boundary slip and wetting properties of interfaces: Correlation of the contact angle with the slip length. *Journal of Chemical Physics,* 124**,** 204701-10.

Wade, T. L., Hoffer, X., Mohammed, A. D., Dayen, J. -F., Pribat, D. & Wegrowe, J. -E. 2007. Nanoporous alumina wire templates for surrounding-gate nanowire transistors. *Nanotechnology***,** 125201-4.

Wall, S. 2010. The history of electrokinetic phenomena. *Current Opinion in Colloid and Interface Science,* 15**,** 119-124.

Wan, Q.-H. 1997. Effect of electrical double-layer overlap on the electroosmotic flow in packed-capillary columns. *Analytical Chemistry,* 69**,** 361-363.

Wang, M., Liu, Y. & Yang, H. 2012. A unified thermodynamic theory for the formation of anodized metal oxide structures. *Electrochimica Acta,* 62**,** 424-432.

Wenzel, T. N. 1949. Surface roughness and contact angle. *Journal of Physical Chemistry,* 53**,** 1466-1467.

Whitby, M., Cagnon, L., Thanou, M. & Quirke, N. 2008. Enhanced fluid flow through nanoscale carbon pipes. *Nano Letters,* 8**,** 2632-2637.

Whitby, M., Cagnon, L., Thanou, M. & Quirke, N. 2009. Enhanced fluid flow through nanoscale carbon pipes. *Nano Letters,* 9**,** 2802-2802.

Whitby, M. & Quirke, N. 2007. Fluid flow in carbon nanotubes and nanopipes. *Nature Nanotechnology,* 2**,** 87-94.

White, H. S. & Bund, A. 2008. Ion current rectification at nanopores in glass membranes. *Langmuir,* 24**,** 2212-2218.

Whyman, G., Bormashenko, E. & Stein, T. 2008. The rigorous derivation of Young, Cassie–Baxter and Wenzel equations and the analysis of the contact angle hysteresis phenomenon. *Chemical Physics Letters,* 450**,** 355-359.

Won, C. Y. & Aluru, N. R. 2007. Water permeation through a subnanometer boron nitride nanotube. *Journal of the American Chemical Society,* 129**,** 2748-2749.

Wu, J., Gerstandt, K., Majumder, M., Zhan, X. & Hinds, B. J. 2011. Highly efficient electroosmotic flow through functionalized carbon nanotube membranes. *Nanoscale,* 3, 3321-3328.

Wu, M. T., Leu, I. C. & Hon, M. H. 2002. Effect of polishing pretreatment on the fabrication of ordered nanopore arrays on aluminum foils by anodization. *Journal of Vacuum Science & Technology B: Microelectronics and Nanometer Structures,* 20**,** 776-782.

Xu, T. T., Piner, R. D. & Ruoff, R. S. 2003. An improved method to strip aluminum from porous anodic alumina films. *Langmuir,* 19**,** 1443-1445.

Yang, Z., Niu, Z., Cao, X., Yang, Z., Lu, Y., Hu, Z. & Han, C. C. 2003. Template synthesis of uniform 1D mesostructured silica materials and their arrays in anodic alumina membranes. *Angewandte Chemie International Edition,* 42**,** 4201-4203.

Yao, S., Hertzog, D. E., Zeng, S., Mikkelsen, J. C. & Santiago, J. G. 2003. Porous glass electroosmotic pumps: design and experiments. *Journal of Colloid Interface Science,* 268**,** 143-153.

Yao, S., Myers, A. M., Posner, J. D., Rose, K. A. & Santiago, J. G. 2006. Electroosmotic pumps fabricated from porous silicon membranes. *Journal of Microelectromechanical Systems,* 15**,** 717-728.

Ye, J., Yin, Q. & Zhou, Y. 2009. Superhydrophilicity of anodic aluminum oxide films: From “honeycomb” to “bird's nest”. *Thin Solid Films,* 517**,** 6012-6015.

Yin, A. J., Li, J., Jian, W., Bennett, A. J. & Xu, J. M. 2001. Fabrication of highly ordered metallic nanowire arrays by electrodeposition. *Applied Physics Letters,* 79**,** 1039-1041.

Young, T. 1805. An essay on the cohesion of fluids. *Philosophical Transactions of the Royal Society of London,* 95**,** 65-87.

Yu, C.-U., Hu, C.-C., Bai, A. & Yang, Y.-F. 2007. Pore-size dependence of AAO films on surface roughness of Al-1050 sheets controlled by electropolishing coupled with fractional factorial design. *Surface and Coatings Technology,* 201**,** 7259-7265.

Yu, W. H., Fei, G. T., Chen, X. M., Xue, F. H. & Xu, X. J. 2006. Influence of defects on the ordering degree of nanopores made from anodic aluminum oxide. *Physics Letters A,* 350**,** 392-395.

Yusko, E. C., An, R. & Mayer, M. 2010. Electroosmotic flow can generate ion current rectification in nano- and micropores. *ACS Nano,* 4**,** 477-487.

Zangle, T. A., Mani, A. & Santiago, J. G. 2009. On the propagation of concentration polarization from microchannel−nanochannel interfaces part II: Numerical and experimental study. *Langmuir,* 25**,** 3909-3916.

Zhang, Q., Chan, K.-Y. & Quirke, N. 2009. Molecular dynamics simulation of water confined in a nanopore of amorphous silica. *Molecular Simulation,* 35**,** 1215-1223.

Zhao, G.-Y., Xu, C.-L., Guo, D.-J., Li, H. & Li, H.-L. 2006. Patterning polycrystalline aluminum by electropolishing at low voltages. *Journal of Solid State Electrochemistry,* 10**,** 266-269.

Zhou, O., Fleming, R. M., Murphy, D. W., Chen, C. H., Haddon, R. C., Ramirez, A. P. & Glarum, S. H. 1994. Defects in carbon nanostructures. *Science,* 263**,** 1744-1747.

Zhu, L., Attard, P. & Neto, C. 2011a. Reliable measurements of interfacial slip by colloid probe atomic force microscopy. I. Mathematical modeling. *Langmuir,* 27**,** 6701-6711.

Zhu, L., Attard, P. & Neto, C. 2011b. Reliable measurements of interfacial slip by colloid probe atomic force microscopy. II. Hydrodynamic force measurements. *Langmuir,* 27**,** 6712-6719.

Appendix A: Dissemination

Listed below are the dissemination outcomes of this research.

A1 Publications

H. Leese, D. Mattia. Wetting of Carbon, Inorganic and Organic Nanochannels. In Nanoscale Liquid Interfaces: Wetting, Patterning, and Force Microscopy at the Molecular Scale, Eds. Thierry Ondarçuhu and Jean-Pierre Aimé, *Pan Stanford Publishing*, 2013, ISBN 978-981-4316-45-3.

H. Leese, V.Bhurtun, K. P. Lee and D. Mattia. Wetting of hydrophilic and hydrophobic nanostructured porous anodic alumina. *Colloids and Surfaces A: Physicochemical and Engineering Aspects,* 2012, doi:10.1016/j.colsurfa.2012.12.010.

K. P. Lee, H. Leese, D. Mattia. Water flow enhancement in hydrophilic nanochannels. *Nanoscale*, 2012, 4(8), 2621-2627.

G. A. Pilkington, E. Thormann, P. M. Claesson, G. M. Fuge, O. J. L. Fox, M. N. R. Ashfold, H. Leese, D. Mattia, W. H. Briscoe. Amontonian frictional behaviour of nanostructured surfaces. *Physical Chemistry Chemical Physics*, 2011, 13(20), 9381.

A2 Submitted for Publication

H. Leese and D. Mattia. Experimental evidence of electroosmotic flow in nanoporous membranes in the region of electric double layer overlap. *Microfluidics and Nanofluidics*, February 2013.

C. Wu*, H. Leese*, D. Mattia, R. R. Dagastine, D. Y. C. Chan and R. F. Tabor. A study of the transport properties of porous anodic aluminium membranes by dynamic atomic force microscopy. *Langmuir*, April 2013.

A3 Manuscripts in Preparation

H. Leese and D. Mattia. Electric Double Layer Overlap and Electroosmostic Flow in Carbon Nanotube Membranes.

H. Leese and D. Mattia. Hydrothermal Treatment of Nanoporous Anodized Alumina Membranes.

B. Quignon, G. A. Pilkington, E. Thormann, P. M. Claesson, H. Leese, D. Mattia, S. A. Davis and W. H. Briscoe. Stick-slip frictional behaviour of nanodomed-surfaces.

A4 Conference Proceedings

[1]H. Leese, D. Mattia. Electroosmosis Pumping in Nanoporous Alumina Membranes. *Procedia Engineering*, 2012, 44, 404-406, http://dx.doi.org/ 10.1016/j.proeng.2012.08.431

[1]H. Leese, K. P. Lee, V. Bhurtun, D. Mattia. Wetting Properties of Nanostructured Bare and Silanized Alumina. *28th Australian Student Colloid Conference*, Newcastle, Australia, Feb 6-10, 2012.

[1]H. Leese, V. Bhurtun, D. Mattia. Wetting properties of alumina nanostructures. *UK Colloids 2011*, London, UK, July 4-6, 2011.

[2]H. Leese, V. Bhurtun, D. Mattia. Wetting Properties of Nanostructured Alumina. *25th European Colloid and Interface Society*, Berlin, Germany, Sept 4-9, 2011.

[2]H. Leese, P. Morawska, D. Mattia. SEM and AFM Characterization of Nanoporous Alumina Membrane. *Microscopy and Analysis Conference 2011*, Bath, UK, Jan 12, 2011.

*Contributed equally to this work.
[1] Oral presentation by the candidate.
[2] Presented as a poster by the candidate.

Appendix B: Preliminary EO Experiments

B1 Holder Design

During the development of the electroosmotic flow experiments a first generation membrane holder was developed. These experiments were crucial to the final developments of the EO rig and membrane holder, which was utilised for the results presented in Chapter 7 and 8. The experiments conducted in the first generation membrane holder were inadequate to measure the EOF due to the over-riding concentration polarization and electrolysis effects caused by the limited buffer capacity, as shown in Figure B1.

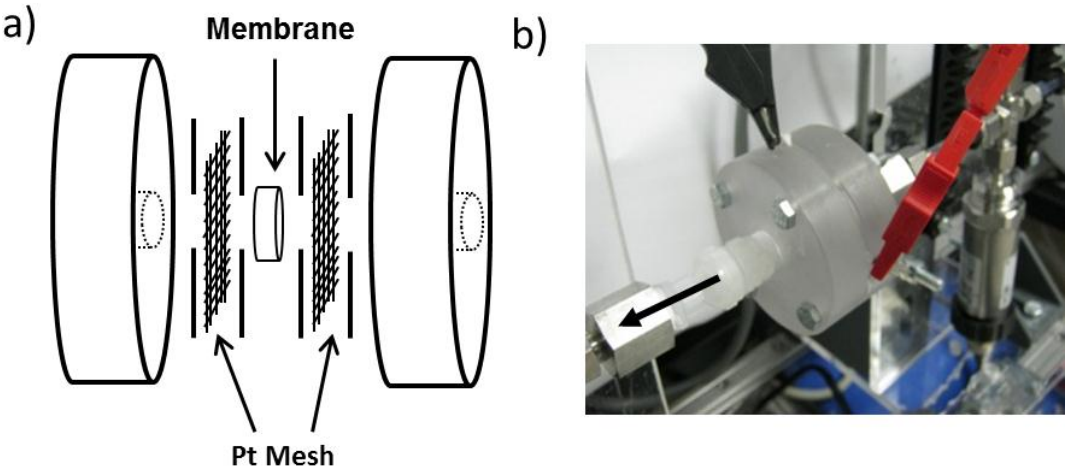

Figure B1 a) Schematic and b) a digital image of the first generation sample holder with no buffer reservoirs.

B2 Preliminary Results

The EO experiments were conducted with a series of potassium chloride (KCl) concentrations, following the concentrations presented in Chen et al. (Chen et al. 2008a). A constant pressure gradient was applied for the experiments, the same method as described in the Materials and Methods chapter. The total volumetric flow rates (pressure-driven and EO) series of applied voltages were recorded and due to concentration polarization and local pH changes that resulted in drastically lower flow rates than predicted (see Figure B2).

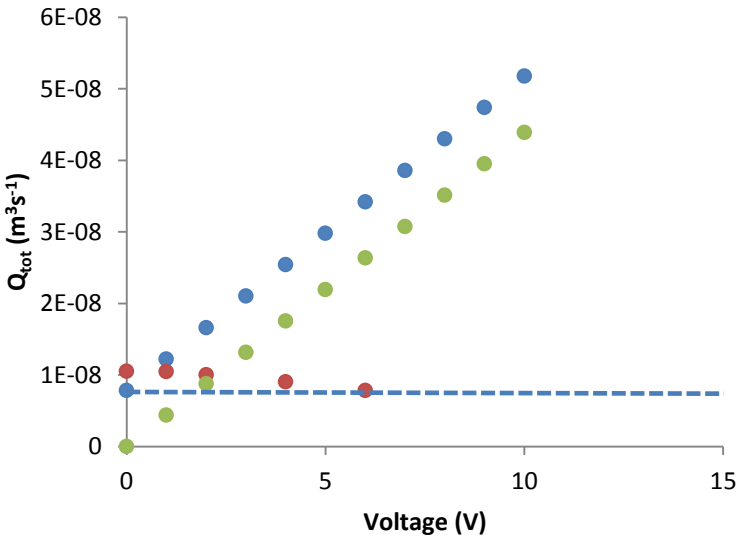

Figure B2 Total volumetric flow rates (pressure-driven + electroosmotic flows) of theoretical (●) calculations and experimental (●) with increasing applied voltage. The theoretical electroosmotic flow rate (●) increases with applied voltage. The blue dashed line represents the pressure-driven flow rate with no external applied voltage.

Appendix C: Example Calculations

This section presents examples for some calculations for this thesis; see the Nomenclature section for full definitions.

C1 Calculation of the theoretical flow rate using the Hagen-Poiseuille Equation

To determine the theoretical flow rate for a given NPAM pore diameter the following calculations were performed.

From Equation 8.1:

$$Q_{HP} = \frac{\phi A_{eff} D_P^2 \Delta P}{32 \tau \mu L}$$

Porosity, ϕ, was calculated by

$$\phi = \frac{N A_P}{A_{eff}}$$

where N is the number of pores, A_P is the area of one pore and A_{eff} is the effective area.

Therefore, for example, if pore diameter, D_P = 30 nm with pressure difference, ΔP = 50 kPa, effective area A_{eff} = 19.5 mm^2, thickness, L = 60 μm, tortuosity, τ = 1 and viscosity, μ at 20°C = 1.003 x 10^{-3} Pa s.

$$Q_{HP} = \frac{0.1 \cdot 1.96\ x\ 10^{-5}\ m^2 \cdot (30\ x\ 10^{-9})^2 \cdot\ 50\ x\ 10^3}{32 \cdot 1 \cdot 1.003\ x\ 10^{-3} \cdot 60\ x\ 10^{-6}}$$

$$Q_{HP} = 4.59\ x\ 10^{11} m^3 s^{-1}$$

C2 Calculation of the Debye Length

For example, to calculate the Debye length of 5 mM sodium tetraborate, using Equation 2.14 the ionic strength of the electrolyte must first be calculated.

$$Ionic\ Strength = \frac{1}{2}(\sum c_i z_i^2)$$

Sodium ion charge = +1, Borate ion charge = – 2 ∴

As there are two Na $= charge \cdot concentration$

$$= 1^2 \cdot (5\ x\ 10^{-3} M \cdot 2)$$

$$= 0.01$$

And one borate ion $= (-2^2) \cdot (5\ x\ 10^{-3} M)$

$$= 0.02$$

Therefore the ionic strength $= \frac{1}{2}(0.01 + 0.02)$

$$= 0.015\ mol\ dm^{-3}$$

$$= 15\ mol\ m^{-3}$$

Therefore to calculate the Debye Length

$$\lambda_D = \left[\frac{\varepsilon_r \varepsilon_0 k_b T}{\sum_i (c_i)_0 z_i^2 e_0^2}\right]^{\frac{1}{2}}$$

$$\lambda_D = \left[\frac{115 \cdot 8.85\ x\ 10^{-12}\ F\ m^{-1} \cdot 1.38\ x\ 10^{-23}\ J\ K^{-1} \cdot 298\ K}{3.022\ x\ 10^{23} mol^{-1} \cdot 15\ mol\ m^{-3} \cdot (1.6022\ x\ 10^{-19} C)^2}\right]^{\frac{1}{2}}$$

$$\lambda_D = 4.532\ x\ 10^{-9}$$

$$\lambda_D = \sim 4.5\ nm$$

C3 Calculation of Dukhin Number

Example calculation of the Dukhin number for a NPAM pore diameter of 80 nm uses Equation 7.4:

$$Du = \frac{z_1 v_1 (s/l)}{F c_0 (z_1^2 v_1 + z_2^2 v_2)}$$

where l is the pore volume over the pore surface area and z_1 and z_2 is the charge of a sodium and borate ion respectively and v_1 and v_2 is the ionic mobility of sodium and borate ions respectively.

$$Du = \frac{1 \cdot 0.682\ m^2 s^{-1} V^{-1} \cdot (1\ x\ 10^{-3} C\ m^{-3} / 2x10^{-8} m)}{96485.34\ C\ mol^{-1} \cdot 5\ x\ 10^{-3}\ mol \cdot (1^2 \cdot 0.682\ m^2 s^{-1} V^{-1} + -2^2 \cdot 2.61\ m^2 s^{-1} V^{-1})}$$

$$Du = 6.48$$

C4 Calculation of Work of Adhesion

The work of adhesion can be calculated using the Young's contact angle of a liquid with the solid surface, θ and the film pressure of the adsorbed liquid, π_e.

From Equation 8.3

$$W_A = \pi_e + \gamma_{LV}(1 + cos\theta)$$

$$W_A = 0.019\ J\ m^{-2} + 0.072\ J\ m^{-2} \cdot (1 + \cos 46)$$

$$W_A = 0.141\ J\ m^{-2}$$

Appendix D: Derivation of Flow through PAAs using AFM

D1 Flow through Porous Anodic Alumina Membranes

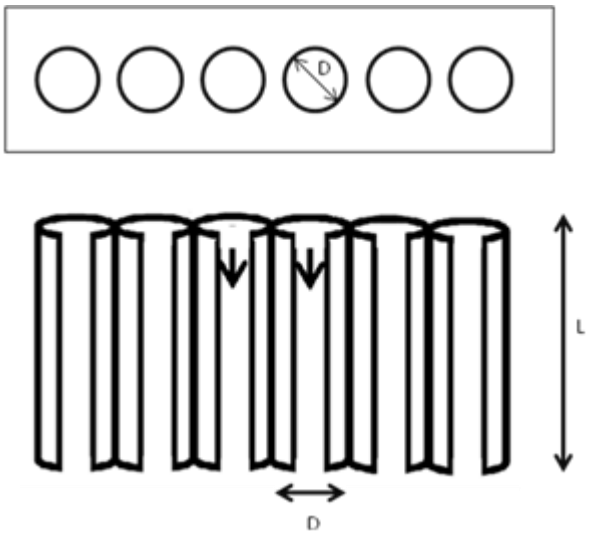

D- Pore diameter
A - Area of membrane
N - Number of pores on membranes
Q - Total flow through membrane
$J = \frac{Q}{A}$ - Flux through membrane
$A_p = \frac{\pi D^2}{4}$ - Area of individual pore
Q_p - Flow through individual pore
$A_m = NA_p$ - Total pore area
$\phi = \frac{NA_p}{A}$ - Pore area fraction

Figure D1 Schematic of porous anodic alumina membranes with pore diameter of D and membrane thickness of L. Definition of key parameters used in describing the flow through the PAAMs is outlined in the list on the right.

It is assumed that the flow through the individual nanochannels can be described using Hagen-Poiseuille equation:

$$Q_p = -\frac{\pi D^4}{128\mu}\frac{\Delta P}{L} \qquad \text{Equation (D.1.1)}$$

Where ΔP and μ are the pressure difference across membrane and fluid dynamic viscosity respectively. Thus the total flow through the pores must be:

$$Q = -\frac{N\pi D^4}{128\mu}\frac{\Delta P}{L} \qquad \text{Equation (D.1.2)}$$

So the fluid flux through the membrane must be:

$$J = \frac{Q}{A}$$

$$J = -\frac{N}{A}\frac{\pi D^4}{128\mu}\frac{\Delta P}{L}$$

From the pore area fraction ϕ in Figure D1 we have $\frac{N}{A} = \frac{\phi}{A_p}$ which can be substituted into the above equation:

$$J = -\frac{\phi}{A_p}\frac{\pi D^4}{128\mu}\frac{\Delta P}{L}$$

$$J = -\frac{\phi D^2}{32\mu}\frac{\Delta P}{L}$$

Define $K = \frac{\phi D^2}{32\mu}$ as the porosity of the membrane will yield the flux of:

$$J = -\frac{K\Delta P}{L} \qquad \text{Equation (D.1.3)}$$

The unit of volumetric flux is m s^{-1} so Equation (D.1.3) gives the fluid velocity in the vertical direction at the surface membrane.

D2 Flow between Two Surfaces

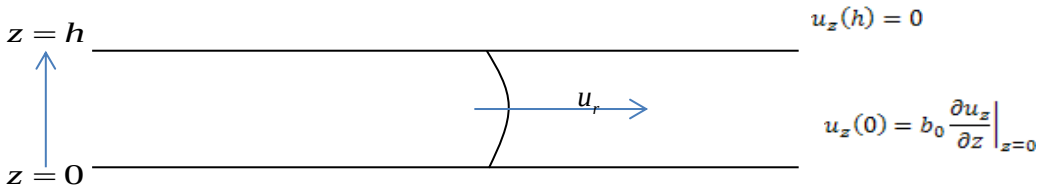

Figure D2 Flow between two solid plates with the upper plate and lower plates experiencing no-slip and slip boundary conditions respectively.

The flow between the silica particle and membrane surface can be modelled as flow between two flat plates. Both plates have zero velocity though it is assumed that the membrane surface can experience slip, so the finite-slip boundary condition is applied to the bottom surface (Figure D2), whilst it is assumed that the silica particle experiences the no-slip condition. The system is very similar to Couette flow with pressure gradient, albeit both surfaces have zero velocity. Nonetheless starting with the Navier-Stokes equation for Couette flow in the r – direction:

$$0 = -\frac{\partial P}{\partial r} + \mu \frac{\partial^2 u_r}{\partial z^2} \qquad \text{Equation (D.2.1)}$$

Integrating the above twice with respect to z will yield:

$$u_r = \frac{1}{2\mu}\frac{\partial P}{\partial r} z^2 + c_1 z + c_2 \qquad \text{Equation (D.2.2)}$$

Where c_1 and c_2 is determined from applying the boundary conditions in Figure D2. This will give the result:

$$u_r = \frac{1}{2\mu}\frac{\partial P}{\partial r}\left[z^2 - \frac{h^2(z+b_0)}{h+b_0}\right] \qquad \text{Equation (D.2.3)}$$

The volumetric flow rate between the plates can be found through integrating the velocity in Equation (D.2.3) from $z = 0$ to $z = h$ which will give:

$$Q = \int_0^h u_r \, dz = -\frac{h^3}{12\mu}\left(\frac{h+4b_0}{h+b_0}\right)\frac{\partial P}{\partial r} \qquad \text{Equation (D.2.4)}$$

D3 Derivation of the Modified Stokes Reynolds Equation

The modified Stokes Reynolds equation can be derived from the continuity equation. We start by describing general fluid velocity in cylindrical coordinates:

$$\boldsymbol{u} = u_r \boldsymbol{e_r} + u_\theta \boldsymbol{e_\theta} + u_z \boldsymbol{e_z}$$

Since there is no angular velocity to the flow then $u_\theta = 0$ so the above equation becomes:

$$\boldsymbol{u} = u_r \boldsymbol{e_r} + u_z \boldsymbol{e_z}$$

As the flow is incompressible then the fluid velocity can be substituted into the incompressible form of the continuity equation:

$$0 = \nabla \cdot \boldsymbol{u}$$
$$0 = \frac{1}{r}\frac{\partial}{\partial r}(r u_r) + \frac{\partial u_z}{\partial z}$$

The continuity equation can be integrated with respect z to form $z = h$ to $z = 0$ where h is the separation of the silica particle to membrane surface:

$$\frac{\partial u_z}{\partial z} = -\frac{1}{r}\frac{\partial}{\partial r}(r u_r)$$
$$\int_0^h \frac{\partial u_z}{\partial z}\, dz = -\frac{1}{r}\int_0^h \frac{\partial}{\partial r}(r u_r)\, dz$$
$$u_z(h) - u_z(0) = -\frac{1}{r}\frac{\partial}{\partial r}\left(r \int_0^h u_r\, dz\right)$$

The $u_z(h)$ and $u_z(0)$ terms on the left hand side of the above equation are the fluid velocity at the silica particle surface and at the membrane surface respectively. Since the silica particle is being pushed down with a velocity of $\frac{dh}{dt}$, then we let $u_z(h) = \frac{dh}{dt}$. On the other hand the velocity at the membrane surface ($u_z(0)$) is dependent on the membrane surface. If this surface is completely solid, then the no-slip boundary condition will hold which results in $u_z(0) = 0$. Substituting this result will yield the normal Stokes Reynolds equation. However if the membrane surface has pores then $u_z(0) = J$, where J is the flux through the membrane which is defined by Equation (D.1.3). Thus integrating the continuity equation will yield:

$$\frac{dh}{dt} + \frac{K\Delta P}{L} = -\frac{1}{r}\frac{\partial}{\partial r}\left(r\int_0^h u_r\, dz\right)$$

Equation (D.2.4) can be substituted into the above to give:

$$\frac{dh}{dt} = \frac{1}{12\mu r}\frac{\partial}{\partial r}\left(rh^3\left[\frac{h+4b_0}{h+b_0}\right]\frac{\partial P}{\partial r}\right) - \frac{K\Delta P}{L} \qquad \text{Equation (D.3.1)}$$

The no-slip and infinite-slip cases can be derived from Equation (D.3.1). The no-slip case can be found through letting the slip length (b_0) be equal to zero, whilst the infinite-slip case can be found by taking the limit of Equation (D.3.1) as $b_0 \to \infty$. Doing this will yield the results:

$$\frac{dh}{dt} = \frac{1}{12\mu r}\frac{\partial}{\partial r}\left(rh^3\frac{\partial P}{\partial r}\right) - \frac{K\Delta P}{L} \qquad \text{Equation (D.3.2)}$$

$$\frac{dh}{dt} = \frac{1}{3\mu r}\frac{\partial}{\partial r}\left(rh^3\frac{\partial P}{\partial r}\right) - \frac{K\Delta P}{L} \qquad \text{Equation (D.3.3)}$$

where Equations (D.3.2) and (D.3.3) are for the no-slip and infinite-slip cases respectively. By assuming the pressure at the back of the membrane is zero, the ΔP term in Equations (D.3.1) to (D.3.3) can be set to P. Also we can let $\alpha = \frac{K}{L}$ and we can merge these equations to form:

$$\frac{dh}{dt} = \frac{1}{12\mu r}\frac{\partial}{\partial r}\left(rH\frac{\partial P}{\partial r}\right) - \alpha P \qquad \text{Equation (D.3.4a)}$$

$$H = \begin{cases} h^3 & \text{No-slip} \\ h^3\left(\frac{h+4b_0}{h+b_0}\right) & \text{Finite-slip} \\ 4h^3 & \text{Full-slip} \end{cases} \qquad \text{Equation (D.3.4b)}$$

D4 Derivation of Perturbation Solution

It is assumed that the silica surface around the centre of the particle has a parabolic profile described by the equation:

$$h(r,t) = h(0,t) + \frac{r^2}{2R} \qquad \text{Equation (D.4.1)}$$

As both surfaces are undeformable, it is possible to change the variables in Equation (D.3.4a) to form the following:

$$\frac{dh}{dt} = \frac{1}{6\mu R}\frac{\partial}{\partial h}\left(H(h-h_0)\frac{\partial P}{\partial h}\right) - \alpha P \qquad \text{Equation (D.4.2)}$$

where R is the particle radius and h_0 is the distance between the two surfaces at the particle centre.

A first order perturbation solution to Equation (D.4.2) assumes that the pressure (P) can be expressed as:

$$P = P_0 + \alpha P_1 \qquad \text{Equation (D.4.3)}$$

which is then substituted into Equation (D.4.2) to form:

$$\frac{dh}{dt} = \frac{1}{6\mu R}\frac{\partial}{\partial h}\left(H(h-h_0)\frac{\partial P_0}{\partial h}\right) + \alpha\left[\frac{1}{6\mu R}\frac{\partial}{\partial h}\left(H(h-h_0)\frac{\partial P_1}{\partial h}\right) - P_0\right] - \alpha^2 P_1$$

By collecting the α terms together, we obtain two independent equations:

$$\frac{dh}{dt} = \frac{1}{6\mu R}\frac{\partial}{\partial h}\left(H(h-h_0)\frac{\partial P_0}{\partial h}\right) \qquad \text{Equation (D.4.4a)}$$

$$0 = \frac{1}{6\mu R}\frac{\partial}{\partial h}\left(H(h-h_0)\frac{\partial P_1}{\partial h}\right) - P_0 \qquad \text{Equation (D.4.4b)}$$

Equation (D.4.4a) is the standard Stokes Reynolds equation and can be solved through integrating twice with respect to h:

$$P_0 = -6\mu R\beta_0 \qquad \text{Equation (D.4.5a)}$$

$$\beta_0 = \int_h^\infty \frac{1}{H(s-h_0)}\left(\int_{h_0}^s \frac{dh}{dt}da\right)ds \qquad \text{Equation (D.4.5b)}$$

The result in Equation (D.4.5) is then substituted into Equation (D.4.4b) to determine P_1:

$$P_1 = -6\mu R\beta_1 \qquad \text{Equation (D.4.6a)}$$

$$\beta_1 = \int_h^\infty \frac{1}{H(s-h_0)}\left(\int_{h_0}^s P_0\, da\right) ds \qquad \text{Equation (D.4.6b)}$$

Both Equations (D.4.5) and (D.4.6) can be substituted back into Equation (D.4.3) to obtain P:

$$P = -6\mu R(\beta_0 + \alpha\beta_1) \qquad \text{Equation (D.4.7)}$$

Force can be found by integrating the pressure with respect separation:

$$F = 2\pi R\int_{h_0}^\infty P\, dh = -12\mu R\int_{h_0}^\infty \beta_0 + \alpha\beta_1\, dh \qquad \text{Equation (D.4.8)}$$

It is possible to substitute Equations (D.3.4b) into the above equation to find the force. Simple expressions can be obtained for the no-slip and infinite-slip cases which are expressed below:

$$F = 6\pi\mu R^2\frac{dh}{dt}\lambda \qquad \text{Equation (D.4.9a)}$$

$$\lambda = \begin{cases} \frac{1}{h} - \frac{\mu R\alpha}{h^3} & \text{No-slip} \\ \frac{1}{4h} - \frac{\mu R\alpha}{16h^3} & \text{Infinite-slip} \end{cases} \qquad \text{Equation (D.4.9b)}$$

No simple expression for the finite-slip case was found but it is possible to use the finite-slip case in Equation (D.3.4b) to develop a numerical scheme to solve Equation (D.4.8).

D5 Initial Separation Values

Table D5-1 Initial Separation Table Closed Pores

Voltage (V)	Slip Length Range (nm)	Slip Length (nm)	Initial Separation (µm)
Flat	0	0	2.29
20	40-60	50	2.03
25	60-100	80	2.12
30	50-70	60	2.06
40	40-90	80	2.14
50	120-180	150	2.25
80	100-300	200	2.15

Table D5-2 Initial Separation Table Open Pores

Voltage (V)	Initial Separation (µm)
Flat	2.36
20	2.61
25	2.58
30	2.12
40	2.12
50	2.10
80	2.21